TECHNISCHE UNIVERSITÄT WIEN

DISSERTATION

Synthesis and Characterisation of One-Dimensional Ge-Based Nanostructures with Metastable Composition

ausgeführt zum Zwecke der Erlangung des akademischen Grades eines

Doktors der technischen Wissenschaften

unter der Leitung von

Privatdoz. Dipl.-Chem. Dr.rer.nat. Sven Barth

E165

Institut für Materialchemie

eingereicht an der Technischen Universität Wien

Fakultät für Technische Chemie

von

Dipl.-Ing. Michael Stanislaus Seifner, BSc.

1025144

Wien, Februar 2019

Dipl.-Ing. Michael S. Seifner

down the river, boy, it takes a long ride, but I take it slow

Giant Rooks

II

Statutory Declaration

I herewith declare that I have authored this thesis independently, that I have not used other than the declared sources/resources, and that I have explicitly marked all material which has been quoted either literally or by content from the used sources.

Eidesstattliche Erklärung

Ich erkläre hiermit an Eides statt, dass ich die vorliegende Dissertation selbstständig und ohne fremde Hilfe verfasst, andere als die angegebenen Quellen und Hilfsmittel nicht benutzt und die den benutzten Quellen wörtlich und inhaltlich entnommenen Stellen als solche erkenntlich gemacht habe.

Acknowledgement

Several people accompanied me during my years as a PhD student and some of them even longer. Without them all of this would not have been possible. Therefore, I would like to thank…

… Sven Barth for guiding me through this thesis, several SEM measurements especially at the beginning of my PhD, and teaching me important aspects of life. Without his patience, knowledge, and encouragement all of this would not have been possible. I am very grateful for the time together and the things I have learned from him.

… our collaboration partners and especially Alois Lugstein, Masiar Sistani, and Max Bartmann for successful joint projects.

… Alois Lugstein for being my secondary examiner and Jürgen Fleig for reviewing my thesis.

… my former colleagues Felix Biegger, Patrik Pertl, Lukas Hrachowina, Felix Jungwirth, and Ivan Zivadinovic. I think we all have learned from each other and friendships have been built. Special thanks to Patrik Pertl for several SEM measurements at the beginning of my PhD and Felix Biegger for the support in the early beginnings.

… Leonie Deilmann for the great support and the friendship which developed during the joint PhD time.

… Michael Taubländer for being a great lab-buddy and his excellent taste in music.

… all colleagues from the university which contributed to the friendly working atmosphere and helped me with measurements or measured samples for me.

… the people from XRC and USTEM for the great support.

… my mother Andrea for her unconditional support and encouragement to go this way.

… my father Gerald for the continuous support throughout the years and for letting me win several sports competitions which gave me self-confidence.

… my sister Franziska for the great time together and her friendship, which is not obvious for siblings. I cannot believe we are living 26 years together now.

… my whole family for the great support and love.

… my friends for supporting me throughout my whole life and the great time together. I will never forget that. Special thanks to my oldest friend Christian.

Abstract

Problems concerning the native oxide of Ge hampered the integration of Ge into the Si-based semiconductor industry. After solving these problems and the successful integration of Ge on Si platforms, the superior properties of Ge in terms of hole and electron mobility when compared to Si have been used to develop novel high-performance devices. Nowadays, efficient doping of Ge which is already well-established for Si is now in the focus of this research field. In addition, metastable compounds based on Ge are of great interest due to the possibility of transforming Ge from an indirect bandgap semiconductor with very poor absorption and emission of light in the mid-IR range into a direct bandgap semiconductor. The down-scaling of material's dimensions towards the nanometre regime enables the growth of materials with special properties and compositions which cannot be observed and reached for bulk materials.

This work focuses on the growth of anisotropic, metastable alloys in a metal-assisted bottom-up growth process by the SLS/VLS-mechanism. The incorporation of the metal growth promoter by solute trapping during the growth of the Ge crystal is targeted which requires a kinetically controlled process at very low temperatures. In the first part of the results section the incorporation of Ga in a Ge crystal matrix via a vapour-phase process is described. The metastable composition of the material contains approximately four times the solubility limit at high temperatures and 50 times the composition limit at the actual growth temperatures. The material is highly conducting and shows metal-like behaviour.

Furthermore, the incorporation of Sn in anisotropic Ge crystals is realised via a solution-based microwave-assisted process. The metastable $Ge_{1-x}Sn_x$ alloy (x = 0.17 - 0.28) nanostructures are formed via homogeneous nucleation and without the use of a template. Several new findings such as the stability of α-Sn at high temperatures, the $Ge_{1-x}Sn_x$ material's stability with and without the presence of metallic Sn as well as the solid-state diffusion mechanism for the material degradation are observed. Based on these results, a phase map is suggested including the kinetic influence on phase evolution. In addition, the physical properties such as conductivity and indirect observation of a direct bandgap material are presented. The results obtained by this microwave approach are used to implement a vapour-phase process for the epitaxial growth of anisotropic, metastable $Ge_{1-x}Sn_x$ alloys with high Sn contents of 19 at. % on a Ge substrate. The size-dependence of a transition zone to accommodate the lattice mismatch between the growing material and the substrate is described. Finally, a direct bandgap of the material (0.29 eV) is demonstrated by photoluminescence. This is a significant step towards the integration of this compound on a Si platform.

The obtained materials are characterised by electron microscopy, X-ray diffraction, IR absorption, and photoluminescence measurements. Furthermore, single NW devices are fabricated to evaluate the electronic properties of metastable $Ge_{1-x}Sn_x$ and $Ge_{1-x}Ga_x$ nanowires. Results obtained in this thesis provide a deeper understanding of synthesis parameters of metastable compounds and demonstrate new approaches for the synthesis of materials achieved under kinetically controlled growth conditions.

Kurzfassung

Die Integration von Ge in die Si-basierte Halbleiterindustrie war aufgrund von Problemen mit dessen nativen Oxid lange Zeit nicht rentabel. Es wurde allerdings ein Weg gefunden diese Probleme zu umgehen und Ge erfolgreich auf Si-Plattformen zu integrieren. Die herausragenden elektrischen Eigenschaften von Ge im Vergleich zu Si konnten ausgenutzt werden, um neuartige Hochleistungsbauteile zu entwickeln. Heutzutage ist das effiziente Dotieren von Ge, welches für Si bereits weitestgehend erforscht ist, im Fokus dieses Forschungsfeldes. Außerdem sind metastabile Ge-Legierungen von großem Interesse, da sie die Möglichkeit bieten Ge von einem indirekten Halbleiter mit schlechter Lichtabsorption und -emission im mittleren Infrarotbereich in einen direkten Halbleiter umzuwandeln. Die Reduktion von Materialdimensionen innerhalb des Nanometerregimes ermöglicht das Wachstum von Materialien mit speziellen Eigenschaften und Zusammensetzungen, welche aus thermodynamischer Sicht unerreichbar wären, können dadurch realisiert werden.

Der Fokus dieser Arbeit liegt auf dem Wachstum anisotroper, metastabiler Legierungen in einem metallunterstützten Bottom-up-Wachstumsprozess mittels SLS/VLS-Mechanismus. Der Einbau des Wachstumskeims durch das Einfangen von Atomen an der Wachstumsfront des wachsenden Ge Kristalls wird in einem kinetisch kontrollierten Prozess bei sehr niedrigen Temperaturen durchgeführt. Im ersten Abschnitt der Arbeit wird über den Einbau von Ga in die Ge-Matrix mithilfe eines Gasphasenprozesses berichtet. Die metastabile Legierung enthält ungefähr die vierfache Menge an Ga im Vergleich zur thermodynamisch festgelegten Löslichkeitsgrenze bei hohen Temperaturen. Dies entspricht dem 50-fachen des thermodynamisch möglichen Einbaus bei der eigentlichen Wachstumstemperatur. Das erzeugte Material ist sehr leitfähig und zeigt metallähnliches Verhalten.

Außerdem wird der Einbau von Sn in einen anisotropen Ge-Kristall, mithilfe eines Mikrowellenprozesses in flüssiger Phase, realisiert. Die metastabilen, nanostrukturierten $Ge_{1-x}Sn_x$-Legierungen ($x = 0.17 - 0.28$) werden durch homogene Nukleation und ohne die Verwendung eines Templates erzeugt. Es können dabei einige neue Erkenntnisse, wie die hohe thermische Stabilität von α-Sn, die Stabilität der $Ge_{1-x}Sn_x$-Legierungen bei An- und Abwesenheit von metallischem Sn sowie ein Zerfall der metastabilen Legierung durch Festphasendiffusion, gewonnen werden. Darauf basierend wird eine Phasenkarte erstellt, die kinetische Einflüsse inkludiert. Außerdem werden physikalische Eigenschaften der hergestellten Materialien, wie die Leitfähigkeit und die indirekte Beobachtung eines direkten Halbleiterverhaltens, präsentiert. Die Ergebnisse der Mikrowellenmethode werden verwendet, um einen Gasphasenprozess für das epitaktische Wachstum von anisotropen, metastabilen $Ge_{1-x}Sn_x$ Legierungen mit hohem Sn Gehalt (19 at. %) auf einem Ge-Substrat zu ermöglichen. Die Größenabhängigkeit einer Übergangzone, die den Unterschied der Gitterparameter zwischen dem Substrat und der wachsenden Legierung ausgleicht, wird untersucht. Schließlich wird die direkte Bandlücke des Materials (0.29 eV) mittels Photolumineszensmessungen bestimmt. Die präsentierte Methode ist ein weiterer Schritt in Richtung der Integration dieser metastabilen Legierung auf eine Si-Plattform.

Die synthetisierten Materialien werden mittels Elektronenmikroskopie, Röntgendiffraktion, IR Absorption und Photolumineszensmessungen charakterisiert. Außerdem werden Einzeldrahtmessungen an metastabilen $Ge_{1-x}Sn_x$- und $Ge_{1-x}Ga_x$-Nanodrähten zur Evaluierung der elektrischen Eigenschaften durchgeführt. Die erhaltenen Resultate dieser Arbeit liefern ein tieferes Verständnis der Syntheseparameter metastabiler Verbindungen und zeigen neue Methoden zur Synthese von Materialien bei kinetisch kontrollierter Prozessführung.

Table of Contents

1 Introduction

For a long time, Ge has not played a role in complementary metal-oxide-semiconductor (CMOS) industry due to the poor quality of the native oxide. GeO_2 is unstable and decomposes to several suboxides which create a high density of traps at the interface to Ge.[1, 2] However, this problem has been solved by the possibility to grow high-κ dielectrics on Ge.[3-8]

Among all known semiconductors, Ge has the highest hole mobility and at the same time higher electron mobility compared to Si. A comparison of Si, Ge, and III/V-semiconductors is shown in Figure 1. Although III/V-semiconductors exhibit very high electron mobilities, the hole mobilities are relatively low due to the larger valence band effective mass and higher carrier-scattering rate for hole transport. Furthermore, the bandgap energy is an important property of a semiconductor targeted for the use in devices such as metal-oxide-semiconductor field-effect transistors (MOSFETs). The bandgap energy should be high enough when compared to the supply voltage to prevent band-to-band tunnelling (BTBT) and thermionic emission resulting in leakage. Although III/V-compounds such as InSb and InAs have high electron mobilities, they are not the ideal candidates for MOSFET-fabrication due to their small bandgap energies. Considering all these points, Ge is an ideal candidate to improve the performance of MOSFETs.[9]
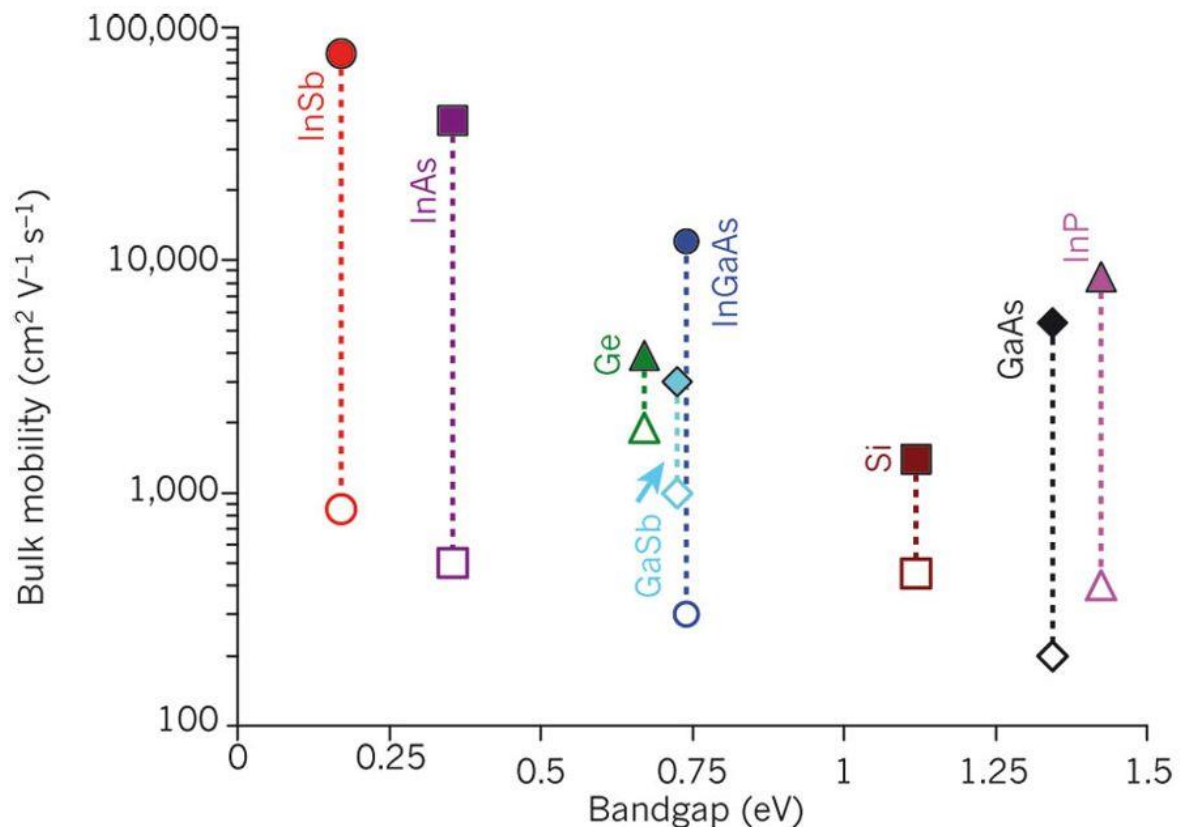

Figure 1: The bulk hole (unfilled symbols)/electron (filled symbols) mobility and the corresponding bandgap energy for different semiconductors. Reproduced with permission from Springer Nature.[9]

Several approaches to integrate Ge on a Si substrate have emerged over the last decades which is a crucial step to process Ge by conventional CMOS techniques. The large lattice mismatch of 4.2 % between Ge and Si results in high defect densities when Ge is epitaxially grown on a Si substrate due to the high internal strain which cannot be compensated after a few monolayers. Misfit dislocations allow the epitaxially grown Ge thin film to relax but at the same time the electrical and optical properties are degraded.[10]

Therefore, $Si_{1-x}Ge_x$ buffer layers are used to either gradually or abruptly, in a few steps, increase the lattice parameter. The Ge layer can then be grown on the buffer layer and defect density is reduced dramatically.[11-16] Another possibility is the epitaxial growth of a thick Ge layer in a two-step process and subsequent thermal annealing to reduce the defect density near the surface.[17-20] Besides these approaches, alternative techniques including wafer bonding,[21] condensation,[22] and lateral liquid-phase epitaxy have emerged.[23]

The ongoing miniaturisation of devices towards the nanometre regime makes the controlled synthesis of suitable building blocks vital. During the last two decades many approaches enabling the morphologically controlled synthesis of Ge nanostructures have been established. A very interesting method for the anisotropic crystal growth of Ge nanostructures is the metal-assisted bottom-up growth.[24]

Group 14 elements can cover a wide range of applications but are limited by their physical properties which includes the indirect bandgap behaviour of Si and Ge. Recently, significant improvements in the electrical and optical properties of group 14 semiconductors by doping/alloying with atoms of different elements have been demonstrated.[25-28] For instance, specific synthesis conditions allow the intentional incorporation of atoms from the seeding metal particle in the growing semiconductor crystal via a metal-supported growth technique.[29-35] However, a controlled incorporation of atoms from the seed beyond the solubility limit, which is ruled by thermodynamics, is still a very challenging task.

The expected effects for the incorporation of impurities in the Ge matrix on the physical properties strongly depend on the element which is used for this purpose. For instance, incorporation of group 13 elements such as Ga which is part of this thesis creates charge carries in the valence band. The resulting shift of the Fermi level can be carried to the limit by alloying beyond the maximum solubility which can lead to a degenerate semiconductor showing metal-like behaviour.

One possibility to dramatically improve the optical properties of Ge can be achieved by alloying Ge with high amounts of Sn which would pave the way for the fabrication of novel optoelectronic devices operating in the mid-infrared (mid-IR) range.[27, 36] However, alloying Ge with the targeted high amount of Sn results in a metastable compound which requires a kinetically driven process for the growth of this material. The interest in realising high Sn incorporation in the Ge host lattice can be confirmed by an increasing number of publications (Figure 2a) and citations of these publications (Figure 2b) focusing on the metastable $Ge_{1-x}Sn_x$ alloy as illustrated in Figure 2.
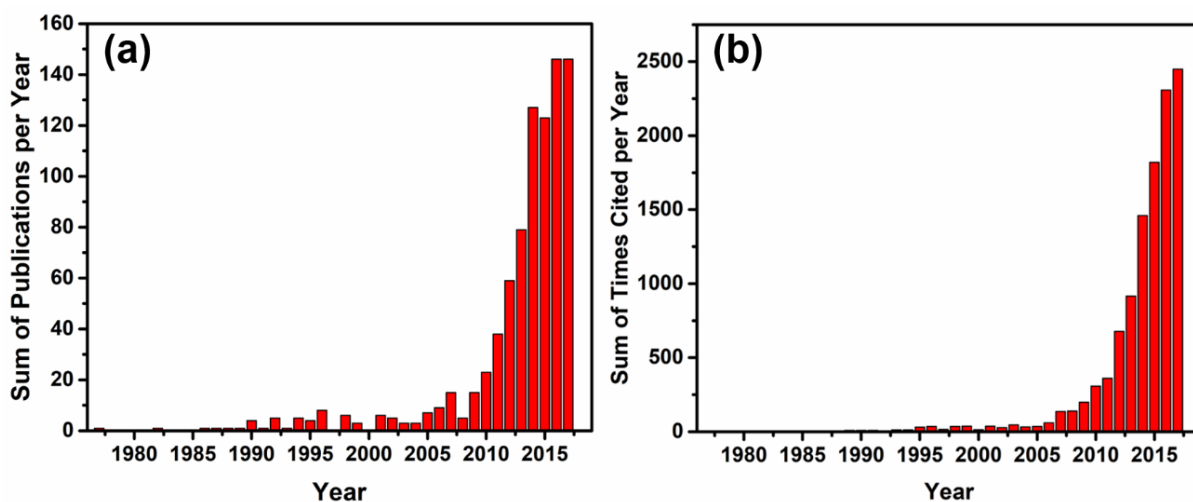
Figure 2: (a) shows the sum of publications per year reporting on $Ge_{1-x}Sn_x$ alloys during the years 1977 - 2018. (b) The sum of citations of publications considered in (a) are plotted for the same time range (www.webofknowledge.com, search item: GeSn or $Ge_{1-x}Sn_x$ or $Ge_{1-y}Sn_y$, 08.02.2019, 15:19).

1.1 Anisotropic Ge nanostructures

Controlling the morphology of a material is a matter of great importance in the materials community. It is well-known from literature that physical properties can be altered due to quantum confinement effects.[37-39] Furthermore, surface effects are more dominant for materials where certain dimensions are scaled down towards the nanometre regime.[40] One-dimensional (1D) Ge nanostructures, such as nanorods (NRs) and nanowires (NWs), are applicable in many research areas including electronics,[41, 42] optoelectronics,[43] sensors,[44, 45] and batteries.[46-48] The term "one-dimensional" describes the morphology of a structure and means that one dimension is outside the nanometre regime (< ~ 100 nm).[24] However, it must be distinguished between two general strategies to produce these structures.

The first approach is based on the controlled removal of atoms from a bulk material to obtain the desired anisotropic structure. The so-called top-down method includes masking techniques in combination with chemical and physical etching. The most prominent benefit of this approach is meticulous morphological control, but at the same time a low throughput and rough surfaces are undesirable.[24]

On the other hand, an anisotropic morphology can be achieved by the controlled nucleation and growth of a crystal using molecular or atomic building-blocks. This bottom-up approach includes synthesis strategies where the crystal growth on certain facets is inhibited[49] or templates force the nucleation and growth of the crystal in a certain direction resulting in the desired geometry.[50-52] In addition, defects on a substrate including screw dislocations can force the controlled nucleation resulting in 1D structures.[53]

1.1.1 The metal-assisted growth of 1D structures

This thesis focuses on the metal-assisted growth of anisotropic structures. Metal particles can act as growth promoter enabling the controlled nucleation and growth of materials including group 14 semiconductors.[24] The first attempt of growing anisotropic structures by a metal-assisted approach can be traced back to a report in the year 1964 where Au facilitates the growth of Si whiskers.[54]

Literature differentiates between vapour- and liquid-phase environments in which the precursor is supplied. Furthermore, it is important to distinguish between the different aggregate states of the metal under growth conditions.[24] The most important terms including information on the conditions during metal-assisted growth of anisotropic materials are vapour-liquid-solid (VLS),[54] vapour-solid-solid (VSS),[55] and solution-liquid-solid (SLS) growth mechanism.[56] Some studies report on metal-assisted growth in a supercritical fluid (SF).[57-60] The notation of these mechanisms contains information on the medium which transports the precursor, the aggregate state of the metal, and the aggregate state of the growing material.

For the synthesis of anisotropic Ge crystals via a bottom-up process based on the supply of Ge by the thermal decomposition of a Ge precursors, certain requirements must be fulfilled. The efficient removal of ligands from the precursor molecule is vital to observe anisotropic Ge crystals with high quality. Depending on the phase in which the process is implemented, further properties of the precursor molecule are important to be applicable for the targeted process including, *e.g.*, vapour pressure and solubility. Common precursor molecules acting as source for the supply of Ge by thermal decomposition are summarised in Table 1. Besides the thermal decomposition of a precursor, reducing agents which are not considered in Table 1 can initiate the decomposition of the precursor molecule at lower temperatures.[61]

Table 1: Common Ge precursors to produce nanostructures via vapour-, solution-, and supercritical fluid-based processes and the temperature of their thermal decomposition.

Precursor	Decomposition temperature (°C)	Phase	Reference
bis[bis(trimethylsilyl)amido]germanium(II)	325/285	vapour/liquid	[62, 63]
bis[π-cyclopentadienyl]germanium(II)	325	vapour	[64]
digermane	300	vapour	[65]
diphenylgermane	400	supercritical fluid	[66]
germane	300	vapour	[67]
n-butylgermane	370	vapour	[68]
oligosilylgermane	170	liquid	[69]
t-butylgermane	300	vapour	[70]

Furthermore, a wide range of metals was investigated in terms of their capability to facilitate the growth of 1D Ge nanostructures. The metals suitable for this purpose are summarised in Table 2 and the related minimum synthesis temperature and the aggregate state of the metal during growth are noted.

Table 2: Summary of metal seeds initiating the growth of 1D Ge structures and minimum growth temperatures in a process where Ge is supplied by the thermal decomposition of a precursor molecule. This table is limited to pure metals without formation of germanides at the growth temperature.

Metal	Minimum growth temperature (°C)	Precursor	Mechanism	Reference
Ag	370	diphenylgermane	SFSS	[59]
Al	400 - 450	diphenylgermane	SFSS	[71]
Au	250	digermane	VSS	[72]
Bi	350	germanium diiodide	SLS	[56]
Ga	170	t-butylgermane	SFLS	[73]
In	180	oligosilylgermane	SLS	[69]
Ir	460	diphenylgermane	SFSS	[74]
Pb	330	diphenylgermane	SFLS	[75]
Sb	650	germanium	VLS	[76]
Sn	230	germanium imides	SLS	[77]

Low melting metals in combination with a precursor decomposing at low temperatures open the possibility to grow anisotropic Ge nanostructures with metastable composition. The seed material can be incorporated in the Ge matrix via the interface of the liquid metal and the growing material in a kinetically controlled process. As result, metastable Ge-based alloys with novel physical properties can be realised by this approach and will be discussed *vide infra*.

1.2 Doping

Altering the electrical properties of Si and Ge by the incorporation of foreign atoms in the crystal lattice is a common method in the semiconductor industry. For the so-called doping of group 14 semiconductors group 13 and 15 elements are of great interest. In a simplified scenario, the foreign atom is supposed to substitute a group 14 atom on a regular lattice position. Ge and Si have a high degree of covalence in bonding which allows the prediction of the generated charge carrier type by the valency of the doped element. Considering this definition group 13 dopants (acceptors) generate additional holes (p-type semiconductor) while group 15 dopants (donors) generate additional electrons (n-type semiconductor) in the group 14 semiconductor. In detail, donors can transfer an extra electron to the conduction band, while acceptors can bind an electron from the valence band resulting in an additional hole in the valence band. Furthermore, it must be distinguished between shallow and deep-level donors/acceptors. The energy levels of shallow donors/acceptors differ by only a small margin from the conduction/valence band energy resulting in a very efficient transfer of the electron. On the other hand, deep-level donors/acceptors are inefficient in generating mobile charge carries and act as undesirable non-radiative recombination centres of electron-hole pairs. A prominent example for unwanted deep-level traps in a semiconductor is the incorporation of Au atoms in the Si matrix when producing Si NWs via the VLS-mechanism using Au as growth promoter.[78-81]

One cubic centimetre of Ge contains approximately $4.4 \cdot 10^{22}$ Ge atoms. For doping of group 14 semiconductors, the range of impurity concentrations cannot be defined easily but is approximately $< 10^{20}$ cm^{-3} (0.23 at. %)[82] which is below the thermodynamically fixed maximum solid solubility of common group 13 and 15 elements in Ge.[83-87] Consequently, the host material retains its crystal structure by the incorporation of dopants. For impurity concentrations $< \sim 10^{20}$ cm^{-3}, the consideration of localised energy levels within the electronic band structure of the pure semiconductor is valid. The situation changes dramatically for highly doped group 14 semiconductors where impurities cannot be longer considered as localised energy levels. Consequently, localised energy levels merge to impurity bands resulting in a significant change of the physical properties of the material, which will be discussed in detail in Chapter 1.3.[82, 88-90]

Ideally, dopants occupy a regular position of the host lattice such as Ge.[91] At thermal equilibrium, vacancies are the predominant intrinsic point defects in Ge and much higher concentrated than interstitial defects due to the lower formation energy of vacancies in Ge.[92-96] At elevated temperatures these vacancies can interact with impurities located at a substitutional site promoting the diffusion in Ge via mobile impurity-vacancy pairs.[97]

The temperature-dependent diffusion coefficients of group 13 and 15 dopants are compared to Ge self-diffusion, which is the diffusion of Ge atoms in Ge bulk-material, in Figure 3. Localised states within the bandgap of Ge formed by impurities and intrinsic defects can be charged depending on whether these states are occupied or not which strongly depends on the location of these states with respect to the Fermi level.[98] Vacancies in n-type Ge are dominated by doubly negatively charged species, while group 15 impurities on a substitutional site are singly positively charged resulting in a strong Coulomb interaction between these species.[99-101] For p-type Ge, neutrally charged vacancies are pronounced and singly negatively charged group 13 impurities on a substitutional site are expected.[91, 100] For n-type (group 15) dopants the diffusion through the Ge matrix can be described by the vacancy

mechanism via a singly negatively charged impurity-vacancy pair.[99, 101, 102] Also the diffusion of group 13 dopants in Ge is mediated via vacancies except for B which forms non-stable B-vacancy pairs and due to the high diffusion activation energy an interstitial mechanism is suggested.[91, 103-105] Diffusivities of group 15 impurities in Ge are much higher compared to group 13 dopants due to smaller Coulomb interactions between the substitutional group 13 dopant and a vacancy.[100] For n-dopants of group 15 a clear increase of the diffusion coefficient can be observed due to the increasing stability of the group 15 impurity-vacancy pair for higher atomic numbers which can be ascribed to elastic interactions.[91] The diffusion coefficients are very important to predict whether a dopant is suitable to achieve the desired doping profile after implantation of the impurity and subsequent thermal annealing which will be discussed *vide infra*.
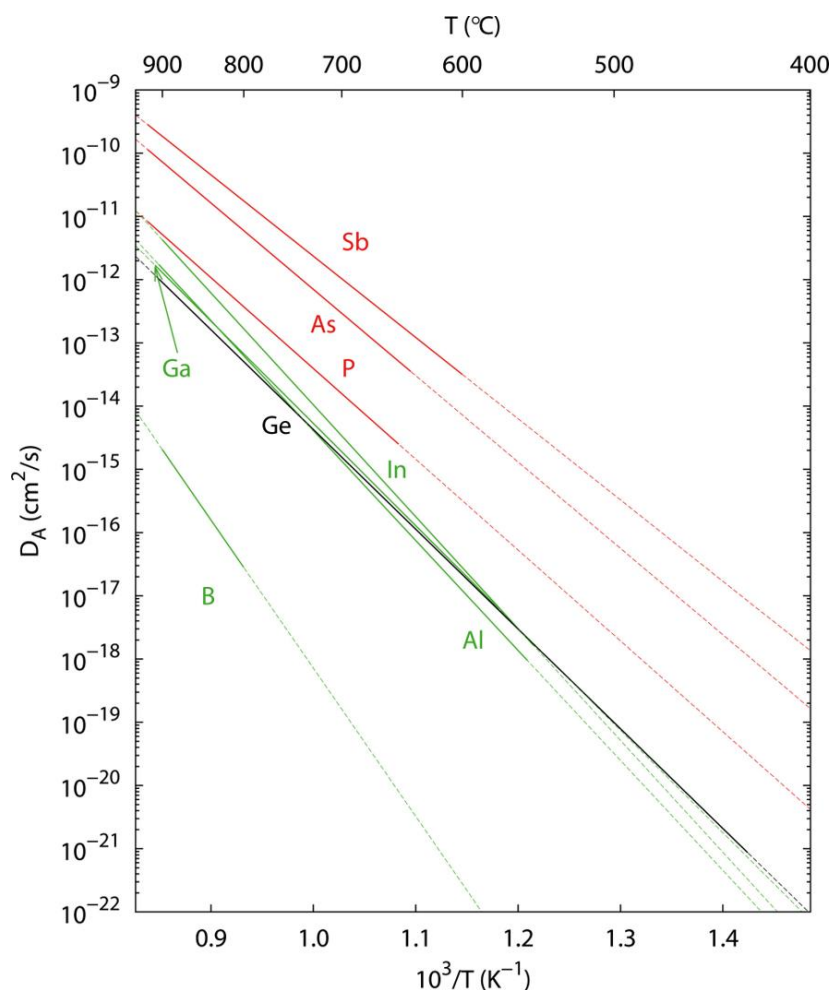

Figure 3: Diffusivities of different dopants in Ge versus temperature. Reproduced with permission from AIP Publishing.[100]

Furthermore, a strong enhancement of donor diffusion for n-doping levels in the extrinsic doping regime can be observed, which means that the carrier concentration is dominated by the doping-level and not by the intrinsic carrier concentration.[99] In contrast to extrinsic semiconductors, the carrier concentration in intrinsic semiconductors strongly depends on the temperature. A possible explanation for this experimental observation can be provided by *ab initio* calculations as shown in Figure 4 predicting a decrease of the formation energy of doubly

negatively charged vacancies by increasing the Fermi level in n-type Ge.[106] Consequently, a higher concentration of impurity-vacancy pairs can be expected for higher Fermi levels which is equal to a higher n-type doping-level.[107]
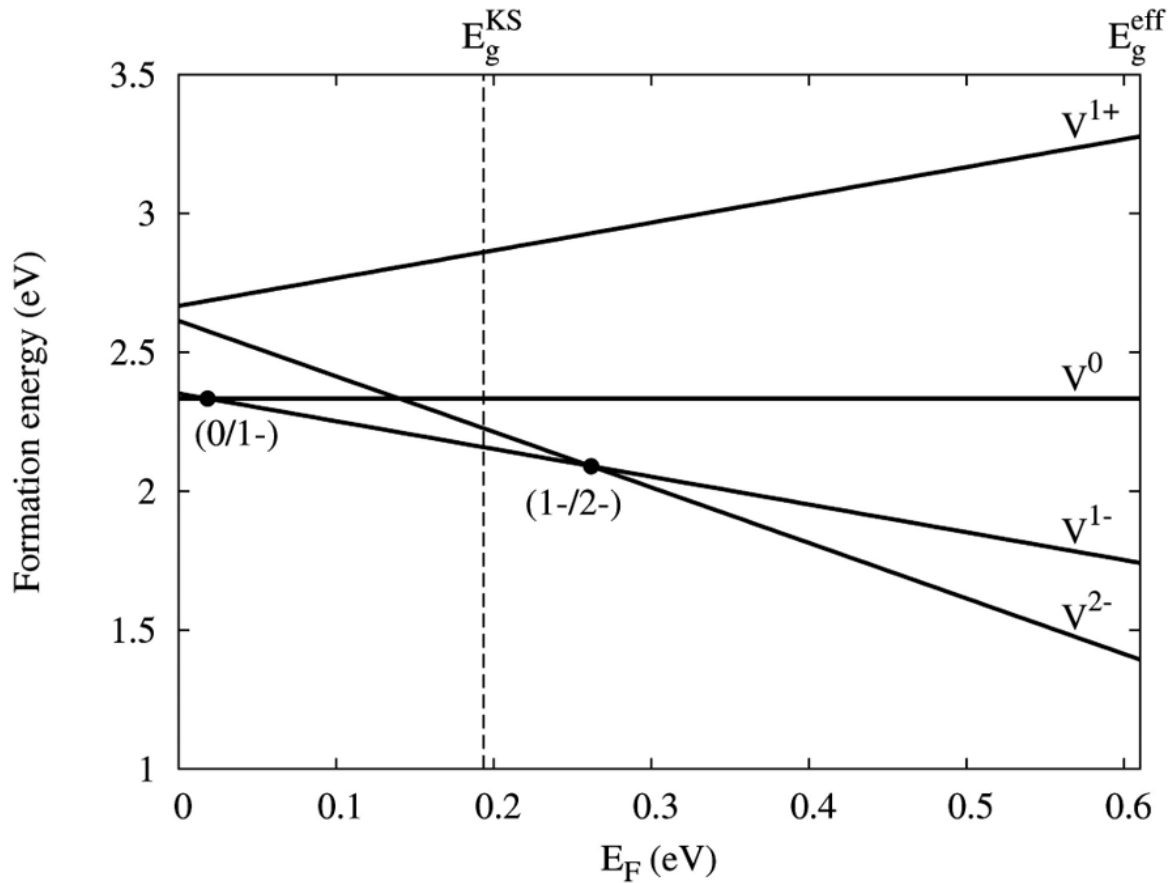

Figure 4: The formation energy of vacancies with different charges is plotted versus the Fermi energy which suggests the predominance of doubly negatively charged vacancies for highly n-doped Ge. Reproduced with permission from AIP Publishing.[106]

1.2.1 Techniques for producing highly doped Ge thin films

Over the years a wide range of different techniques to produce n- and p-type doped Ge thin films have been developed. It has been shown that for n-type doping P is a very promising candidate due to the higher solubility in Ge, the lower activation energy for creating electrically active impurities, and lower diffusivity in Ge resulting in a much higher maximum active dopant concentration when compared to As and Sb. The maximum solubility of P in Ge is $6 \cdot 10^{20}$ cm^{-3} (1.36 at. %) which is the highest value when compared to As ($2 \cdot 10^{20}$ cm^{-3}/0.45 at. %) and Sb ($1.5 \cdot 10^{19}$ cm^{-3}/0.03 at. %).[83, 108]

In the case of p-type doping B is of great interest. As discussed earlier, the formation of B-vacancy pairs is energetically not favourable and a diffusion mechanism mediated by interstitial defects which are not common in Ge is suggested.[91-96, 103] Therefore, high active dopant concentrations can be reached with B due to the high solid solubility (> 10^{20} cm^{-3} over a wide temperature regime) and the low diffusion tendency in Ge in a moderate temperature regime.[83, 109, 110]

In general, the production of highly n-type doped Ge thin films is more complicated compared to highly p-type doped Ge. This phenomenon can be ascribed to the high diffusivities of group 15 impurities in Ge resulting in broad dopant spatial distributions and a high deactivation mediated by negatively charged vacancies.[100, 107]

Different techniques for doping Ge with P can be found in literature and are discussed in terms of achievable active dopant concentrations and the state of the doping profile. The alternative doping methods for the standard ion implantation technique can be grouped into *in situ* and *ex situ* techniques.

By ion implantation of P and subsequent rapid thermal annealing (RTA) of the Ge thin film at 500 °C maximum electrically active dopant concentrations up to $5 \cdot 10^{19}$ cm^{-3} are obtained along the doping profile. The repetition of implantation and RTA leads to electrically active dopant peak concentrations up to $1 \cdot 10^{20}$ cm^{-3}. At an implantation dose of $6 \cdot 10^{14}$ P cm^{-2} per cycle the depth of the doping profile is approximately 200 nm.[111]

Ex situ approaches including gas immersion laser doping (GILD)[112] and spin-on dopant (SOD)[113] avoid ion implantation and the resulting lattice damage giving electrically active dopant concentrations higher than $1 \cdot 10^{19}$ cm^{-3} and box-like doping profiles.

Co-doping, which means the incorporation of dopants during the growth of a Ge thin film (*in situ*), can be performed by chemical vapour deposition (CVD)[114-117] or molecular beam epitaxy (MBE)[118] approaches resulting in electrically active dopant concentrations in the range of $1 \cdot 10^{19}$ cm^{-3} - $8 \cdot 10^{19}$ cm^{-3}. Furthermore, deep box-like doping profiles can be achieved by this method.

A very promising technique to obtain highly P-doped Ge is the so-called δ-doping. In a typical process, Ge thin films are deposited via MBE[119-121] or CVD[122, 123] followed by P precursor (PH$_3$ or P$_2$) dosing. The dosed molecules are adsorbed on the Ge surface and thermally incorporated within the Ge surface layer. In a further step, Ge is again grown epitaxially on top of the P-enriched surface. This process can be repeated to produce stacked δ-doped layers with arbitrary thickness. The δ-doped layers are few nanometres thick and separated by very thin Ge spacers (down to 2 nm) to prevent dopant diffusion. At the end of the process a Ge capping layer is deposited on top of the stacked δ-doped layers. Electrically active dopant concentrations up to $1.8 \cdot 10^{20}$ cm^{-3} are demonstrated and a sharp box-like shaped doping profile near the surface is achieved by this technique.[121]

In addition, ion implantation is a possible strategy to reach high doping levels for p-type doping of Ge with B.[109, 110, 124] The drawbacks of ion implantation namely lattice damage and a high number of electrically inactive impurity-defect clusters, which are congregates of more than two point defects, are less problematic in the case of B-doping resulting in a high dopant activation right after the implantation. Hole concentrations up to $2 \cdot 10^{20}$ cm^{-3} have been reported which is a desired doping level for many applications.[110]

Besides ion implantation, a high number of *in situ* approaches can be found in literature including CVD[125-127] and MBE.[128, 129] *In situ* B-doping of epitaxially grown Ge on Si with different substrate orientations via an ultra-high vacuum CVD (UHVCVD) process is presented in literature. For Ge grown on Si(100) which is the standard in the semiconductor industry, electrically active dopant concentrations up to $4 \cdot 10^{19}$ cm^{-3} can be obtained.[127]

The higher tendency of n-type dopants to form deep-level impurity-vacancy clusters compared to p-type dopants results in a higher amount of electrically inactive impurities for

group 15.[130, 131] In addition, electrically inactive defect clusters can be formed for impurity concentrations > 10^{20} cm^{-3} and deactivate group 15 dopants.[99, 105, 107] As already discussed above, dopant deactivation for B-doped Ge is not that much pronounced when compared to n-doping due to predominant neutrally charged vacancies in p-type Ge.[91, 100] However, thermal annealing and activation of the impurity after ion implantation via recrystallisation of the Ge crystal lattice is a crucial step due to the induced lattice damage by this method. The lattice damage which is more pronounced for implantation of atoms with higher atom mass has to be limited by keeping the implantation energy/dose as low as possible.[132]

Standard techniques for thermal annealing of semiconductors are furnace annealing (FA),[133-135] RTA,[109] flash lamp annealing (FLA),[136] laser annealing (LA),[135, 137] and solid-phase epitaxial regrowth (SPER).[138] High dopant activation is observed by B implantation in Ge with subsequent thermal annealing[103, 109, 139] but even without.[110] On the other hand, thermal annealing of group 15-doped Ge by ion implantation is critical in terms of substrate loss[140] and dose losses caused by out-diffusion.[137] Substrate loss is a phenomenon emerging by the thermal annealing of uncapped Ge substrates and describes the loss of Ge material during this process. However, the origin of this effect still remains unclear.[140] However, dopant activation for P-doped Ge produced by ion implantation and subsequent thermal annealing is well-studied and demonstrated successfully in literature.[111, 141-143]

In addition, much research effort is put into point defect engineering strategies to reduce extrinsic donor diffusion and to increase the electrically active dopant concentration. Impurity-vacancy pairs cause diffusion of group 13 (excluding B) and 15 dopants in Ge.[97] Therefore, the main approaches to prevent dopant diffusion are creating self-interstitials during the ion implantation which then can recombine with vacancies during the thermal annealing[144, 145] and co-doping of electrically inactive impurities for trapping vacancies.[105, 131, 146-149]

1.2.2 Devices

In the recent past, diodes,[150-154] photodetectors,[155-158] transistors,[4, 7, 159-173] and lasers[25, 26] based on Ge have been developed. Therefore, the controlled incorporation of impurities to achieve high-quality p-n-junctions with shallow junction depths is a crucial step to obtain electronic and optoelectronic devices with high performances.[174]

Several approaches for the formation of high-quality p$^+$-n- and n$^+$-p-junctions based on Ge haven been presented which resulted in the fabrication of high-performance Ge-based diodes.[150-154] In addition, Ge photodetectors with p-i-n-junctions have been realised and their performances are comparable to state-of-the-art In$_{1-x}$Ga$_x$As (InGaAs) photodetectors.[155-158]

A high number of Ge p-MOSFETs with excellent hole mobilities can be found in literature.[4, 7, 159, 161-166] On the other hand, the performance of Ge n-MOSFETs is still limited by the parasitic resistance of the source/drain which can be assigned to the already discussed complexity of n-type doping for Ge. However, the first high-performance Ge n-MOSFET has been presented recently. LA after the implantation of the dopant results in a high dopant activation and a significantly reduced sheet resistance due to the high-quality n$^+$-p Ge junctions.[168] The complexity of n-type doping for Ge n-MOSFETS can also be overcome by the substitution of highly n-type doped source and drain using a metal source/drain MOSFET configuration.[169, 170, 175, 176]

Additional architectures for field-effect transistors (FETs) based on Ge NWs are presented in literature.[41, 42, 171-173, 177] Ge NWs with few diameters showing quantum confinement effects are very promising building blocks for MOSFETs due to ballistic transport and conductance quantisation.[178, 179] However, the formation of an electrical contact between a metal and the Ge NW is a crucial and highly investigated step to obtain low parasitic resistance of source/drain. Fermi level pinning due to the high density of metal-induced gap states is very common for metal/Ge contacts resulting in high Schottky barriers for electrons. Therefore, Fermi level depinning is the key to obtain a low parasitic resistance of source/drain.[169, 180-182]

Ge lasers working in the mid-IR range require high n-doping levels to shift the Fermi level towards the minimum of the direct Γ-valley which forces the electrons to occupy the Γ-valley and is vital due to the indirect bandgap behaviour of Ge.[183, 184] The successful implementation of optically[25] and electrically[26] pumped Ge lasers has been demonstrated in literature.

1.3   Hyperdoping

Doping beyond the thermodynamically fixed solubility limit accompanied by a high carrier concentration can be called "hyperdoping" and has the potential to alter the physical properties of semiconductors dramatically due to the formation of impurity bands which can additionally interact with conduction or valence band.[82, 88-90] However, to achieve hyperdoping kinetically controlled processes must be established resulting in material compositions which are not thermodynamically stable.

For Si and Ge, effects including the metal-insulator transition, sub-band gap optical absorption, and localised surface plasmon resonances can be observed by hyperdoping.[185-187] The incorporation of deep-level dopants in Si such as chalcogens,[186, 188] Ti,[189] and Au[190] is a highly interesting field of research due to the potential of realising Si-based short-wavelength infrared (IR) photodetectors. Furthermore, the intermediate-band formation in highly deep-level doped Si NWs could overcome the Shockley-Queisser limit by extending the energy range of absorbed photons which would be a breakthrough in the solar cell community.[188, 191-195]

The existence of deep-level traps in chalcogen-doped Ge shows the possibility of deep-level impurity bands also for Ge.[196] In this respect, the incorporation of high S concentrations into Ge by a pulsed laser process obtained an external quantum efficiency higher than 100 % for the produced photodiode.[197]

Recently, a high amount of Al incorporation was observed in Al-assisted bottom-up grown Si NWs via the VLS-mechanism (Figure 5).[29-31] An electrically active dopant concentration of approximately $1 \cdot 10^{19}$ cm^{-3} for Si NWs has been reported by this approach.[29] A detailed investigation of the incorporation mechanism of Al in the Si matrix is presented and homogeneously distributed Al contents of 4.3 at. % which are far beyond the maximum solid solubility of Al in Si are obtained.[198] Solute trapping[199, 200] at step edges during the step-flow growth[201, 202] of the bilayers is identified as reason for this observation.[31] The determined growth rate is quite low making incorporation beyond the thermodynamic limit implausible by the suggested model. However, the high incubation time required for the nucleation is identified as the growth rate-determining step. Therefore, the required time for the step to grow across the whole NW diameter is low enough to enable high Al incorporation. Furthermore, a temperature-dependence of the Al incorporation is observed. At 410 °C the incorporation of

0.4 at. % is achieved, while at 470 °C Al contents up to 4.3 at. % are reached. This observation points out that not only the rate of thermally activated atomic jumps but also other parameters have to be taken into account and incorporation of impurities via the VLS-mechanism is different for each binary system.[30, 31]
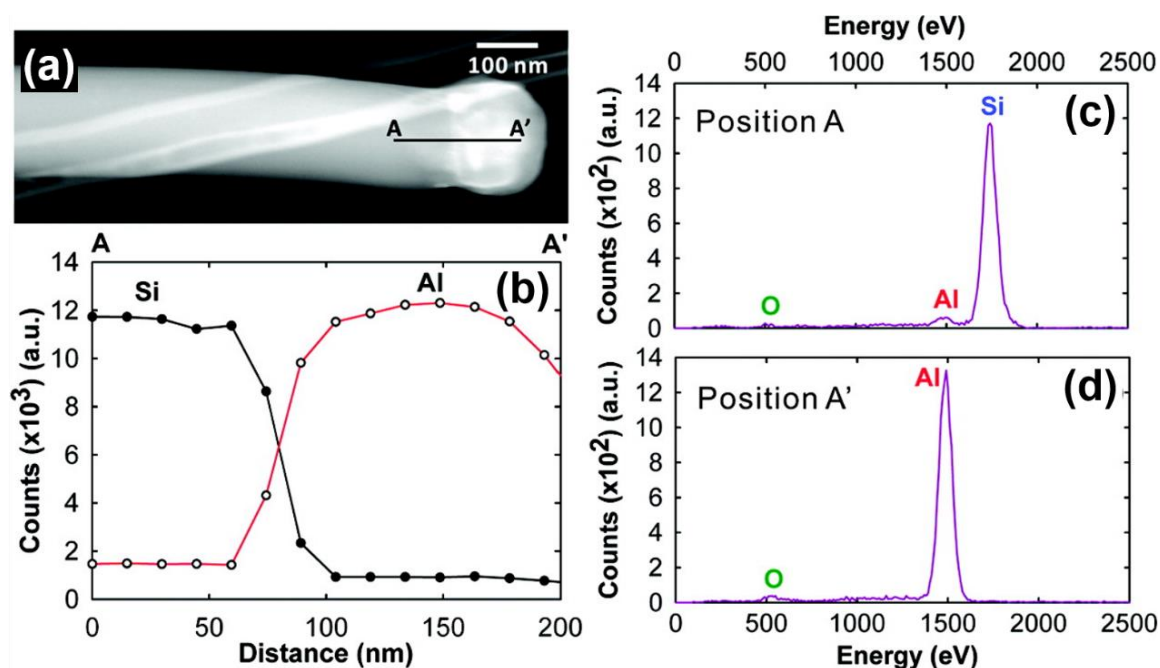

Figure 5: (a) shows an annular dark-field transmission electron microscopy (TEM) image of an Al-seeded Ge NW. (b) An energy dispersive X-ray spectroscopy (EDX) line-scan is collected along the line indicated in (a). EDX spectra collected from (c) position A which is within the NW body and (d) position A' which belongs to the Al seed. Reproduced with permission from American Chemical Society.[29]

Growth promoters considered for the metal-assisted bottom-up growth of Ge NWs by the thermal decomposition of a precursor molecule which have potential of being incorporated in the NW matrix can be found in Table 2. However, high incorporation shall be achieved by a kinetically controlled process which requires low growth temperatures and at the same time high growth rates. The minimum growth temperature is limited by the decomposition temperature of the Ge precursor at which the metal should be in the liquid aggregate state to ensure a higher probability for incorporation in the Ge lattice. Ir has a very high melting point and can therefore be ruled out for this purpose. Furthermore, Ag and Au create deep-level traps in Ge,[203] while Pb[204] and Sn[205] can be used for altering the band structure of Ge. Therefore, only Al, Bi, Ga, In, and Sb can be considered as growth promoters having the potential of being incorporated into the Ge lattice during the VLS-growth and increasing the charge carrier concentration dramatically. However, under the used synthesis parameters no incorporation in the Ge matrix is observed for Al-,[71] Bi-,[56] and Sb-facilitated[76] growth of Ge NWs.

In contrast, high incorporation of In in Ge NWs via a low temperature synthesis approach can be achieved. Although In contents up to approximately 2 at. % are obtained, no data on the electrically active dopant concentration is provided making statements about the efficiency of this approach impossible.[69] A procedure for the production of Ga-doped Ge NWs by the

incorporation of Ga from the growth seed is presented in this thesis and explained in detail *vide supra* (Chapter 3.1).

Besides synthesis strategies based on the thermal decomposition of a precursor, Ge microwires (MWs) using Ga, In, Bi, Hg, and alloys of these elements as growth promoter are produced in an electrochemical liquid-liquid-solid (ec-LLS) approach at temperatures below 100 °C.[32-35, 206-211] The observed impurity levels and resistivities of Ge MWs are summarised in Table 3.

Table 3: Summary of metal incorporation in Ge MWs synthesised via the ec-LLS approach.[32-35, 206]

Growth promoter	Impurity level (at. %)	Resistivity (Ω·cm)	Reference
Ga	~ 10	1.5	[33]
$Ga_{0.832}In_{0.168}$	~ 10 (Ga), < 10^{-1} (In)	~ $5 \cdot 10^{-3}$	[35]
In	0.14	$3.8 \cdot 10^{-5}$ (estimated)	[32]
$Bi_{0.213}In_{0.787}$	~ 6 (In), ~ 3 (Bi)	$3.2 \cdot 10^{-3}$	[34]
Hg	-	0.4	[206]

Although extraordinary high amounts of Ga, In, and Bi are incorporated in the Ge matrix only a small fraction seems to be electrically active. A reason for the high resistivity considering such high dopant concentrations could be related to crystallinity issues, high 2- and 1-dimensional defect densities, non-substitutional incorporation of the dopant, and electrically inactive impurity-defect clusters.[33-35] In seems to be incorporated at substitutional sites of the Ge crystal lattice quite efficiently at process temperatures of 95 °C. However, it must be considered that the resistivity is just estimated by the blue-shift in the absorption spectrum whereby results from this report should be questioned critically.[32]

Figure 6 shows the maximum solid solubility of $Bi^{[212]}/In^{[213]}$ in Ge which is approximately $7 \cdot 10^{16}$ cm^{-3} ($1.6 \cdot 10^{-4}$ at. %)/$4 \cdot 10^{18}$ cm^{-3} ($9.1 \cdot 10^{-3}$ at. %) and clearly points out the potential of achieving high dopant concentrations by the ec-LLS approach. Nevertheless, it should be considered that resistivity values are far too high for such high dopant concentrations. This raises the question where the electrically inactive impurities are located and if metal clusters homogeneously dispersed in the Ge matrix and/or high defect densities may cause the observed slight/missing reduction of resistivity when compared to intrinsic Ge.[214, 215]

The incorporation of high amounts of Al, Ga, In, P, As, and Sb in Ge nanocrystals can be enabled via a solution-based process.[216] The binary phase diagrams of Ge with these elements suggest an incorporation beyond the solubility limit at the chosen synthesis temperature of 300 °C.[84-87, 213, 217] However, no free charge carries could be observed via optical absorption and electron paramagnetic resonance (EPR) spectroscopy. Ligand-bonding to impurities as well as surface and bulk defects are suggested as main reasons for this observation.[216]

A microwave-assisted solution-based process for hyperdoping Ge nanocrystals facilitates Bi concentrations up to 2 at. %[218] which is far above the maximum solid solubility of approximately $1.6 \cdot 10^{-4}$ at. % Bi in Ge.[212] X-ray diffraction (XRD) measurements confirm the successful incorporation of Bi in the Ge lattice leading to a shift of the Ge reflections towards smaller 2θ values and exclude the presence of a crystalline Bi phase; however, this does not

exclude clustering of Bi in a size range being X-ray amorphous. Increased conductivity values are obtained for incorporation of Bi as determined by resistance measurements of Bi-doped Ge nanocrystal films and can be assigned to both higher free charge carrier densities and lower bandgap energies.[218]
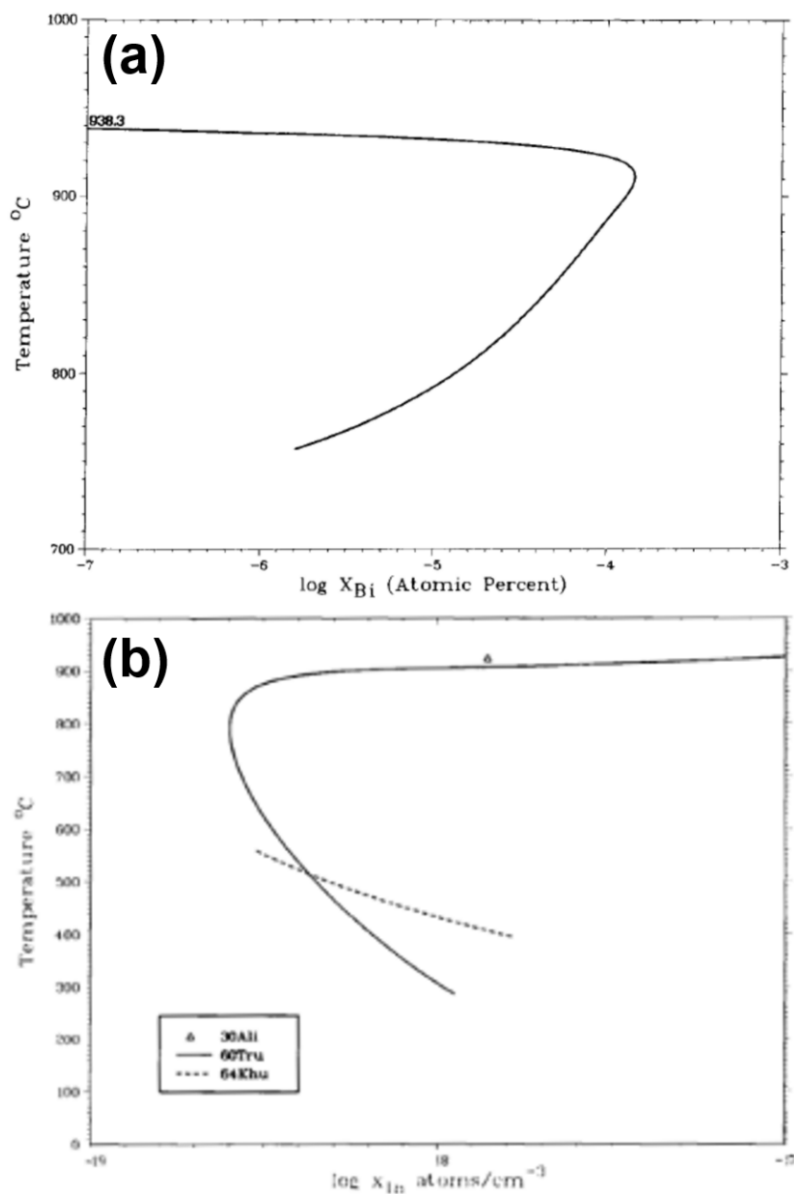

Figure 6: This diagram represents the temperature-dependent solid solubility of (a) Bi[212] and (b) In[213] in Ge. Reproduced with permissions from Springer Nature.[212, 213]

1.4 Group 14 alloys

In the last decades, several approaches have been developed to alter the physical properties of group 14 semiconductors. Besides strain engineering, which allows to adjust the band structure of the semiconductor, alloys of group 14 elements show superior physical properties, when compared to their pure group 14 counterpart.[219] In particular, the binary alloys including $Si_{1-x}Ge_x$ and $Ge_{1-x}Sn_x$, as well as the ternary $Si_xGe_{1-x-y}Sn_y$ alloy have been investigated.[220-222]

The most important physical properties of Ge and Si are summarised in Table 4.[223, 224] Si and Ge are indirect bandgap semiconductors which makes them inefficient as absorbers or emitters of light for optoelectronic devices working in the mid-IR range. The binary alloys are following Vegard's law, which defines the lattice parameter of solid solutions as a linear combination of the lattice parameters of the pure components, quite accurately.[225, 226] In addition, physical properties of α-Sn are included to provide information about trends of certain properties.[223]

Table 4: The most important physical properties of Si, Ge, and α-Sn are summarised.[223, 224]

	Si	**Ge**	**α-Sn**
Crystal structure	Diamond cubic	Diamond cubic	Diamond cubic
Lattice constant (nm)	0.5431	0.5646	0.6489
Direct bandgap energy (eV)	3.22	0.800	-0.41
Indirect bandgap energy (eV)	1.12	0.664	0.14
Electron mobility ($cm^2 \cdot V^{-1} \cdot s^{-1}$)	1400	3900	-
Hole mobility ($cm^2 \cdot V^{-1} \cdot s^{-1}$)	450	1900	-

The binary phase diagrams of Ge-Si[227] and Ge-Sn[228] illustrated in Figure 7 clearly point out the impossibility of growing $Ge_{1-x}Sn_x$ with high Sn contents in a thermodynamically controlled process while the $Si_{1-x}Ge_x$ alloy can be synthesised by such an approach. The Ge-Si systems shows miscibility over the whole composition range (Figure 7a), while the Ge-Sn system contains a miscibility gap (Figure 7b). The Ge-Sn phase diagram already suggests that in the case Sn contents exceeding the solubility are desired the material synthesis must be carried out under conditions far away from the thermodynamic equilibrium. According to the inset in Figure 7b, the maximum solid solubility of Sn in Ge is approximately 1 at. % which makes kinetically driven processes for the growth of $Ge_{1-x}Sn_x$ with higher Sn contents vital. Similarly, thermodynamic considerations suggest a miscibility gap at high Sn contents for the ternary phase diagram of the Ge-Sn-Si system limiting the composition range for the ternary alloy when grown in a thermodynamically driven process.
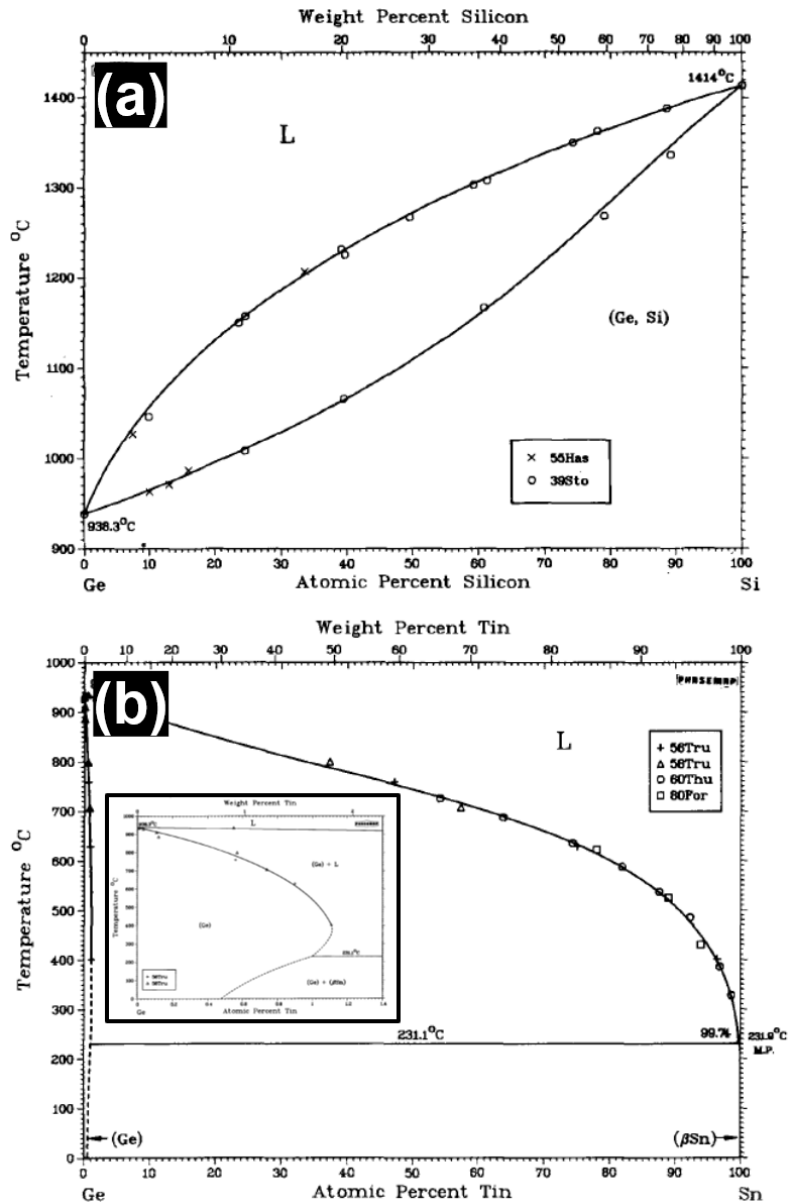
Figure 7: Binary phase diagrams of (a) the Ge-Si[227] and (b) the Ge-Sn system[228] highlight (b) the limitations but also (a) the possibility of growing group 14 alloys over a wide composition range in a thermodynamic process. Reproduced with permissions from Springer Nature.[227, 228]

1.4.1 Solid solution

In contrast to Sn-containing group 14 alloys, the $Si_{1-x}Ge_x$ alloy (diamond structure) does not offer the possibility to grow a direct bandgap semiconductor. However, with increasing Ge content the bandgap of $Si_{1-x}Ge_x$ shrinks accompanied by an increase of the absorption coefficients over a wide spectral range.[224] Although Ge is an indirect bandgap semiconductor, the relatively high absorption coefficients make Ge and Ge-rich $Si_{1-x}Ge_x$ alloys of great interest for novel optoelectronic devices which show higher performances when compared to their Si-based counterparts.[158, 229]

Besides the optical properties, according to Table 4, Ge has essential advantages concerning the electron but especially hole mobility when compared to Si which makes Ge the material of choice for certain electronic devices requiring a high-mobility hole channel.[9]

The main problem of growing high-quality Ge thin films on Si is the lattice mismatch of 4.2 % resulting in a strained Ge layer with high surface roughness. The strain can be released by 1D defects like misfit dislocations which impair the optical and electrical properties of Ge thin films due to acting as non-radiative recombination centres for charge carriers.[10] Defect density can be decreased by using $Si_{1-x}Ge_x$ as a buffer layer which reduces the lattice mismatch between Si and the targeted Ge layer.[10, 13, 229, 230] In addition to growing high-quality Ge, $Si_{1-x}Ge_x$ can also be used as buffer layer for the growth of III/V-semiconductors on Si by adapting the lattice parameter and making the desired material compatible with Si which is of great interest for novel optoelectronic devices.[231, 232]

A controlled lattice mismatch between a buffer layer and the targeted Ge layer can even make strain engineering possible. Uni- and biaxial compressive/tensile strain in Ge lead to a degeneration of the valence band altering hole and electron mobility significantely.[233]

1.4.2 Metastable alloys

Group 14 materials with bandgap energies in the mid-IR range would be easy to integrate on a Si platform but are inefficient due to their indirect bandgap behaviour. III/V-semiconductors are established as very promising materials for efficient light absorption and emission in this wavelength-range; however, the complexity of integration on Si remains challenging.[234, 235] Therefore, other approaches covering the transition of group 14-based alloys from indirect to direct bandgap materials are of great interest. Ge can be converted to a direct bandgap semiconductor at 1.9 % in-plane tensile strain.[236] However, such high strain levels cannot be achieved easily. Therefore, other approaches must be considered to reach the transition of Ge into a direct bandgap semiconductor.

A very important point concerning the optical properties of the $Ge_{1-x}Sn_x$ alloy is the fact that one pure component of this alloy namely α-Sn is a topological zero-bandgap semiconductor (= topological semimetal) with a direct bandgap of -0.41 eV and an indirect bandgap of 0.14 eV. According to theoretical and experimental studies, there exists a crossover of the indirect and direct bandgap energy of $Ge_{1-x}Sn_x$ making the transition of Ge into a direct bandgap semiconductor possible. This crossover is determined to occur by alloying Ge with approximately 8.5 at. % - 10 at. % Sn.[27, 205, 237] The composition dependency of the physical properties must be known in detail to enable an adaptation of the growth process targeting a material with defined properties. Bandgap energies of different transitions are plotted against the Sn content in Figure 8a.[205] The transition into a direct bandgap semiconductor by alloying Ge with Sn and the impact on the band structure is illustrated in Figure 8b - d. The experimental evidence of the transition can be brought by temperature-dependent photoluminescence (PL) measurements. Ge with indirect bandgap behaviour shows a decrease of the Γ-valley signal for decreasing temperature, while Ge with direct bandgap behaviour shows an increase of the Γ-valley emission, which is clearly shown for $Ge_{1-x}Sn_x$ thin films grown on a Ge buffer layer on Si in Figure 8e.[27] Furthermore, a blue-shift of the PL signal is expected when temperature is decreased, which also leads to sharper PL peaks, and laser power is increased.[238] Besides the transition of an indirect to a direct semiconductor, the $Ge_{1-x}Sn_x$ alloy is converted into a topological semimetal at x > 0.41. Also for the ternary $Si_xGe_{1-x-y}Sn_y$ alloy the possibility of an indirect-to-direct bandgap semiconductor transition is predicted theoretically and can be found in the composition range of 0 < x ≤ 0.20.[239]

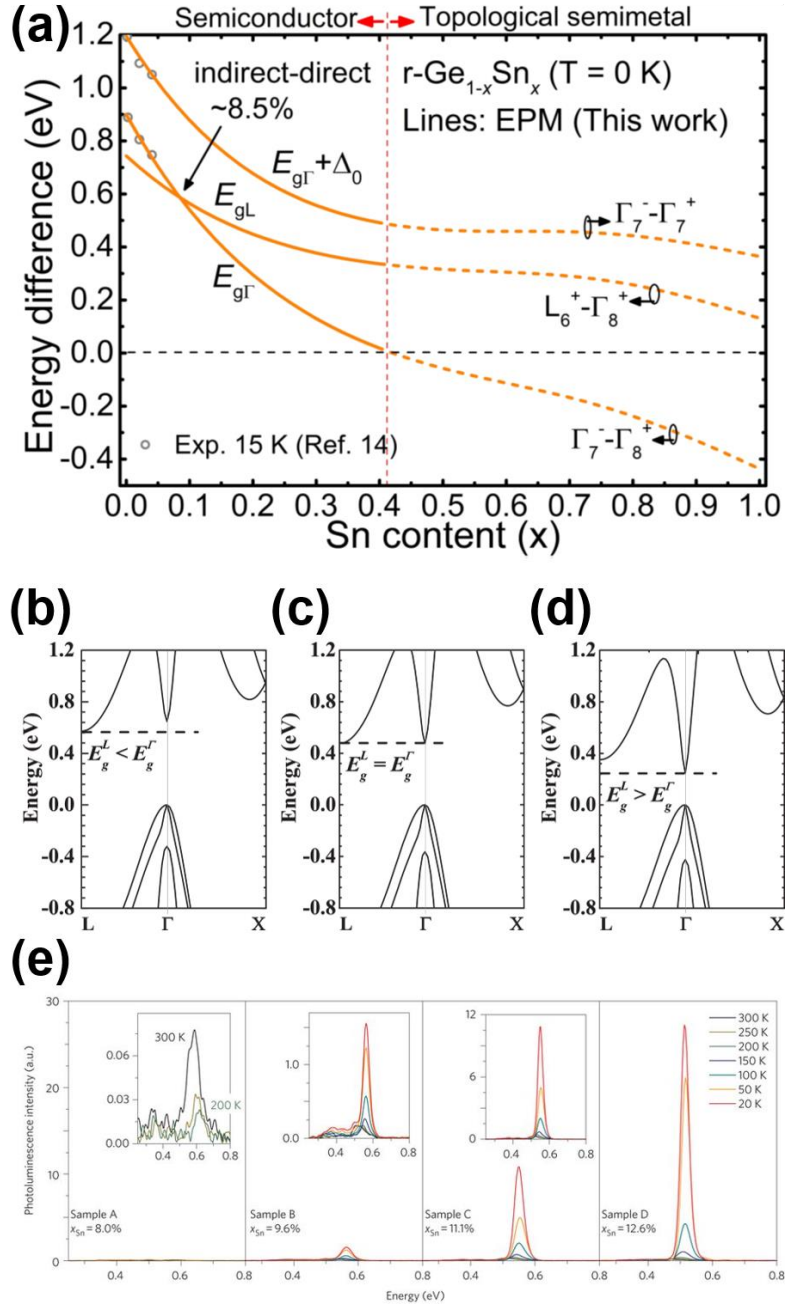**Figure 8:** (a) The calculated energy differences of certain energy bandgaps for $Ge_{1-x}Sn_x$ semiconductor (solid lines) and semimetal (dashed lines). The transition into a direct bandgap semiconductor for strain-relaxed $Ge_{1-x}Sn_x$ at 0 K is expected at approximately 8.5 at. %.[205] The electronic band structure of $Ge_{1-x}Sn_x$ (b) before, (c) directly at, and (d) after the indirect-to-direct bandgap semiconductor transition is highlighted.[240] (e) Temperature-dependent PL measurements of $Ge_{1-x}Sn_x$ alloys with Sn compositions around the indirect-to-direct bandgap semiconductor transition point are shown.[27] Reproduced with permissions from American Physical Society, AIP Publishing, and Springer Nature.[27, 205, 240]

The electrical properties of $Ge_{1-x}Sn_x$ strongly depend on the Sn content. Figure 9 shows the Γ-electron mobility for different Sn contents and the strong influence of compressive strain, which must be considered for the epitaxial growth of $Ge_{1-x}Sn_x$ thin films on a Ge substrate/buffer.[241, 242] The electron mobility as well as the Γ-valley population increase by increasing the Sn content which is highlighted in Figure 9a. Electron mobility of $Ge_{1-x}Sn_x$ is dominated by L-electrons for Sn contents below the indirect-to-direct bandgap semiconductor

transition due to the low population of Γ-electrons. Even after exceeding the Sn content making $Ge_{1-x}Sn_x$ to a direct bandgap semiconductor, which leads to an increase of the population of Γ-electrons, the electron mobility is still dominated by L-electrons caused by the strong inter-valley Γ-L-scattering limiting Γ-electron mobility. By increasing the difference between Γ- and L-valley, Γ-electron mobility (Figure 9b) as well as the effective electron mobility (Figure 9c) increase dramatically.[241]
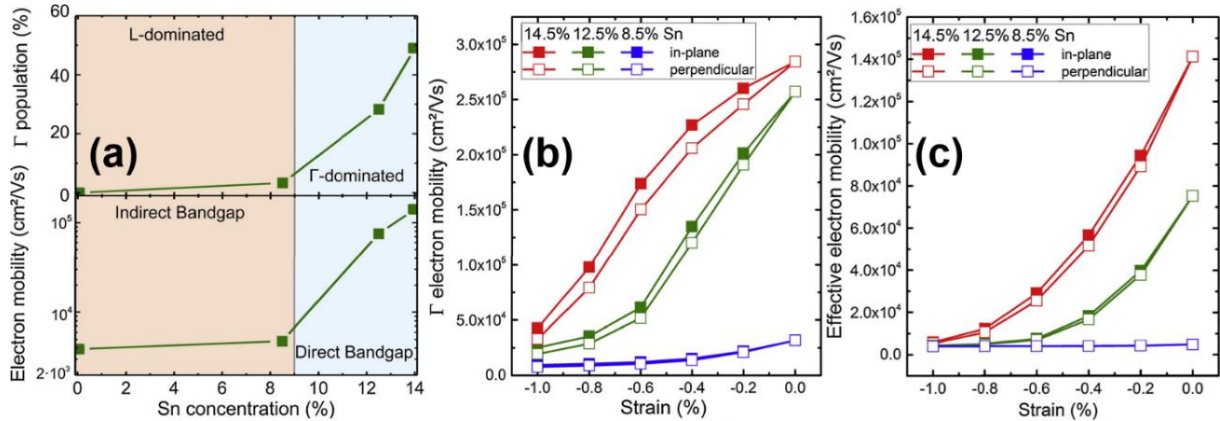
Figure 9: (a) The Γ-valley population (top) and the electron mobility (bottom) of $Ge_{1-x}Sn_x$ alloys with different Sn content are calculated for 300 K and 10^{14} cm^{-3} electron density. (b) Γ-electron and (c) effective electron mobility of $Ge_{1-x}Sn_x$ for different Sn contents considering biaxial strain are presented. Reproduced with permission from Elsevier.[241]

1.4.2.1 Direct bandgap $Ge_{1-x}Sn_x$ thin film growth

The direct growth of $Ge_{1-x}Sn_x$ thin films on Si showing direct bandgap behaviour appeared to be very challenging due to the large lattice mismatch of Ge and Si (> 4 %). Some main problems include non-planar surfaces after growth and very high threading dislocation densities.[243] However, fully-relaxed, epitaxial $Ge_{1-x}Sn_x$ thin films directly grown on Si by MBE,[244] CVD,[67, 245-248] and sputter deposition[249] are described in literature. Most probably, no PL measurements of directly grown $Ge_{1-x}Sn_x$ thin films on Si can be found in literature due to the high dislocation density observed by this approach.

The high 1D defect density can be avoided/reduced by growing a relaxed Ge buffer layer on Si. The critical layer thickness, which is larger due to the smaller lattice mismatch between $Ge_{1-x}Sn_x$ and Ge when compared to Si, should be exceeded to obtain relaxed $Ge_{1-x}Sn_x$ thin films showing direct bandgap behaviour and good optoelectronic properties.[27] $Ge_{1-x}Sn_x$ thin films grown pseudomorphically, which means growing a material on a substrate that dictates the crystal structure and the lattice parameter of this material, on Ge do not show a transition into a direct bandgap semiconductor.[219] High-quality direct bandgap $Ge_{1-x}Sn_x$ thin films grown on a relaxed Ge buffer layer using MBE[250] and CVD[27, 36, 251-255] are reported by several groups. Such high-quality films showing direct bandgap behaviour can be obtained on a relaxed Ge buffer layer by growing thick $Ge_{1-x}Sn_x$ films where the defects are accumulated in a certain zone next to the Ge buffer layer (Figure 10).[256] In the recent past, high-quality direct bandgap $Ge_{1-x}Sn_x$ thin films with high Sn contents are grown pseudomorphically or partially relaxed on step-graded $Ge_{1-x}Sn_x$ buffer layers. The 1D defect density can be reduced dramatically by this approach leading to $Ge_{1-x}Sn_x$ thin films with excellent optoelectronic properties which paves the way for laser applications based on this material.[257, 258]

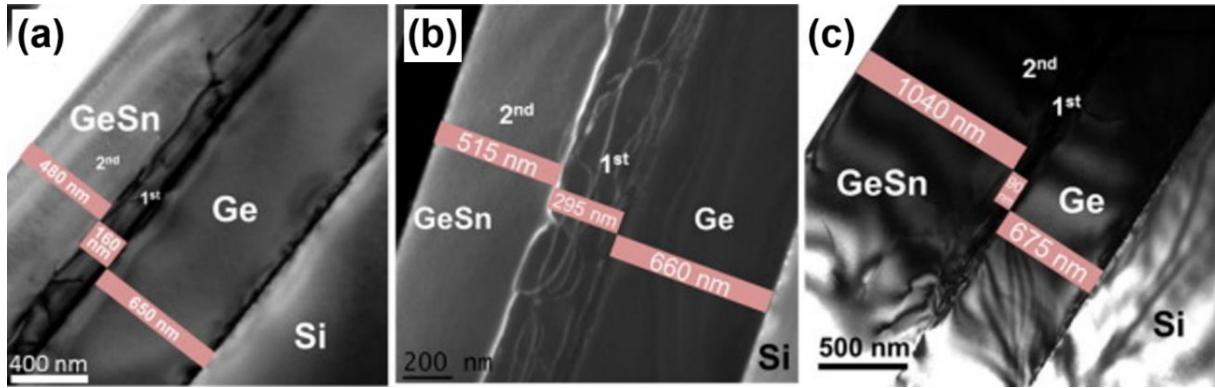**Figure 10:** (a - c) TEM images show $Ge_{1-x}Sn_x$ thin film growth on a strain-relaxed Ge buffer layer deposited on a Si substrate. The $Ge_{1-x}Sn_x$ thin films consist of a small defective layer next to the Ge buffer layer and on top a defect-poor $Ge_{1-x}Sn_x$ layer. $Ge_{1-x}Sn_x$ layer thicknesses are (a) 640 nm, (b) 810 nm, and (c) 1130 nm and grown under either (a + c) N_2 or (b) H_2 ambient. Reproduced with permission from Elsevier.[256]

Besides these approaches, direct bandgap $Ge_{1-x}Sn_x$ thin films with high Sn content can be epitaxially grown on III/V-semiconductors. High crystal quality and low defect densities can be reached by this method due to the possibility of lattice parameter engineering when varying the composition of an InGaAs substrate.[259-261] Furthermore, Sn incorporation up to 27 at. % has been observed for the epitaxial growth of $Ge_{1-x}Sn_x$ thin films on an InP substrate.[262, 263] However, this approach again raises the issue of integrating these substrates on a Si platform.[234, 235]

1.4.2.2 Anisotropic $Ge_{1-x}Sn_x$ alloys

Anisotropic $Ge_{1-x}Sn_x$ nanostructures can be synthesised via bottom-up or top-down approaches. In a top-down approach high-quality $Ge/Ge_{0.92}Sn_{0.08}$ multilayer stacks are grown on a Ge-on-insulator (GOI) substrate. Subsequently, a fin structure is patterned via electron beam lithography (EBL) and reactive ion etching (RIE) with Cl_2 removes the material not covered with photoresist. Finally, selective etching of Ge via RIE using CF_4 as process gas results in vertically stacked $Ge_{0.92}Sn_{0.08}$ NWs.[264] Selective etching of Ge was first suggested for the production of strain-relaxed $Ge_{1-x}Sn_x$ microdiscs.[265]

However, there is a very limited number of reports on bottom-up grown anisotropic $Ge_{1-x}Sn_x$ alloys with high Sn contents (> 8.5 at. %).[77, 266-271] A liquid-phase approach is the first report in literature targeting the bottom-up growth of anisotropic Ge with high Sn incorporation and will be presented as part of this thesis in Chapter 3.2.[77, 266, 267]

The first vapour-phase approach is based on Au and Au-Ag alloys as promoter for VLS-growth of direct bandgap $Ge_{1-x}Sn_x$ NWs with Sn contents up to 9.2 at. % by the simultaneous supply of a Ge and a Sn precursor.[272] Further investigations on this system suggest a high impact of growth kinetics on the maximum Sn incorporation which is demonstrated by the variation of Au-Ag composition and Sn precursor.[268]

Another approach for high Sn incorporation up to 13 at. % in anisotropic $Ge_{1-x}Sn_x$ is based on the epitaxial growth of $Ge_{1-x}Sn_x$ on the sidewalls of Ge NWs resulting in core-shell structures. Direct bandgap room temperature emission at 0.465 eV and a strong enhancement of light absorption is observed for these structures.[269] In a further study the connection between

residual misfit strain and Sn incorporation in Ge/Ge$_{1-x}$Sn$_x$ core-shell NWs is investigated in detail and illustrated in Figure 11.[270]
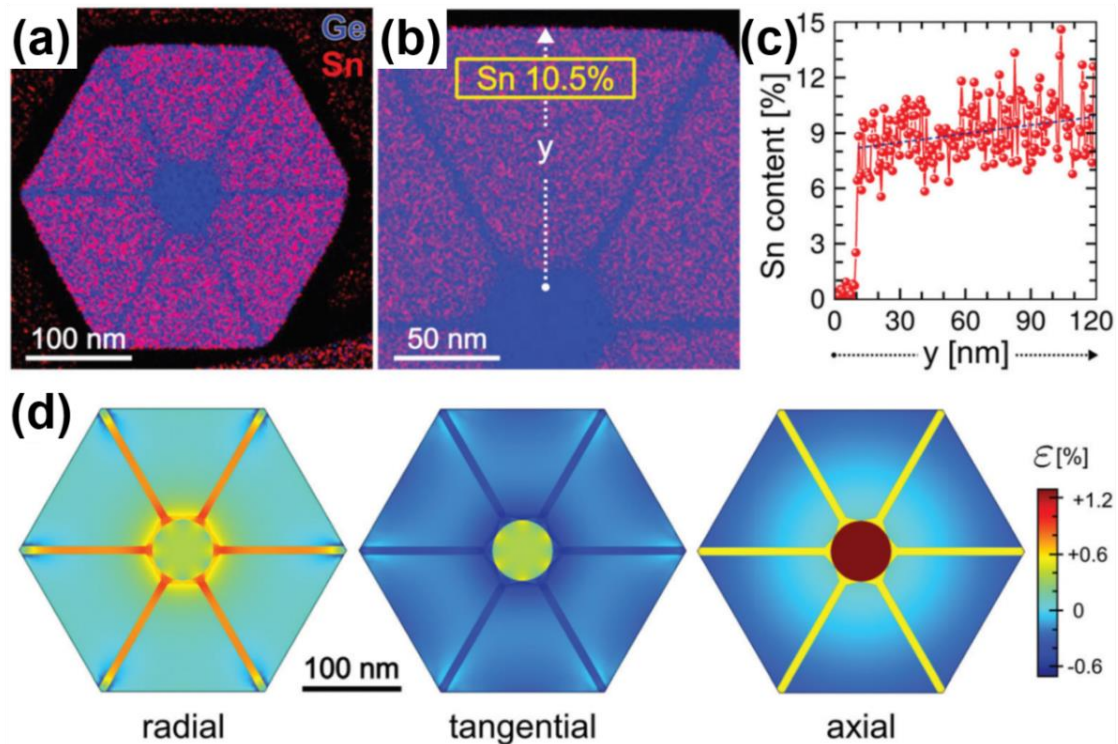

Figure 11: Cross-sectional EDX mapping of a Ge/Ge$_{1-x}$Sn$_x$ core-shell NW is shown in (a). (b) A Sn content of 10.5 at. % is obtained by quantifying the EDX spectrum of the region within the yellow rectangle. (c) An EDX line-scan from the core towards the shell surface which is indicated in (b) is collected showing an increase of Sn concentration towards the shell surface. (d) shows colour maps of the radial, tangential and axial component of the strain field. Experimental results are brought in line with results computed by the finite element method by assuming a composition gradient from 8 at. % to 10.5 at. % Sn (core to shell) and stripes (hexagon vertices) containing 5 at. % Sn. Reproduced with permission from Royal Society of Chemistry.[270]

Very recently, the in-plane growth of Ge$_{1-x}$Sn$_x$ NWs on a Si substrate at low temperatures is described and Sn contents up to 22 at. % are reported. In this process, SnO$_2$ particles are placed on a Si substrate (Figure 12a). Subsequently, the particles are partially reduced using a H$_2$ plasma (Figure 12a) and a hydrogenated amorphous Ge layer is deposited (Figure 12b). Finally, the temperature is raised above the eutectic temperature of the Ge-Sn system (231 °C) to initiate in-plane NW growth (Figure 12c + d). Amorphous Ge is dissolved by Sn and Ge$_{1-x}$Sn$_x$ is deposited at the Sn/SnO$_2$ interface. The presence of SnO$_2$ is described to be vital for in-plane growth of Ge$_{1-x}$Sn$_x$ NWs due to preventing the liquid Sn from splitting and wetting during the supersaturation process of the Sn growth promoter.[271]

However, a closer look on STEM-EDX measurements presented in this study points out the presence of a thin SiO$_2$ layer on top of the Si substrate. This could be an explanation for the high Sn content of the Ge$_{1-x}$Sn$_x$ alloy observed by this approach due to the absence of strain effects induced by the Si substrate which would counteract the incorporation.
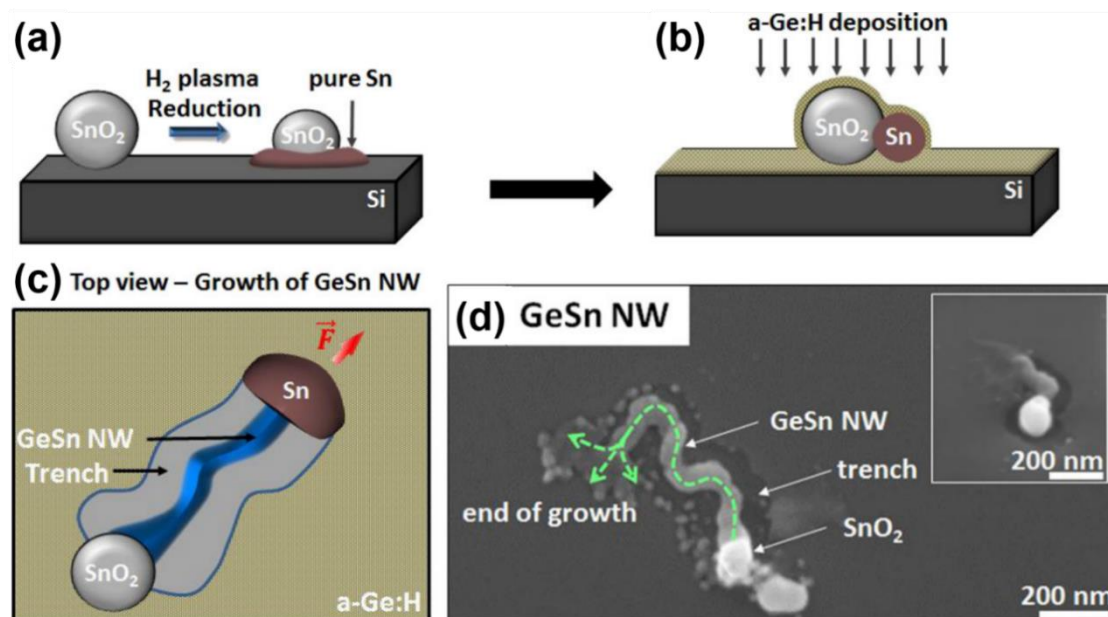
Figure 12: (a + b) show a schematic illustration of (a) the partial reduction of SnO_2 using a H_2 plasma and (b) the deposition of a hydrogenated amorphous Ge layer. (c) A top-view schematic illustration points out the dissolution of the hydrogenated amorphous Ge layer by liquid Sn and the redeposition of crystalline material as the driving force for the observed in-plane $Ge_{1-x}Sn_x$ NW growth. (d) A top-view scanning electron microscopy (SEM) image highlights the observed in-plane structures with description of the present components. Reproduced with permission from American Chemical Society.[271]

1.4.2.3 $Ge_{1-x}Sn_x$ nanocrystals

For the synthesis of $Ge_{1-x}Sn_x$ nanocrystals it must be distinguished between vapour- and solution-based processes. The first attempts of producing $Ge_{1-x}Sn_x$ nanocrystals were realised by a non-equilibrium epitaxial growth process where Ge and Sn are co-deposited on an ultrathin SiO_2 film with pre-deposition of Ge forming small voids in the SiO_2 film. $Ge_{1-x}Sn_x$ nanocrystals obtained by this approach contain up to 8 at. % Sn.[273-279] Further gas-phase approaches include laser photolysis reaction of a Ge and Sn precursor[280] as well as MBE-based[281-285] and sputtering[286] techniques. The thermal annealing of a thin, compressively strained $Ge_{0.825}Sn_{0.175}$ layer epitaxially grown on a Ge(100) substrate which is capped with Ge can result in the formation of $Ge_{0.5}Sn_{0.5}$ nanocrystals.[281] A similar strategy demonstrates the formation of a $Ge_{0.96}Sn_{0.04}$ nanocrystal-based film embedded in Si.[282] The epitaxial growth of $Ge_{0.986}Sn_{0.014}$ nanocrystals on Si nanopillar arrays has been investigated.[285] Furthermore, Sputtering Ge on self-assembled Sn nanodots on a SiO_2/Si substrate enables the growth of $Ge_{1-x}Sn_x$ nanocrystalline thin films with Sn contents up to 27.3 at. % at very low temperatures of 150 °C.[286]

Recently, studies concerning the solution-based synthesis of $Ge_{1-x}Sn_x$ nanocrystals with high control over a wide composition and crystal size range can be found in literature. In a typical synthesis Ge and Sn halides/amides are mixed with a high-boiling primary amine which can act as ligand and solvent at the same time. In addition, reducing and surface-active agents can be added to the mixture for the particle formation. The $Ge_{1-x}Sn_x$ nanocrystals are typically synthesised at temperatures of approximately 300 °C.[287-293]

The successful incorporation of Sn in the Ge matrix is confirmed by XRD and Raman spectroscopy. In addition, the influence of Sn content and crystal size on the bandgap energy

has been investigated for solution-grown $Ge_{1-x}Sn_x$ nanocrystals. These studies describe quantum confinement effects in very small $Ge_{1-x}Sn_x$ nanocrystals (3.4 nm - 4.6 nm) leading to a blue-shift of the bandgap energies when compared to bulk $Ge_{1-x}Sn_x$ alloys.[287] Nearly simultaneously, similar results have been described by an independent study, which includes thermal stability measurements.[288]

Further studies point out the possibility of shifting the light emission range towards the visible spectrum by varying the nanocrystal size (1 nm - 3 nm) for $Ge_{1-x}Sn_x$ with Sn contents enabling direct bandgap behaviour.[289, 290] $Ge_{1-x}Sn_x$/CdS core-shell nanocrystals show a strong enhancement of light emission when compared to $Ge_{1-x}Sn_x$ nanocrystals without CdS shell. The authors explain this effect by the epitaxial relation between $Ge_{1-x}Sn_x$ and CdS and the reduction of surface oxidation.[291]

However, the reported blue-shift of the absorbed[288, 289]/emitted[289-291, 293] light observed in these studies exceeds the energy-shift of light emission obtained for quantum-confined Ge nanocrystals for same diameters dramatically[294] although high amounts of Sn are incorporated which should result in smaller bandgap energies. Therefore, optical properties reported for $Ge_{1-x}Sn_x$ nanocrystals should be questioned critically and further investigations are needed to clarify the strong blue-shift.

1.4.2.4 Devices based on $Ge_{1-x}Sn_x$ alloys

The outstanding electrical and optical properties of $Ge_{1-x}Sn_x$ in combination with being compatible with CMOS-based processes make this material to an interesting candidate for novel devices. The strong increase of the effective electron mobility by alloying Ge with high amounts of Sn allows the formation of high-performance n-type MOSFETs.[295-297] A $Ge_{0.955}Sn_{0.045}$ n-type MOSFET with a very high electron mobility of 440 $cm^2 \cdot V^{-1} \cdot s^{-1}$ has been demonstrated.[297] In addition, p-type MOSFETs are of great interest due to the increased hole mobility of $Ge_{1-x}Sn_x$ alloys when compared to pure Ge.[28, 298, 299] A 66 % higher hole mobility and 64 % lower source/drain resistance for a $Ge_{0.947}Sn_{0.053}$ p-type MOSFET when compared to a Ge control device have been described.[28] Besides these devices, $Ge_{1-x}Sn_x$ with high Sn contents can yield high-performance tunnelling FETs (TFETs) due to the efficient direct BTBT.[242, 300]

The broad wavelength-coverage of $Ge_{1-x}Sn_x$ and the possibility to convert the material into a direct bandgap semiconductor make this alloy to a potential candidate for efficient optoelectronic devices working in the mid-IR. In recent years, several groups developed photodiodes[36, 253, 301-311] and photodetectors[312-320] based on $Ge_{1-x}Sn_x$. Interestingly, a $Ge_{0.89}Sn_{0.11}$ photodiode revealing device performances competitive with extended-InGaAs photodiodes dominating the market was presented recently.[36]

Besides photodiodes working in the mid-IR range, lasers in this wavelength-regime acting as light source for applications in the field of tele- and data-communication are of great interest nowadays and successfully implemented by several groups using $Ge_{1-x}Sn_x$ as active material. The existence of a direct bandgap group 14 laser on Si which exhibit modal gain has been demonstrated in 2015 setting a benchmark for future studies on $Ge_{1-x}Sn_x$.[27] For mid-IR laser applications it must be considered that the quality of the $Ge_{1-x}Sn_x$ thin film should be very high in terms of defect density. Furthermore, the layer should be at least partially relaxed with a high amount of homogeneously distributed Sn in the Ge matrix to obtain the required direct bandgap semiconductor. Since this first report on lasing in purely group 14 containing devices, several reports have been published verifying these findings and extending the emission range.[252, 254, 257, 321-325]

2 Motivation

For a long time, Ge has not been integrated in the CMOS industry due to the lack of thermal stability of the native oxide.[1, 2] The possibility of growing high-κ dielectrics on Ge has solved this problem and brought back the interest in Ge due to both high electron and hole mobility.[3-8] Techniques to implement Ge on a Si-based system with high quality are well-advanced.[11-20]

The next step is to promote the controlled alteration of the physical properties of Ge by doping and alloying with other elements. The controlled incorporation of impurity atoms in Ge is critical and often limited by thermodynamics which makes the synthesis of Ge-based materials possessing high dopant activation or impurity concentrations beyond the solid solubility quite complicated. During the last decades, progress in overcoming these problems have been achieved.[29-31, 33-35, 197, 206, 218, 267] However, the synthesis of anisotropic Ge with altered physical properties by the incorporation of impurity atoms is not investigated in detail.

This thesis is aiming to provide a solution for the realisation of an efficient impurity incorporation in the Ge host lattice by kinetically controlled processes for the growth of anisotropic, metastable Ge-based materials via self-seeding. The goal is to incorporate Ga beyond the solubility limit in an anisotropic Ge crystal by developing a kinetically controlled vapour-based process and to determine changes in the physical properties of the resulting material.

A similar approach based on self-seeding is targeted for the Ge-Sn system to realise the transition of Ge from an indirect to a direct bandgap semiconductor with the possibility to adjust the direct bandgap energy by a controlled incorporation of Sn in the Ge host lattice. Therefore, the aimed process must be performed at low temperatures and high growth rates are targeted to enable an efficient incorporation of atoms from the Sn seed in the growing anisotropic material. First attempts shall be performed via a solution-based process to gather information concerning the nucleation and growth of anisotropic $Ge_{1-x}Sn_x$ nanostructures. Subsequently, the gained knowledge should enable the growth of anisotropic, metastable $Ge_{1-x}Sn_x$ nanostructures in a vapour-phase process.

This thesis targets the further development of Ge-based materials by providing synthesis strategies for highly metastable Ge-based materials with significantly altered physical properties.

3 Results

3.1 Paper 1

Direct Synthesis of Hyperdoped Germanium Nanowires

Doping Ge with group 13 and 15 elements is a well-established approach to alter the physical properties of this material. The incorporation of impurity atoms in a host lattice is often limited by the low solubility of the desired element. Doping above the solubility limit determined by thermodynamics is called hyperdoping and requires a kinetically driven process. The metastable product resulting from such a process distinguishes from the undoped Ge by drastic changes in the physical properties.

In this study metal-assisted bottom-up grown Ge NWs with high p-doping levels using Ga as the seed material are synthesised. The low eutectic temperature of the Ga-Ge system and the decomposition temperature of the used Ge precursor at the chosen synthesis parameters enable the VLS-growth at temperatures down to 210 °C.

Ge NWs are grown on a silicone substrate in a steel cell. Therefore, the silicone substrate is infiltrated by (pentamethylcyclopentadienyl)gallium(I) and t-butylgermane is added as Ge precursor before heating up to 210 °C. Electron microscopy is used for the structural and compositional characterisation of the obtained Ge NWs. Figure 13 illustrates the high density of NWs on the silicone substrate and the excellent quality of the elongated Ge crystal. The NWs reveal an average diameter of ~ 100 nm and lengths of several micrometres. In addition, the STEM-EDX mapping in the inset of Figure 13a confirms the Ga-mediated VLS-growth of these NWs showing the Ga reservoir terminating the Ge NW.
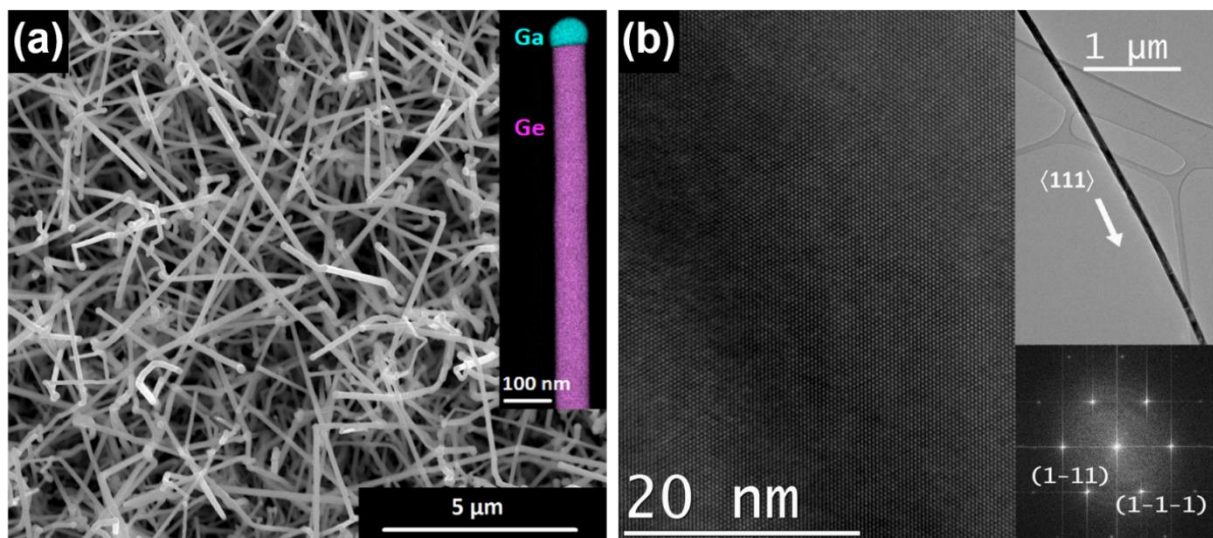

Figure 13: The high density of Ge NWs on the silicone substrate is shown in the SEM image in (a) including STEM-EDX mapping of the tip region of a NW (inset). High crystallinity of the Ge body is confirmed by HRTEM in (b). The TEM image and the FFT pattern shown as insets of (b) are indicative for the predominant ⟨111⟩ growth direction of those NWs.

The composition of the NW body was determined by STEM-EDX giving a Ga content of 3.51 at. % ± 0.29 at. % (1σ), which is far above the solubility limit of ~ 0.07 at. % Ga at 210 °C according to the Ga-Ge phase diagram in Figure 14.[87]
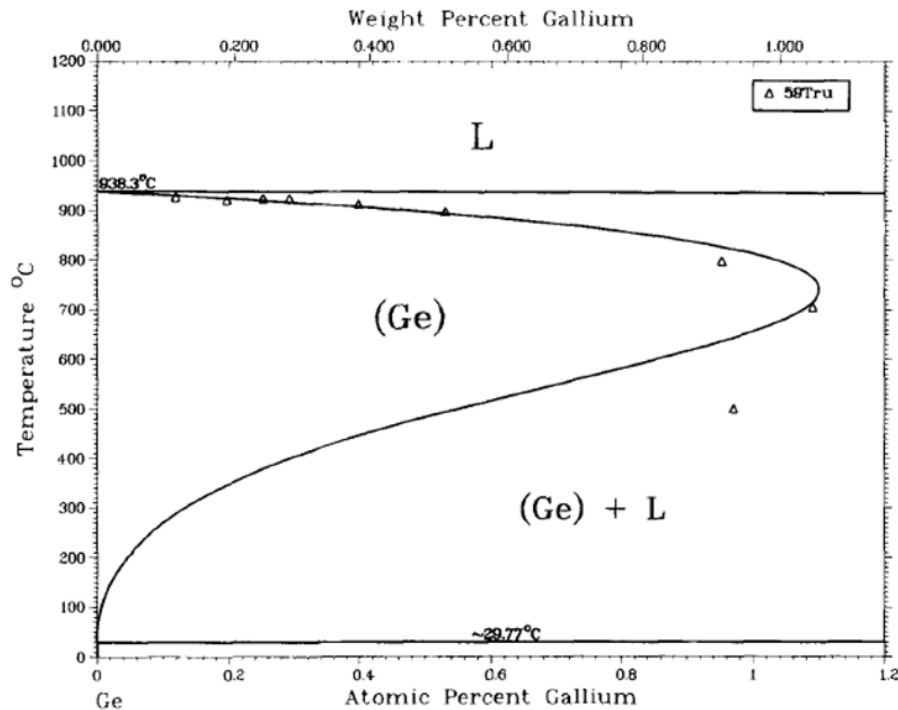

Figure 14: Ga-Ge phase diagram with low solubility of ~ 0.07 at. % Ga in the Ge crystal at a growth temperature of 210 °C. Reproduced with permission from Springer Nature.[87]

STEM-EDX mapping (Figure 15a) and STEM-EDX point measurements (Figure 15b + c) show the homogenous distribution of Ga within the NW. STEM-EDX point measurements along the radial direction of the NW shown in Figure 15b allow the exclusion of Ge deposition on the sidewalls of Ga-hyperdoped Ge NWs due to the replication of the Ge signal in the Ga channel.

A step-flow process leading to successive addition of bilayers is the common growth mode of bottom-up grown Si and Ge NWs.[31, 202, 326-329] The growth rate of the crystal is thereby defined as the thickness of a bilayer divided by the time required for the nucleation and the complete growth of one bilayer.[31, 202] The high amounts of Ga incorporated in the Ge matrix far above the solubility limit of this system can be explained by solute trapping at step edges during the NW growth.[30, 31] The efficiency of the incorporation process is benefited by the similar atomic radii of Ge and Ga. Solute trapping, leading to an incorporation of the impurity atoms far beyond the solubility limit of a system, can be observed for Al-seeded Si NWs.[29-31] However, the growth rate of the NWs obtained in this study is quite low which counteracts a high Ga incorporation. According to literature, a viable explanation for the efficient solute trapping is the fact that the time required for the addition of one bilayer is the sum of the incubation time and the time between the nucleation and the complete growth of the bilayer. In the system described in this study the incubation time is expected to be very long leading to a slow growth rate while the addition of a bilayer once a nucleus is formed could be very fast enabling efficient solute trapping.[31]
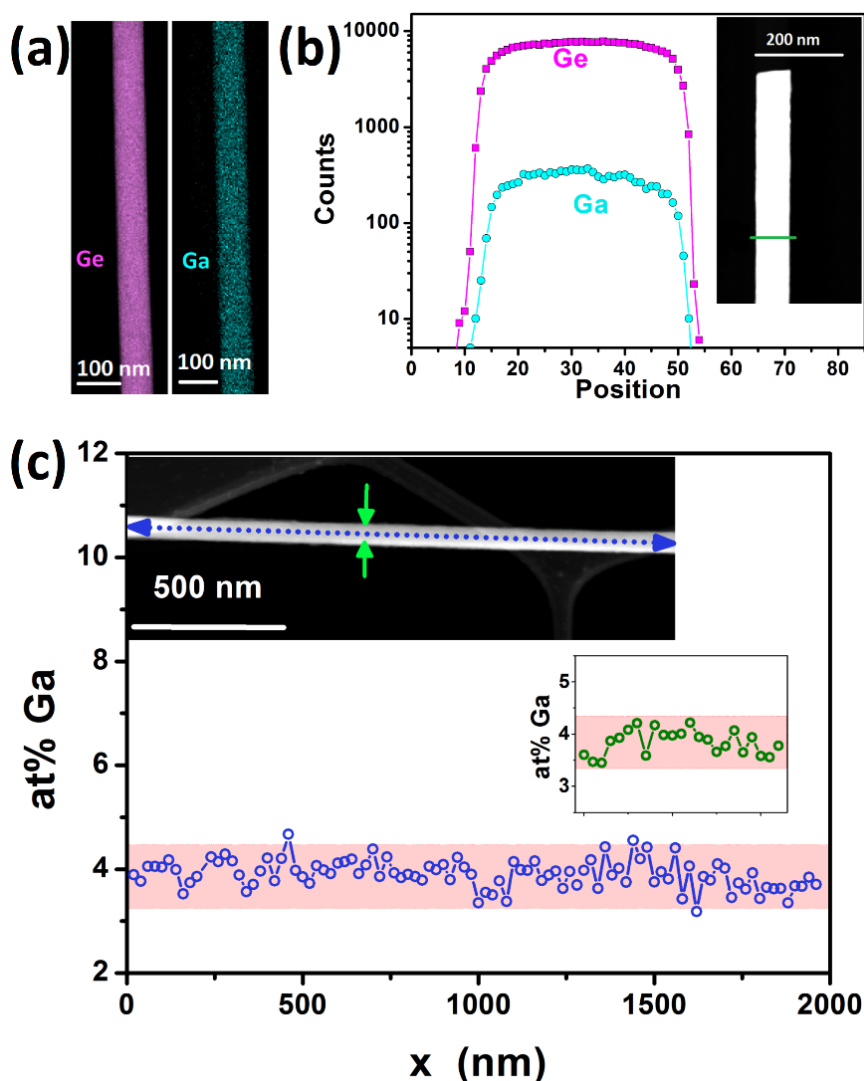
Figure 15: (a) STEM-EDX mapping of the Ge NW body indicating a homogeneous distribution of Ga in the Ge matrix. (b) The radial profile of the Ge NW illustrates the absence of a core-shell structure and no signs of Ga surface segregation can be observed. (c) STEM-EDX point measurements along the NW axis and in radial direction suggest a random incorporation of Ga which can be expected for a solute trapping process. The red area of ± 0.5 at. % Ga shows that the determined Ga concentrations vary within the tolerance of the used method.

The thermal stability of the metastable highly doped Ge NWs is crucial if implementation in an electronic device is targeted. Therefore, the NWs are thermally annealed in a tube furnace at different temperatures under reducing atmosphere. Ga diffusion in Ge is well-described in literature and compared to other p-dopants quite slow.[100, 330, 331] The slow diffusion rate of Ga in the Ge crystal leads to a high thermal stability of the metastable material. Therefore, no structural and compositional changes of the NWs can be observed for annealing at 250 °C for 10 h although the metastable material is grown at 210 °C. STEM-EDX mapping reveals a homogenous distribution of Ga without segregation at the surface and an unaltered average Ga content. Figure 16 highlights a NW annealed at 400 °C for 6 h. The thermal annealing initiates segregation processes leading to enrichment of Ga at twin boundaries of the Ge NW body (Figure 16a) and Ga nanoparticles attached to the Ge surface (Figure 16b). The resulting Ga distribution in the Ge matrix is inhomogeneous as expected for partially decomposed metastable materials.
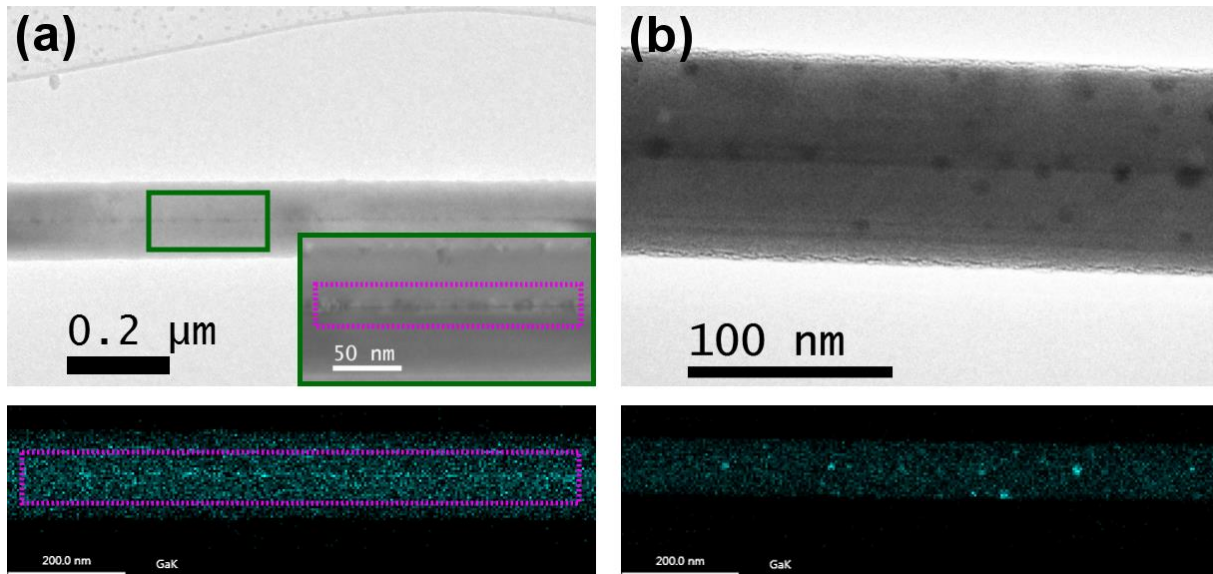
Figure 16: (a + b) show a Ge NW annealed at 400 °C for 6 h. In (a) segregation of Ga at the twin interface (purple frame) can be observed while in (b) a high number of Ga clusters are attached to the surface of the NW. STEM-EDX mappings of Ga confirm the assignment of the dark areas in the TEM images to segregated metallic Ga.

The electronic properties of the synthesised Ge NWs with high Ga content are evaluated using single NW devices. For this reason, the NWs are contacted by Al pads. Figure 17 shows *I-V* measurements of Ga-doped Ge NWs with different diameters in two-point configuration. Ga-doped Ge NWs show a three orders of magnitude lower resistance (reciprocal slope of curves in Figure 17a) compared to intrinsic, Au-seeded Ge NWs. The highly conductive Ga-doped Ge NWs do not reveal any noticeable field-effect response in the back-gated NW FET geometry. Besides the high conductivity, these structures can sustain current densities of more than 12 MA·cm^{-2} before device failure which is approximately 25 times higher than observed for Au-seeded Ge NWs with similar diameters (recalculated value from a study).[332] Four-probe measurements on Ga-doped Ge NWs lead to the conclusion that the conductivity variation observed for different NWs in Figure 17a are diameter-independent and can be attributed to differences of the contact resistance (Figure 17b). In this study resistivity values of ~ 300 µΩ·cm for Ga-doped Ge NWs are measured. Based on these results, an electrically active impurity concentration of ~ 5·10^{20} cm^{-3} can be expected. These values can be obtained by comparison of the measured resistivity to tables in literature where impurity concentrations of group 13 atoms are associated to the electronic properties.[333] This leads to the conclusion that one third of the incorporated 3.5 at. % Ga (1.5·10^{21} cm^{-3}) occupies an electrically active site of the Ge lattice.
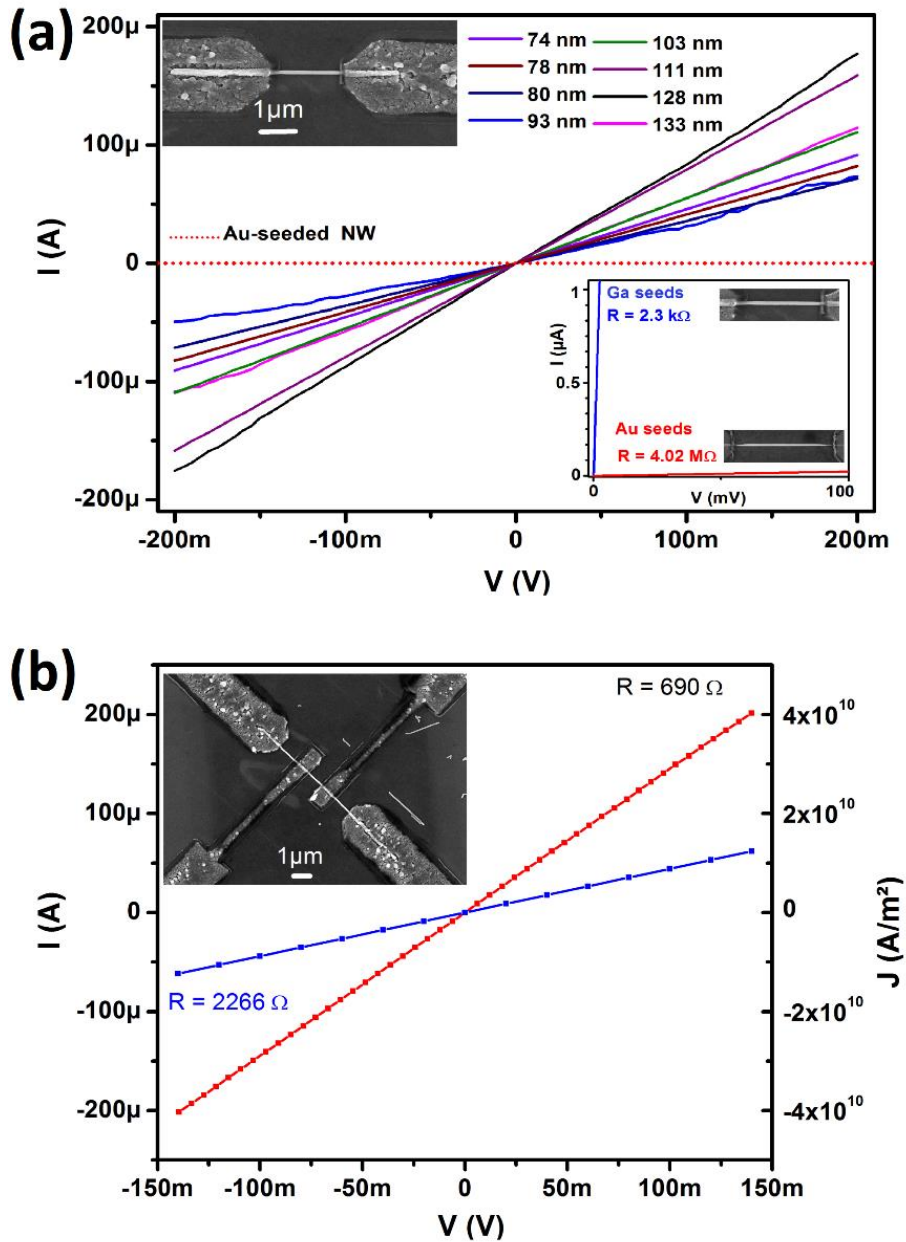
Figure 17: (a) The electronic properties of single NW devices in two-point geometry, using Ga-doped Ge NWs with different diameters, are determined. For comparison, the *I-V* curve of a single NW device using an intrinsic, Au-seeded Ge NW as building block is added. The inset on the top shows a SEM image of a fabricated device. The resistances (reciprocal slope of curves) of a Ga-doped Ge NW and a Au-seeded NW are illustrated in the inset on the bottom to highlight the strong deviation of the electronic properties of both materials. (b) points out the high influence of the contact resistance on the overall resistance of the device evaluated by determining the electronic properties of a single NW device in four-point geometry.

Decreasing the temperature of a semiconductor leads to lower charge carrier densities resulting in an increase of the resistance. Ga-hyperdoped Ge NWs behave totally different from a semiconductor. The resistance decreases at lower temperatures followed by a plateau at temperatures near 0 K which can be attributed to a metal-like behaviour and is illustrated in Figure 18. The Mott-transition, a possible scenario for doped semiconductors, leading to an increase of the resistance at lower temperatures due to freezing out of electrons, could not be

observed.[185] These measurements confirm the high doping level of the here presented NWs. The temperature-dependence of the resistivity of Ga-hyperdoped and Au-seeded Ge NWs is compared in the inset on the top of Figure 18. The Au-seeded Ge NW shows the well-known resistivity behaviour of a semiconductor while the resistivity of the Ga-hyperdoped Ge NW is only slightly dependent on a temperature variation. At room temperature the resistivity of the Au-seeded Ge NW shows a three to four orders of magnitude higher resistivity compared to the Ga-hyperdoped Ge NW. At temperatures near 0 K the resistivity differs even stronger (10 orders of magnitude). The inset on the bottom of Figure 18 shows a jump of the resistance at 1.6 K upon further cooling below 4 K. The resistance drop at 1.6 K could be associated to the metal-superconductor transition of the Al electrodes. The shift of the critical temperature from 1.1 K to 1.6 K can be attributed to enrichment of Al with oxygen impurities which is well-known from literature for sputtered Al under similar conditions used in this study.[334] The resistance drop can be easily suppressed by applying a weak overcritical magnetic field of less than 250 mT. A metal-superconductor transition of the Ga-hyperdoped Ge NWs cannot be observed in the measured temperature range 300 K - 0.269 K.
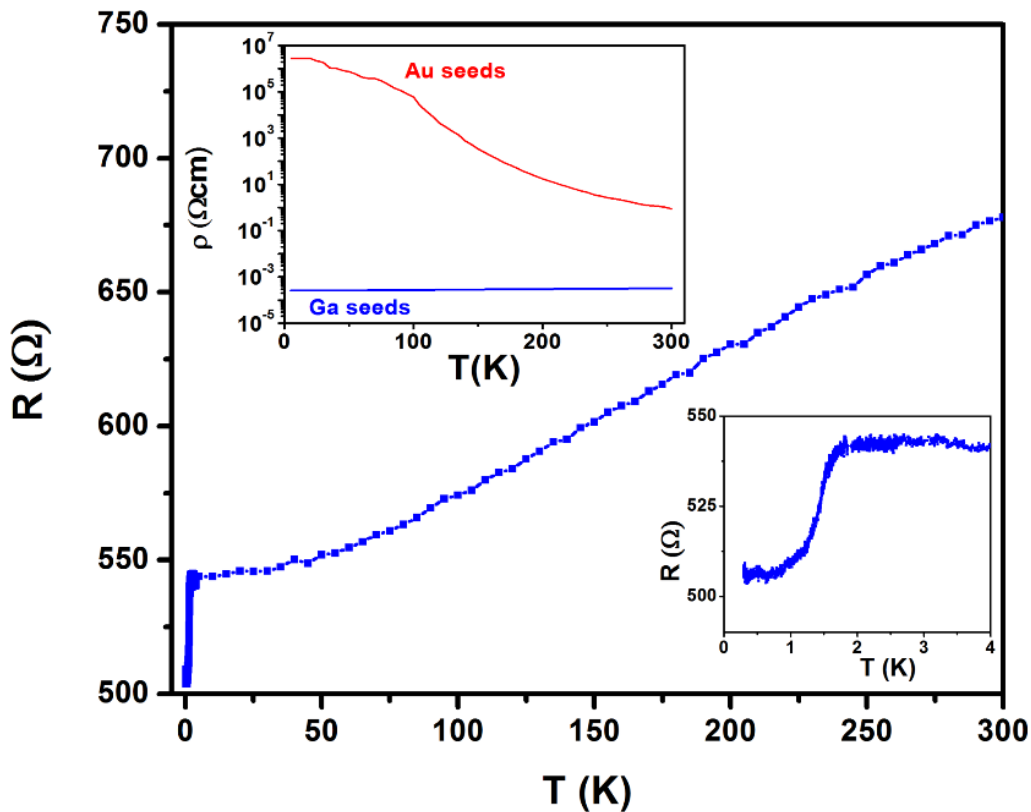

Figure 18: The temperature-dependence of the resistance in the temperature range 300 K - 0.269 K is measured in a four-point configuration and allows the attribution of metal-like behaviour to the here presented Ga-hyperdoped Ge NWs. The inset on the top shows the resistance evolution in a four-probe configuration. The temperature range 4 K - 0.269 K is measured in a two-probe configuration displayed in the inset on the bottom showing a drop in the resistance due to the metal-superconductor transition of the Al contacts.

3.2 Paper 2 + 3

Pushing the Composition Limit of Anisotropic Ge$_{1-x}$Sn$_x$ Nanostructures and Determination of Their Thermal Stability

and

Electrical Characterization and Examination of Temperature-Induced Degradation of Metastable Ge$_{0.81}$Sn$_{0.19}$ Nanowires

Ge becomes a direct bandgap material by alloying with 8.5 at. % - 10 at. % Sn[27, 205, 237] which is far above the solubility limit of Sn in the Ge matrix.[228] The metastable nature of these alloys makes it necessary to work in a kinetically controlled growth regime which is not trivial and requires high growth rates at low temperatures.

Ge$_{1-x}$Sn$_x$ NRs with Sn contents up to 28 at. %, which is the most Sn-containing anisotropic Ge$_{1-x}$Sn$_x$ alloy reported to date, are synthesised in a solution-based microwave-assisted bottom-up growth process using Sn as metal seed. In this approach Sn is used as growth promoter to ensure the incorporation of Sn in the Ge matrix is not limited by the supply of Sn. In contrast to surface-bound nanostructures and thin films, no growth template is used that can facilitate the Sn incorporation but also causes strain due to lattice mismatch between the growing Ge$_{1-x}$Sn$_x$ and the crystalline substrate. Microwave-assisted heating and stirring of the mixture enable a homogenous temperature profile inside the reaction volume leading to homogeneous nucleation of the nanostructures. The precursor mixture containing homo- and heterometallic imidocubane species is decomposed at very low temperatures of about 140 °C. Despite the low temperatures used to decompose the precursor mixture, the reactivity of the precursor species is high enough to obtain high growth rates of approximately 600 nm·min^{-1}.

The time-dependent evolution of phases and morphologies has been investigated for processes at a decomposition temperature of 140 °C for which the precursor pre-treatment was optimised (Figure 19). All characterisations are performed on structures that underwent a cooling-down process which could alter the crystallographic, morphological and compositional properties of the product. Nevertheless, *in situ* observations cannot be performed with the used equipment which makes a detailed discussion of the results vital. Initially, globular β-Sn particles are formed by the decomposition of the Sn-rich homometallic imidocubane species present in the precursor mixture (Figure 19a). Subsequently, Ge is delivered by the decomposition of Sn-rich heterometallic imidocubane species. This process causes a slow enrichment of the β-Sn particles with Ge which triggers a transformation of the β-Sn phase partly/completely into teardrop-shaped α-Sn/β-Sn heterodimers/α-Sn particles (Figure 19b). XRD measurements support the presence of the α-Sn phase at the stage where teardrop-shaped structures represent the dominating morphology of the isolated product (Figure 19e). Overlay images of STEM-EDX elemental mappings of teardrop-shaped and globular structures shown in the insets of Figure 19a + b differ significantly in the overall Ge content. Prolonged decomposition times lead to the decomposition onset of Ge-rich hetero- and homometallic imidocubanes. Supply of high amounts of Ge atoms to the system supersaturates the β-Sn part of the heterodimer and the subsequent template-assisted growth of Ge$_{1-x}$Sn$_x$ on the α-Sn part is initiated (Figure 19c). The template-assisted growth can also explain the high amount of Sn incorporated in these structures due to the same crystal structure of α-Sn and α-Ge and the larger lattice parameter of α-Sn. Further Ge supply leads to the elongation of the Ge$_{1-x}$Sn$_x$ segment (Figure 19d). The completely transformed α-Sn

particles could be inactive in terms of $Ge_{1-x}Sn_x$ nanostructure growth due to the absence of the β-Sn acting as reservoir at temperatures below the melting point of Sn which enables the supply of the decomposed Ge directly to the α-Sn/β-Sn interface. This is supported by the fact that even after the elongation regime some teardrop-shaped structures are present in the mixture.
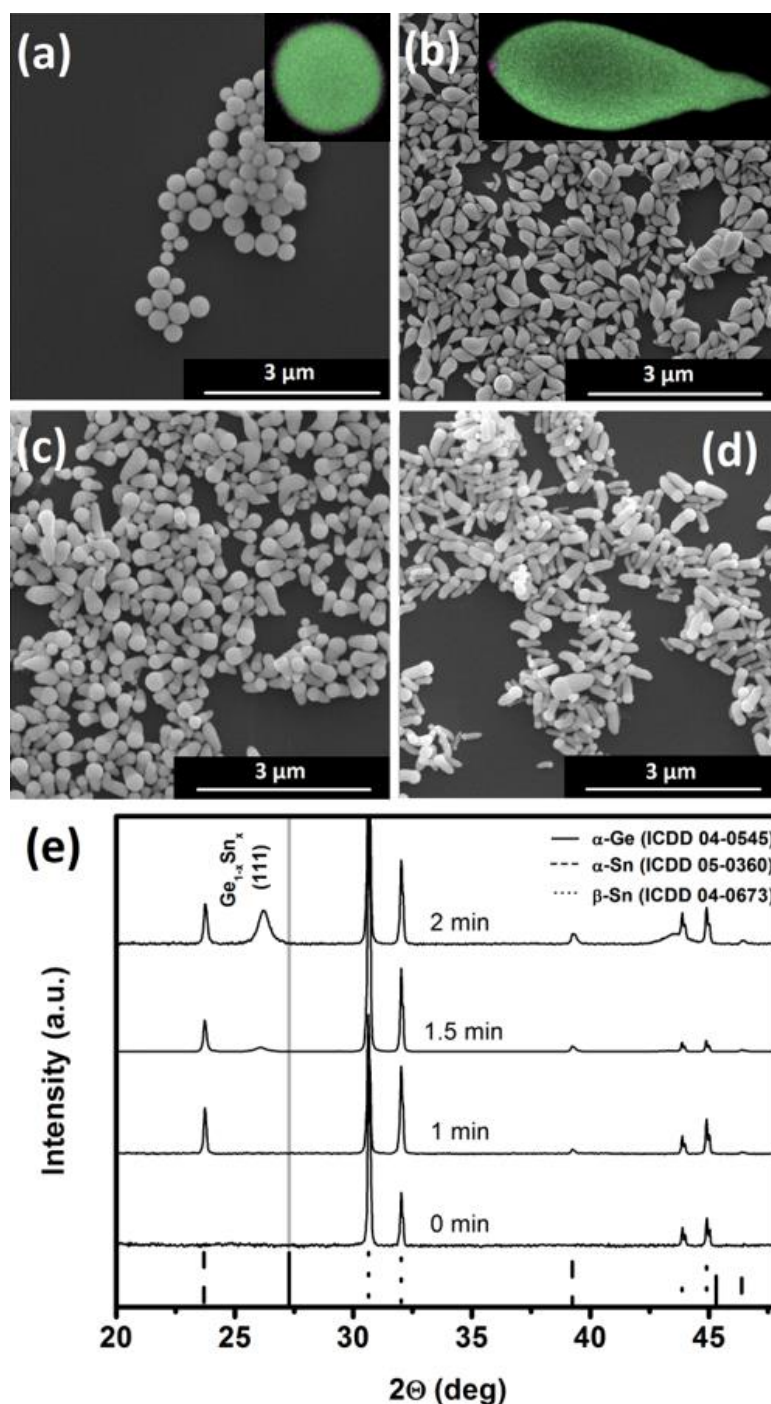

Figure 19: SEM images of the obtained structures after (a) 0 min, (b) 1 min, (c) 1.5 min, and (d) 2 min of decomposition are acquired and the associated XRDs are shown in (e). Overlay images of STEM-EDX elemental mappings of Sn and Ge of (a) globular and (b) teardrop-shaped structures are shown as insets of (a + b). The overall Ge content of the globular β-Sn particle formed at 140 °C is 0.4 at. %. In contrast, the teardrop-shaped α-Sn particle has a Sn content of 0.75 at. % (excluding the small Ge nucleus).

After conducting the elongation of the heterodimers, the structures are isolated and characterised by electron microscopy. The high crystallinity of the product is illustrated in Figure 20, while the FFT pattern in the inset suggests the predominant growth in the ⟨111⟩ direction.
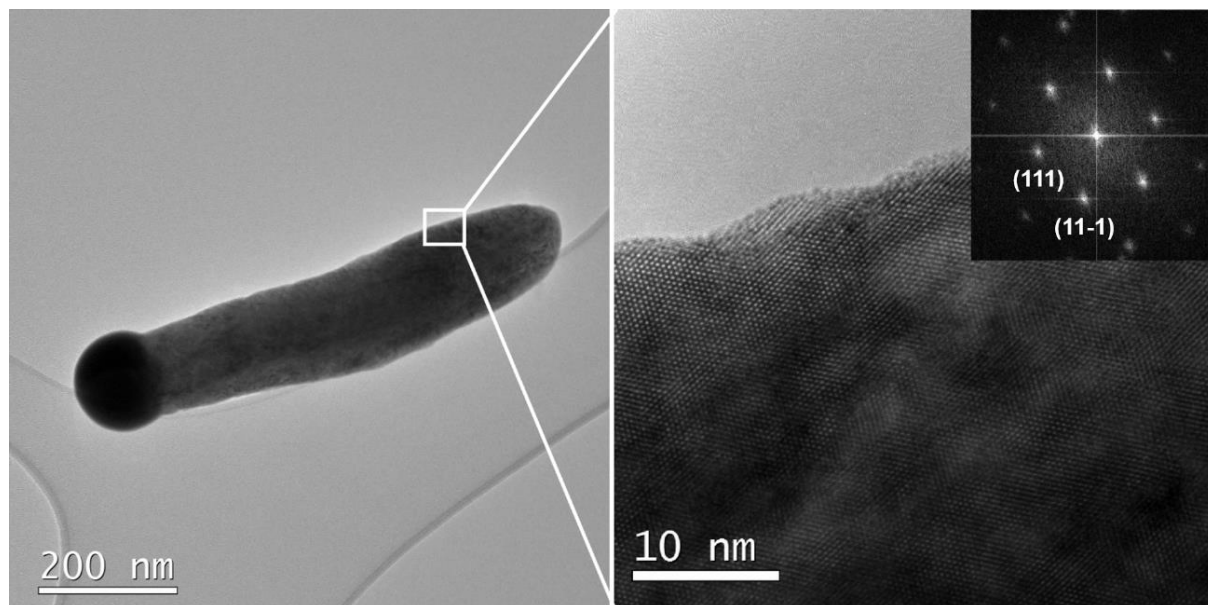
Figure 20: The HRTEM image of a selected area of the NR shown in the TEM image illustrates the high crystal quality of the synthesised $Ge_{1-x}Sn_x$ nanostructures. The FFT pattern in the inset reveals a predominant growth of the anisotropic $Ge_{1-x}Sn_x$ alloys in the ⟨111⟩ direction.

The presence of α-Sn particles acting as a template for the $Ge_{1-x}Sn_x$ growth is confirmed by combining STEM-EDX mapping and XRD measurements of the NRs (Figure 21). The determination of the shift of the Ge reflection in the XRD caused by the incorporation of Sn in the Ge lattice which increases the lattice parameter of Ge allows the calculation of the Sn content of the $Ge_{1-x}Sn_x$ alloy by using β-Sn reflections as standard and Vegard's law for quantification. This method is giving a Sn content of 27.5 at. %. The STEM-EDX mapping of a $Ge_{1-x}Sn_x$ alloy segment in Figure 21b shows a homogenous distribution of 27.9 at. % ± 0.9 at. % Sn in the Ge matrix. Both methods of quantification result in similar Sn contents suggesting a strain-relaxed $Ge_{1-x}Sn_x$ alloy. A small area of 150 nm between the α-Sn template and the $Ge_{1-x}Sn_x$ alloy segment with constant Sn content shows a gradient in Sn content due to the step-wise reduction of the influence of the α-Sn template on the growing $Ge_{1-x}Sn_x$ alloy.
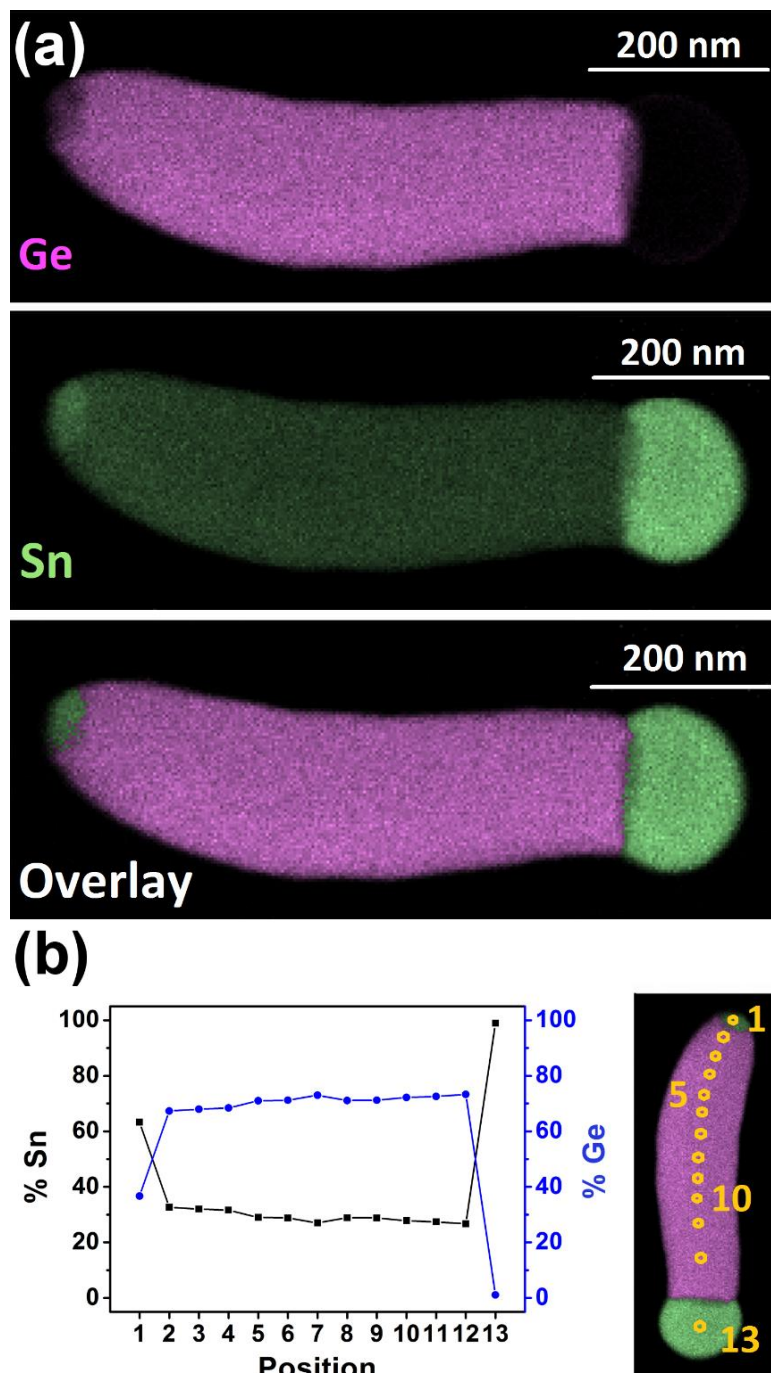
Figure 21: (a) Sn is distributed homogenously within the Ge matrix which is confirmed by STEM-EDX mappings. In addition, a small α-Sn nucleus is visible at the nucleation site of the NR. (b) EDX point measurements highlight the local Sn content along the NR axis and show a long segment of constant Sn content between the two extremes.

Furthermore, NRs with smaller elongated structures located at the nucleation site and terminated by a Sn particle can be found when increasing the decomposition temperature slightly and are shown in Figure 22. These structures do not have an α-Sn region as shown in the STEM-EDX mapping in Figure 22b. This implies that higher decomposition temperatures lead to the decomposition of the α-Sn phase resulting in a $Ge_{1-x}Sn_x$ alloy and a Sn particle. The segregated Sn particle can act as an active site for NW growth during the subsequent elongation regime.
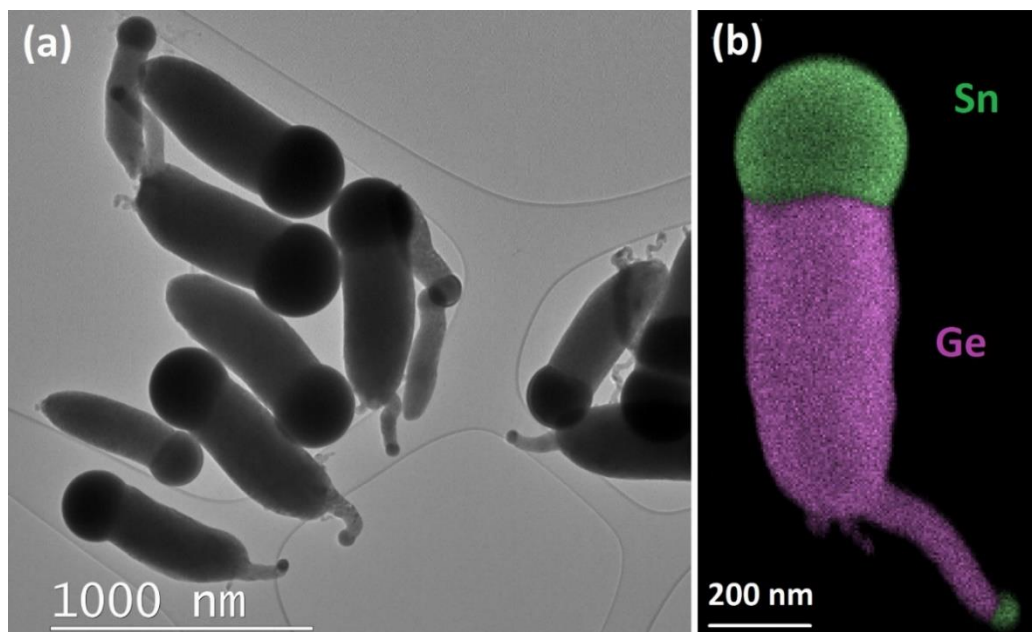
Figure 22: (a) The TEM image of $Ge_{1-x}Sn_x$ NRs synthesised at slightly higher temperatures than 140 °C shows additional NW growth at the nucleation site of the NRs. The absence of the α-Sn area observed at lower temperatures is featured with STEM-EDX mapping in (b).

The Ge-Sn phase diagram illustrated in Figure 7b clearly shows the absence of a thermodynamically stable α-Sn phase at 140 °C.[228] If the α-Sn phase would be formed in the cooling-down step, $Ge_{1-x}Sn_x$ NRs with high Sn contents due to the epitaxial growth on an α-Sn template could not be observed. Therefore, the α-Sn phase must be formed at 140 °C. According to the phase diagram α-Sn is stable below 14 °C. Consequently, there are only three reasonable options for the reported observations. The first explanation could be based on an epitaxial growth of α-Sn on a small Ge nucleus. It is well-known in literature that α-Sn can be epitaxially grown on III/V-crystals in zinc blende crystal structure including InSb and CdTe.[335-337] Therefore, Ge with diamond cubic crystal structure could act as template if the stress induced by the lattice mismatch of α-Ge and α-Sn can be relieved. In this case the high surface area of nanoparticles could realise the relief of the stress. According to literature, Ge can act as a secondary nucleus for the growth of α-Sn.[338] Another option is the stabilisation of the metastable α-Sn phase by alloying with Ge. Hints for this process can also be found in literature and reveal an increased stability of α-Sn for a Ge content of 1.22 at. % (0.75 wt. %) up to approximately 60 °C.[339] Similar effects on the stability of α-Sn are found for alloying α-Sn with Si.[340] Another aspect which is suggested in Figure 23, is the presence of a peritectoid being present in the Ge-Sn phase diagram making α-Sn to a thermodynamically stable phase at temperatures as high as 180 °C. A possible explanation why the peritectoid could not be identified in experimental studies before can be found in the way such phase diagrams are determined. A mixture of both elements is completely melted, cooled down, and held at a certain temperature. After crossing the eutectic line of the phase diagram, β-Sn and α-Ge phase are in equilibrium. At a temperature below the eutectic temperature, where α-Sn could be formed, the temperature is too low to overcome the activation barrier (lattice energy of β-Sn and α-Ge) for the following reaction:

$$\beta\text{-Sn} + \alpha\text{-Ge} \leftrightarrow \alpha\text{-Sn}.$$

The lattice energy of α-Ge is very high due to the covalent character of the Ge bond. In this study the Ge atoms are supplied to the β-Sn phase in their atomic form. Therefore, the activation barrier can be decreased by this approach at low temperatures. It should be considered that a peritectoid could be part of the Ge-Sn phase diagram leading to an alternative phase diagram as shown in Figure 23.
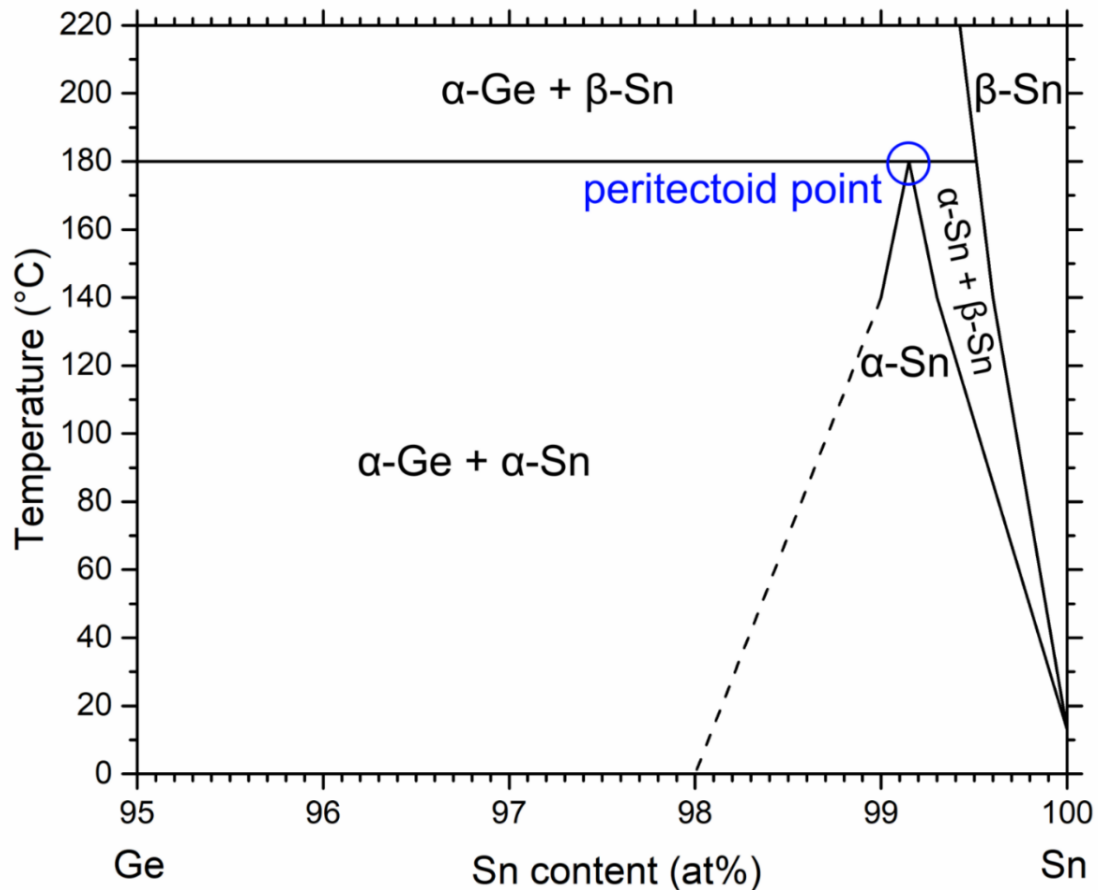

Figure 23: Alternative schematic phase diagram of Ge-Sn based on the determination of the present phases and the corresponding compositions found in samples produced at different temperatures.

The possibility of a peritectoid in the Ge-Sn system can be supported by thermodynamic data found in literature.[341] In the schematic representation of the Gibbs energy curves of the Ge-Sn system at 140 °C shown in Figure 24 some considerations lead to an interesting result. First, the Gibbs energy of pure Ge with diamond cubic crystal structure is higher than the Gibbs energy of pure Sn with diamond cubic crystal structure in the observed temperature range. A miscibility gap between α-Ge and α-Sn due to the large difference of the atomic radii is expected leading to the red curve in Figure 24. Furthermore, the Gibbs energy of β-Sn is only slightly lower than the Gibbs energy of α-Sn at 140 °C. Although the exact energy curves of both phases are unknown, the slight difference of the Gibbs energies of α-Sn and β-Sn combined with the possibility of a greater difference of the Gibbs energies of α-Ge and tetragonal Ge could enable a thermodynamically stable α-Sn phase at 140 °C.
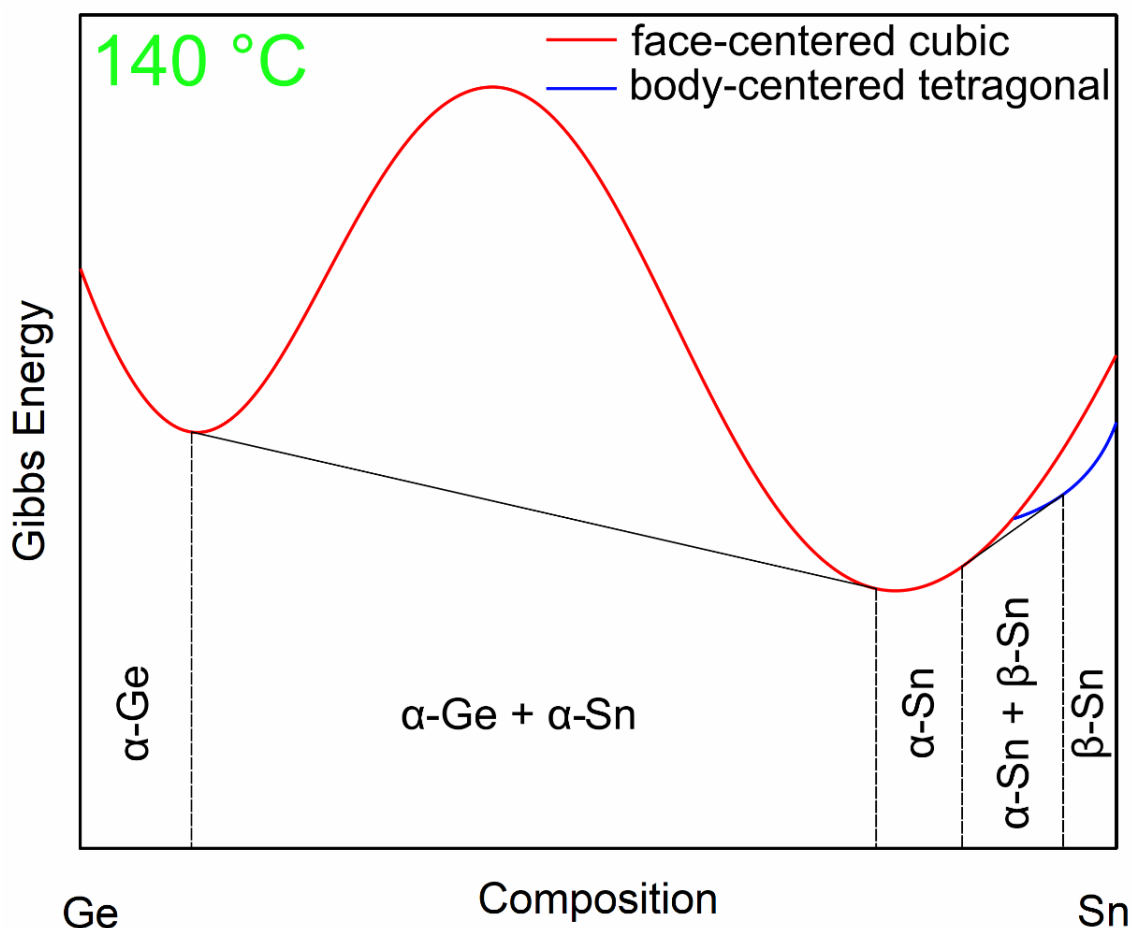
Figure 24: The schematic representation of the Gibbs energy curves of the Ge-Sn system at 140 °C reveals the possibility of a thermodynamically stable α-Sn phase supporting the presence of a peritectoid in this system. Thermodynamic data of the Ge-Sn system[341] are used for the construction of the schematic representation of possible Gibbs energy curves of the Ge-Sn system.

In a kinetically driven process, the growth temperature and the growth kinetics play a major role for the observed incorporation of Sn in the Ge lattice. In addition, the unusual presence of the α-Sn phase at 140 °C enables the incorporation of very high amounts of Sn due to a template effect. A phase map including kinetics and the alternative phase diagram shown in Figure 23 is illustrated in Figure 25a. In this phase map, trends concerning the maximum Sn incorporation for a certain set of synthesis parameters are combined. It should be considered that the growth temperature cannot be altered without changing the growth kinetics at the same time. However, a general trend is known from literature and observed in our studies.[342] Higher growth temperatures lead to lower Sn contents in $Ge_{1-x}Sn_x$ layers and nanostructures. On the other hand, comparing isothermal growth conditions with variations in precursor composition, such as an exchange of dodecylamine by n-octylamine, can alter the growth kinetics. For the same decomposition duration, the NRs obtained by using n-octylamine instead of dodecylamine grow much longer (see Figure 25b) suggesting a higher growth rate of these structures and consequently a higher Sn content of 32 at. % can be observed.
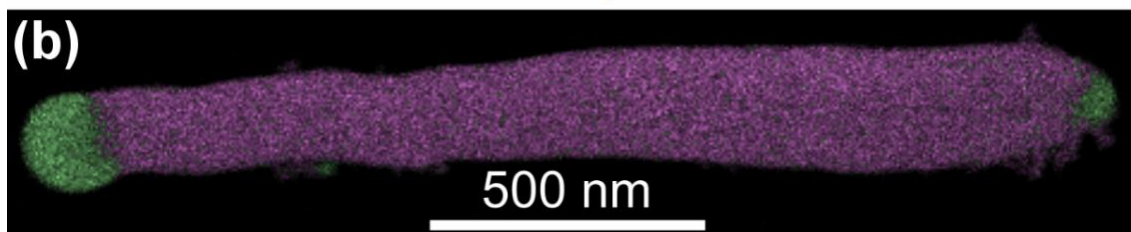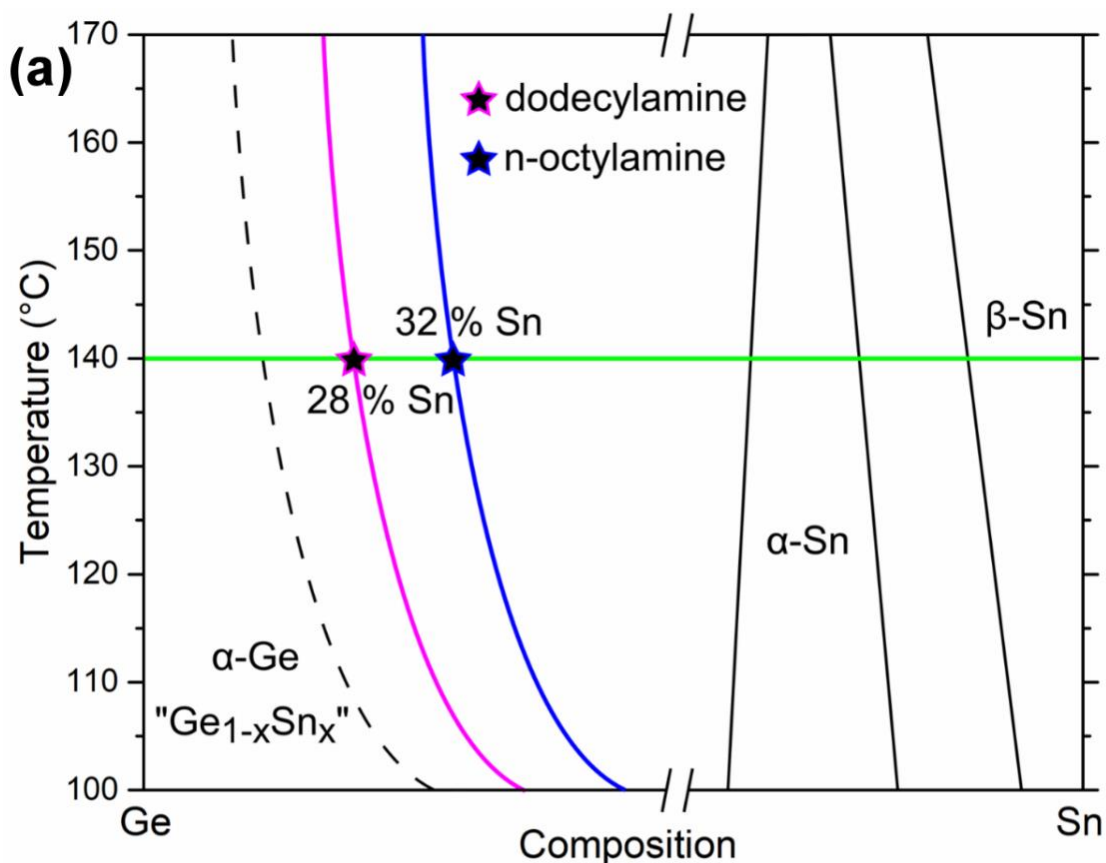
Figure 25: (a) A phase map including the alternative phase diagram shown in Figure 23 shows the impact on the observed alloy composition of $Ge_{1-x}Sn_x$ if a certain synthesis parameter is altered. (b) The STEM-EDX mapping of a $Ge_{1-x}Sn_x$ NR using n-octylamine as solvent and ligand reveals a higher Sn content of the $Ge_{1-x}Sn_x$ alloy when compared to the typical process using dodecylamine. The higher Sn incorporation can be attributed to a higher growth rate of these structures.

Metastable $Ge_{1-x}Sn_x$ is a very interesting material for novel devices making the evaluation of the thermal stability of this alloy vital. The delay of segregation can be explained by the fact that the formation of β-Sn defects is a statistical process depending on temperature, time, and Sn content. Variable-temperature XRD measurements under H_2 atmosphere are performed on $Ge_{1-x}Sn_x$ NRs with a Sn content of 28 at. %. High-temperature XRD measurements of as-grown $Ge_{1-x}Sn_x$ NRs are shown in Figure 26 and reveal decomposition of the material at 160 °C. Highly interesting is the fact that after removal of the metallic Sn seeds by treatment with diluted hydrochloric acid (HCl), the thermal stability of $Ge_{1-x}Sn_x$ NRs is increased by nearly 70 °C. Long-time stability is assumed at 120 °C due to an unaltered $Ge_{1-x}Sn_x$ (111) reflection after 6 h of annealing at that temperature.
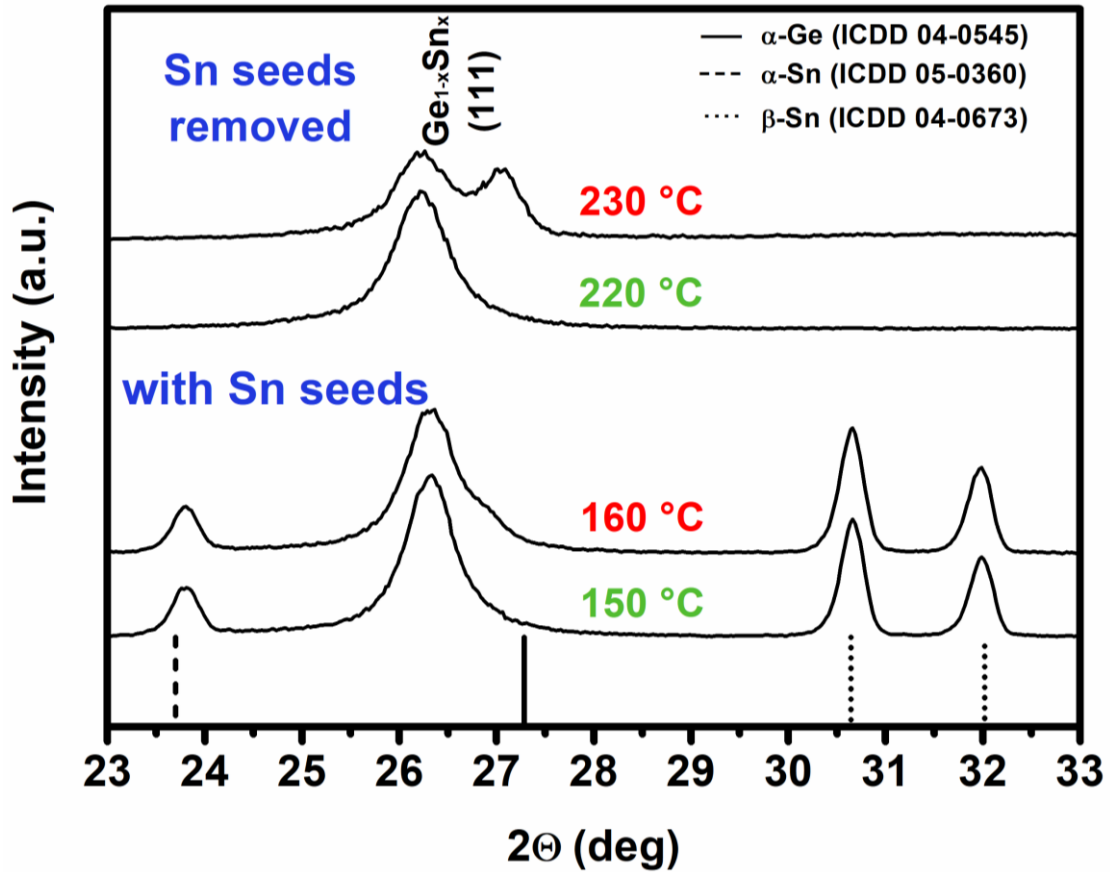
Figure 26: Variable-temperature XRD measurements of $Ge_{1-x}Sn_x$ NRs containing the Sn seeds show a broadening of the $Ge_{1-x}Sn_x$ (111) reflection towards lower Sn concentrations starting at 160 °C. The broadening of the $Ge_{1-x}Sn_x$ (111) reflection is accompanied by an increase of the β-Sn reflections. $Ge_{1-x}Sn_x$ NRs after removal of the Sn seeds show a broadening of the $Ge_{1-x}Sn_x$ (111) reflection towards lower Sn concentrations at significantly higher temperatures.

The underlying mechanisms of the decomposition of this metastable material should be discussed in detail. A suitable method to get information about the decomposition is *in situ* TEM using a heating holder. Selected images of an *in situ* TEM movie of a $Ge_{1-x}Sn_x$ NR heated up to 200 °C is presented in Figure 27a - f. The decomposition process starts with a change of the $Sn/Ge_{1-x}Sn_x$ interface. Subsequently, diffusion of solid Sn through the NR body within the boundaries of the NR towards the α-Sn nucleus is observed. A permanent diffraction contrast due to β-Sn can be observed at the end of the decomposition process. STEM-EDX mappings and TEM images of a $Ge_{1-x}Sn_x$ NR after a heat treatment at 180 °C show Sn-enriched areas along the NR body where at the same time nearly no Ge is present (Figure 27g - i). At the nucleation site a high amount of Ge is replaced by Sn suggesting a simultaneous, but spatially separated Ge and Sn diffusion. Therefore, metastable $Ge_{1-x}Sn_x$ with high Sn content must be dissolved and still metastable $Ge_{1-y}Sn_y$ with lower tin content ($x > y$) must be deposited. The driving force for this process can be attributed to the gain of lattice energy when going towards pure Ge. At higher temperatures Sn is mainly located at the nucleation site of the NRs and the remaining Sn in the NR body is not homogenously distributed. Sn seems to have a strong impact on the thermal stability of metastable $Ge_{1-x}Sn_x$ alloys which should be considered when using this material for devices.

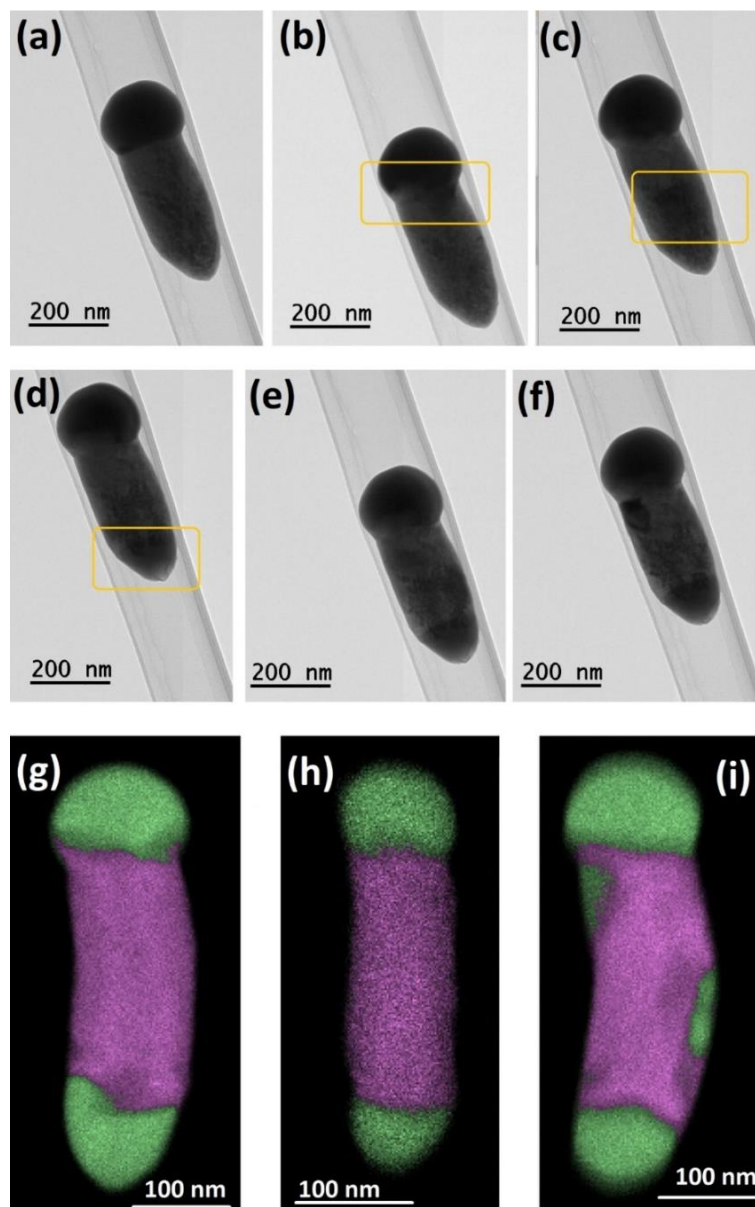**Figure 27**: TEM images (a - f) picked out of an *in situ* TEM movie charting the decomposition process of $Ge_{1-x}Sn_x$ NRs at 200 °C and pointing out the ongoing processes. (a) shows an as-grown $Ge_{1-x}Sn_x$ NR. (b) The $Sn/Ge_{1-x}Sn_x$ interface starts to change followed by (c) a diffusion of Sn through the NR body within the boundaries of the structure. (d) A permanent diffraction contrast due to β-Sn is observed at the nucleation site of the $Ge_{1-x}Sn_x$ NR. (e + f) show ongoing diffusion processes. At higher temperatures (g + h) β-Sn is often located at the nucleation site of the NRs while at (i) lower temperatures Sn-rich areas are also found along the NR body.

A second temperature regime for the synthesis of $Ge_{1-x}Sn_x$ NWs has been described in previous publications of our group showing that at higher temperatures indeed a lower amount of Sn can be incorporated into the Ge matrix and at the same time no α-Sn nucleus is present. Variable-temperature XRD measurements of the $Ge_{1-x}Sn_x$ NWs are in good agreement with the observations made for the $Ge_{1-x}Sn_x$ NRs. The $Ge_{1-x}Sn_x$ NWs with a Sn content of 17 at. % - 19 at. % show higher thermal stability than the NRs with 28 at. % of Sn incorporated into the Ge matrix. The increased thermal stability after removal of the metallic Sn seeds confirm the observations described before.

In addition to the here presented growth study of $Ge_{1-x}Sn_x$ NRs and NWs, the optical properties of the synthesised nanostructures are determined and presented in Figure 28. As known from literature, a higher concentration of Sn incorporated on substitutional sites of the Ge crystal lattice leads to a decrease of the bandgap energies. The direct bandgap energy shrinks to a greater extent than the indirect bandgap energy leading to the transition into a direct bandgap material.[205] In this work, Tauc plots from IR absorption measurements are used to determine the direct bandgap energy of $Ge_{1-x}Sn_x$ NRs and NWs. As expected, the $Ge_{1-x}Sn_x$ NRs have a significantly smaller direct bandgap energy (0.29 eV) than the $Ge_{1-x}Sn_x$ NWs with lower Sn content (0.40 eV).
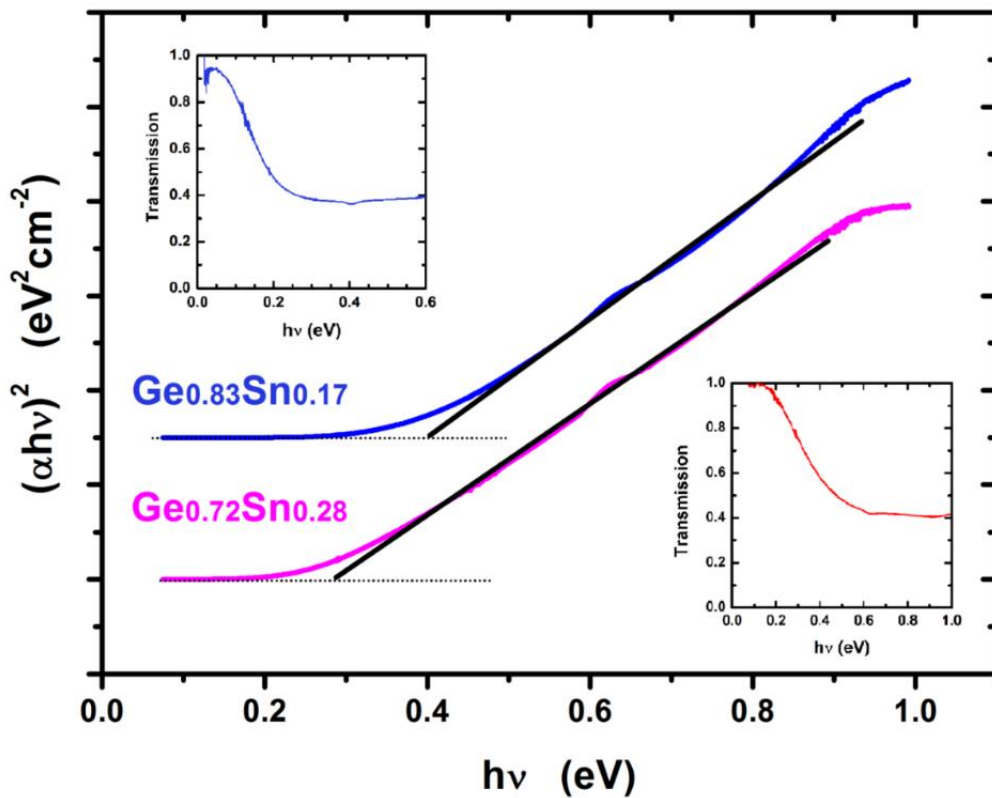

Figure 28: Tauc plots obtained by IR absorption measurements (insets) enable the determination of the direct bandgap energy of $Ge_{1-x}Sn_x$ NWs and NRs.

Besides the optical properties, $Ge_{1-x}Sn_x$ NWs with a Sn content of 19 at. % ($Ge_{0.81}Sn_{0.19}$ NWs) are suitable building blocks for single NW devices enabling the determination of their electronic properties. Devices in two-point and four-point geometry are fabricated. Therefore, the Sn seeds are removed by treatment with diluted HCl due to the observed destabilising effect of metallic Sn on the metastable $Ge_{1-x}Sn_x$ alloy. The SEM image in Figure 29a confirms the successful removal of Sn by this treatment. The XRD measurement of a NW sample after HCl treatment in the inset of Figure 29a shows the absence of β-Sn and unaltered $Ge_{1-x}Sn_x$ reflections. Sn is distributed homogenously along the NW axis which is confirmed via STEM-EDX point measurements on a $Ge_{0.81}Sn_{0.19}$ NW before HCl treatment in Figure 29b. In addition, the Sn-rich area at the tip of the NW suggests a SLS-mechanism for the growth in this temperature regime.
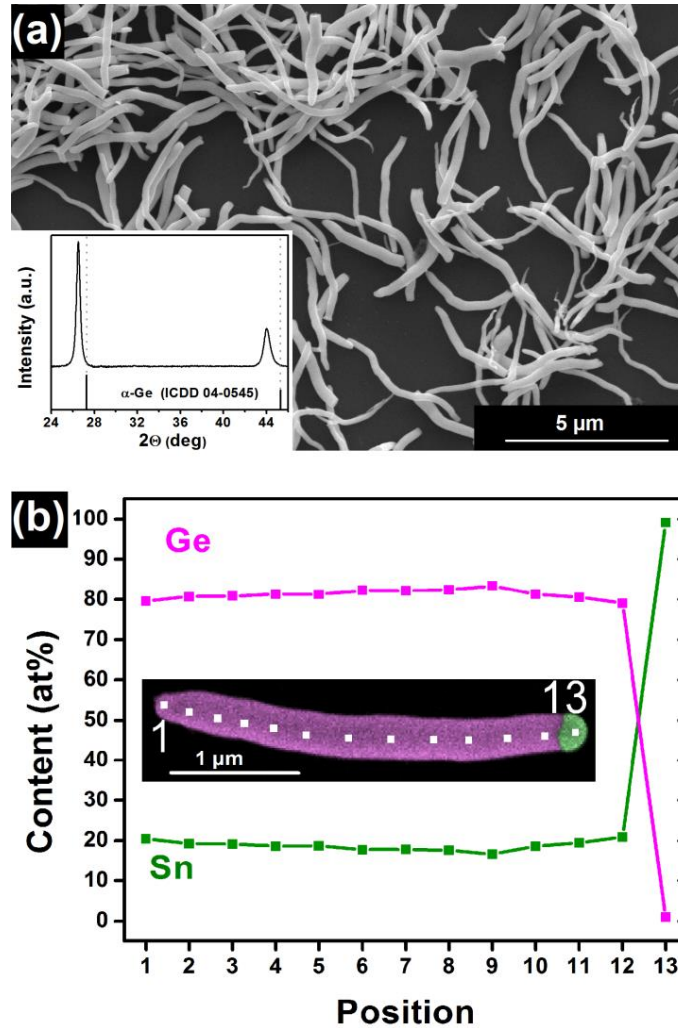
Figure 29: (a) The SEM image confirms the successful removal of metallic Sn from the tips of the NWs by treatment with diluted HCl. The inset in (a) shows an XRD measurement highlighting the present phases after the acid treatment. β-Sn reflections are not present while $Ge_{1-x}Sn_x$ reflections are unaltered. (b) STEM-EDX point measurements on a $Ge_{0.81}Sn_{0.19}$ NW before HCl treatment confirm the homogenous distribution of Sn along the NW axis and a Sn growth seed is present at the tip of the NW as expected for metal-seeded bottom-up growth of anisotropic structures.

$Ge_{0.81}Sn_{0.19}$ NWs are drop-casted on a Si substrate with a 100 nm thick, thermally grown SiO_2 layer. The NWs are contacted by Au using standard EBL, deposition of metal by evaporation, and subsequent lift-off techniques. *I-V* curves obtained from measurements of the single NW devices in two-point geometry using $Ge_{0.81}Sn_{0.19}$ NWs with different diameters are presented in Figure 30a. In contrast to a study on electronic transport measurements of Au-Ge interfaces obtained by Au-seeded Ge NW growth which show the presence of a Schottky barrier, these devices reveal ohmic behaviour.[343] However, the incorporation of Sn in the Ge lattice has a strong impact on the charge carrier mobilities in the specific sub-bands of this material as described in several theoretical studies leading to high current levels.[241, 242] No clear trend concerning the influence of the NW diameter on the resistance can be observed. This hints towards a small contribution of a $Ge_{0.81}Sn_{0.19}$ NW to the overall resistance and a strong influence of the contact resistances. For comparison, a single NW device using an intrinsic, Au-seeded NW with similar dimensions grown in a CVD process is fabricated. The

44

electric current measured for $Ge_{0.81}Sn_{0.19}$ NW devices is approximately two orders of magnitude higher than for the comparison device confirming the low resistivity of $Ge_{0.81}Sn_{0.19}$ NWs. In addition, no gating-effect could be observed when performing field-effect measurements with these devices.

Single NW devices in four-point geometry are used to break down the contribution of the $Ge_{0.81}Sn_{0.19}$ NW resistance to the overall resistance. Therefore, two- and four-terminal measurements shown in Figure 30b are performed suggesting that four fifths of the overall resistance can be attributed to the contact resistances. Improving the quality of the contact resistances is not trivial due to several limitations arising by using $Ge_{1-x}Sn_x$ with such a high Sn content. Ni pads, which show very good performances when used as contacting metal for Ge and $Ge_{1-x}Sn_x$ with low Sn content, require high temperatures for the reaction with Ge to form germanides which is necessary for a high-quality contact.[344] Moreover, Sn contacts can be ruled out as a contacting metal due to the expected dissolution of metastable $Ge_{0.81}Sn_{0.19}$ and redeposition of still metastable $Ge_{1-x}Sn_x$ with lower Sn content at low temperatures altering the properties of the material. A possible improvement of the contacts could be achieved by the removal of the SnO_2 layer of the $Ge_{0.81}Sn_{0.19}$ NWs formed during treatment with oxygen plasma to get rid of organic groups attached to the NW surface. Pre-treatment with hydrofluoric acid (HF) could remove organic groups efficiently without the formation of SnO_2 on the surface and would therefore be a suitable process step for the improvement of the contacts.
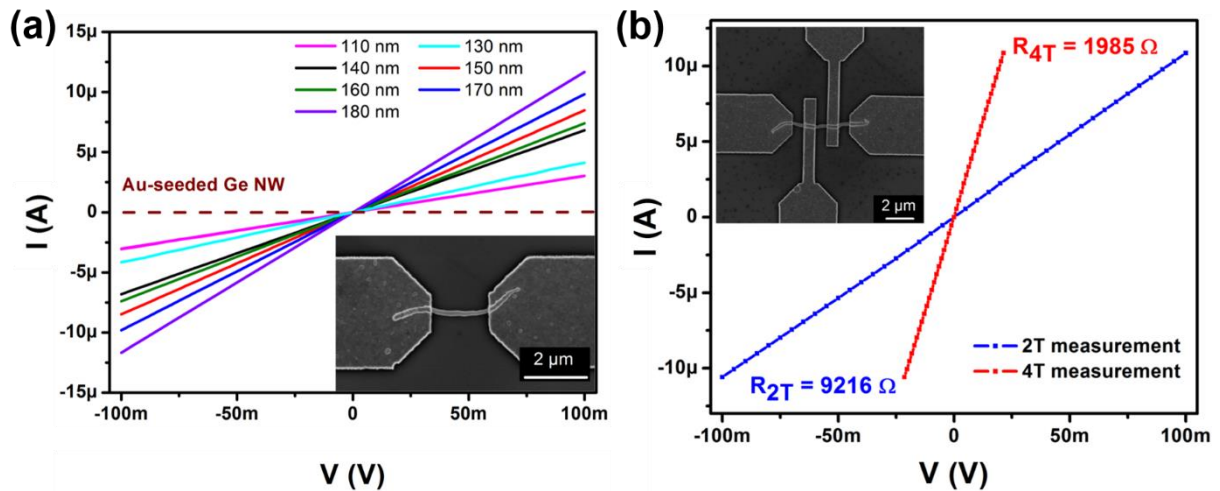

Figure 30: (a) Two-point measurements of single NW devices using $Ge_{0.81}Sn_{0.19}$ NWs with different diameters reveal very low resistances when compared to a single NW device using an intrinsic, Au-seeded Ge NW as building block. The inset in (a) shows a SEM image of a typical single NW device in two-point geometry. (b) Two- and four-terminal measurements are performed on the same $Ge_{0.81}Sn_{0.19}$ NW to determine the influence of the contact resistances on the overall resistance suggesting a very low resistance of $Ge_{0.81}Sn_{0.19}$ NWs. The single NW device in four-point geometry used for these measurements is shown in the SEM image as inset of (b).

In addition, the temperature-dependence of the resistivity in the range 298 K - 10 K is measured for a device in four-point geometry using a 170 nm thick $Ge_{0.81}Sn_{0.19}$ NW as building block. The resistivity upon temperature variation is plotted in Figure 31 for different materials including an intrinsic and a Ga-hyperdoped Ge NW for comparison. The intrinsic Ge NW clearly shows an increase of resistivity for several orders of magnitude upon cooling towards 10 K

(semiconducting behaviour). The $Ge_{0.81}Sn_{0.19}$ and the Ga-hyperdoped Ge NW distinguish by a moderate resistivity. The inset in Figure 31 enables the attribution of semiconducting behaviour to the $Ge_{0.81}Sn_{0.19}$ NW and quasi-metallic behaviour to the Ga-hyperdoped Ge NW. However, $Ge_{0.81}Sn_{0.19}$ NWs show two orders of magnitude lower resistivity values at room temperature compared to the intrinsic Ge NW. At 10 K the difference in resistivity values between the $Ge_{0.81}Sn_{0.19}$ and the intrinsic Ge NW is even more striking and in the range of eight orders of magnitude. The huge difference of the resistivity values is caused by the slight temperature-dependence of the resistivity for $Ge_{0.81}Sn_{0.19}$ NWs compared to intrinsic Ge NWs. The decreased resistivity of $Ge_{0.81}Sn_{0.19}$ NWs can be caused by the increased carrier mobilities[345] and slight increase of carrier concentration.[346]
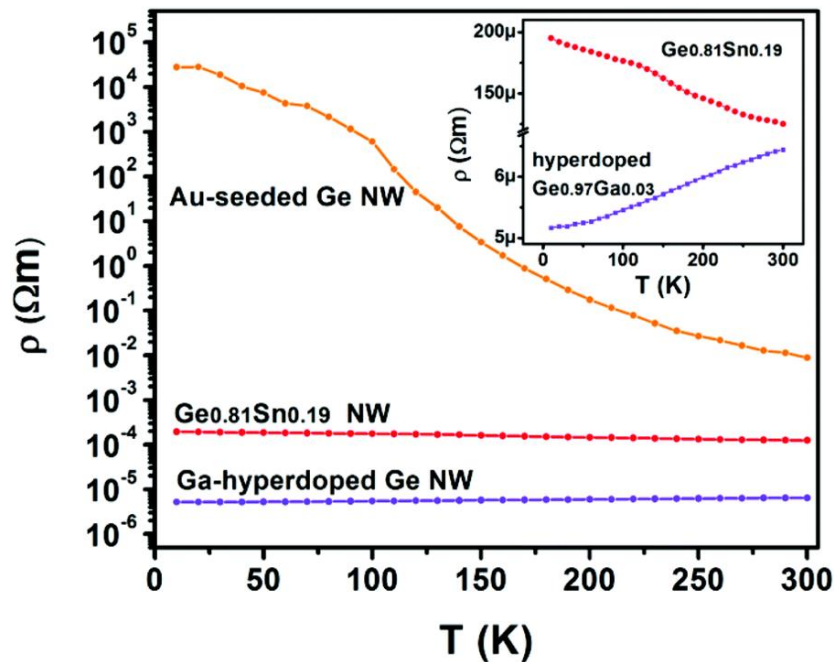

Figure 31: The temperature-dependence of the resistivity is measured for a 170 nm thick $Ge_{0.81}Sn_{0.19}$ NW implemented on a single NW device in four-point geometry. For comparison, curves from an intrinsic, Au-seeded and a Ga-hyperdoped Ge NW are added. The inset reveals a semiconducting behaviour for the $Ge_{0.81}Sn_{0.19}$ NW, while the Ga-hyperdoped Ge NW behaves like a metal.

Variable-temperature XRD measurements reveal segregation processes occurring at moderate temperatures, especially if the metastable $Ge_{1-x}Sn_x$ alloy is in contact with metallic Sn. Changes in the composition of $Ge_{1-x}Sn_x$ NWs should have a strong impact on the performance of single NW devices built by this material. High-temperature XRD measurements in Figure 32a clearly show the starting segregation process at 260 °C for $Ge_{0.81}Sn_{0.19}$ NWs pre-treated with diluted HCl to remove the Sn seeds. Keeping in mind that these analyses have been performed with short holding times, a long-time thermal stability should be approximately 40 °C - 50 °C lower. Therefore, devices in two-point geometry are annealed at 250 °C under inert atmosphere in 15 min steps to initiate the controlled decomposition with subsequent measurement of the electronic properties. In Figure 32b XRD measurements of a sample before and after the annealing clearly show the appearance of β-Sn and the splitting of the $Ge_{1-x}Sn_x$ (111) reflection after this treatment hinting towards a partial decomposition of these NWs.
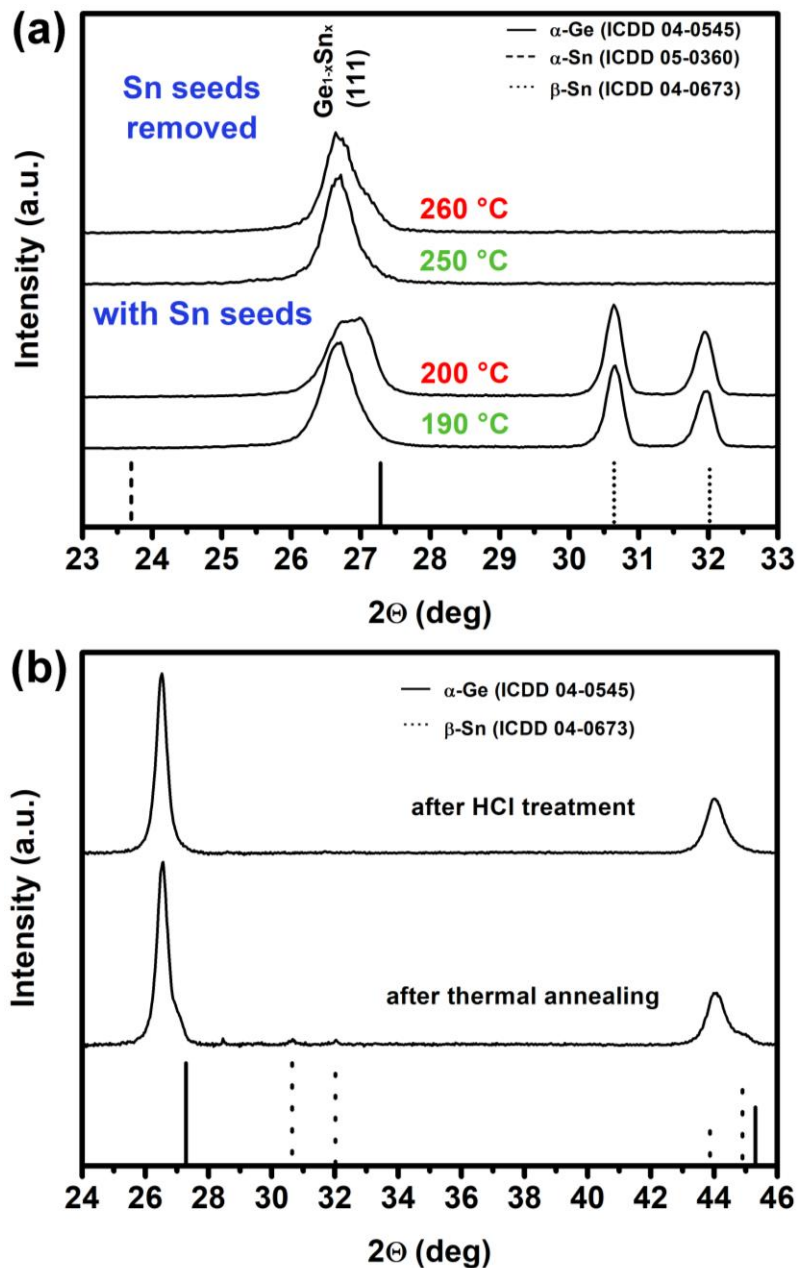
Figure 32: (a) Variable-temperature XRD measurements of as-grown $Ge_{0.81}Sn_{0.19}$ NWs reveal a broadening of the $Ge_{1-x}Sn_x$ (111) reflection starting at 190 °C. After removal of the Sn seeds by HCl treatment, $Ge_{0.81}Sn_{0.19}$ NWs show short-time stability up to 250 °C. (b) The successful removal of Sn seeds from as-grown $Ge_{0.81}Sn_{0.19}$ NWs is demonstrated by XRD measurements. After thermal annealing at 250 °C a broadening of the $Ge_{1-x}Sn_x$ (111) reflection can be observed, hinting towards decomposition of the metastable alloy into still metastable $Ge_{1-x}Sn_x$ with lower Sn content accompanied by segregation of β-Sn which explains the occurrence of reflections attributed to this phase.

After the first annealing step approximately one half of the built devices failed, which will be discussed in detail below. One of the eventually failing devices provided an electronic signal after the first annealing step but fails again after the second annealing step. All the other devices could be characterised in terms of their electronic properties even after the last annealing step. Figure 33a highlights three types of device behaviour. The first case (α) shows an increase in resistivity (contact resistances included) which can be attributed to the

47

decomposition of the $Ge_{0.81}Sn_{0.19}$ NW resulting in areas along the NW body where less amounts of Sn are incorporated in the Ge lattice leading to a decrease of the carrier mobility. In the second case (β) a decreasing resistivity upon annealing is followed by an increase in resistivity. While the increase in resistivity can be again explained by the decomposition of the material resulting in a Sn distribution illustrated in Figure 33b, the decreasing resistivity is assigned to the increased quality of the $Au/Ge_{1-x}Sn_x$ contact. The third case (γ) represents the continuous decrease in resistivity due to the absence of the decomposition of the metastable material shown in Figure 33c.
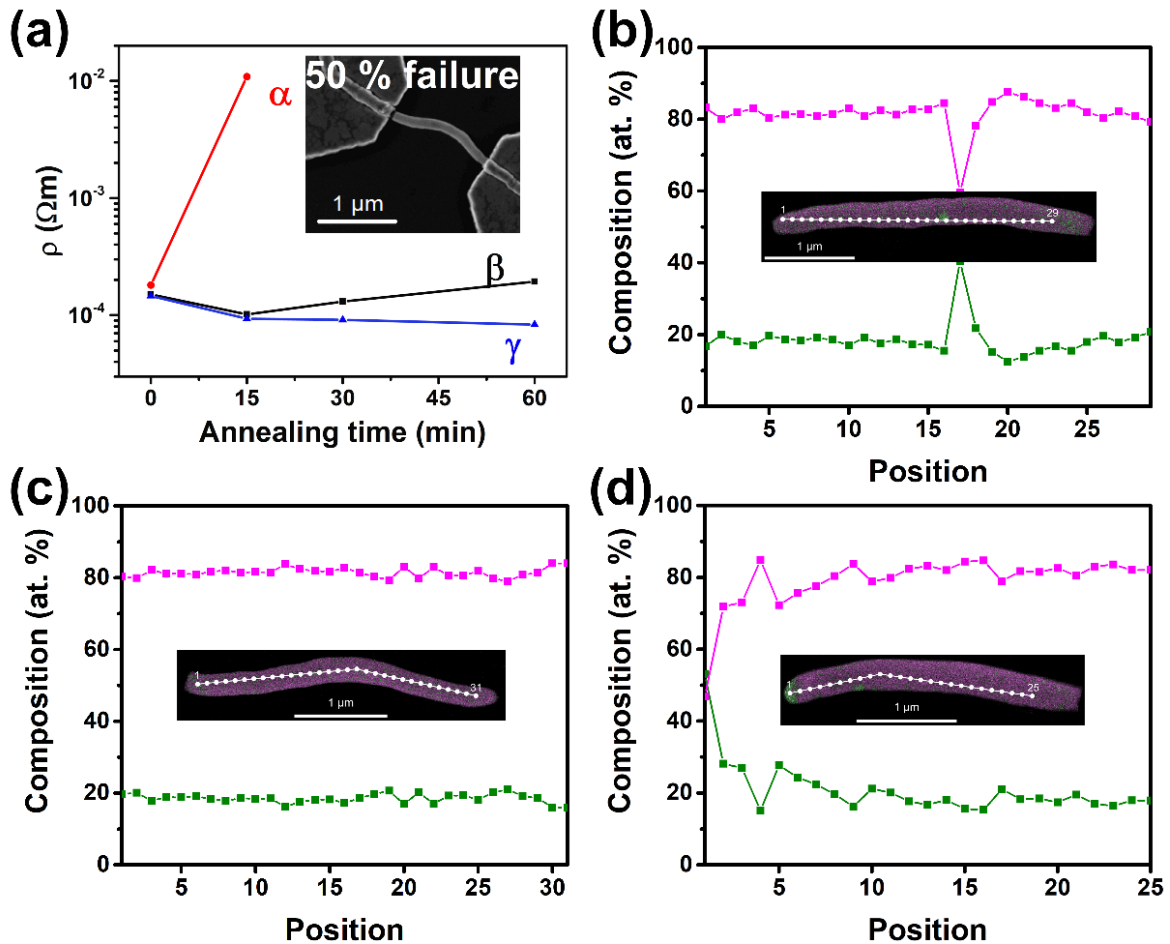

Figure 33: (a) The behaviour of single NW devices upon annealing can be classified into three cases. One half of the used devices show device failure (α) by a fracture of the $Ge_{0.81}Sn_{0.19}$ NW next to the Au contact (inset). Furthermore, it must be distinguished between devices where the resistivity decreases followed by an increase of resistivity due to degradation of the $Ge_{0.81}Sn_{0.19}$ NW at 250 °C (β) and devices where the resistivity decreases continuously during the annealing due to the increasing quality of the $Au/Ge_{0.81}Sn_{0.19}$ contact. (b - d) STEM-EDX point measurements of individual $Ge_{0.81}Sn_{0.19}$ NWs annealed for 60 min at 250 °C enable the assignment of the different device behaviours to a state of the annealed NW.

A typical device failure is caused by a fracture of the NW material next to the Au contact as shown in the inset of Figure 33a. This could be attributed to a $Ge_{1-x}Sn_x$ material with a very inhomogeneous distribution of Sn supported by STEM-EDX point measurements and a STEM-EDX mapping shown in Figure 33d. Two aspects must be considered for the occurrence of the fracture at this specific point of the NW including material transport

48

phenomena and strain. Segregated Sn next to the Au contact can easily be removed from the NW material due to the high mobility of Sn in Au and therefore mass transport from the NW to the electrode pad.[347] The resulting necked area of the NW located next to the Au contact can act as pre-determined breaking point due to the structural weakening. In addition, the segregation of Sn leads to a change of the lattice parameter of the redeposited $Ge_{1-x}Sn_x$ alloy with lower Sn content. The thereby generated mechanical tensile strain can result in the fracture of the NW. The observed failure is most likely a combination of all the discussed scenarios.

3.3 Paper 4

Epitaxial $Ge_{1-x}Sn_x$ Nanowire and Nanocone Growth using Sn Growth Seeds: Effects of the Seed Diameter and Photoluminescence Properties

In Chapter 3.2 the successful growth of metastable, anisotropic $Ge_{1-x}Sn_x$ nanostructures via self-seeding in a solution-based microwave-assisted process without the use of a template is presented. However, the integration of this material on a Si platform via CMOS compatible processing is a further step towards tapping the full potential of metastable, anisotropic $Ge_{1-x}Sn_x$ nanostructures.

Therefore, the self-seeding of metastable, anisotropic $Ge_{1-x}Sn_x$ nanostructures studied in Chapter 3.2 is adapted to enable the growth of these structures via metalorganic CVD (MOCVD) in a modified cold-wall reactor. The epitaxial growth of anisotropic $Ge_{1-x}Sn_x$ nanostructures on a Ge(111) substrate is targeted in a two-step process. Sn is deposited on the substrate via the thermal decomposition of bis[(dimethyl)amido]tin(II) supplied by a precursor flux generated by the partial pressure of the compound and applying a dynamic vacuum (~ $1·10^{-3}$ mbar). This initial step is followed by the thermal decomposition of t-butylgermane in a batch reaction. Immediately after the growth process, the sample is disconnected from the graphite susceptor and transferred into a RIE etcher (CF_4/O_2 process-gas) to remove an amorphous Ge layer deposited on the substrate and on the sidewall of the anisotropic $Ge_{1-x}Sn_x$ nanostructures. After RIE the samples are treated with diluted HCl to remove SnO_2 and Sn seeds (if still present).

All samples are characterised by electron microspopy (Figure 34). A top-view SEM image in Figure 34a shows globular structures and anisotropic structures growing not perpendicular to the substrate surface. A cross-sectional SEM image (Figure 34b) and a SEM image of a 30°-tilted sample (Figure 34c) allows the identification of anisotropic nanostructures growing perpendicular to the Ge substrate surface and therefore appearing circular in the bird's eye view. These anisotropic structures are removed mechanically from the Ge substrate and transferred to a lacey carbon Cu grid for TEM characterisation. A TEM image of an anisotropic nanostructure clearly shows the presence of a growth promoter at the tip of the strongly tapered NW as expected for NW growth via the VLS-mechanism (Figure 34d). The strong tapering of the NW can either be attributed to growth of Ge on the sidewall of the NW or incorporation of Sn in the Ge matrix which is also observed for self-seeded GaAs and InP NWs.[348-350] The HRTEM image in Figure 34e of the same NW reveals the high crystallinity of the material. The FFT pattern (inset of Figure 34e) suggests the growth of this NW in the ⟨111⟩ direction which can be expected for the epitaxial growth of Ge NWs on a Ge(111) substrate.
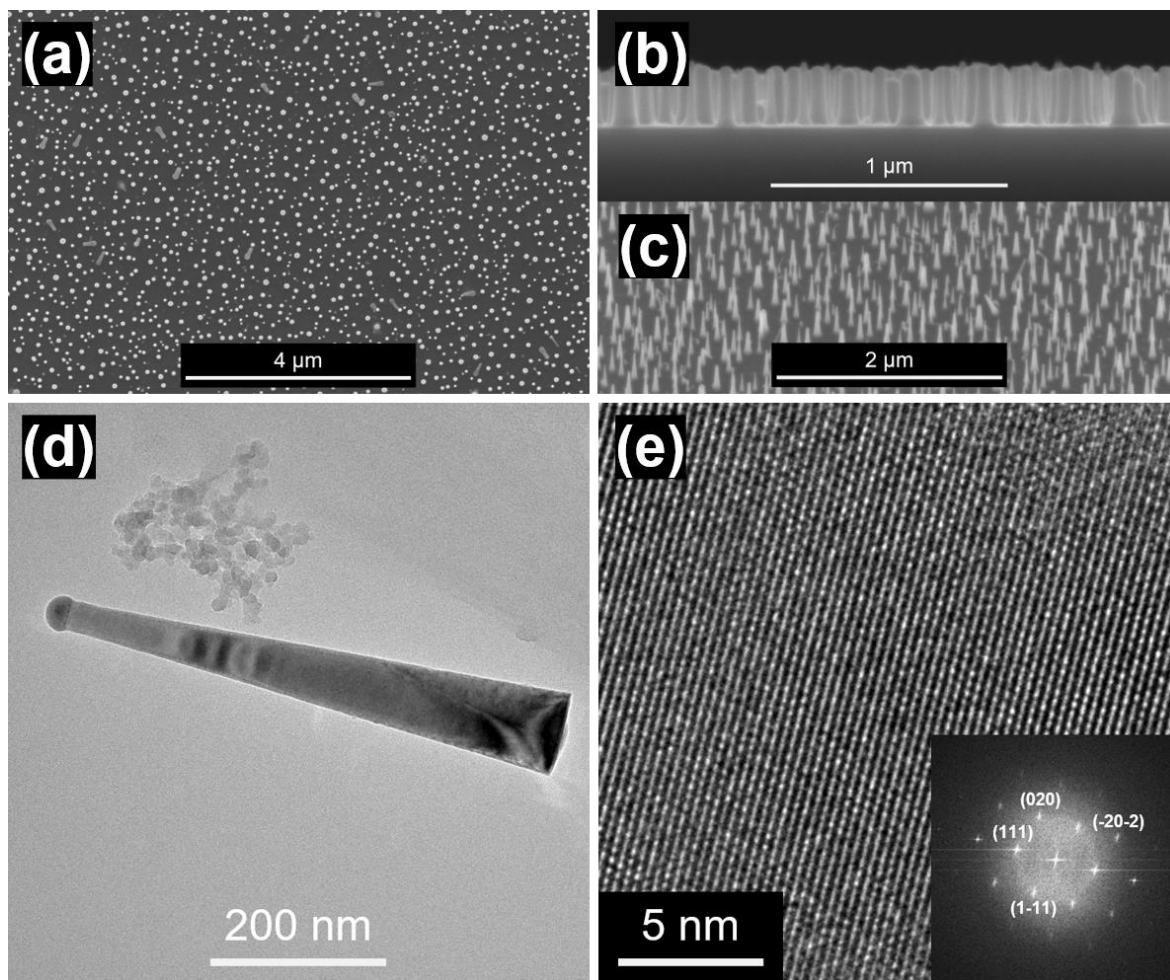
Figure 34: (a) Top-view SEM image of a sample where Sn is deposited on a Ge(111) substrate via MOCVD followed by the supply of Ge via thermal decomposition of t-butylgermane in a batch MOCVD process. SEM images of (b) a cross-section and (c) a 30°-tilted sample are presented. (d) A TEM image of a $Ge_{1-x}Sn_x$ NW is illustrated. The corresponding HRTEM image is shown in (e). The FFT pattern illustrates the growth along the $\langle 111 \rangle$ axis.

STEM-EDX mappings of as-grown nanostructures and nanostructures after RIE (30 s) of the sample shown in Figure 34 are performed (Figure 35). The yellow bars in Figure 35a + b can be used to illustrate differences in diameters of a Ge/Sn overlay STEM-EDX map (Figure 35a) and the elemental map for Sn (Figure 35b) of an as-grown NW. The difference in diameter at the same NW position reveals the presence of a Ge-rich shell deposited on the sidewall of a tapered $Ge_{1-x}Sn_x$ NW. Sn is distributed homogenously within the Sn-rich body. The Sn growth promoter is located at the tip of the $Ge_{1-x}Sn_x$ NW suggesting the self-seeded growth of anisotropic $Ge_{1-x}Sn_x$ NWs via the VLS-mechanism. STEM-EDX maps of these structures after RIE (Figure 35c + d) show the successful removal of the Ge-rich shell due to selective etching of Ge which is indicated by equal red bars.
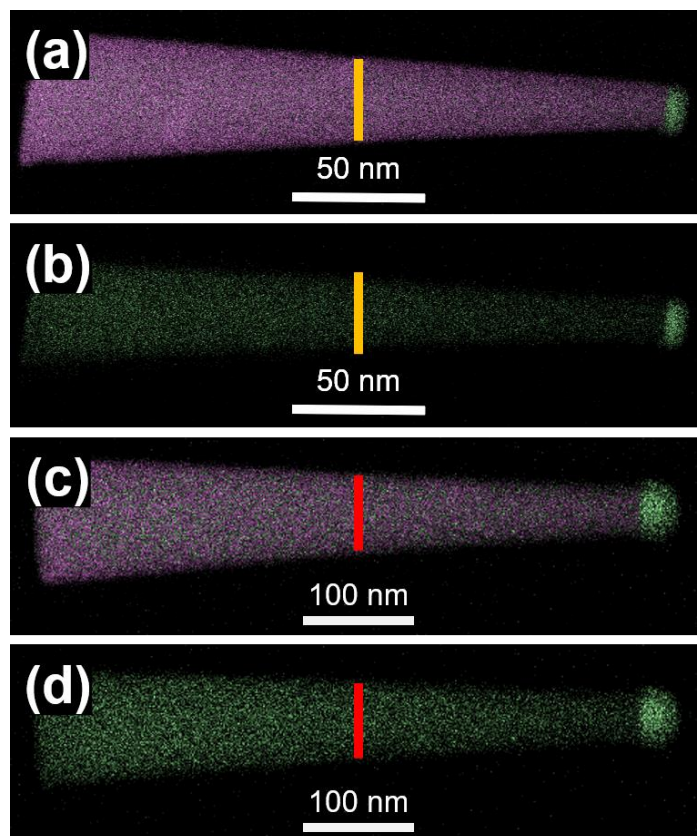
Figure 35: (a + c) Overlay of STEM-EDX elemental mappings and (b + d) STEM-EDX elemental mappings of Sn (a + b) before and (c + d) after RIE with a CF_4/O_2 gas-mixture (35 W, 700 mTorr, 30 s) of a $Ge_{1-x}Sn_x$ NW are presented. The yellow bars in (a + b) have the same size and point out the presence of a Ge shell covering the tapered $Ge_{1-x}Sn_x$ NW body. (c + d) After RIE the Ge shell is not present any longer which is highlighted by equal red bars.

Prolonged etching up to 75 s of $Ge_{1-x}Sn_x$ NWs results in the formation of an O- and Sn-enriched shell acting as an etching barrier (Figure 36). However, a treatment with diluted HCl after RIE is required to remove the SnO_2 and any metallic Sn located at the tip of the NWs.
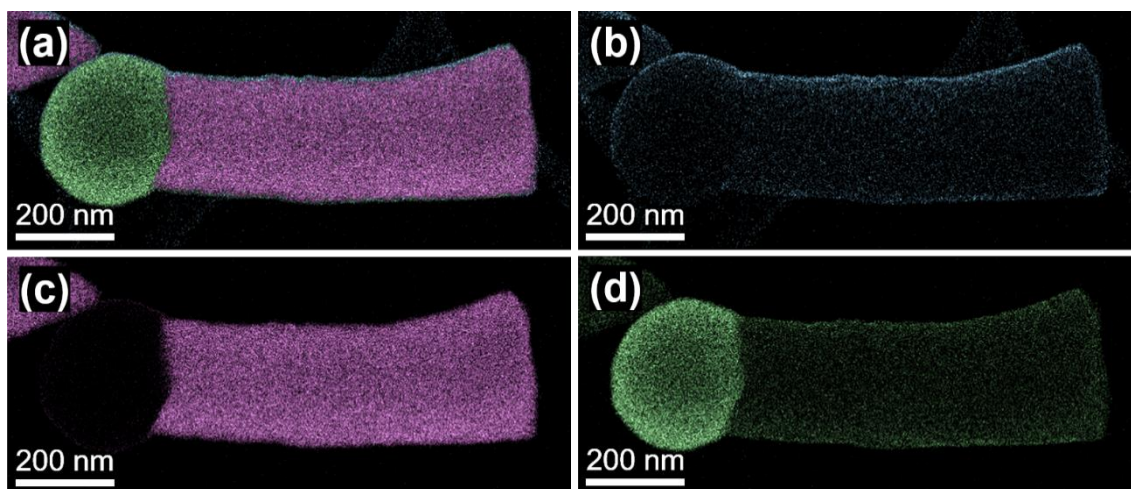

Figure 36: (a) Overlay of STEM-EDX elemental mappings and STEM-EDX elemental mappings of (b) O, (c) Ge, and (d) Sn of a $Ge_{1-x}Sn_x$ NW after RIE for 75 s (35 W, 700 mTorr) are shown. The $Ge_{1-x}Sn_x$ NW body is covered with a thin (b) O- and (d) Sn-enriched layer.

A statistical evaluation using top-view SEM images of the sample shown in Figure 34a reveals the mean diameter of the $Ge_{1-x}Sn_x$ NWs' base is 81 nm ± 22 nm (1σ) and only a small fraction of 2.3 % growing off axis (Figure 37).

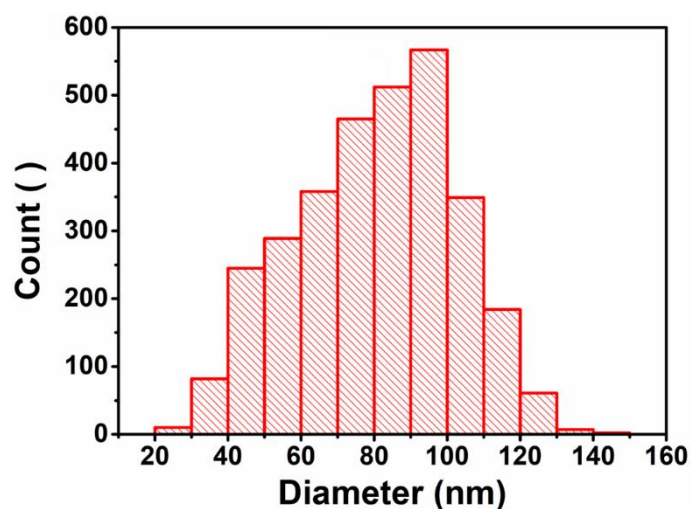**Figure 37:** Statistical evaluation of $Ge_{1-x}Sn_x$ NW base-diameter by using top-view SEM images as presented in Figure 34a.

A strong impact of the Sn particle diameter on the morphology of the anisotropic nanostructures is observed. While smaller Sn particles result in the growth of NWs and nanocones (NCs), bigger growth promoters form micropillars (MPs) and in-plane NWs. The SEM image of a 30°-tilted sample in Figure 38a shows $Ge_{1-x}Sn_x$ MPs and in-plane NWs (black circles). A schematic representation in Figure 38b highlights the chronological sequence of the two-step growth and possible morphologies which strongly depend on the Sn particle diameter. The Sn particle diameter can be adjusted by the duration of the Sn deposition and the substrate temperature.
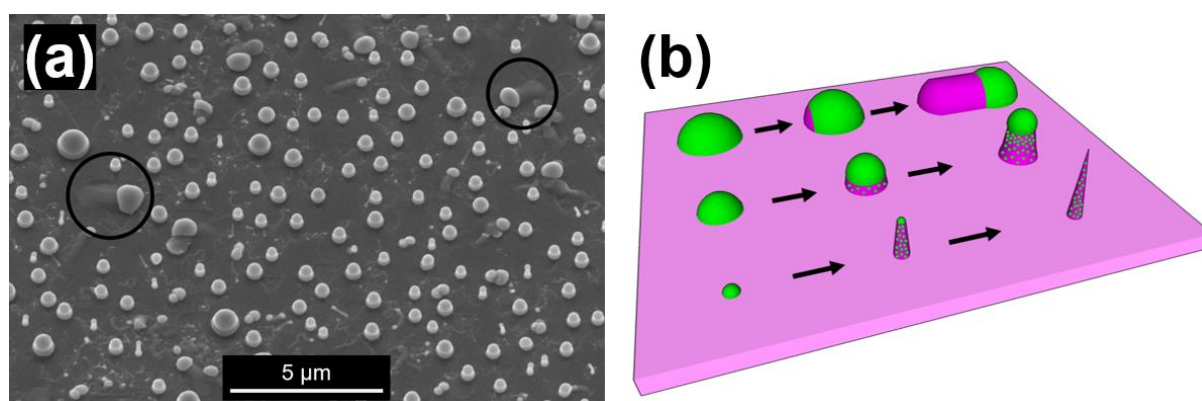

Figure 38: (a) SEM image of a 30°-tilted sample with thick in-plane NWs (black circles) and MPs. A schematic presentation of structures observed in this process is shown in (b).

STEM-EDX point measurements on the $Ge_{1-x}Sn_x$ NW presented in Figure 35c + d (after RIE) show a constant value of 19.3 at. % ± 0.9 at. % (1σ) incorporated along the NW axis without signs of Sn clustering.
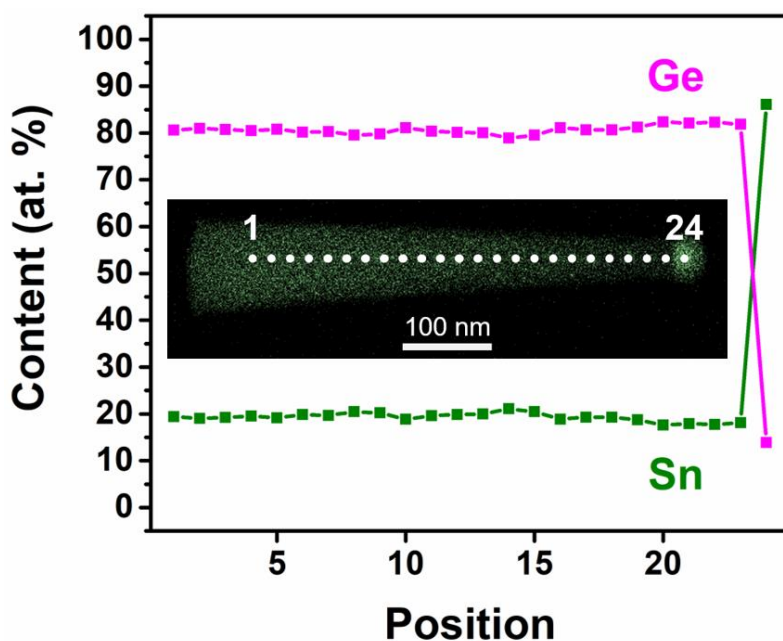
Figure 39: STEM-EDX point measurements along the axis of a $Ge_{1-x}Sn_x$ NW after RIE.

Depending on the growth conditions $Ge_{1-x}Sn_x$ NWs can be terminated by the full consumption of the Sn seeds which results in $Ge_{1-x}Sn_x$ NCs. A STEM image of such a nanostructure is highlighted in Figure 40a and STEM-EDX maps are recorded. This characterisation illustrates that for nanostructures containing a small Ge shell the STEM-EDX point measurements can be corrected using geometrical relations. The determined and corrected average Sn content (20.5 at. % ± 1.1 at. % (1σ)) is in reasonable agreement with results obtained for NWs and NCs without a Ge shell (Figure 40e).
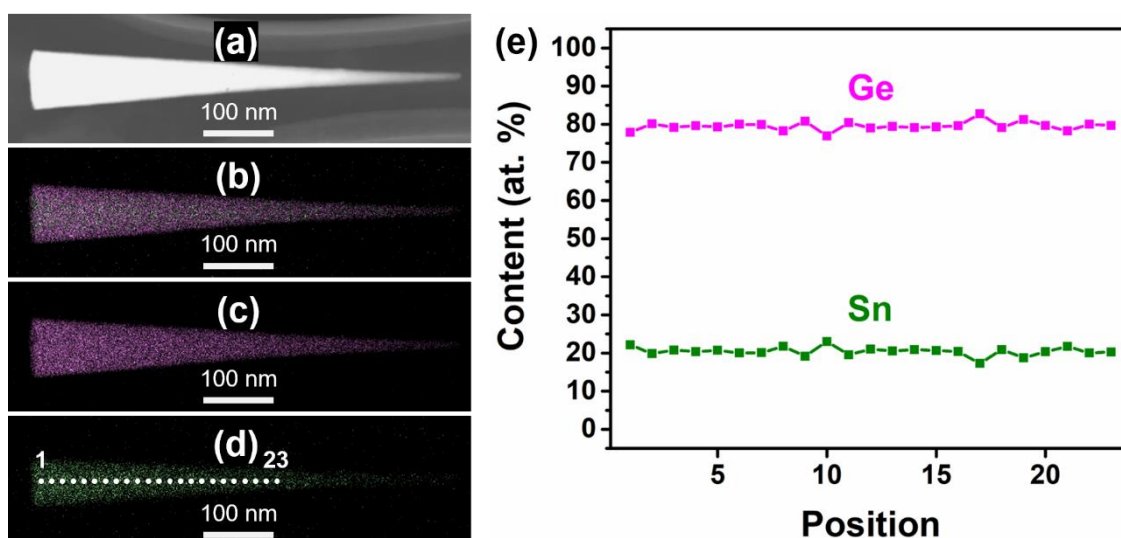
Figure 40: (a) presents a STEM image of a $Ge_{1-x}Sn_x$ NW where the Sn seed is completely consumed during the growth. (b) Overlay of STEM-EDX elemental mappings and individual (c) Ge and (d) Sn STEM-EDX elemental mappings of the $Ge_{1-x}Sn_x$ NW highlighted in (a) show the presence of a thin Ge layer. (e) STEM-EDX point measurements along the dotted line highlighted in (d) suggest a homogeneous incorporation of Sn in the Ge matrix. The Sn contents observed by STEM-EDX are corrected due to the thin Ge layer and the elemental distribution is illustrated in (e).

Information concerning the area between the Ge substrate and the growing nanostructure is lost due to the removal of these structures from the substrate using mechanical force. Therefore, lamellae are prepared for a sample with $Ge_{1-x}Sn_x$ MPs and in-plane NWs and a sample containing thin $Ge_{1-x}Sn_x$ NWs. STEM-EDX mappings of a $Ge_{1-x}Sn_x$ MP with a base-diameter of 1.1 µm are presented in Figure 41a - c. The darker area underneath the Sn seed is caused by a defective Pt protection layer during the lamella formation resulting in a channelling effect of the Sn single crystal. Therefore, preferential thinning of Ge and $Ge_{1-x}Sn_x$ is observed in this area. The interface between the Sn seed and the $Ge_{1-x}Sn_x$ MP is very sharp (Figure 41a). A strong tapering of this structure can be attributed to the incorporation of Sn which is confirmed by STEM-EDX point measurements (Figure 41d). However, these measurements reveal a significant gradient of Sn incorporation with low Sn content for $Ge_{1-x}Sn_x$ growing on top of the Ge substrate and continuous increasing values for the material growing in the process.

This observation can be explained by an initial pseudomorphical growth of the $Ge_{1-x}Sn_x$ on the Ge substrate. Therefore, the incorporation of Sn which leads to an expansion of the Ge crystal lattice is limited by the templating effect of the Ge crystal lattice of the substrate. The range of efficiency of the templating effect induced by the Ge substrate strongly depends on the possibility of the $Ge_{1-x}Sn_x$ alloy to relieve internal strain. In a recently published study, Sn contents of approximately 15 at. % are achieved for $Ge_{1-x}Sn_x$ thin films epitaxially grown on a Ge buffer layer approximately 500 nm away from the Ge surface which is in good agreement with results from this work showing a maximum Sn content of 15.4 at. % for a length of 430 nm.[251]
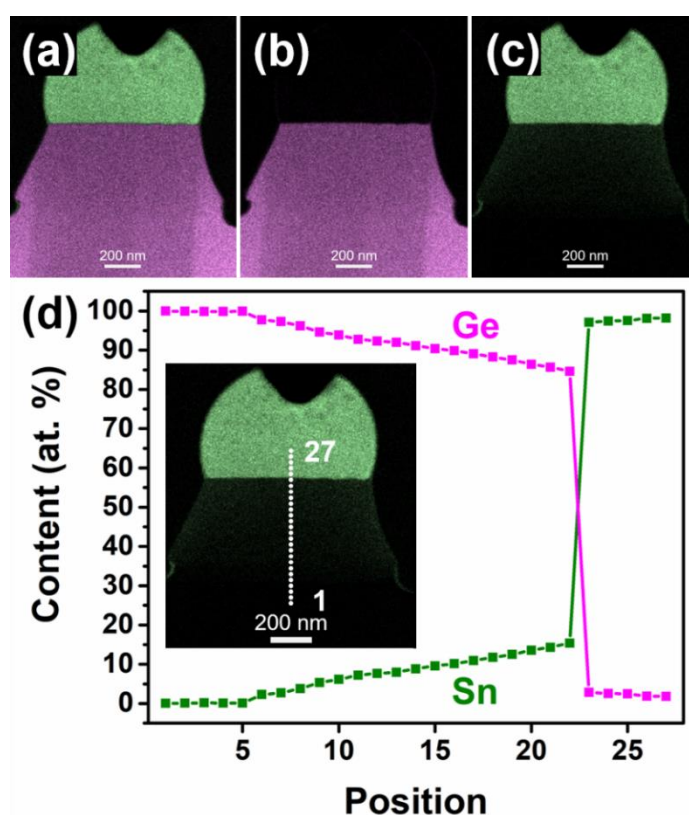
Figure 41: STEM-EDX mappings of a thick, epitaxially grown $Ge_{1-x}Sn_x$ MP observed on a lamella of the sample presented in Figure 36a are shown. The (a) overlay image of the elemental mappings of (b) Ge and (c) Sn points out the sharp interface between the Sn seed and the thick $Ge_{1-x}Sn_x$ MP. (d) STEM-EDX point measurements highlight the gradient of Sn incorporation caused by strain-effects induced by the Ge substrate.

A STEM image of an in-plane NW next to the Sn seed and the corresponding STEM-EDX mappings are highlighted in Figure 42. The internal strain caused by the templating effect of the Ge substrate cannot be relieved easily in this growth-scenario resulting in very low Sn contents of approximately 4 at. %.
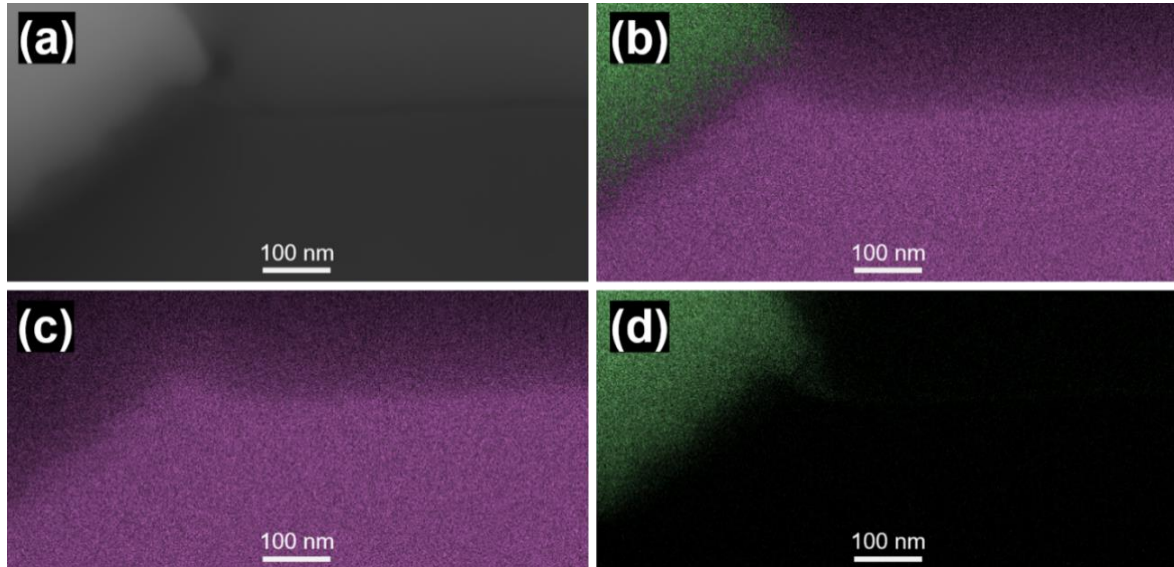
Figure 42: (a) STEM image of an in-plane $Ge_{1-x}Sn_x$ NW observed on a lamella of the sample presented in Figure 36a. The (b) overlay image of the STEM-EDX elemental mappings and STEM-EDX elemental mappings of (c) Ge and (d) Sn are shown. Incorporation of Sn in the Ge matrix is low in these structures (~ 4 at. %) due to the compressing effect of the Ge substrate counteracting this process.

In contrast to the $Ge_{1-x}Sn_x$ MPs and in-plane NWs, $Ge_{1-x}Sn_x$ NWs have the possibility to relieve internal strain more efficiently by dilatation. Figure 43a - c show STEM-EDX elemental mappings of a $Ge_{1-x}Sn_x$ NW with a much smaller diameter (~ 95 nm) compared to the $Ge_{1-x}Sn_x$ MP presented in Figure 41. STEM-EDX point measurements reveal a transition zone of 80 nm resulting in a maximum Sn content of approximately 20 at. %. This very narrow transition zone compared to the $Ge_{1-x}Sn_x$ MP and $Ge_{1-x}Sn_x$ thin films grown on a Ge buffer layer reveals the capability of nanostructures to relieve internal strain more efficiently.
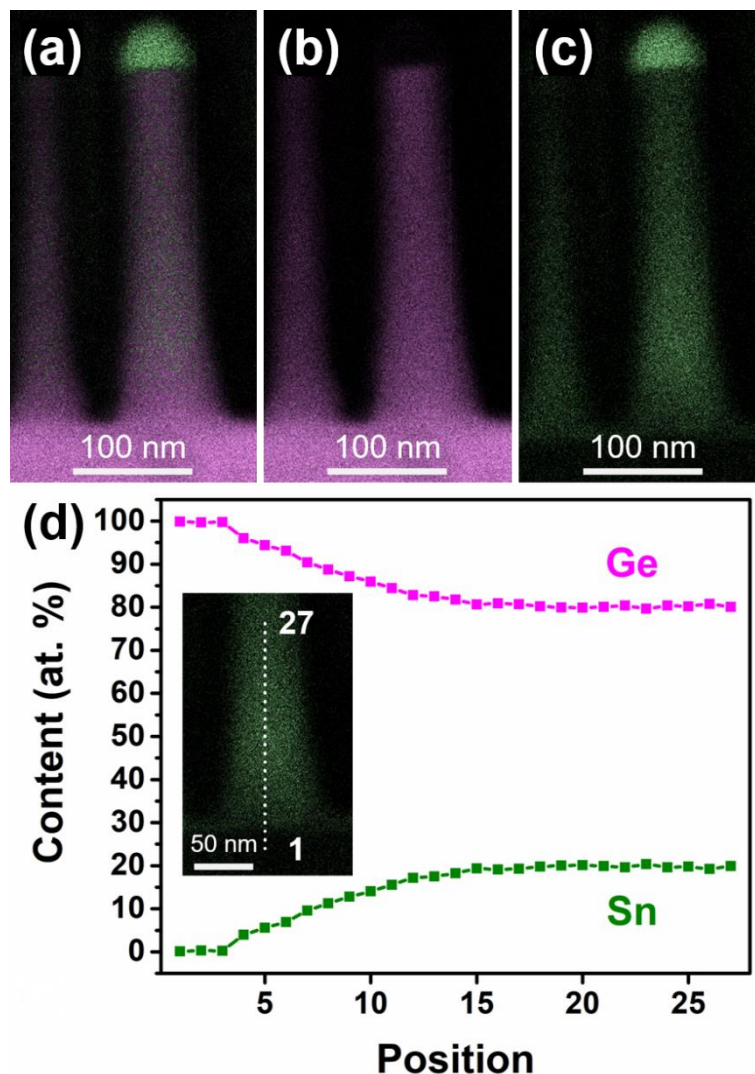
Figure 43: The (a) overlay image of the STEM-EDX elemental mappings and STEM-EDX elemental mappings of (b) Ge and (c) Sn of a thin, epitaxially grown $Ge_{1-x}Sn_x$ NW observed on a lamella of the sample presented in Figure 34 are shown. (d) STEM-EDX point measurements highlight the gradient of Sn incorporation caused by strain-effects induced by the Ge substrate.

Moreover, the possibility to elongate $Ge_{1-x}Sn_x$ MPs by adapting the growth conditions is investigated. Therefore, the amount of Ge precursor (200 µl), the substrate temperature (360 °C), and the decomposition time (45 min) are increased. The STEM image and the corresponding STEM-EDX mappings in Figure 44 clearly show the successful elongation of $Ge_{1-x}Sn_x$ MPs to $Ge_{1-x}Sn_x$ MWs. However, the increase of substrate temperature and decomposition time exceed the limit of the as-grown material's thermal stability. The prolonged thermal exposure results in the segregation of elemental Sn manifesting in Sn-enriched areas along the MW axis and the growth of small NWs on the surface of the $Ge_{1-x}Sn_x$ MW.

The overall Sn content of the MW body (Sn seed excluded) is determined to be 6.52 at. % which is incorporated in the Ge matrix before segregation occurs. $Ge_{1-x}Sn_x$ alloys epitaxially grown on a Ge buffer layer at comparable temperatures (350 °C - 400 °C) reveal Sn contents of approximately 5 at. % - 12 at. % which is in good agreement with these results.[342] Furthermore, the remaining $Ge_{1-x}Sn_x$ alloy of the segregated MW contains up to 3.56 at. % Sn. According to literature, a 750 nm thick strain-relaxed $Ge_{1-x}Sn_x$ film grown on a Ge buffer layer which contains 4.8 at. % Sn shows thermal stability upon annealing at 350 °C for 30 min.[351] As

discussed in Chapter 3.2 segregation of Sn in $Ge_{1-x}Sn_x$ alloy is a statistical process depending on temperature, time, and Sn content. The amount of Sn incorporated in $Ge_{1-x}Sn_x$ MWs for the chosen growth conditions is slightly too high to withstand the synthesis process.
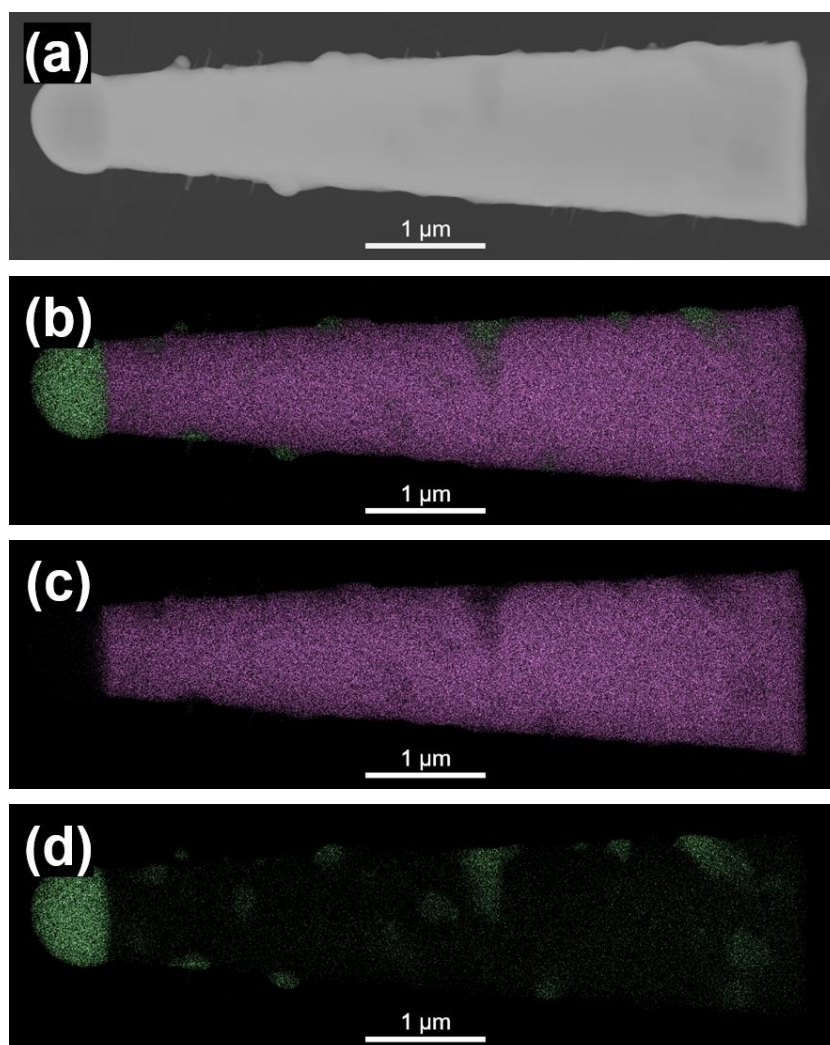
Figure 44: (a) STEM image of a strongly elongated $Ge_{1-x}Sn_x$ MP realised by increasing the amount of Ge precursor (200 µl), the substrate temperature (360 °C), and the decomposition time (45 min). The (b) overlay image of the STEM-EDX elemental mappings and STEM-EDX elemental mappings of (c) Ge and (d) Sn clearly point out the segregation of the $Ge_{1-x}Sn_x$ alloy at these growth conditions.

The optical properties of $Ge_{0.81}Sn_{0.19}$ NWs epitaxially grown on Ge are evaluated by temperature- and laser power-dependent PL measurements (Figure 45). For both PL series a signal in the range 2.76 µm - 2.00 µm (0.45 eV - 0.62 eV) can be attributed to the Sb-doped Ge substrate showing indirect bandgap behaviour. The direct bandgap PL signal located at 4.28 µm (0.29 eV) for room temperature can be assigned to the $Ge_{0.81}Sn_{0.19}$ NWs which is in good agreement with theoretical[205] and experimental[325] studies on thin films showing direct bandgap energies for similar compositions in the same range (Figure 45a). Furthermore, a blue-shift of the PL signal upon cooling (Figure 45a) and for increased laser powers (Figure 45b) is observed. The increase of the PL signal upon cooling (Figure 45a) and for higher laser powers (Figure 45b) is a strong hint for the transition of Ge into a direct bandgap semiconductor and these observations agree well with a study about optical transitions in direct

bandgap $Ge_{1-x}Sn_x$ alloys.[238] According to literature, the clear evidence of PL from a direct bandgap semiconductor which is dominated by band-to-band recombination is provided by validation of the direct proportionality between the integrated PL intensity (I) and the excitation power (P) (I ~ P^m with m = 1).[238, 352] Therefore, the integrated PL intensity is plotted versus the excitation power in a double logarithmic diagram. The slope of the curve is very close to 1 which proves that a $Ge_{0.81}Sn_{0.19}$ NW epitaxially grown on Ge is a direct bandgap semiconductor.

Figure 46: PL measurements for $Ge_{0.81}Sn_{0.19}$ NWs epitaxially grown on a Ge(111) substrate for different (a) temperatures and (b) laser powers.

4 Summary

In this thesis two Ge-based material systems with metastable composition and altered physical properties have been prepared. Therefore, kinetically controlled met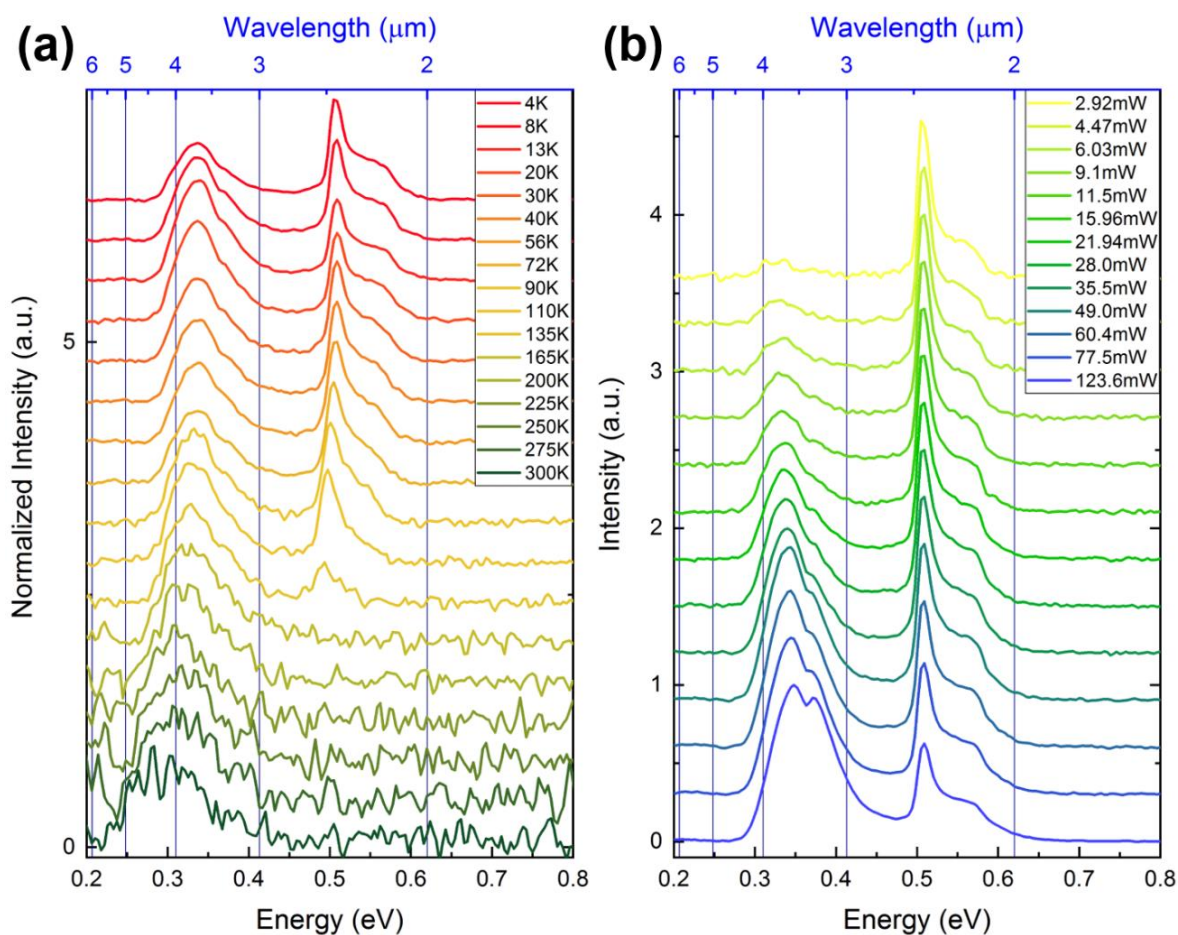al-assisted bottom-up growth processes are developed to successfully incorporate the metal of the growth seed in the evolving crystal.

The first part of this work illustrates the successful incorporation of Ga in the Ge matrix via self-seeding at temperatures down to 210 °C. The Ga incorporation efficiency exceeds the maximum solid solubility of Ga in Ge 3 - 4 times and is approximately 50 times higher than the binary phase diagram would predict at these growth temperatures. The electronic properties of Ga-hyperdoped Ge NWs are evaluated using single NW devices. Extremely high carrier concentrations can be obtained suggesting that one third of the incorporated 3.5 at. % Ga ($1.5 \cdot 10^{21}$ cm^{-3}) are electrically active. Temperature-dependent resistivity evolution reveals a quasi-metallic behaviour of these highly doped Ge NWs. Clustering of Ga within the Ge matrix is excluded by measuring the resistance at temperatures down to 0.269 K without a transition to the superconducting regime. The material is stable for at least 24 h at 250 °C, while segregation of Ga is observed at 400 °C as can be expected for a metastable material treated at higher temperatures.

The second part of this work deals with the growth of anisotropic, metastable Ge$_{1-x}$Sn$_x$ alloys. The first investigated approach for the synthesis of Ge$_{1-x}$Sn$_x$ with high Sn contents is a solution-based microwave-assisted process via homogeneous nucleation and without the use of a template. Ge$_{1-x}$Sn$_x$ NRs with Sn contents up to 28 at. % are synthesised at temperatures as low as 140 °C. The high Sn incorporation can be attributed to the *in situ* formation of α-Sn acting as template for the growth of Ge$_{1-x}$Sn$_x$, even though its thermal stability is reported being well below the growth temperatures. For the growth of Ge$_{1-x}$Sn$_x$ NWs with Sn contents up to 19 at. % the presence of *in situ* formed α-Sn is not observed. Characterisation of the obtained Ge$_{1-x}$Sn$_x$ material using electron microscopy and XRD allow to suggest a phase map for this approach including kinetic parameters such as growth rate and thermal stabilities of materials growing in different temperature regimes.

The thermal stability of the synthesised Ge$_{1-x}$Sn$_x$ alloys is evaluated by variable-temperature XRD measurement under H$_2$ atmosphere showing a strong dependence on the Sn content. Moreover, the presence of metallic Sn can induce the degradation of the metastable material and reduce the stability by approximately 70 °C. In addition, a highly unusual degradation by solid diffusion of Sn and the dissolution and redeposition of Ge$_{1-x}$Sn$_x$ with altered composition is observed below the melting temperature of Sn. The physical properties are investigated, and IR absorption measurements illustrate a direct bandgap for both products. As expected, increasing the Sn content in Ge$_{1-x}$Sn$_x$ leads to a smaller direct bandgap energy which is confirmed by these measurements.

Single NW devices are fabricated using Ge$_{0.81}$Sn$_{0.19}$ NWs. The resistivity of these NWs is much lower when compared to Au-seeded intrinsic Ge NWs. The limited thermal stability of Ge$_{0.81}$Sn$_{0.19}$ NWs leads to segregation events when heated above the previously investigated stability window. The electronic properties are measured after the heat treatment leading to three different scenarios. The first scenario leads to a decrease of resistivity due to the better quality of the Au-Ge$_{0.81}$Sn$_{0.19}$ contact caused by the heat treatment in combination with an unaltered Ge$_{1-x}$Sn$_x$ NW. However, some devices fail or show increasing resistivities due to the segregation of the Ge$_{0.81}$Sn$_{0.19}$ NWs.

The insights obtained by this microwave approach are used to implement a vapour-phase process for the epitaxial growth of anisotropic, metastable Ge$_{1-x}$Sn$_x$ alloys on a Ge(111)

substrate. In a two-step process $Ge_{1-x}Sn_x$ NWs, MPs, and in-plane NWs can be grown. A strong dependence of the Sn growth promoter's diameter on the morphology is observed. Furthermore, Sn contents for epitaxially grown $Ge_{1-x}Sn_x$ NWs on a Ge substrate up to 19.3 at. % are obtained by this approach. Moreover, a diameter-dependent transition zone revealing a significant gradient of Sn incorporation is observed, while a high amount of strain due to the lattice mismatch of 2.94 % between the Ge substrate and the growing $Ge_{0.81}Sn_{0.19}$ NW can be compensated within 80 nm. In contrary, MPs show typical Sn concentration profiles as described for thin films being in the regime of hundreds of nanometres.

The high quality of the material manifests in PL with the expected wavelength of 4.28 µm (0.29 eV) associated with a direct bandgap at room temperature and increasing intensity at lower temperatures and higher fluence. These measurements suggest the successful transition of Ge into a direct bandgap semiconductor.

5 Literature

1. Fukuda, Y., et al. *Japanese Journal of Applied Physics* **2005,** *44*, 6981-6984.
2. Molle, A., et al. *Applied Physics Letters* **2006,** *89*, 083504.
3. Delabie, A., et al. *Applied Physics Letters* **2007,** *91*, 082904.
4. Martin, S. C., et al. *IEEE Electron Device Letters* **1989,** *10*, 325-326.
5. Chui, C. O., et al. In *A sub-400°C germanium MOSFET technology with high-κ dielectric and metal gate*, Digest. International Electron Devices Meeting, **2002;** 437-440.
6. Nicholas, G., et al. *IEEE Electron Device Letters* **2007,** *28*, 825-827.
7. Mitard, J., et al. In *Record ION/IOFF performance for 65nm Ge pMOSFET and novel Si passivation scheme for improved EOT scalability*, 2008 IEEE International Electron Devices Meeting, **2008;** 1-4.
8. Pillarisetty, R., et al. In *High mobility strained germanium quantum well field effect transistor as the p-channel device option for low power (Vcc = 0.5 V) III-V CMOS architecture*, 2010 International Electron Devices Meeting, **2010;** 6.7.1-6.7.4.
9. Pillarisetty, R. *Nature* **2011,** *479*, 324-8.
10. Fitzgerald, E. A. *Materials Science Reports* **1991,** *7*, 87-142.
11. Xie, Y. H., et al. *Applied Physics Letters* **1993,** *63*, 2263-2264.
12. Engelhardt, C. M., et al. *Solid-State Electronics* **1994,** *37*, 949-952.
13. Currie, M. T., et al. *Applied Physics Letters* **1998,** *72*, 1718-1720.
14. Madhavi, S., et al. *Journal of Applied Physics* **2001,** *89*, 2497-2499.
15. Irisawa, T., et al. *Japanese Journal of Applied Physics* **2001,** *40*, 2694-2696.
16. Koester, S. J., et al. *IEEE Electron Device Letters* **2000,** *21*, 110-112.
17. Ye, H., et al. *Science and Technology of Advanced Materials* **2014,** *15*, 024601.
18. Colace, L., et al. *Applied Physics Letters* **1998,** *72*, 3175-3177.
19. Luan, H.-C., et al. *Applied Physics Letters* **1999,** *75*, 2909-2911.
20. Nayfeh, A., et al. *Applied Physics Letters* **2004,** *85*, 2815-2817.
21. Taraschi, G., et al. *Solid-State Electronics* **2004,** *48*, 1297-1305.
22. Nakaharai, S., et al. *Applied Physics Letters* **2003,** *83*, 3516-3518.
23. Hashimoto, T., et al. *Applied Physics Express* **2009,** *2*, 066502.
24. Barth, S., et al. *Progress in Materials Science* **2010,** *55*, 563-627.
25. Liu, J., et al. *Optics Letters* **2010,** *35*, 679-81.
26. Camacho-Aguilera, R. E., et al. *Optics Express* **2012,** *20*, 11316-20.
27. Wirths, S., et al. *Nature Photonics* **2015,** *9*, 88-92.
28. Genquan, H., et al. In *High-mobility germanium-tin (GeSn) P-channel MOSFETs featuring metallic source/drain and sub-370 °C process modules*, 2011 International Electron Devices Meeting, **2011;** 16.7.1-16.7.3.
29. Ke, Y., et al. *Nano Letters* **2009,** *9*, 4494-9.
30. Moutanabbir, O., et al. *ACS Nano* **2011,** *5*, 1313-20.
31. Moutanabbir, O., et al. *Nature* **2013,** *496*, 78-82.
32. Mahenderkar, N. K., et al. *ACS Nano* **2014,** *8*, 9524-9530.
33. Fahrenkrug, E., et al. *Chemistry of Materials* **2015,** *27*, 3389-3396.
34. DeMuth, J., et al. *Crystal Growth & Design* **2017,** *18*, 677-685.
35. Acharya, S., et al. *ACS Applied Nano Materials* **2018,** *1*, 5553-5561.
36. Tran, H., et al. *Journal of Applied Physics* **2018,** *124*, 013101.
37. Taylor, B. R., et al. *Chemistry of Materials* **1998,** *10*, 22-24.
38. Bostedt, C., et al. *Applied Physics Letters* **2004,** *84*, 4056-4058.
39. Bruno, M., et al. *Physical Review B* **2005,** *72*, 153310.
40. Roduner, E. *Chemical Society Reviews* **2006,** *35*, 583-92.
41. Wang, D., et al. *Applied Physics Letters* **2003,** *83*, 2432-2434.
42. Greytak, A. B., et al. *Applied Physics Letters* **2004,** *84*, 4176-4178.
43. Staudinger, P., et al. *Nano Letters* **2018,** *18*, 5030-5035.
44. Samà, J., et al. *Sensors and Actuators B: Chemical* **2017,** *243*, 669-677.

45. Hrachowina, L., et al. *ACS Sensors* **2018,** *3*, 727-734.
46. Chan, C. K., et al. *Nano Letters* **2008,** *8*, 307-9.
47. Chockla, A. M., et al. *ACS Applied Materials & Interfaces* **2012,** *4*, 4658-64.
48. Kennedy, T., et al. *Nano Letters* **2014,** *14*, 716-23.
49. Peng, X., et al. *Nature* **2000,** *404*, 59-61.
50. Mohan, P., et al. *Nanotechnology* **2005,** *16*, 2903-2907.
51. Noborisaka, J., et al. *Applied Physics Letters* **2005,** *87*, 093109.
52. Mohan, P., et al. *Applied Physics Letters* **2006,** *88*, 133105.
53. Sears, G. W. *Acta Metallurgica* **1955,** *3*, 361-366.
54. Wagner, R. S., et al. *Applied Physics Letters* **1964,** *4*, 89-90.
55. Persson, A. I., et al. *Nature Materials* **2004,** *3*, 677-81.
56. Lu, X., et al. *Journal of the American Chemical Society* **2005,** *127*, 15718-9.
57. Hanrath, T., et al. *Journal of the American Chemical Society* **2002,** *124*, 1424-9.
58. Tuan, H. Y., et al. *Chemistry of Materials* **2005,** *17*, 5705-5711.
59. Barth, S., et al. *Nano Letters* **2011,** *11*, 1550-5.
60. Holmes, J. D., et al. *Science* **2000,** *287*, 1471-3.
61. Prabakar, S., et al. *Chemistry of Materials* **2010,** *22*, 482-486.
62. Baxter, D. V., et al. *Chemical Vapor Deposition* **1995,** *1*, 49-51.
63. Gerung, H., et al. *Journal of the American Chemical Society* **2006,** *128*, 5244-50.
64. Mathur, S., et al. *Chemistry of Materials* **2004,** *16*, 2449-2456.
65. Bramblett, T. R., et al. *Journal of Applied Physics* **1995,** *77*, 1504-1513.
66. Lu, X. M., et al. *Nano Letters* **2004,** *4*, 969-974.
67. Bauer, M., et al. *Applied Physics Letters* **2002,** *81*, 2992-2994.
68. Shimizu, T., et al. *Nano Letters* **2009,** *9*, 1523-6.
69. Aghazadeh Meshgi, M., et al. *Chemistry of Materials* **2017,** *29*, 4351-4360.
70. Inuzuka, Y., et al. *Thin Solid Films* **2016,** *602*, 7-12.
71. Richards, B. T., et al. *Journal of Materials Chemistry C* **2014,** *2*, 1869.
72. Kodambaka, S., et al. *Science* **2007,** *316*, 729-32.
73. Pertl, P., et al. *Monatshefte für Chemie - Chemical Monthly* **2018,** *149*, 1315-1320.
74. Tuan, H.-Y., et al. *Angewandte Chemie* **2006,** *118*, 5308-5311.
75. Seifner, M. S., et al. *Materials Letters* **2016,** *173*, 248-251.
76. Sun, X., et al. *Journal of Vacuum Science & Technology B* **2007,** *25*, 415.
77. Barth, S., et al. *Chemical Communications* **2015,** *51*, 12282-5.
78. Bemski, G. *Physical Review* **1958,** *111*, 1515-1518.
79. Sprokel, G. J., et al. *Journal of The Electrochemical Society* **1965,** *112*, 200.
80. Bullis, W. M. *Solid-State Electronics* **1966,** *9*, 143-168.
81. Allen, J. E., et al. *Nature Nanotechnology* **2008,** *3*, 168-73.
82. Luque, A., et al. *Physica B-Condensed Matter* **2006,** *382*, 320-327.
83. Trumbore, F. A. *Bell System Technical Journal* **1960,** *39*, 205-233.
84. McAlister, A. J., et al. *Bulletin of Alloy Phase Diagrams* **1984,** *5*, 341-347.
85. Olesinski, R. W., et al. *Bulletin of Alloy Phase Diagrams* **1985,** *6*, 262-266.
86. Olesinski, R. W., et al. *Bulletin of Alloy Phase Diagrams* **1985,** *6*, 250-254.
87. Olesinski, R. W., et al. *Bulletin of Alloy Phase Diagrams* **1985,** *6*, 258-262.
88. Pankove, J. I., et al. *Physical Review* **1962,** *126*, 956-962.
89. Camacho-Aguilera, R., et al. *Applied Physics Letters* **2013,** *102*, 152106.
90. Sommers, H. S. *Physical Review* **1961,** *124*, 1101-1110.
91. Riihimaki, I., et al. *Applied Physics Letters* **2007,** *91*, 091922.
92. Sueoka, K., et al. *Materials Science in Semiconductor Processing* **2006,** *9*, 494-497.
93. Śpiewak, P., et al. *Journal of Crystal Growth* **2007,** *303*, 12-17.
94. Moreira, M. D., et al. *Physical Review B* **2004,** *70*, 115215.
95. Pinto, H. M., et al. *Materials Science in Semiconductor Processing* **2006,** *9*, 498-502.
96. Vanhellemont, J., et al. *Journal of Applied Physics* **2007,** *101*, 036103.
97. Chroneos, A. *Materials Science in Semiconductor Processing* **2012,** *15*, 691-696.
98. Pantelides, S. T. *Reviews of Modern Physics* **1978,** *50*, 797-858.
99. Brotzmann, S., et al. *Journal of Applied Physics* **2008,** *103*, 033508.
100. Chroneos, A., et al. *Applied Physics Reviews* **2014,** *1*, 011301.

101. Bracht, H., et al. *Materials Science in Semiconductor Processing* **2006,** *9*, 471-476.
102. Tahini, H., et al. *Applied Physics Letters* **2011,** *99*, 072112.
103. Uppal, S., et al. *Journal of Applied Physics* **2001,** *90*, 4293-4295.
104. Janke, C., et al. *Journal of Materials Science: Materials in Electronics* **2006,** *18*, 775-780.
105. Chroneos, A., et al. *Journal of Applied Physics* **2007,** *102*, 083707.
106. Śpiewak, P., et al. *Journal of Applied Physics* **2008,** *103*, 086103.
107. Simoen, E., et al. *Journal of Applied Physics* **2009,** *106*, 103516.
108. Vanhellemont, J., et al. *Materials Science in Semiconductor Processing* **2012,** *15*, 642-655.
109. Chui, C. O., et al. *Applied Physics Letters* **2003,** *83*, 3275-3277.
110. Suh, Y. S., et al. *IEEE Transactions on Electron Devices* **2005,** *52*, 2416-2421.
111. Kim, J., et al. *Applied Physics Letters* **2012,** *101*, 112107.
112. Cammilleri, D., et al. *Thin Solid Films* **2008,** *517*, 75-79.
113. Jamil, M., et al. *IEEE Electron Device Letters* **2011,** *32*, 1203-1205.
114. Cai, Y., et al. *Journal of Applied Physics* **2012,** *112*, 034509.
115. Hartmann, J. M., et al. *Journal of Crystal Growth* **2012,** *347*, 37-44.
116. Dilliway, G., et al. *ECS Transactions* **2006,** *3*, 599-609.
117. Yu, H.-Y., et al. *Current Applied Physics* **2013,** *13*, 1060-1063.
118. Luong, T. K. P., et al. *Thin Solid Films* **2014,** *557*, 70-75.
119. Scappucci, G., et al. *Journal of Crystal Growth* **2011,** *316*, 81-84.
120. Scappucci, G., et al. *Nanotechnology* **2011,** *22*, 375203.
121. Mattoni, G., et al. *ACS Nano* **2013,** *7*, 11310-11316.
122. Camacho-Aguilera, R. E., et al. *Optical Materials Express* **2012,** *2*, 1462.
123. Yamamoto, Y., et al. *Solid-State Electronics* **2013,** *83*, 25-29.
124. Jones, K. S., et al. *Journal of Applied Physics* **1987,** *61*, 2469-2477.
125. Yamamoto, Y., et al. *Thin Solid Films* **2010,** *518*, S44-S47.
126. Chang, T.-H., et al. *Thin Solid Films* **2014,** *551*, 53-56.
127. Han, G., et al. *ECS Transactions* **2013,** *50*, 1025-1030.
128. Kesan, V. P., et al. *Applied Physics Letters* **1991,** *59*, 852-854.
129. Kim, S., et al. *IEEE Electron Device Letters* **2013,** *34*, 1217-1219.
130. Coutinho, J., et al. *Defect and Diffusion Forum* **2008,** *273-276*, 93-98.
131. Simoen, E., et al. *Materials Science in Semiconductor Processing* **2006,** *9*, 634-639.
132. Satta, A., et al. *Journal of The Electrochemical Society* **2006,** *153*, G229-G233.
133. Carroll, M. S., et al. *Semiconductor Science and Technology* **2007,** *22*, S164-S167.
134. Koike, M., et al. *Journal of Applied Physics* **2008,** *104*, 023523.
135. Tsouroutas, P., et al. *Materials Science in Semiconductor Processing* **2008,** *11*, 372-377.
136. Wündisch, C., et al. *Applied Physics Letters* **2009,** *95*, 252107.
137. Tsouroutas, P., et al. *Journal of Applied Physics* **2009,** *105*, 094910.
138. Duffy, R., et al. *ECS Transactions* **2011,** *35*, 185-192.
139. Satta, A., et al. *Applied Physics Letters* **2005,** *87*, 172109.
140. Ioannou, N., et al. *Applied Physics Letters* **2008,** *93*, 101910.
141. Satta, A., et al. *Journal of Vacuum Science & Technology B* **2006,** *24*, 494.
142. Satta, A., et al. *Applied Physics Letters* **2006,** *88*, 162118.
143. Chui, C. O., et al. *Applied Physics Letters* **2005,** *87*, 091909.
144. Bracht, H., et al. *Physical Review Letters* **2009,** *103*, 255501.
145. Schneider, S., et al. *Applied Physics Letters* **2011,** *98*, 014101.
146. Brotzmann, S., et al. *Physical Review B* **2008,** *77*, 235207.
147. Chroneos, A., et al. *Journal of Applied Physics* **2009,** *106*, 063707.
148. Impellizzeri, G., et al. *Journal of Applied Physics* **2011,** *109*, 113527.
149. Chroneos, A. *Journal of Applied Physics* **2009,** *105*, 056101.
150. Park, J.-H., et al. *Applied Physics Letters* **2008,** *93*, 193507.
151. Hyun-Yong, Y., et al. *IEEE Electron Device Letters* **2009,** *30*, 1002-1004.
152. Cheng, S.-L., et al. *Optics Express* **2009,** *17*, 10019.
153. Thareja, G., et al. *IEEE Electron Device Letters* **2011,** *32*, 838-840.

154. Thareja, G., et al. *IEEE Electron Device Letters* **2011,** *32*, 608-610.
155. Hyun-Yong, Y., et al. *IEEE Electron Device Letters* **2009,** *30*, 1161-1163.
156. Famà, S., et al. *Applied Physics Letters* **2002,** *81*, 586-588.
157. Masini, G., et al. *Advances in Optical Technologies* **2008,** *2008*, 1-5.
158. Michel, J., et al. *Nature Photonics* **2010,** *4*, 527-534.
159. Huang, C. H., et al. In *Very low defects and high performance Ge-on-insulator p-MOSFETs with Al2O3 gate dielectrics*, 2003 Symposium on VLSI Technology. Digest of Technical Papers (IEEE Cat. No.03CH37407), **2003;** 119-120.
160. Kuzum, D., et al. In *Interface-Engineered Ge (100) and (111), N- and P-FETs with High Mobility*, 2007 IEEE International Electron Devices Meeting, **2007;** 723-726.
161. Zhang, R., et al. *IEEE Transactions on Electron Devices* **2012,** *59*, 335-341.
162. Caymax, M., et al. *Journal of The Electrochemical Society* **2009,** *156*, H979.
163. Hutin, L., et al. *IEEE Electron Device Letters* **2010,** *31*, 234-236.
164. Liu, L.-J., et al. In *Ultralow EOT and high mobility Ge pMOSFETs with in-situ H2O plasma grown GeO2 and HfON gate dielectric*, 2013 International Symposium on VLSI Technology, Systems and Application (VLSI-TSA), **2013;** 1-2.
165. Simoen, E., et al. *Materials Science in Semiconductor Processing* **2012,** *15*, 588-600.
166. Xie, R., et al. *IEEE Transactions on Electron Devices* **2009,** *56*, 1330-1337.
167. Zhang, L., et al. *IEEE Electron Device Letters* **2013,** *34*, 732-734.
168. Thareja, G., et al. In *High performance germanium n-MOSFET with antimony dopant activation beyond 1x1020 cm-3*, 2010 International Electron Devices Meeting, **2010;** 10.5.1-10.5.4.
169. Kobayashi, M., et al. *Journal of Applied Physics* **2009,** *105*, 023702.
170. Li, R., et al. *Thin Solid Films* **2006,** *504*, 28-31.
171. Burchhart, T., et al. *Nano Letters* **2009,** *9*, 3739-42.
172. Burchhart, T., et al. *Nanotechnology* **2010,** *21*, 435704.
173. Burchhart, T., et al. *Nanotechnology* **2011,** *22*, 035201.
174. Huang, J., et al. *Applied Physics Letters* **2005,** *87*, 173507.
175. Nishimura, T., et al. *Applied Physics Express* **2008,** *1*, 051406.
176. Takahashi, T., et al. In *Proof of Ge-interfacing concepts for metal/high-k/Ge CMOS Ge-intimate material selection and interface conscious process flow*, 2007 Ieee International Electron Devices Meeting, Vols 1 and 2, **2007;** 697-700.
177. Brunbauer, F. M., et al. *Nano Letters* **2015,** *15*, 7514-8.
178. Sistani, M., et al. *Nano Letters* **2017,** *17*, 4556-4561.
179. Claeys, C., et al., *Germanium-Based Technologies: From Materials to Devices*. Elsevier Science: 2011.
180. Leonard, F., et al. *Nature Nanotechnology* **2011,** *6*, 773-83.
181. Dimoulas, A., et al. *Applied Physics Letters* **2006,** *89*, 252110.
182. Nishimura, T., et al. *Applied Physics Letters* **2007,** *91*, 123123.
183. Liu, J., et al. *Optics Express* **2007,** *15*, 11272-11277.
184. Xiaochen, S., et al. *IEEE Journal of Selected Topics in Quantum Electronics* **2010,** *16*, 124-131.
185. Mott, N. F. *Reviews of Modern Physics* **1968,** *40*, 677-683.
186. Berencén, Y., et al. *Scientific Reports* **2017,** *7*, 43688.
187. Luther, J. M., et al. *Nature Materials* **2011,** *10*, 361-6.
188. Berencén, Y., et al. *Advanced Materials Interfaces* **2018,** *5*, 1800101.
189. Mathews, J., et al. *Applied Physics Letters* **2014,** *104*, 112102.
190. Mailoa, J. P., et al. *Nature Communications* **2014,** *5*, 3011.
191. Luque, A., et al. *Physical Review Letters* **1997,** *78*, 5014-5017.
192. Luque, A., et al. *Progress in Photovoltaics: Research and Applications* **2001,** *9*, 73-86.
193. Marti, A., et al. *Physical Review Letters* **2006,** *97*, 247701.
194. Martí, A., et al. *Thin Solid Films* **2006,** *511-512*, 638-644.
195. Luque, A., et al. *Advanced Materials* **2010,** *22*, 160-74.
196. Grimmeiss, H. G., et al. *Physical Review B* **1988,** *37*, 6916-6928.
197. Sun, K., et al. *IEEE Photonics Journal* **2016,** *8*, 1-10.

198. Murray, J. L., et al. *Bulletin of Alloy Phase Diagrams* **1984,** *5*, 74-84.
199. White, C. W., et al. *Journal of Applied Physics* **1980,** *51*, 738-749.
200. Galenko, P. *Physical Review E* **2007,** *76*, 031606.
201. Reitano, R., et al. *Journal of Applied Physics* **1994,** *76*, 1518-1529.
202. Wen, C. Y., et al. *Physical Review Letters* **2010,** *105*, 195502.
203. Tyler, W. W. *Journal of Physics and Chemistry of Solids* **1959,** *8*, 59-65.
204. Huang, W. Q., et al. *Journal of Alloys and Compounds* **2017,** *701*, 816-821.
205. Lan, H. S., et al. *Physical Review B* **2017,** *95*, 201201.
206. Carim, A. I., et al. *Journal of the American Chemical Society* **2011,** *133*, 13292-5.
207. Gu, J., et al. *Nano Letters* **2012,** *12*, 4617-23.
208. Fahrenkrug, E., et al. *Nano Letters* **2014,** *14*, 847-52.
209. Ma, L., et al. *Journal of The Electrochemical Society* **2014,** *161*, D3044-D3050.
210. DeMuth, J., et al. *Crystal Growth & Design* **2016,** *16*, 7130-7138.
211. Ma, L., et al. *RSC Advances* **2016,** *6*, 78818-78825.
212. Olesinski, R. W., et al. *Bulletin of Alloy Phase Diagrams* **1986,** *7*, 535-540.
213. Olesinski, R. W., et al. *Bulletin of Alloy Phase Diagrams* **1985,** *6*, 536-539.
214. Conwell, E. *Proceedings of the IRE* **1952,** *40*, 1327-1337.
215. Zhang, S., et al. *Nano Letters* **2009,** *9*, 3268-74.
216. Ruddy, D. A., et al. *The Journal of Physical Chemistry Letters* **2013,** *4*, 416-21.
217. Olesinski, R. W., et al. *Bulletin of Alloy Phase Diagrams* **1986,** *7*, 219-222.
218. Tabatabaei, K., et al. *Chemistry of Materials* **2017,** *29*, 7353-7363.
219. Gupta, S., et al. *Journal of Applied Physics* **2013,** *113*, 073707.
220. Soref, R., *Group IV photonics for the mid infrared.* SPIE: 2013; Vol. 8629, p 15.
221. Soref, R. *Nature Photonics* **2010,** *4*, 495-497.
222. D'Costa, V. R., et al. *Thin Solid Films* **2010,** *518*, 2531-2537.
223. Kasper, E., et al. *Photonics Research* **2013,** *1*, 69-76.
224. Kasper, E., et al. *ECS Transactions* **2008,** *16*, 893-904.
225. Vegard, L. *Zeitschrift für Physik* **1921,** *5*, 17-26.
226. Gencarelli, F., et al. *Journal of Applied Physics* **2015,** *117*, 095702.
227. Olesinski, R. W., et al. *Bulletin of Alloy Phase Diagrams* **1984,** *5*, 180-183.
228. Olesinski, R. W., et al. *Bulletin of Alloy Phase Diagrams* **1984,** *5*, 265-271.
229. Samavedam, S. B., et al. *Applied Physics Letters* **1998,** *73*, 2125-2127.
230. Luryi, S., et al. *IEEE Transactions on Electron Devices* **1984,** *31*, 1135-1139.
231. Bakkers, E. P., et al. *Nature Materials* **2004,** *3*, 769-73.
232. Liu, H., et al. *Nature Photonics* **2011,** *5*, 416-419.
233. Fischetti, M. V., et al. *Journal of Applied Physics* **1996,** *80*, 2234-2252.
234. Fang, S. F., et al. *Journal of Applied Physics* **1990,** *68*, R31-R58.
235. Kawanami, H. *Solar Energy Materials and Solar Cells* **2001,** *66*, 479-486.
236. El Kurdi, M., et al. *Journal of Applied Physics* **2010,** *107*, 013710.
237. Ghetmiri, S. A., et al. *Applied Physics Letters* **2014,** *105*, 151109.
238. Stange, D., et al. *ACS Photonics* **2015,** *2*, 1539-1545.
239. Zhu, Z., et al. *Physical Chemistry Chemical Physics* **2015,** *17*, 21605-10.
240. Lu Low, K., et al. *Journal of Applied Physics* **2012,** *112*, 103715.
241. Schulte-Braucks, C., et al. *Solid-State Electronics* **2017,** *128*, 54-59.
242. Schulte-Braucks, C., et al. *Applied Physics Letters* **2015,** *107*, 042101.
243. Kasper, E., et al. *Thin Solid Films* **2012,** *520*, 3195-3200.
244. Kormos, L., et al. *Surface and Interface Analysis* **2017,** *49*, 297-302.
245. Wirths, S., et al. *ECS Journal of Solid State Science and Technology* **2013,** *2*, N99-N102.
246. Wirths, S., et al. *ECS Transactions* **2013,** *50*, 885-893.
247. Grzybowski, G., et al. *ECS Transactions* **2013,** *50*, 865-874.
248. Bauer, M. R., et al. *Solid State Communications* **2003,** *127*, 355-359.
249. Tsukamoto, T., et al. *Journal of Materials Science* **2015,** *50*, 4366-4370.
250. Khiangte, K. R., et al. *Solid State Communications* **2018,** *284-286*, 88-92.
251. Assali, S., et al. *Journal of Applied Physics* **2019,** *125*, 025304.
252. Stange, D., et al. *ACS Photonics* **2016,** *3*, 1279-1285.

253.	Senaratne, C. L., et al. *Journal of Applied Physics* **2016,** *120*, 025701.
254.	Al-Kabi, S., et al. *Applied Physics Letters* **2016,** *109*, 171105.
255.	Al-Kabi, S., et al. *Journal of Electronic Materials* **2016,** *45*, 6251-6257.
256.	Margetis, J., et al. *Journal of Crystal Growth* **2017,** *463*, 128-133.
257.	Thai, Q. M., et al. *Applied Physics Letters* **2018,** *113*, 051104.
258.	Grant, P. C., et al. *AIP Advances* **2018,** *8*, 025104.
259.	Harris, J. S., et al. *ECS Transactions* **2013,** *50*, 601-605.
260.	Lin, H., et al. *Thin Solid Films* **2012,** *520*, 3927-3930.
261.	Chen, R., et al. *Applied Physics Letters* **2011,** *99*, 181125.
262.	Zaima, S., et al. *ECS Transactions* **2013,** *50*, 897-902.
263.	Nakamura, M., et al. *Thin Solid Films* **2012,** *520*, 3201-3205.
264.	Xin, X., et al. In *Formation of vertically stacked germanium-tin (Ge1-xSnx) nanowires using a selective dry etch technique*, Silicon-Germanium Technology and Device Meeting (ISTDM), 2014 7th International, **2014;** 167-168.
265.	Gupta, S., et al. *Nano Letters* **2013,** *13*, 3783-90.
266.	Seifner, M. S., et al. *Chemistry of Materials* **2015,** *27*, 6125-6130.
267.	Seifner, M. S., et al. *Chemistry of Materials* **2017,** *29*, 9802-9813.
268.	Doherty, J., et al. *Journal of Materials Chemistry C* **2018,** *6*, 8738-8750.
269.	Assali, S., et al. *Nano Letters* **2017,** *17*, 1538-1544.
270.	Albani, M., et al. *Nanoscale* **2018,** *10*, 7250-7256.
271.	Azrak, E., et al. *The Journal of Physical Chemistry C* **2018,** *122*, 26236-26242.
272.	Biswas, S., et al. *Nature Communications* **2016,** *7*, 11405.
273.	Nakamura, Y., et al. *Journal of Applied Physics* **2007,** *102*, 124302.
274.	Nakamura, Y., et al. *Applied Physics Letters* **2007,** *91*, 013109.
275.	Nakayama, Y., et al. *Japanese Journal of Applied Physics* **2007,** *46*, L1176-L1178.
276.	Nakamura, Y., et al. *Journal of Applied Physics* **2009,** *106*, 014309.
277.	Naruse, N., et al. *Applied Physics Letters* **2009,** *94*, 093104.
278.	Nakamura, Y., et al. *Journal of Physics D: Applied Physics* **2012,** *45*, 035304.
279.	Kikkawa, J., et al. *Journal of Applied Physics* **2013,** *113*, 074302.
280.	Cho, Y. J., et al. *Physical Chemistry Chemical Physics* **2013,** *15*, 11691-5.
281.	Tonkikh, A. A., et al. *Crystal Growth & Design* **2014,** *14*, 1617-1622.
282.	Oliveira, F., et al. *Journal of Applied Physics* **2015,** *117*, 125706.
283.	Di Bartolomeo, A., et al. *Nanotechnology* **2016,** *27*, 485707.
284.	Schlykow, V., et al. *Nanotechnology* **2018,** *29*, 415702.
285.	Schlykow, V., et al. *Applied Physics Letters* **2016,** *109*, 202102.
286.	Chen, N. L., et al. *Japanese Journal of Applied Physics* **2017,** *56*, 050301.
287.	Esteves, R. J. A., et al. *Chemistry of Materials* **2015,** *27*, 1559-1568.
288.	Ramasamy, K., et al. *Chemistry of Materials* **2015,** *27*, 4640-4649.
289.	Esteves, R. J. A., et al. *Chemical Communications* **2016,** *52*, 11665-11668.
290.	Hafiz, S. A., et al. *The Journal of Physical Chemistry Letters* **2016,** *7*, 3295-301.
291.	Boote, B. W., et al. *Chemistry of Materials* **2017,** *29*, 6012-6021.
292.	Demchenko, D. O., et al. *The Journal of Physical Chemistry C* **2017,** *121*, 18299-18306.
293.	Tallapally, V., et al. *Nanoscale* **2018,** *10*, 20296-20305.
294.	Takeoka, S., et al. *Physical Review B* **1998,** *58*, 7921-7925.
295.	Gupta, S., et al. In *Towards high mobility GeSn channel nMOSFETs: Improved surface passivation using novel ozone oxidation method*, 2012 International Electron Devices Meeting, **2012;** 16.2.1-16.2.4.
296.	Fang, Y. C., et al. *ACS Applied Materials & Interfaces* **2015,** *7*, 26374-80.
297.	Liu, T.-H., et al. *IEEE Electron Device Letters* **2018,** *39*, 468-471.
298.	Gupta, S., et al. In *GeSn Technology: Extending the Ge Electronics Roadmap*, 2011 International Electron Devices Meeting, **2011;** 16.6.1-16.6.4.
299.	Maeda, T., et al. *Japanese Journal of Applied Physics* **2015,** *54*, 04DA07.
300.	Wirths, S., et al. *Applied Physics Letters* **2013,** *102*, 192103.
301.	Stange, D., et al. *Optics Express* **2016,** *24*, 1358-67.
302.	Chang, C., et al. *Japanese Journal of Applied Physics* **2016,** *55*, 04EH03.

303. Schwartz, B., et al. *Optics Letters* **2015,** *40*, 3209-12.
304. Gallagher, J. D., et al. *Applied Physics Letters* **2015,** *106*, 091103.
305. Gallagher, J. D., et al. *Applied Physics Letters* **2015,** *107*, 123507.
306. Gallagher, J. D., et al. *Journal of Applied Physics* **2015,** *117*, 245704.
307. Oehme, M., et al. *IEEE Photonics Technology Letters* **2014,** *26*, 187-189.
308. Du, W., et al. *Applied Physics Letters* **2014,** *104*, 241110.
309. Gupta, J. P., et al. *Applied Physics Letters* **2013,** *102*, 251117.
310. Roucka, R., et al. *Applied Physics Letters* **2011,** *98*, 061109.
311. Oehme, M., et al. *IEEE Photonics Technology Letters* **2011,** *23*, 1751-1753.
312. Xu, S., et al. *Optics Express* **2018,** *26*, 17312-17321.
313. Wang, W., et al. *Optics Express* **2018,** *26*, 10305-10314.
314. Pandey, A. K., et al. *IEEE Sensors Journal* **2018,** *18*, 5842-5852.
315. Huang, Y. H., et al. *Optics Letters* **2017,** *42*, 1652-1655.
316. Pham, T. N., et al. *Electronics Letters* **2015,** *51*, 854-856.
317. Zhang, Q., et al. *IEEE Photonics Journal* **2015,** *7*, 1-8.
318. Peng, Y. H., et al. *Applied Physics Letters* **2014,** *105*, 231109.
319. Oehme, M., et al. *Optics Express* **2014,** *22*, 839-46.
320. Conley, B. R., et al. *Applied Physics Letters* **2014,** *105*, 221117.
321. Buca, D., et al. *2016 IEEE International Electron Devices Meeting* **2016**, 22.3.1-22.3.4.
322. Margetis, J., et al. *ACS Photonics* **2018,** *5*, 827-833.
323. Margetis, J., et al. *Applied Physics Letters* **2018,** *113*, 221104.
324. Reboud, V., et al. *Applied Physics Letters* **2017,** *111*, 092101.
325. Dou, W., et al. *Optics Letters* **2018,** *43*, 4558-4561.
326. Golovin, A. A., et al. *Journal of Applied Physics* **2008,** *104*, 074301.
327. Hofmann, S., et al. *Nature Materials* **2008,** *7*, 372-5.
328. Wen, C. Y., et al. *Science* **2009,** *326*, 1247-50.
329. Wen, C. Y., et al. *Nano Letters* **2010,** *10*, 514-9.
330. Dunlap, W. C. *Physical Review* **1954,** *94*, 1531-1540.
331. Impellizzeri, G., et al. *Journal of Applied Physics* **2009,** *106*, 013518.
332. Lugstein, A., et al. *Nanotechnology* **2013,** *24*, 065701.
333. Sze, S. M., et al. *Solid-State Electronics* **1968,** *11*, 599-602.
334. Cohen, R. W., et al. *Physical Review* **1968,** *168*, 444-450.
335. Asom, M. T., et al. *Applied Physics Letters* **1989,** *55*, 1439-1441.
336. Farrow, R. F. C., et al. *Journal of Crystal Growth* **1981,** *54*, 507-518.
337. Villaflor, A. B., et al. *Journal of Crystal Growth* **1995,** *150*, 779-784.
338. Vnuk, F. *Journal of Crystal Growth* **1980,** *48*, 486-488.
339. Ewald, A. W. *Journal of Applied Physics* **1954,** *25*, 1436-1437.
340. Gallerneault, W. M. T., et al. *Journal of Applied Physics* **1983,** *54*, 4200-4201.
341. Feutelais, Y., et al. *Calphad* **1996,** *20*, 109-123.
342. von den Driesch, N., et al. *Chemistry of Materials* **2015,** *27*, 4693-4702.
343. Leonard, F., et al. *Physical Review Letters* **2009,** *102*, 106805.
344. Nishimura, T., et al. *Solid-State Electronics* **2011,** *60*, 46-52.
345. Mukhopadhyay, B., et al. *Physica Status Solidi B* **2017,** *254*, 1700244.
346. Nakatsuka, O., et al. *Japanese Journal of Applied Physics* **2010,** *49*, 04DA10.
347. Yamada, T., et al. *Materials Science and Engineering: A* **2005,** *390*, 118-126.
348. Novotny, C. J., et al. *Applied Physics Letters* **2005,** *87*, 203111.
349. Colombo, C., et al. *Physical Review B* **2008,** *77*.
350. Dubrovskii, V. G., et al. *Nano Letters* **2015,** *15*, 5580-4.
351. Zaumseil, P., et al. *APL Materials* **2018,** *6*, 076108.
352. Schmidt, T., et al. *Physical Review B* **1992,** *45*, 8989-8994.

6 Appendix

6.1 Papers

In this chapter the peer-reviewed papers discussed in Chapter 3 are listed in their original form:

1. *Direct Synthesis of Hyperdoped Germanium Nanowires*

2. *Pushing the Composition Limit of Anisotropic $Ge_{1-x}Sn_x$ Nanostructures and Determination of Their Thermal Stability*

3. *Electrical Characterization and Examination of Temperature-Induced Degradation of Metastable $Ge_{0.81}Sn_{0.19}$ Nanowires*

4. *Epitaxial $Ge_{1-x}Sn_x$ Nanowire and Nanocone Growth using Sn Growth Seeds: Effects of the Seed Diameter and Photoluminescence Properties*

ACS NANO

ARTICLE

Direct Synthesis of Hyperdoped Germanium Nanowires

Michael S. Seifner,[†,#] Masiar Sistani,[‡,#] Fabrizio Porrati,[§] Giorgia Di Prima,[§] Patrik Pertl,[†] Michael Huth,[§] Alois Lugstein,[‡] and Sven Barth*,[†]

[†]Institute of Materials Chemistry, TU Wien, Getreidemarkt 9, 1060 Vienna, Austria
[‡]Institute of Solid State Electronics, TU Wien, Floragasse 7, 1040 Vienna, Austria
[§]Physikalisches Institut, Goethe-Universität, Max-von-Laue-Street 1, 60438 Frankfurt am Main, Germany

S Supporting Information

ABSTRACT: A low-temperature chemical vapor growth of Ge nanowires using Ga as seed material is demonstrated. The structural and chemical analysis reveals the homogeneous incorporation of ∼3.5 at. % Ga in the Ge nanowires. The Ga-containing Ge nanowires behave like metallic conductors with a resistivity of about ∼300 $\mu\Omega$cm due to Ga hyperdoping with electronic contributions of one-third of the incorporated Ga atoms. This is the highest conduction value observed by *in situ* doping of group IV nanowires reported to date. This work demonstrates that Ga is both an efficient seed material at low temperatures for Ge nanowire growth and an effective dopant changing the semiconductor into a metal-like conductor.

KEYWORDS: germanium, nanowires, hyperdoping, gallium, quasi-metallic, semiconductor
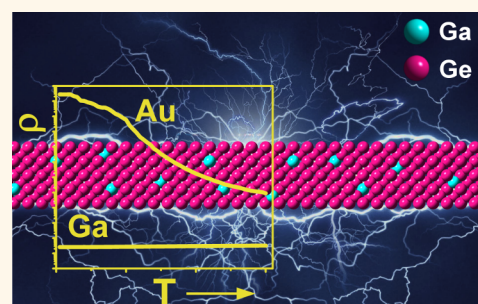
Anisotropic Ge nanostructures have been used as active components for different applications including field effect transistors,[1] lithium ion batteries,[2] solar cells,[3] and humidity sensors.[4] Ge nanowires (NWs) have been successfully prepared by different methods in bottom-up and top-down approaches.[5] The most popular synthesis approach is the use of metal growth promoters in bottom-up processes including vapor−liquid−solid (VLS),[6] supercritical-fluid−liquid−solid (SCFLS),[7] and solution−liquid−solid (SLS)[8] mechanisms as well as the growth by solid metal seeds.[9] Many metallic growth seeds have been described in the literature to result in highly crystalline Ge NWs.[9−11] For some of the above-mentioned applications doping of the NWs is a prerequisite, which can be achieved either by external sources during crystal growth[12−14] or by the incorporation of atoms from metal seeds[15−18] used for the realization of anisotropic crystal constitution. The incorporation of dopants in the Ge matrix has recently been the focus of several studies, and rather effective doping with heavy group III atoms has been observed in low-temperature growth of Ge NWs using In as seeding material[19] and also for Bi in Ge nanoparticles.[20] The electrical properties of the In-containing Ge NWs have not been investigated, which might be related to pronounced twinning of the NWs derived by that approach. Therefore, the actual activity and effect of the nature of the incorporated In atoms on the electronic properties are unknown. In contrast, Bi-containing Ge nanoparticles exhibit an increased charge carrier density when compared to undoped Ge crystals prepared by the same method.[20]

Even though Ga is known to be an excellent p-dopant for Ge, to the best of our knowledge, Ga has not been used for vapor-based growth strategies of Ge nanostructures in the past. The electrodeposition using Ga as nucleation sites for the growth of Ge microwires, the so-called electrochemical liquid−liquid growth mode, is the only exception where Ga was identified as an effective growth promoter.[21,22] This type of growth using Ga as an electrode and seed leads to protuberances along the microwires. The Ga-seeded microwires typically showed highly pronounced tapering and incorporation of 8−10 at. % Ga in the Ge matrix. This is accompanied by p-type behavior in the electronic properties.[21] However, the dopant activation was poor and the carrier concentration was several orders of magnitude lower than the actual Ga concentration.[22]

First indications for suitable conditions of Ga-mediated Ge NW growth can be deduced from the binary Ge−Ga phase diagram. The Ga/Ge eutectic is very close to the melting point of Ga (29.8 °C) with only 0.006 at. % Ge (<1 at. % at 200 °C) in the Ga melt (Figure S1 in the Supporting Information; SI).[23] According to the classification of metal particles acting as catalysts for NW formation, Ga can be considered to be a "type B" catalyst with a eutectic containing less than 1 at. % of the semiconductor material and the absence of germanide phases in the binary phase diagram.[24]

Our study illustrates that Ga can be an efficient metal growth seed for single-crystalline Ge NWs at temperatures slightly above 200 °C in vapor phase syntheses. During the synthesis ~3.51 ± 0.29 at. % Ga is incorporated in the growing Ge matrix, leading to the formation of a material with dramatically altered electronic properties. Such hyperdoped Ge NWs with ~5 × 10^{20} cm^{-3} active p-dopant atoms will exhibit quasi-metallic conductivity.

RESULTS AND DISCUSSION

Scanning electron microscopy (SEM) imaging reveals a high density of Ge NWs achieved using a Ga-mediated low-temperature chemical vapor deposition (CVD) synthesis approach as shown in Figure 1a. A very slight tapering is
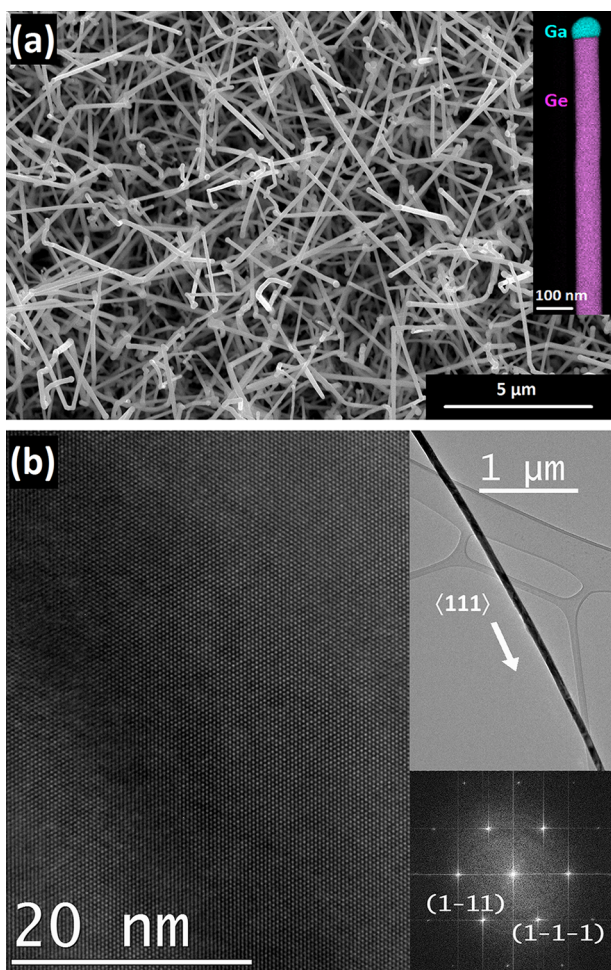

Figure 1. (a) SEM image of Ge NWs grown by Ga seeding at 210 °C for 6 h. The inset shows a STEM EDX mapping indicating the Ga particle at the tip of the NWs. (b) High-resolution TEM image of a selected Ga-seeded Ge NW revealing the single-crystalline nature of the material. The growth along the ⟨111⟩-axis can be determined by the fast Fourier transformation in the inset.

discernible in these NWs, and the diameters average about 100 nm, while typical lengths are several micrometers. A scanning transmission electron microscopy energy dispersive X-ray spectroscopy (STEM-EDX) map for Ga and Ge near the NW tip is shown in the inset of Figure 1a, nicely visualizing the Ga particle at the tip of the Ge NWs. Transmission electron microscopy (TEM) was used to study microstructural proper-

ties of the Ge NWs. For that purpose Ge NWs were deposited onto lacey carbon grids by direct transfer using shear force. The single-crystalline nature of the Ga-seeded Ge NWs is revealed by high-resolution TEM as illustrated in Figure 1b. The fast Fourier transformation (FFT) pattern shown in the inset depicts the growth direction of the Ge NWs to be along the ⟨111⟩ axis, which is the typical orientation for group IV NWs of this diameter.[25] Slight tapering can also be noticed in the TEM image of the inset along a NW of several micrometers and is discussed *vide infra*.

The local composition of the NWs has been determined by STEM-EDX. The Ga particle terminating the NW contains ≤1 at. % Ge according to EDX data, which is slightly higher than the expected value at room temperature. According to the phase diagram, Ge is essentially immiscible in Ga at room temperature (0.006 at. %), but the liquid phase at the growth temperature of 210 °C contains up to 1 at. % Ge.[23] Conversely, according to the phase diagram at the growth temperatures applied here a maximum of ~0.07 at. % Ga should be expected in the Ge NWs.[23] However, STEM-EDX mapping of a NW section reveals a much higher homogeneously distributed concentration of Ga in the Ge matrix (Figure 2a). The average Ga content determined by EDX in these NWs is 3.51 ± 0.29 at. % (1σ standard deviation). For an overview of NWs in the diameter range 65−150 nm see Figure S2 of the Supporting Information. The accuracy of all EDX values should be
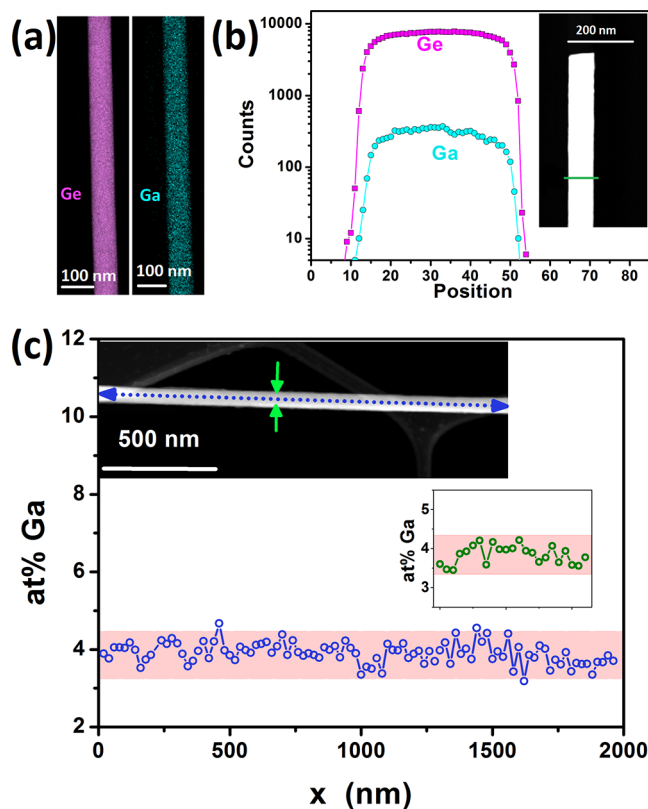

Figure 2. (a) STEM-EDX mapping of a Ga-seeded Ge NW showing the homogeneous distribution of Ga in the Ge matrix and (b) the Ga signal across a NW replicating the shape of the Ge signal very well. (c) Ga concentration profiles along the NW axis for a distance of 2 μm (blue) and a radial concentration profile (green). The shaded red area was included to represent an uncertainty interval of ±0.5 at. % immanent to EDX.

considered to potentially deviate by ±0.5 at. % due to the limited sensitivity of the method. Complementary bulk quantification of hyperdoped Ge NW samples using laser-assisted inductively coupled plasma mass spectrometry (LA-ICP-MS) reveals high concentrations of Ga in the Ge NWs. The most accurate comparison of the data obtained by EDX and LA-ICP-MS is based on Ge nanorod samples after removal of all access Ga on the surface, suggesting an overestimation of ∼0.5 at. % by EDX analysis. These investigations will be published in detail elsewhere. An EDX line scan across a typical NW shows the replication of the Ge signal in the Ga channel, and no hints toward a potential core−shell formation have been observed (Figure 2b). This is a representative result for different positions along a NW. The diminishing NW diameter along its axis can be attributed to the incorporation of the Ga growth promoter in the Ge NW body and not caused by an additional vapor−solid growth of Ge on the NW sidewalls.[15]

EDX line scans along the Ge NW growth axis reveal a quite homogeneous distribution of Ga with only a minor fluctuation around 3.91 ± 0.27 at. % (1σ) as illustrated in Figure 2c. A radial scan as illustrated in the inset of Figure 2c shows a similar distribution (3.86 ± 0.24 at. %; 1σ). In general, EDX profiles display fluctuations around a mean value in the 3−4 at. % range and thus indicate a random incorporation of Ga in the Ge NW matrix, as can be expected from a self-doping process involving the catalyst particle. In contrast, doping profiles will differ along the NW axis when impurities are preferentially incorporated via vapor−solid growth on the sidewalls, leading to tapering of the NWs.[12]

The remarkably high Ga concentration might be a consequence of solute trapping at step edges during the Ge NW growth. This model has been discussed for the incorporation of Al in Si NWs, where unusually high Al concentrations in the Si NW body have been observed.[17,26] According to the literature, the group IV NW growth can proceed with successive addition of bilayers through a step flow process,[27] and during this process catalyst atoms can be trapped in the bilayer due to the high growth rate. However, the NW growth presented here is quite slow when considering the growth time of hours. Nevertheless, a step flow process to form the bilayer could be assumed as being fast even though the overall growth rate is slow. The actual bilayer growth via step flow requires an initial nucleation event with a distinct energy barrier that has to be overcome. A reason for the small overall growth rate can be the slow decomposition of the Ge precursor and thus an extended time span for the buildup of sufficient supersaturation in the Ga growth seed to overcome the nucleation barrier. Once the new layer is growing, the supersaturation drops dramatically and enrichment of the growing materials has to take place before a new layer forms. The actual efficiency of incorporation during this crystal growth process is most likely due to the similar atomic radii of Ga and Ge and therefore an absence of strain by the incorporation of Ga in the Ge lattice.[28] Therefore, we propose the same model of solute trapping as applied to Al incorporation in Si NWs.[17] Within this scenario the observed high Ga content in the Ge matrix becomes plausible. A direct experimental proof of the trapping of the Ga growth promoter in the Ge matrix during the Ge NW growth could most probably be achieved using a combined strategy of presented methods for Al-seeded Si NWs, but would ideally require in situ TEM imaging facilities.[27,29] However, the high Ga concentration trapped in the Ge matrix represents a metastable material composition. At temperatures

close to the growth temperature no changes in the composition could be recorded for heating cycles of 10 h at 250 °C due to limited and very slow diffusion processes at these temperatures. Typical for metastable compositions, increased annealing temperatures lead to diffusion processes and thus Ga segregation. This effect can be illustrated best monitoring twin structures, which are a minor fraction in the nanowire samples. Figure S3 shows a twin along the axis of a $Ge_{0.97}Ga_{0.03}$ NW grown at 230 °C without a sign of Ga enrichment at the interface even after 10 h at 250 °C, while a similar twin heated for 6 h at 400 °C shows not only strain effects in the TEM but also Ga enrichment/segregation at the interface of both crystals in the STEM-EDX. The twin structures are ideal to illustrate this effect because the mobility of the segregated Ga at interfaces is limited when compared to a surface diffusion. Similar phase separation of a component in a metastable Ge-based alloy can be found in the well-known GeSn system when the crystalline phase is heated above a threshold temperature, which depends on the initial composition.[30]

The electronic properties of the hereafter called $Ge_{0.97}Ga_{0.03}$ NWs have been determined after treatment in 2% hydrofluoric acid to remove any Ga from the NWs surface. The NWs have been deposited on Si substrates with a 100 nm thick, thermally grown SiO_2 layer by dry transfer and contacted by aluminum pads fabricated by electron-beam lithography, sputter deposition, and lift-off techniques. Two-terminal I−V measurements of $Ge_{0.97}Ga_{0.03}$ NWs with different diameters as well as an intrinsic Ge NW grown by Au-mediated CVD are shown in Figure 2a.

The $Ge_{0.97}Ga_{0.03}$ NW devices integrated in two-point measurement modules show ohmic behavior as expected for a highly doped semiconductor in conjunction with very high current levels. The thereof calculated resistance of the hyperdoped $Ge_{0.97}Ga_{0.03}$ NWs is about 3 orders of magnitude lower than for the intrinsic Ge NW and thus amply illustrates the strong impact of the incorporation of the Ga seed material in the Ge crystal (lower inset of Figure 3a). Due to the high conductivity values of the $Ge_{0.97}Ga_{0.03}$ NWs, we neither expected nor could measure any noticeable field effect response in the back-gated NW field effect transistor. Also, in low-temperature resistance measurements in transverse magnetic fields we found a negligibly small magnetoresistance effect. Spread in the two-probe I−V characteristics of different NWs (see Figure S4 of the Supporting Information) could be traced back to variations in the individual contact resistances by complementary four-probe measurements. From four-point measurements exemplarily shown in Figure 3b, we determined resistivity values quite typically to be as large as 300 $\mu\Omega$cm for $Ge_{0.97}Ga_{0.03}$ NWs, while intrinsic Ge NWs grown by using Au as growth promoter reveal resistivity values of about 11 Ωcm[30] as described in the literature.

From the resistivity values measured in this study we deduce an electronically active impurity concentration of ∼5 × 10²⁰ cm⁻³ for p-dopants, such as Ga, in bulk Ge samples using literature data.[31] This is far above the solubility limit of Ga in Ge at thermodynamic equilibrium, which would lead to a maximum Ga concentration of 3.1×10^{19} cm⁻³ (∼0.07 at. %) according to the phase diagram.[23] Therefore, the value determined here suggests that approximately one-third of the ∼3.5 at. % Ga atoms (1.5×10^{21} cm⁻³) are electronically active and are expected to be at substitutional sites in the Ge lattice. In addition, $Ge_{0.97}Ga_{0.03}$ NWs can withstand remarkably high
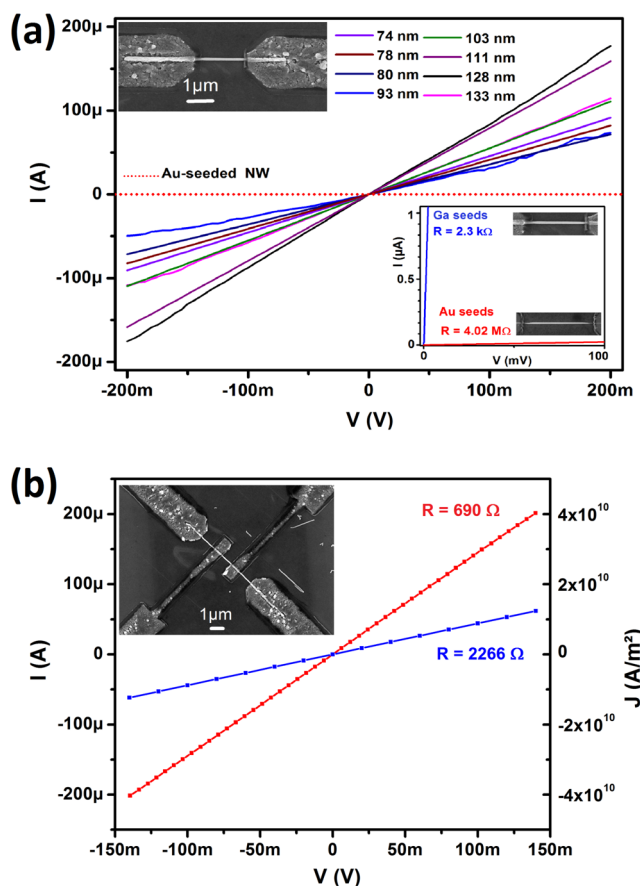
Figure 3. (a) Two-probe $I-V$ measurements of $Ge_{0.97}Ga_{0.03}$ NW devices of different diameters as well as a Au-seeded Ge NW for comparison. (b) The influence of contact resistances can be illustrated in four-point geometry and compared with a two-terminal measurement using the same NW.

currents of more than 1 mA, corresponding to about 12 MA/cm,[2] before device failure occurs (Figure S4 inset).

In contrast, electrodeposition of Ge micro/nanowires using Ga as electrode material also leads to the incorporation of Ga in the Ge matrix but results in strongly tapered nano/microwires as well as p-type semiconductor behavior.[21,22] Even though these anisotropic Ge structures contain twice or three times as much Ga (8−10 at. %) when compared to the material described herein, the effect on the electronic properties is very low. The actual number of electronically active Ga atoms is determined to be about 2.3×10^{15} cm^{-3}, correlating to $\sim10^{-7}$ at. % of electronically active Ga dopants. The differences could be related to temperature effects during growth (40 °C for electrodeposition vs 210 °C in this study), the actual growth rate, crystal quality, and Ga being incorporated at actual substitutional sites. The extraordinarily large effect on the electronic properties can be also manifested comparing the impact of ~5 at. % Al incorporation in Si NWs, where only a density of $\sim1 \times 10^{19}$ cm^{-3} electronically active impurities has been observed. These values are more than ~50 times lower than we have observed in the hyperdoped $Ge_{0.97}Ga_{0.03}$ NWs.

Temperature-dependent resistance measurements have been recorded for $Ge_{0.97}Ga_{0.03}$ NW devices in four-terminal configurations and compared to Au-seeded Ge NWs. The Au-seeded and thus nominally intrinsic Ge NW shows an increase in resistivity of 6 orders of magnitude under cooling from 300 to 4 K, while the $Ge_{0.97}Ga_{0.03}$ NWs exhibit a weakly

metallic-like temperature-dependent resistivity decrease with a residual resistance ratio of about 1.2 (Figure 4). A similar
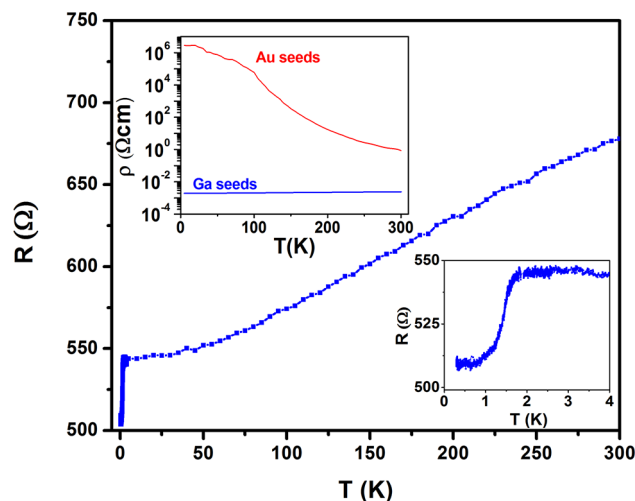

Figure 4. Evolution of resistance during cooling in the temperature range 300−0.269 K. The upper inset shows a comparison of the resistivity of a Au-seeded intrinsic Ge NW and a $Ge_{0.97}Ga_{0.03}$ NW measured in four-point configuration in the temperature range 4−300 K. The lower right inset shows a drop in resistance at ~1.6 K that has been obtained in two-point geometry and is displayed with a constant offset of 1020 Ω due to the influence of contact resistance.

behavior is reported for other dopants, such as group VI elements in Si, showing the same temperature dependence when unusually high concentrations of dopants are incorporated in the semiconductor crystal.[32] In these studies the notion "hyperdoping" was coined and represents concentrations of the dopants exceeding their thermodynamic solubility limit.[33,34] These high-impurity concentrations can form a new impurity band that leads to a transition of the semiconductor to a metallic-like conductor (semiconductor−metal transition) instead of an impurity state within the band gap of the semiconductor for small and intermediate doping levels. Hence, following this reasoning the $Ge_{0.97}Ga_{0.03}$ NWs are hyperdoped with Ga due to their described electronic behavior and the high Ga level representing ~50 times the solubility limit at the growth temperature and exceeding even 3−4 times the maximum solubility observed at high temperatures.[23]

Upon further cooling, a small drop in resistance of ~30 Ω at 1.6 K is observed (Figure 4 inset and Figure S5), which is suppressed at the lowest temperature of 0.269 K by applying a weak overcritical magnetic field of less than 250 mT (Figure S6). This resistance drop is associated with the Al electrodes used in the two-probe measurement that have been fabricated by sputtering and are expected to contain a small amount of oxygen impurities, causing the critical temperature increase of Al (1.1 K in the clean limit) to 1.6 K.[35] The $Ge_{0.97}Ga_{0.03}$ NW measured down to 0.269 K did not show a superconducting transition, but a possible onset of superconductivity below this temperature cannot be ruled out by this study

CONCLUSION

We demonstrate the successful Ga-assisted growth of Ge NWs at low temperatures of 210 °C. This process leads to hyperdoping of the Ge NWs with Ga concentrations of $\sim3.5 \pm 0.29$ at. %, which is ~50 times higher than the solubility limit

at this temperature. The high Ga incorporation efficiency is probably due to solute trapping during the growth of Ge bilayers. Hyperdoping of Ga in Ge leads to metal-like behavior conductivity of the NWs, and the importance of contact resistances in devices prepared using Al as contact material was identified.

METHODS

All synthetic procedures and handling of the chemicals for the nanostructure synthesis have been carried out using Schlenk techniques or an argon-filled glovebox (MBraun). Solvents were dried over sodium and stored in a glovebox. The (pentamethylcyclopentadienyl)gallium(I) precursor (Ga(C_5Me_5); GaCp*) was prepared using sonochemical synthesis of GaI and subsequent salt elimination using KCp* in dry benzene according to the literature.[36] *tert*-Butylgermane (TBG; (C_4H_9)GeH$_3$) was purchased from Gelest.

Nanostructure Synthesis. *tert*-Butylgermane [76 mg (572 μmol)−152 mg (1144 μmol)] was loaded in a 5 mL cell from HIP using a glovebox. The silicone substrates were infiltrated by GaCp* and introduced in the cell before the vessel was closed. Heating this vessel for 6−12 h at temperatures of 210−230 °C results in the growth of dense nanowire meshes on the silicone substrate. Data presented herein are limited to the NWs grown at 210 °C.

Post growth annealing was performed in a quartz tube at 250−400 °C for 6−10 h under a 10% H_2/90% N_2 atmosphere to test the stability of the material.

Nanostructure Characterization. The Ge NWs were analyzed using a FEI Inspect F50 scanning electron microscope. The Ge NWs were deposited on lacey carbon copper grids by dry transfer using shear force for TEM characterization (Plano). In this study, a FEI TECNAI F20 operated at 200 kV and equipped with high angle annular dark field (HAADF) STEM and EDX detectors was used. The limited accuracy of the EDX analysis can lead to a potential deviation by ±0.5 at. % of the values stated here. The elemental maps were recorded and quantified using the AMETEK TEAM package. The images were recorded and treated using Digital Micrograph software. LA-ICP-MS measurements were performed using a commercially available laser ablation system (New Wave 213, ESI, Fremont, CA, USA) with a frequency-quintupled 213 nm Nd:YAG laser in combination with a quadrupole ICP-MS instrumentation (Thermo iCAP Qc, ThermoFisher Scientific, Bremen, Germany). For quantification, ^{69}Ga was compared with the ^{76}Ge signal while standards of metal ratios between 1:99 and 5:95 Ga/Ge were prepared using the metal halogenides dissolved in aqueous potassium hydroxide.

Electrical Characterization. The vapor-grown Ge NWs were deposited by dry transfer onto a highly p-doped Si substrate with a 100 nm thick, thermally grown SiO$_2$ layer and predefined macroscopic Ti−Au bonding pads. Individual NWs were contacted with 150 nm thick Al pads by electron beam lithography, Al sputter deposition preceded by a HI dip (5 s using 14 % HI to remove any germanium oxide), and lift-off techniques.

The electrical measurements at room-temperature and ambient conditions were performed using a combination of a semiconductor analyzer (HP 4156B) and a probe station. To minimize the influence of ambient light as well as electromagnetic fields, the probe station was placed in a dark box.

Low-temperature measurements (4−300 K) were performed in vacuum at a pressure of approximately 2.5 × 10^{-5} mbar using a ^{4}He cryostat (Cryo Industries CRC-102) and a semiconductor analyzer (Keysight B1500A). Temperature-dependent resistance measurements in the range 0.269−4 K were performed in a ^{3}He cryostat employing a sourcemeter (Keithley, 2600) in two-probe configuration at a fixed current of 1 μA. Magnetic field dependent measurements were done using a NbTi superconducting solenoid.

ASSOCIATED CONTENT

ⓢ Supporting Information

The Supporting Information is available free of charge on the ACS Publications website at DOI: 10.1021/acsnano.7b07248.

> Experimental procedures as well as a detailed description of the characterization methods, an overview of determined Ga content in several NWs, a *J/V* plot of several devices in two-point geometry, a low-temperature resistance plot, and a *B/R* plot at temperatures between 0.269 and 1.6 K (PDF)

AUTHOR INFORMATION

Corresponding Author

*E-mail: sven.barth@tuwien.ac.at. Fax: +43 158801 165 99. Tel: +43 158801 165 207.

ORCID

Michael S. Seifner: 0000-0001-9101-5520
Masiar Sistani: 0000-0001-5730-234X
Michael Huth: 0000-0001-7415-465X
Alois Lugstein: 0000-0001-5693-4775
Sven Barth: 0000-0003-3900-2487

Author Contributions

#M. S. Seifner and M. Sistani contributed equally.

Notes

The authors declare no competing financial interest.

REFERENCES

(1) Wang, D.; Wang, Q.; Javey, A.; Tu, R.; Dai, H.; Kim, H.; McIntyre, P. C.; Krishnamohan, T.; Saraswat, K. C. Germanium Nanowire Field-Effect Transistors with SiO2 and High-κ HfO2 Gate Dielectrics. *Appl. Phys. Lett.* **2003**, *83*, 2432−2434.

(2) Kennedy, T.; Mullane, E.; Geaney, H.; Osiak, M.; O'Dwyer, C.; Ryan, K. M. High-Performance Germanium Nanowire-Based Lithium-Ion Battery Anodes Extending over 1000 Cycles Through *in Situ* Formation of a Continuous Porous Network. *Nano Lett.* **2014**, *14*, 716−723.

(3) Yun, J.-H.; Park, Y. C.; Kim, J.; Lee, H.-J.; Anderson, W. A.; Park, J. Solution-Processed Germanium Nanowire-Positioned Schottky Solar Cells. *Nanoscale Res. Lett.* **2011**, *6*, 287.

(4) Samà, J.; Seifner, M. S.; Domènech-Gil, G.; Santander, J.; Calaza, C.; Moreno, M.; Gràcia, I.; Barth, S.; Romano-Rodríguez, A. Low Temperature Humidity Sensor Based on Ge Nanowires Selectively Grown on Suspended Microhotplates. *Sens. Actuators, B* **2017**, *243*, 669−677.

(5) Barth, S.; Hernandez-Ramirez, F.; Holmes, J. D.; Romano-Rodriguez, A. Synthesis and Applications of One-Dimensional Semiconductors. *Prog. Mater. Sci.* **2010**, *55*, 563−627.

(6) Wagner, R. S.; Ellis, W. C. Vapor-Liquid-Solid Mechanism of Single Crystal Growth. *Appl. Phys. Lett.* **1964**, *4*, 89−90.

(7) Holmes, J. D.; Johnston, K. P.; Doty, R. C.; Korgel, B. A. Control of Thickness and Orientation of Solution-Grown Silicon Nanowires. *Science* **2000**, *287*, 1471−1473.

(8) Trentler, T. J.; Hickman, K. M.; Goel, S. C.; Viano, A. M.; Gibbons, P. C.; Buhro, W. E. Solution-Liquid-Solid Growth of Crystalline III-V Semiconductors - an Analogy to Vapor-Liquid-Solid Growth. *Science* **1995**, *270*, 1791−1794.

(9) Lensch-Falk, J. L.; Hemesath, E. R.; Perea, D. E.; Lauhon, L. J. Alternative Catalysts for VSS Growth of Silicon and Germanium Nanowires. *J. Mater. Chem.* **2009**, *19*, 849−857.

(10) O'Regan, C.; Biswas, S.; Petkov, N.; Holmes, J. D. Recent Advances in the Growth of Germanium Nanowires: Synthesis, Growth Dynamics and Morphology Control. *J. Mater. Chem. C* **2014**, *2*, 14−33.

(11) Seifner, M. S.; Pertl, P.; Bernardi, J.; Biswas, S.; Holmes, J. D.; Barth, S. Lead-Supported Germanium Nanowire Growth. *Mater. Lett.* **2016**, *173*, 248−251.

(12) Perea, D. E.; Hemesath, E. R.; Schwalbach, E. J.; Lensch-Falk, J. L.; Voorhees, P. W.; Lauhon, L. J. Direct Measurement of Dopant Distribution in an Individual Vapour-Liquid-Solid Nanowire. *Nat. Nanotechnol.* **2009**, *4*, 315−319.

(13) Zhang, S.; Hemesath, E. R.; Perea, D. E.; Wijaya, E.; Lensch-Falk, J. L.; Lauhon, L. J. Relative Influence of Surface States and Bulk Impurities on the Electrical Properties of Ge Nanowires. *Nano Lett.* **2009**, *9*, 3268−3274.

(14) Tutuc, E.; Chu, J. O.; Ott, J. A.; Guha, S. Doping of Germanium Nanowires Grown in Presence of PH3. *Appl. Phys. Lett.* **2006**, *89*, 3.

(15) Wacaser, B. A.; Reuter, M. C.; Khayyat, M. M.; Wen, C.-Y.; Haight, R.; Guha, S.; Ross, F. M. Growth System, Structure, and Doping of Aluminum-Seeded Epitaxial Silicon Nanowires. *Nano Lett.* **2009**, *9*, 3296−3301.

(16) Barth, S.; Koleśnik, M. M.; Donegan, K.; Krstić, V.; Holmes, J. D. Diameter-Controlled Solid-Phase Seeding of Germanium Nanowires: Structural Characterization and Electrical Transport Properties. *Chem. Mater.* **2011**, *23*, 3335−3340.

(17) Moutanabbir, O.; Isheim, D.; Blumtritt, H.; Senz, S.; Pippel, E.; Seidman, D. N. Colossal Injection of Catalyst Atoms into Silicon Nanowires. *Nature* **2013**, *496*, 78−82.

(18) Allen, J. E.; Hemesath, E. R.; Perea, D. E.; Lensch-Falk, J. L.; Li, Z. Y.; Yin, F.; Gass, M. H.; Wang, P.; Bleloch, A. L.; Palmer, R. E.; Lauhon, L. J. High-Resolution Detection of Au Catalyst Atoms in Si Nanowires. *Nat. Nanotechnol.* **2008**, *3*, 168−173.

(19) Aghazadeh Meshgi, M.; Biswas, S.; McNulty, D.; O'Dwyer, C.; Alessio Verni, G.; O'Connell, J.; Davitt, F.; Letofsky-Papst, I.; Poelt, P.; Holmes, J. D.; Marschner, C. Rapid, Low-Temperature Synthesis of Germanium Nanowires from Oligosilylgermane Precursors. *Chem. Mater.* **2017**, *29*, 4351−4360.

(20) Tabatabaei, K.; Lu, H.; Nolan, B. M.; Cen, X.; McCold, C. E.; Zhang, X.; Brutchey, R. L.; van Benthem, K.; Hihath, J.; Kauzlarich, S. M. Bismuth Doping of Germanium Nanocrystals through Colloidal Chemistry. *Chem. Mater.* **2017**, *29*, 7353−7363.

(21) Fahrenkrug, E.; Gu, J.; Jeon, S.; Veneman, P. A.; Goldman, R. S.; Maldonado, S. Room-Temperature Epitaxial Electrodeposition of Single-Crystalline Germanium Nanowires at the Wafer Scale from an Aqueous Solution. *Nano Lett.* **2014**, *14*, 847−852.

(22) Fahrenkrug, E.; Biehl, J.; Maldonado, S. Electrochemical Liquid−Liquid−Solid Crystal Growth of Germanium Microwires on Hard and Soft Conductive Substrates at Low Temperature in Aqueous Solution. *Chem. Mater.* **2015**, *27*, 3389−3396.

(23) Olesinski, R. W.; Abbaschian, G. J. The Ga−Ge (Gallium-Germanium) System. *Bull. Alloy Phase Diagrams* **1985**, *6*, 258−262.

(24) Schmidt, V.; Wittemann, J. V.; Senz, S.; Gosele, U. Silicon Nanowires: A Review on Aspects of their Growth and their Electrical Properties. *Adv. Mater.* **2009**, *21*, 2681−2702.

(25) Schmidt, V.; Senz, S.; Gosele, U. Diameter-Dependent Growth Direction of Epitaxial Silicon Nanowires. *Nano Lett.* **2005**, *5*, 931−935.

(26) Moutanabbir, O.; Senz, S.; Scholz, R.; Alexe, M.; Kim, Y.; Pippel, E.; Wang, Y.; Wiethoff, C.; Nabbefeld, T.; Meyer zu Heringdorf, F.; Horn-von Hoegen, M. Atomically Smooth p-Doped Silicon Nanowires Catalyzed by Aluminum at Low Temperature. *ACS Nano* **2011**, *5*, 1313−1320.

(27) Wen, C. Y.; Tersoff, J.; Reuter, M. C.; Stach, E. A.; Ross, F. M. Step-Flow Kinetics in Nanowire Growth. *Phys. Rev. Lett.* **2010**, *105*, 195502.

(28) Cordero, B.; Gomez, V.; Platero-Prats, A. E.; Reves, M.; Echeverria, J.; Cremades, E.; Barragan, F.; Alvarez, S. Covalent Radii Revisited. *Dalton Trans.* **2008**, 2832−2838.

(29) Chagnon, D.; Pippel, E.; Senz, S.; Moutanabbir, O. Metal Seed Loss Throughout the Nanowire Growth: Bulk Trapping and Surface Mass Transport. *J. Phys. Chem. C* **2016**, *120*, 2932−2940.

(30) Seifner, M. S.; Hernandez, S.; Bernardi, J.; Romano-Rodriguez, A.; Barth, S. Pushing the Composition Limit of Anisotropic Ge1−xSnx Nanostructures and Determination of Their Thermal Stability. *Chem. Mater.* **2017**, *29*, 9802−9813.

(31) Sze, S. M.; Irvin, J. C. Resistivity, Mobility and Impurity Levels in GaAs, Ge, and Si at 300 K. *Solid-State Electron.* **1968**, *11*, 599−602.

(32) Ertekin, E.; Winkler, M. T.; Recht, D.; Said, A. J.; Aziz, M. J.; Buonassisi, T.; Grossman, J. C. Insulator-to-Metal Transition in Selenium-Hyperdoped Silicon: Observation and Origin. *Phys. Rev. Lett.* **2012**, *108*, 026401.

(33) Zhou, S.; Pi, X.; Ni, Z.; Luan, Q.; Jiang, Y.; Jin, C.; Nozaki, T.; Yang, D. Boron- and Phosphorus-Hyperdoped Silicon Nanocrystals. *Part. Part. Syst. Charact.* **2015**, *32*, 213−221.

(34) Zhou, S.; Liu, F.; Prucnal, S.; Gao, K.; Khalid, M.; Baehtz, C.; Posselt, M.; Skorupa, W.; Helm, M. Hyperdoping Silicon with Selenium: Solid vs. Liquid Phase Epitaxy. *Sci. Rep.* **2015**, *5*, 8329.

(35) Cohen, R. W.; Abeles, B. Superconductivity in Granular Aluminum Films. *Phys. Rev.* **1968**, *168*, 444−450.

(36) Jutzi, P.; Schebaum, L. O. A Novel Synthetic Route to Pentaalkylcyclopentadienylgallium(I) Compounds. *J. Organomet. Chem.* **2002**, *654*, 176−179.

Pushing the Composition Limit of Anisotropic Ge$_{1−x}$Sn$_x$ Nanostructures and Determination of Their Thermal Stability

Michael S. Seifner,[†][ORCID] Sergi Hernandez,[‡,§] Johannes Bernardi,[||] Albert Romano-Rodriguez,[‡,§] and Sven Barth*,[†][ORCID]

[†]Institute of Materials Chemistry, TU Wien, Getreidemarkt 9, 1060 Vienna, Austria
[‡]MIND-Department of Electronics, Universitat de Barcelona (UB), Martí i Franquès 1, 08028 Barcelona, Spain
[§]Institute of Nanoscience and Nanotechnology (IN2UB), Universitat de Barcelona (UB), Martí i Franquès 1, 08028 Barcelona, Spain
[||]University Servicecenter for TEM (USTEM), TU Wien, Wiedner Hauptstrasse 8-10, 1040 Vienna, Austria

S *Supporting Information*

ABSTRACT: Ge$_{1−x}$Sn$_x$ nanorods (NRs) with a nominal Sn content of 28% have been prepared by a modified microwave-based approach at very low temperature (140 °C) with Sn as growth promoter. The observation of a Sn-enriched region at the nucleation site of NRs and the presence of the low-temperature α-Sn phase even at elevated temperatures support a template-assisted formation mechanism. The behavior of two distinct Ge$_{1−x}$Sn$_x$ compositions with a high Sn content of 17% and 28% upon thermal treatment has been studied and reveals segregation events occurring at elevated temperatures, but also demonstrates the temperature window of thermal stability. *In situ* transmission electron microscopy investigations revealed a diffusion of metallic Sn clusters through the Ge$_{1−x}$Sn$_x$ NRs at temperatures where the material composition changes drastically. These results are important for the explanation of distinct composition changes in Ge$_{1−x}$Sn$_x$ and the observation of solid diffusion combined with dissolution and redeposition of Ge$_{1−y}$Sn$_y$ ($x > y$) exhibiting a reduced Sn content. Absence of metallic Sn results in increased temperature stability by ∼70 °C for Ge$_{0.72}$Sn$_{0.28}$ NRs and ∼60 °C for Ge$_{0.83}$Sn$_{0.17}$ nanowires (NWs). In addition, a composition-dependent direct bandgap of the Ge$_{1−x}$Sn$_x$ NRs and NWs with different composition is illustrated using Tauc plots.
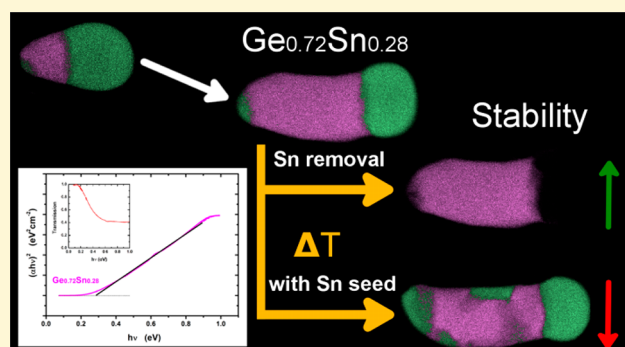
INTRODUCTION

Group IV semiconductor nanowires are potential building blocks for different fields of application including electronic and optoelectronic devices.[1] However, the performance of Si- and Ge-based materials in optics and photonics is limited by their indirect bandgap. Theoretical and experimental reports describe a modification of the Ge band structure to make direct gap emission more favorable by using tensile or uniaxial strain.[2−4] Alternatively, the light emission and absorption characteristics of Ge change dramatically, when a threshold concentration exceeds ∼8−10% Sn in Ge$_{1−x}$Sn$_x$ rendering it in a direct bandgap material which was experimentally observed[5,6] and also calculated.[7,8] Ge$_{1−x}$Sn$_x$ is compatible with CMOS processing based on Si technology and therefore an ideal candidate for infrared optoelectronics and optical devices, such as infrared lasers,[5,9−11] photodetectors,[12,13] or light-emitting diodes.[14−16] In addition, the electronic properties are also altered upon Sn incorporation in the Ge matrix which should result in an enhanced electron and hole mobility making Ge$_{1−x}$Sn$_x$ interesting for high-speed electronics.[17−21] An incorporation of Sn in the Ge lattice in a bottom-up synthesis should be carried out under kinetic control, because the binary

phase diagram reveals the low equilibrium solubility of Sn in Ge (<1%).[22] Aside from thin-film growth studies and postgrowth etching to prepare desired morphologies,[23] reports on Ge$_{1−x}$Sn$_x$ nanostructures are emerging.[24−28] Morphological control has been achieved creating core−shell Ge/Ge$_{1−x}$Sn$_x$[29] using Ge NWs as templates and non-template-based metal-seed-supported growth of Ge$_{1−x}$Sn$_x$ nanowires via gas-phase[30,31] and solution-based synthesis.[32,33] To date, the compositions vary in these reports on the growth of anisotropic Ge$_{1−x}$Sn$_x$ nanostructures with the highest values being in the range 9−13% Sn.[29,30,33] Moreover, a transition to a semimetallic behavior with interesting applications can be expected when the Sn content is increased above 41%.[34] Data confirming such high Sn concentrations in Ge$_{1−x}$Sn$_x$ with high crystallinity have only been rarely described in the literature with limited information about their actual homogeneity with maximum Sn contents of ∼30%.[25−27,35−37] The thermal stability of thin films with different composition is reported, but these reports do not

usually cover higher tin contents >15%; the heat treatment is limited to a short time, e.g., by rapid thermal annealing, and the films are usually highly strained.[38−40]

This paper provides insight in the formation mechanism of anisotropic $Ge_{1−x}Sn_x$ structures at temperatures as low as 140 °C leading to a Sn content of 28%, while the formation of α-Sn and its impact on the nucleation in this low-temperature process is elaborated. Two distinct compositions have been reliably synthesized with two different temperature profiles and pretreatment processes leading to Sn contents of ∼17% and ∼28% and without additional nucleation of branches or substructures. Thermal stabilities of these two alloy compositions are determined by variable-temperature X-ray diffraction (XRD) and subsequent microscopy studies. Our study reveals the strong influence of metallic Sn on the thermal stability of the $Ge_{1−x}Sn_x$ materials. Infrared (IR) absorption was used to characterize the materials' properties and clearly shows the strong impact of direct bandgaps in the absorption spectra for both compositions.

■ EXPERIMENTAL SECTION

Chemicals. Butyl lithium, hexamethyldisilazane, $SnCl_2$, 1,1,3,3-tetramethyldisilioxane, and $GeCl_4$ were purchased from Sigma-Aldrich. All solvents were dried using standard procedures and stored over molecular sieve. All manipulations and syntheses have been conducted using Schlenk techniques or using an argon-filled glovebox. $LiN(Si(CH_3)_3)_2$ was prepared in hexane and purified by sublimation under reduced pressure. The $GeCl_2\cdot$dioxane complex was prepared according to a published procedure.[41] The syntheses of $Sn(N(Si(CH_3)_3)_2)_2$ and $Ge(N(Si(CH_3)_3)_2)_2$ were prepared by a modified procedure published by Lappert et al. using a salt metathesis reaction.[42]

Dodecylamine (98%, Sigma-Aldrich) was kept for 2 h at 40 °C under dynamic vacuum and was distilled three times under reduced pressure. In the first distillation step high-molecular byproducts were separated. For the second and third distillation 0.5−1 mL of $Sn(N(Si(CH_3)_3)_2)_2$ was added to 200 mL of dodecylamine to separate all undesired chemicals as high-molecular residue which would react with $Sn(N(Si(CH_3)_3)_2)_2$ and $Ge(N(Si(CH_3)_3)_2)_2$ in the following material synthesis.

n-Octylamine was purified analogous to dodecylamine without reducing the pressure during distillation because of the low boiling point. Squalane (98%, TCI) was distilled two times under reduced pressure.

Nanostructure Preparation. Ge NRs/NWs were grown in 10 mL glass cells (Anton Paar GmbH) at temperatures between 120 and 230 °C. The handling of the chemicals as well as the filling of the reaction vessels were carried out in a glovebox under stringent precautions against water.

In a typical experiment, 2 mL of dodecylamine was transferred in a glass cell for microwave synthesis. Dodecylamine was kept very close to the melting point. First, $Sn(N(Si(CH_3)_3)_2)_2$ and subsequently $Ge(N(Si(CH_3)_3)_2)_2$ were added to dodecylamine, and the glass cell was sealed with a Teflon-coated silicone cap. Independent of the ratio of $Sn(N(Si(CH_3)_3)_2)_2$ and $Ge(N(Si(CH_3)_3)_2)_2$, all samples prepared in this study have the same total concentration of 38 mM precursor to make a comparison possible. The vial was then transferred to the microwave reactor (Monowave 300; Anton Paar GmbH; frequency, 2.46 GHz) with an IR temperature control unit within 3 min. The precursor solution underwent a temperature program and was cooled down by a gas stream afterward. The synthesized structures were collected by adding toluene (3 mL) and subsequent centrifugation. The collected solid material was redispersed in toluene and centrifuged again to remove the dodecylamine. This step was repeated with ethanol another three times, and with toluene a further three times. The product was stored under ambient conditions in toluene.

Further information about the pretreatment of the precursor mixture for the synthesis of $Ge_{1−x}Sn_x$ NWs with 17% Sn is given in our previous paper.[33] For the synthesis of $Ge_{1−x}Sn_x$ NRs with higher Sn content the following temperature programs were chosen: pretreatment 1 (PT1), (i) heat as fast as possible to 110 °C, (ii) cool down to 60 °C, (iii) hold for 10 min, (iv) heat as fast as possible to 140−160 °C, (v) hold temperature for 0−10 min, (vi) cool down to 55 °C; pretreatment 2 (PT2), (i) heat as fast as possible to 60 °C, (ii) hold temperature for 40 min, (iii) heat as fast as possible to 140−160 °C, (v) hold temperature for 0−10 min, (vi) cool down to 55 °C.

Nanostructure Characterization. The $Ge_{1−x}Sn_x$ NRs and NWs were analyzed using an FEI Inspect F50 scanning electron microscope (SEM). The $Ge_{1−x}Sn_x$ NRs/NWs were deposited on lacey carbon copper grids (Plano) for transmission electron microscope (TEM) characterization. In this study, an FEI TECNAI F20 operated at 200 kV and equipped with a high-angle annular dark field (HAADF) STEM and EDX detector was used. The elemental maps were recorded using the EDAX TEAM package, and the quantification was calculated using the Ge(K) and Sn(L) signals. For the values included in the manuscript, inherent limits in accuracy related to EDX have to be considered (±0.5%). The images were recorded and treated using Digital Micrograph software. *In situ* heating experiments in the TEM were performed using a Gatan heating holder 652.

The X-ray diffraction (XRD) patterns were recorded on a PANalytical X-Pert PRO PW 3050/60 instrument in Bragg−Brentano geometry and Cu Kα radiation. High-temperature XRD (HTXRD) measurements were carried out on a PANalytical MPD Pro in grazing incidence mode with an incidence angle of 4° and Cu Kα radiation under hydrogen atmosphere. X-pert Highscore software was used for analysis of the measured data.

Transmission measurements were performed using the PerkinElmer Frontier FT-IR spectrometer in mid-IR mode. The spectra were acquired from 220 to 8000 cm^{-1}, with a 4 cm^{-1} resolution, using 64 scans. A reference spectrum of the substrate was also acquired under the same conditions, thus allowing a determination of the NR and NW sample transmittance by rationing their spectrum against the one from the substrate. Then, the absorbance α (absorption coefficient times the thickness) was evaluated just by applying the logarithm (i.e., $-\ln(T)$, where T is the transmittance). For the determination of the bandgap energy, we have employed the Tauc-plot method considering a direct bandgap of a material, which consists of a representation of $(\alpha h\nu)^2$ versus $h\nu$, with $h\nu$ being the energy of the incident photons; the intersection of the linear trend at high energies with the abscissa axis will provide the bandgap energy of the analyzed material.

■ RESULTS AND DISCUSSION

Low-Temperature Growth Regime. The microwave synthesis in dodecylamine has been previously described for synthesis temperatures of 230 °C.[33] A modified procedure has been developed to allow a controlled nucleation and growth of $Ge_{1−x}Sn_x$ nanostructures at temperatures as low as 140 °C requiring a certain pretreatment before the growth is initiated. Two pretreatment procedures (PT1, 10 min; PT2, 40 min) have been successfully applied and result in a material with identical morphology and composition (Figure S1). These investigations also allow us to identify different intermediate structures in the evolution of NRs and NWs.

The structural evolution at these low temperatures includes the formation of globular particles, which convert into teardrops, heterodimeric structures, and finally nanorods as shown in Figure 1a−d. Associated with the morphological changes, specific phases can be observed as shown in Figure 1e. The XRD patterns show α-Sn, β-Sn, and Ge reflections with a specific shift toward lower angles as expected for the formation of $Ge_{1−x}Sn_x$. The first crystalline phase that can be observed is β-Sn with a typical globular shape in the SEM image (Figure 1a), which is often observed for low-melting metallic particles. This phase is present in all XRD patterns in Figure 1. The second diffractogram contains the typical low-temperature,
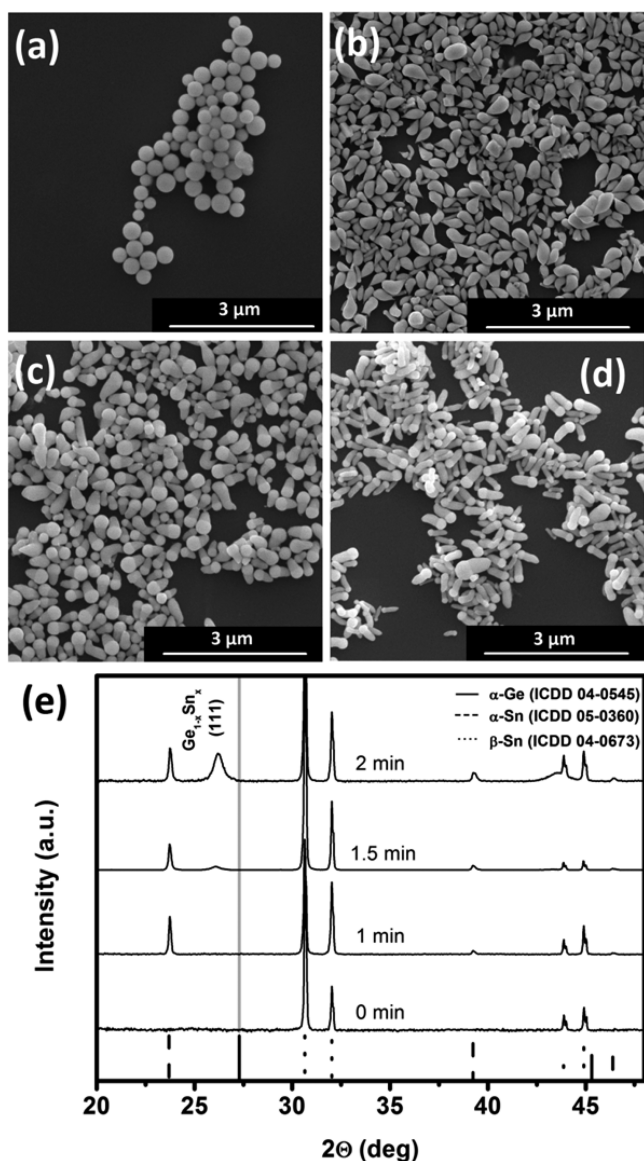
Figure 1. SEM images showing products obtained using PT1 and thermal decomposition at 140 °C for (a) 0, (b) 1, (c) 1.5, and (d) 2 min. The XRD patterns in part e correspond to the material shown in parts a−d. The vertical gray line corresponds to the Ge (111) reflection of the reference, serving as visual guide, and allows clear observation of the large shift in the reflection for $Ge_{1-x}Sn_x$.

cubic α-Sn phase represented by the appearance of teardrop structures in addition to some remaining globular particles (Figure 1b). The α-Sn phase can be stabilized at higher temperatures (>13 °C) by the incorporation of Ge[43] or template effects on lattice-matched substrates,[44,45] both of which could be responsible for the appearance of α-Sn. The data observed here do not allow a definite assignment to either of the aforementioned triggers/processes for the phase transition from β- to α-Sn, but the incorporation of Ge is described *vide infra* suggesting that the actual Ge content is responsible for the stabilization of this phase. Similarly, α-Sn has been also observed with other metal incorporation, such as Li.[46]

After 1.5 min, the first reflections associated with $Ge_{1-x}Sn_x$ are evident, which are more prominent after prolonged decomposition because of the extension of the $Ge_{1-x}Sn_x$

segment in the nanorods as can be expected from the SEM images (Figure 1c,d). The shift in the Ge reflections can be correlated to the concentration of Sn using the lattice constant of the cubic phase of tin (α-Sn, 6.489 Å, JCPDS 00-005-0390), which is isostructural to cubic Ge (5.658 Å), according to Vegard's law. This calculated value is quite accurate for structures where no strain from a substrate has to be taken into account;[25−27,30] however, for highly accurate determination of the composition of surface-bound epitaxial layers, a small deviation is corrected by the bowing parameter which is highly dependent on the literature reports.[47−49] In an earlier report, we quantified the Sn concentration via EDX using the Sn(K) line, which leads to an underestimation of the actual Sn content in $Ge_{1-x}Sn_x$ NWs.[33] In addition, the large variation of the related Raman shift in the literature on thin epitaxial films can be misleading.[50−53]

TEM images of NRs clearly show a quasi-hemispherical segment and the NR body with different diffraction contrast (Figure 2a). Focusing on the NR body by high-resolution (HR)TEM reveals the high crystallinity, which is also illustrated in the sharp fast Fourier transformation (FFT) pattern of Figure 2a. The local Sn concentration in the $Ge_{1-x}Sn_x$ NRs has been evaluated using scanning transmission electron microscopy (STEM) energy dispersive X-ray spectroscopy (EDX) mapping using the Sn(L) and the Ge(K) line for quantification. The elemental mapping reveals the homogeneous distribution of Sn in the Ge matrix without any sign of clustering in the NR body (Figure 2b).

The $Ge_{1-x}Sn_x$ NRs grown at 140 °C show two distinct sites of Sn enrichment located at both extremes on the NRs. The bigger globular part is located at the growth front of the NRs as described before for NWs grown at 230 °C, while a small section of Sn enrichment is located at the nucleation site. This is a general phenomenon for these NRs derived at 140 °C as illustrated in additional STEM-EDX mappings of NRs in the Supporting Information (Figure S2). A transition zone of slightly higher Sn content (~32%; 100−150 nm transition zone) can be found between this Sn-rich area and the constant $Ge_{0.72}Sn_{0.28}$ composition within the NR body. An overview of EDX point measurements is shown in Figure 2c. The Sn-rich zone at the nucleation site can be associated with a remaining α-Sn segment acting as a template for the $Ge_{1-x}Sn_x$ phase formation. The Sn concentration determined by EDX in the NR body of 27.9 ± 0.9% (content according to XRD, 27.5%; abbreviated hereafter as $Ge_{0.72}Sn_{0.28}$), which is roughly 15% Sn higher than previously reported values of ~12−13% Sn in core−shell NWs[29] and 9% Sn in NWs of constant diameter.[30]

At slightly higher growth temperatures of 160 °C, the aforementioned Sn-rich particle at the nucleation site can completely phase separate and act as a second growth seed for a thinner NR as shown in Figure 3. This thinner NR has a diameter of ~50 nm and the same composition as the thicker nanorod (Ø = 210 nm) with 26.5% Sn, while the initial nucleation area shows a higher Sn percentage (32%). This comparison illustrates a diameter-independent composition for NR diameters of 50−250 nm at these low temperatures and rather epitaxial growth on an initial seed with partial relaxation and formation of the most stable composition at the given growth conditions.

Without the pretreatment, the nanostructures tend to form NRs with secondary, "parasitic" structures protruding from the initial nucleation site, and uncontrolled nucleation of undefined, branched structures as illustrated in Figure S3 are
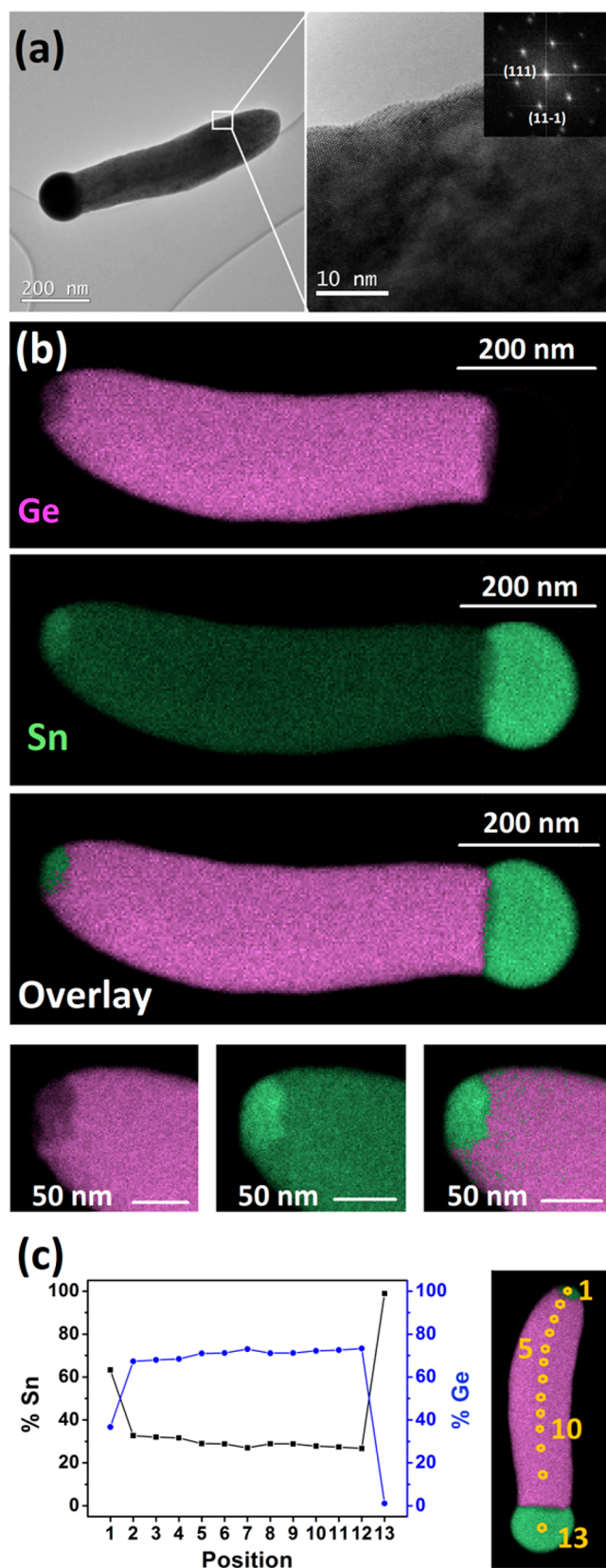
Figure 2. (a) TEM and HRTEM image of $Ge_{1-x}Sn_x$ NRs grown at 140 °C including the corresponding FFT image as an inset. The STEM-EDX mapping in part b shows a homogeneous Sn distribution and an accumulation of Sn at both extremes. The previously[33] not observed accumulation at the initial nucleation site is magnified, and the mapping in higher resolution clearly shows a region with high Sn

Figure 2. continued

content. An overview of point EDX measurements in part c shows the transition from a slightly higher concentration of ~32% to 27.9 ± 0.9% segment (point 5−12) after ~150 nm from the Sn-enriched nucleation site of the NR displayed in part b.
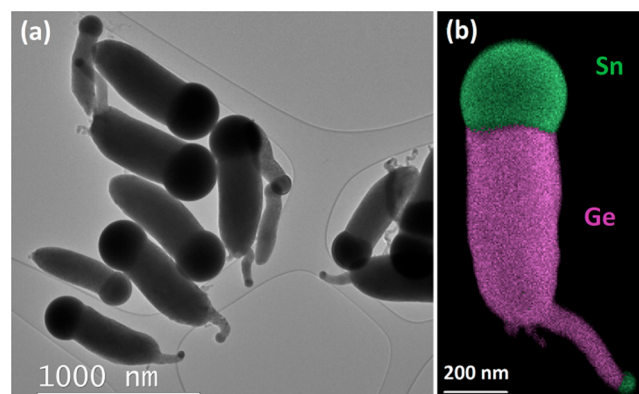
Figure 3. Decomposition of the precursor mixture at 160 °C using pretreatment PT1 leads to a secondary growth of a second NR from the initially formed Sn-rich segment described in Figure 2. (a) TEM and (b) STEM-EDX images show the obtained structures.

observed. In a separate set of experiments, the dodecylamine was substituted by n-octylamine, and the growth was repeated under identical conditions with the same pretreatment at temperatures of 130−160 °C. The elongated structures contain an even higher Sn content in the NR body (32.1 ± 0.5% Sn according to EDX, Figure S4) and could be interesting for applications taking advantage of semimetallic properties;[54] however, the structures tend to form secondary nucleation centers at the surface leading to uncontrolled branching (especially at early stages of the $Ge_{1-x}Sn_x$ crystal formation with a nominal Sn content of 35.6%), which can be related to different decomposition rates of the formed metallorganic intermediates and correlated changes in the nuclei formation and growth kinetics. The formation of the secondary nucleation sites can be most likely attributed to thermal instability of the $Ge_{1-x}Sn_x$ composition as described *vide infra*.

According to the results observed here, a growth mechanism for these NRs growing at 140 °C is proposed (Figure 4a). The pretreated precursor mixture contains homometallic Sn species leading to the formation of *β*-Sn particles as a first step. The *β*-Sn particles contain ≤0.4% Ge averaged over the whole particle according to STEM-EDX analysis. Figure S5a shows the Ge predominantly accumulated at the Sn surface, while the majority of Ge can be expected to be distributed within the *β*-Sn particle at elevated temperatures and separation that occurs upon cooling. These globular *β*-Sn particles are converted to teardrop shaped *α*-Sn by additional gradual incorporation of Ge that stabilizes this cubic Sn phase.[43] The *α*-Sn phase is expected to form via solid diffusion requiring a critical Ge concentration (~0.7−1.0% according to EDX analyses of several particles similar to the one shown in Figure S5b). A critical parameter at this stage is the initially slow rate of Ge precursor decomposition leading to a gradual increase in Ge content. While the Ge concentration must be high enough for the conversion to *α*-Sn, the local concentration should also be low enough to avoid an initial nucleation of a $Ge_{1-x}Sn_x$ particle. A complete or a partial conversion to the *α*-Sn particles

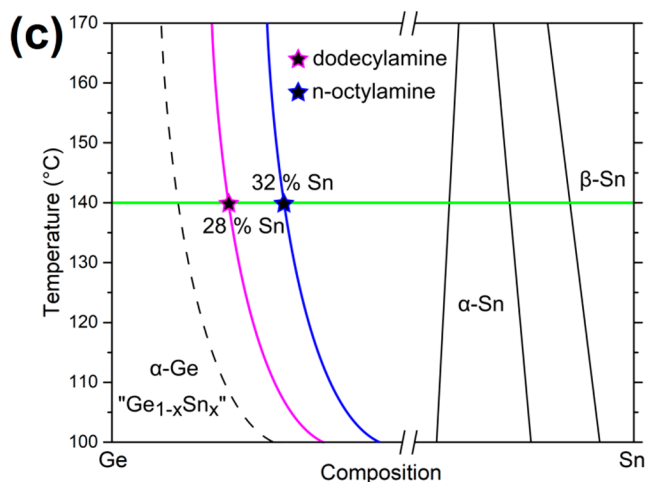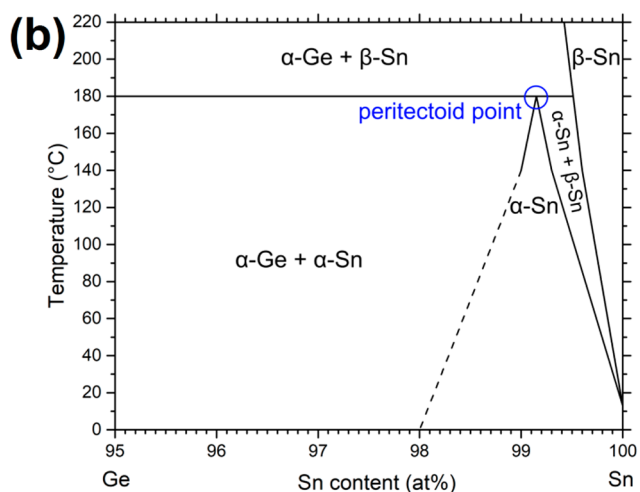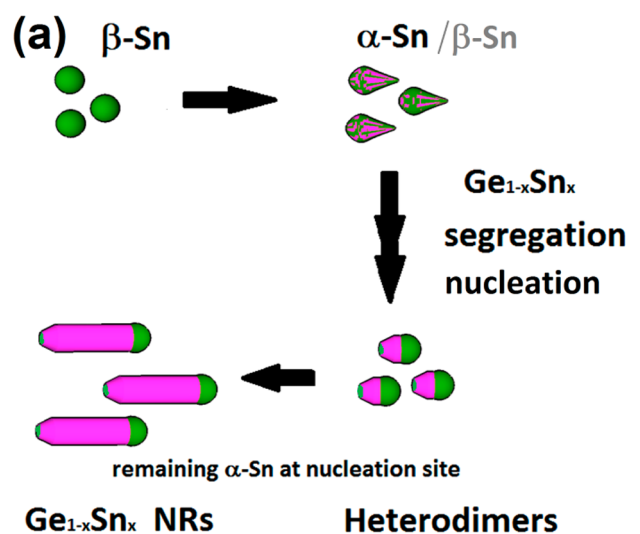**Figure 4.** (a) Schematic representation of the low-temperature nucleation of $Ge_{1-x}Sn_x$ NRs at 140 °C. The corresponding SEM images are displayed in Figure 1a−d, and STEM-EDX images in Figure S5 support this suggestion. (b) Schematic representation of the Sn-rich side of a phase map and the assumption of a peritectoidic transformation and the existence of α-Sn at temperatures below 180 °C. (c) The phase map shows a suggested miscibility gap between the α-Sn phase and an α-Ge phase with parameter-dependent composition variation ($Ge_{1-x}Sn_x$) for two solvents/ligands.

can be expected under growth conditions with the possibility of coexisting Sn phases. Unfortunately this growth stage could not be fully investigated because of potential material modification during the cooling of the material in the microwave process and no possibility of rapid quenching with the used equipment. However, the presence of an α-Sn phase is important for the formation of NRs with such a high Sn content as discussed below.

Increased thermal input accelerates the decomposition kinetics of the precursor species, and thus no α-Sn can be formed because of a quick oversaturation of the Sn particle and the subsequent nucleation of a $Ge_{1-x}Sn_x$ crystal (similar to a nucleus observed in Figure S5c formed at 180 °C). In addition, increased growth temperatures reduce the probability of an α-Sn phase formation. This indicates already that the exclusive nucleation/formation of the $Ge_{1-x}Sn_x$ segment with highest Sn content relies on a specific Ge supersaturation and the probability of an α-Sn phase forming at the given experimental conditions.

Further reaction at the growth temperature of 140 °C leads to the observation of a typical quasi-hemispherical β-Sn part in $Ge_{1-x}Sn_x$/Sn heterodimers. These structures can be formed by a destabilization through an ongoing supersaturation of a fully developed α-Sn teardrop with formation of an associated $Ge_{1-x}Sn_x$ nucleus and a subsequent collapse of the crystal structure by diffusion processes. Another possibility that should not be neglected would be the nucleation of $Ge_{1-x}Sn_x$ in a possible Sn phase mixture with the α-Sn acting as template. Subsequent growth of the $Ge_{1-x}Sn_x$ segment proceeds through decomposition of more Ge-rich precursor species after the initial nucleus formation and appears to be a quick process according to Figure 1. The growth of the highly crystalline metastable $Ge_{1-x}Sn_x$ with this extremely high Sn content should be facilitated at low temperature because of reduced Sn incorporation at increasing temperatures.[55] The α-Sn phase can act as a template for epitaxial growth of highly Sn-rich $Ge_{1-x}Sn_x$ (mismatch to cubic Ge of ∼ 15% for pure α-Sn) facilitating crystal growth of the thermodynamically unfavorable composition. Indication of a formation of $Ge_{1-x}Sn_x$ without any tensile strain and the most favorable constant composition at a given parameter set are observed ∼100−150 nm from the nucleation seed where a constant composition is observed along the NRs. Figure S5d−f in the Supporting Information illustrates different stages of the NR evolution from the formed heterodimers with two distinct Sn areas present in all the different stages after the $Ge_{1-x}Sn_x$ segregation.

We do not consider the generally accepted solute trapping at step edges during the nanowire growth to be the major driving force for the formation of $Ge_{1-x}Sn_x$ at these low temperatures as suggested for other metastable compositions in NWs.[56,57] A slightly modified process should be at play because the step-edge-based growth typically also suggests that the nanowire growth can proceed with the successive addition of bilayers through a step flow process[58] and oscillating supersaturation during the layer formation.[59] The $Ge_{1-x}Sn_x$ NRs and NWs grown in these microwave processes usually do not show a sharp interface with a specific atomic plane terminating the semiconductor segment at the interface to the metal particle, and thus the model might not be fully applicable.

These suggestions on the growth mechanism are based on the morphologies and phases observed after the cool-down procedure and without information on processes occurring *in situ* during the growth. Thus, the information about the initial

stage before the $Ge_{1-x}Sn_x$/Sn heterodimer formation is not entirely clear and might require more experiments with modified setups allowing either *in situ* monitoring or rapid quenching.

The described growth regime differs from the 230 °C samples, because these 230 °C derived NWs do not show additional secondary growth at the nucleation site nor a remaining Sn particle.[32] Moreover, the different pretreatment leads to a change in the ratio of the precursor species in the mixture.[32] Long-term treatment for the growth at 230 °C does not lead to nucleation in the heating step similar to the here-described scenario for the 140 °C nucleation. The structure formation for the 230 °C growth exclusively takes place at the higher-temperature regime which can be illustrated by different growth stages/lengths of these NWs. The structures are only observed after the high-temperature growth cycle, and thus the formation at lower temperatures in these specific sets of experiments can be excluded.

Observations described above for the growth of $Ge_{0.72}Sn_{0.28}$ at 140 °C do not correlate with the conventional Ge/Sn phase diagram (Figure S6). A traditional binary phase diagram is obtained under thermodynamic equilibrium conditions. Therefore, such diagrams are not suitable to explain a kinetically driven formation of metastable phases, such as $Ge_{1-x}Sn_x$ with high Sn contents, which differ significantly from the equilibrium composition. However, we coin a term for such a descriptive or schematic representation as a "phase map" that includes some kinetic effects/phase compositions. For a phase map as presented and suggested herein, we have to consider phases and compositions formed under a specific parameter set. In this specific case, the formation of $Ge_{1-x}Sn_x$ with a metastable composition as well as the either metastable, or simply not under regular conditions, observable α-Sn phase should be discussed.

According to the phase evolution encountered here for Sn depending on the Ge content, a representation of the Sn-rich side of the phase map should include a peritectoidic reaction (α-Sn ↔ α-Ge + β-Sn; a solid–solid reaction below 180 °C; Figure 4b). However, the formation of this α-Sn phase relies on the incorporation of Ge atoms in the initial β-Sn lattice without segregation or Ge nucleus formation. This incorporation in the solid phase can be supported by the high mobility of surface atoms of low-melting metals such as Sn and has a stabilizing effect on the crystal phase. One can anticipate this peritectoidic α-Sn phase being a thermodynamically stable phase that is simply not being observed in the conventional heating and cooling experiments that are used for conceiving a phase diagram because of the very slow reaction rates of two solid phases being β-Sn and α-Ge. Providing the Ge in atomic form speeds up this process, and we can observe the phase in this study. In addition, energetic considerations suggest that there is only a small energy difference between the two Sn phases at the growth temperature of 140 °C.[60] Higher Ge contents will not be incorporated in α-Sn, and α-Ge will nucleate. More reliable statements on α-Sn being thermodynamically stable or simply being a metastable phase would require more elaborate calculations, which also consider the high energy gain upon α-Ge crystal formation.

The existence of a miscibility gap between the two isostructural α-Sn and α-Ge phases showing no solid solubility over the full range of compositions could be related to early predictions by Hume-Rothery.[61] Stability issues can be related to the size differences of Sn and Ge, which are in this case

~15% representing a threshold value between the existence of solid solutions over a wide composition range and the occurrence of a large miscibility gap associated with low solubility <1% as observed in the Ge/Sn phase diagram.[61] A threshold for maximum Sn composition of the stable $Ge_{1-x}Sn_x$ alloy should be dependent on growth kinetics and growth temperature as schematically illustrated on the Ge-rich side in the phase map in Figure 4c. Our phase map suggests the formation of the α-Sn phase with a miscibility gap toward an α-Ge phase, representing the metastable $Ge_{1-x}Sn_x$ solid solution with compositions associated with growth kinetics and growth temperature. The purple, blue, and dashed lines represent the maximum $Ge_{1-x}Sn_x$ composition obtained for three specific parameter sets. Since growth kinetics are very important during the $Ge_{1-x}Sn_x$ crystal growth, e.g., with a solute-trapping model in the case of nanowire growth, a higher or lower growth rate could result in a material with higher or lower Sn content. At the same time, a temperature-dependent factor has to be considered for the phase map with a known tendency of diminishing Sn incorporation in $Ge_{1-x}Sn_x$ with increasing temperature.[55] The isothermal line at 140 °C in Figure 4c traverses the schematic purple and blue transition lines of maximum Sn content in the $Ge_{1-x}Sn_x$ alloy. These crossing points represent the composition in the $Ge_{0.72}Sn_{0.28}$ NR and $Ge_{0.68}Sn_{0.32}$ NWs for the same set of parameters (pretreatment and temperature profile) but different solvent and ligands of the precursors as described *vide supra*.

Thermal Stability of $Ge_{1-x}Sn_x$ NRs and NWs. For an investigation into the stability of anisotropic $Ge_{1-x}Sn_x$ structures with very high Sn content (17% and 28% as starting compounds), variable high-temperature (HT) XRD experiments in the temperature range 120−500 °C have been performed. To the best of our knowledge there is no report available on the thermal stability of $Ge_{1-x}Sn_x$ material, which is also in contact with a metallic phase.

In a first set of experiments, $Ge_{0.83}Sn_{0.17}$ NWs have been prepared as described before,[33] and a thin film of the NWs has been heated while recording the XRD patterns. The temperature is increased in 10 °C steps and kept at the temperature for 10 min before the measurement is started, which takes 20 min. Therefore, changes over time can have an uncertainty of ~10 °C if the effects are only observed after an initial delay. The β-Sn reflections can be considered as an internal standard until this phase melts at ~230 °C. The shifted Ge reflections due to the enlarged unit cell upon the incorporation of Sn have to be considered for the stability tests since the shift is directly related to the composition by Vegard's law. Figure 5 shows no changes in the position of the reflections up to temperatures of 190 °C. At 200 °C the reflection broadens toward higher angles, and a new composition with lower Sn content is observed (~6% Sn). With a further increase of temperature, a continuous decrease of Sn content is observed, and at 500 °C only 3.5% Sn is left in the structure. The $Ge_{0.83}Sn_{0.17}$ with Sn growth seed attached is stable for at least 6 h at 160 °C without any noticeable changes in the XRD patterns (Figure S7), while at 180 °C the compound shows a noticeable onset of decomposition after 1 h with Sn segregation and a shift in the reflection maxima to the aforementioned ~6% Sn composition (Figure S8).

The $Ge_{0.72}Sn_{0.28}$ NRs with attached Sn growth seeds have been investigated as described before in the temperature range 120−500 °C (Figure 6a). No changes in the XRD patterns are observed up to 150 °C. A shoulder of the Ge (111) reflection evolves toward higher 2θ angles at 160 °C, and the signal

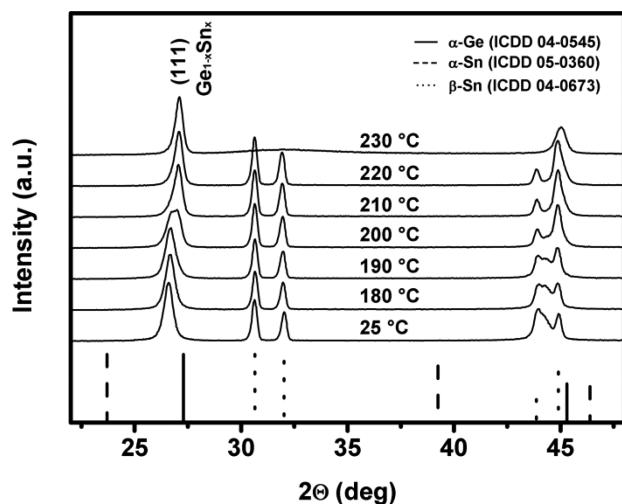**Figure 5.** Variable-temperature XRD showing the phase and evolution of the position of reflections in the temperature range 25−230 °C for $Ge_{0.83}Sn_{0.17}$ NWs with Sn growth seed.

clearly splits at 170 °C into two reflections with a new composition of $Ge_{0.90}Sn_{0.10}$ and the original $Ge_{0.72}Sn_{0.28}$ composition. At temperatures of 180−190 °C a shoulder representing the higher tin concentration is still present with diminishing intensity while only one reflection representing ~6% Sn remains at 210 °C. This composition is very close to the value observed for the $Ge_{0.83}Sn_{0.17}$ NW starting material containing ~6% at the same temperature. An identical value of 3.5% Sn is observed for both starting compounds after temperature treatment at 500 °C for 30 min and prior ramping as described for all variable-temperature experiments. The 3D representation of the significant temperature window is illustrated in Figure 6b and shows in addition to the shift of the $Ge_{1−x}Sn_x$ (111) reflection an increase in the β-Sn content, which can be expected upon thermally induced spinoidal decomposition of crystalline $Ge_{1−x}Sn_x$ in a material $Ge_{1−y}Sn_y$ with lower Sn content ($x > y$) and the segregation of Sn. Since these relevant conversion temperatures are below the melting point of Sn, a solid diffusion can be expected.

The onset of thermal decomposition is represented by the appearance of a shoulder of the Ge (111) reflection toward higher angles starting at temperatures of 160 °C in Figure 6. However, the as-prepared $Ge_{0.72}Sn_{0.28}$ composition decomposes slowly at a static temperature of 140° (Figure 6c, and Figure S9) held for 6 h. The onset of the decomposition requires time, and since the temperature is only held for 30 min at each temperature in the variable-temperature study in Figure 6a, this effect is only observed at higher temperatures. An unchanged composition and thus associated stability of $Ge_{0.72}Sn_{0.28}$ with Sn seeds attached is observed at 120° for 6 h as illustrated in Figure 6c, and Figure S10. The changes in the XRD pattern associated with a material conversion to $Ge_{1−x}Sn_x$ with lower Sn content in the isothermal heating experiments shows an exponential decay of the $Ge_{0.72}Sn_{0.28}$ starting compound after an initial incubation period. An example of this behavior is shown in Figure S11 for a 6 h heating cycle of as-grown $Ge_{0.72}Sn_{0.28}$ NRs at 150 °C.

We assign the peak splitting to the destabilization of the $Ge_{0.72}Sn_{0.28}$ and related gain of lattice energy by the formation of a more thermodynamically favorable composition, which requires additional energy for the conversion by diffusing
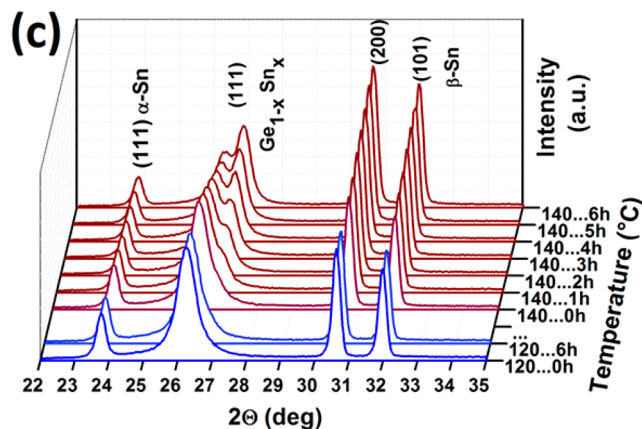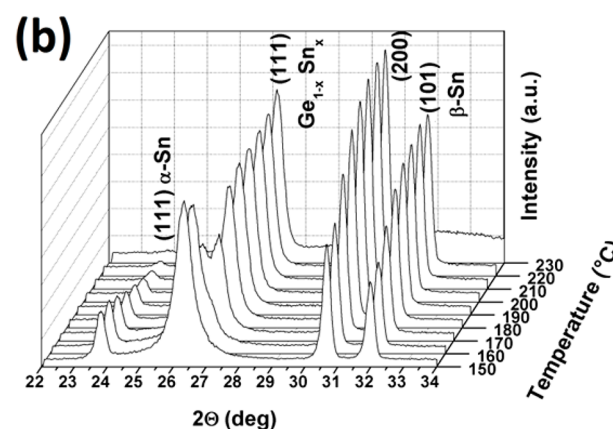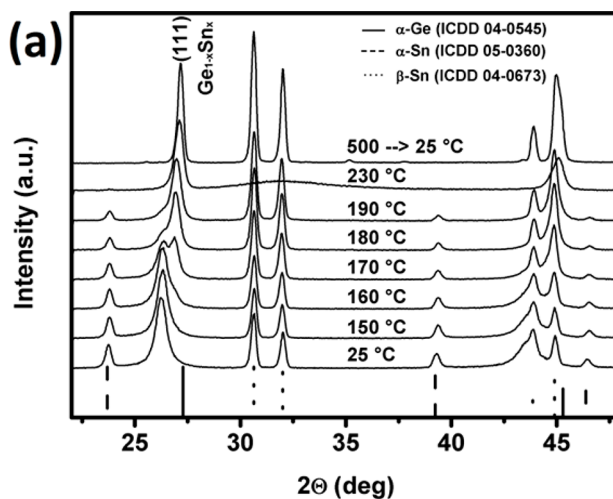

Figure 6. (a) Variable-temperature XRD showing the phase evolution in the temperature range 25−230 °C and the XRD pattern for the 500 °C treated sample cooled down to 25 °C starting with $Ge_{0.72}Sn_{0.28}$ NRs containing the Sn growth seeds. (b) 3D representation of the most interesting region for the phase evolution. (c) XRD patterns showing the static temperature treatment at 120 °C (blue) and 140 °C (brown) for $Ge_{0.72}Sn_{0.28}$ NRs as starting compound.

species. Hence the decomposition and rearrangement of the Ge lattice should occur at lower temperatures in the $Ge_{0.72}Sn_{0.28}$ sample because approximately every fourth atom in the cubic lattice is a Sn atom. After the splitting of the signal and temperatures above 160 °C the subsequent segregation of Sn is

9808

a gradual effect. Theory predicts that the number of defects with Sn in octahedral configuration increases with growth temperature, and therefore the alloy should be less stable because of Sn in 6-fold coordination, thus contributing to Sn segregation.[62] However, extended X-ray absorption fine structure investigations on $Ge_{1-x}Sn_x$ with x_{max} = 13% illustrate that Sn preferentially resides on substitutional sites, and no indices of this 6-fold coordination are observed.[49] In addition, the low synthesis temperature and the well-matched values for XRD and EDX results presented here should account for mainly substitutional incorporation of Sn in the cubic lattice also for the high Sn content. Future studies will be focused on evaluating the nature of Sn coordination in the $Ge_{1-x}Sn_x$ NRs and NWs. It should be noted that the α-Sn phase prevails up to 220 °C, and the reflections merely show a decrease of intensity above 180 °C before finally melting at 230 °C. The total α-Sn content is a combination of α-Sn teardrop particles as well as the small particle in the NRs at the nucleation site. High temperature stability of the α-Sn phase is also observed for epitaxial layers[63] (up to 130 °C) and for α-Sn confined in nanotubes with melting temperatures up to 700 °C,[64] which is ~470 °C above the melting temperature of β-Sn.

The segregation of Sn from the $Ge_{1-x}Sn_x$ NRs and NWs upon temperature treatment should result in morphological changes. All samples heated to high temperatures of 500 °C clearly show the formation of additional Sn particles on individual structures or a network connected by liquefied drops on locations of initially high density of NRs or NWs (Figures S12a,b and S13a,b). Even more interesting is the fate of segregated Sn related to obvious changes in the $Ge_{1-x}Sn_x$ composition below the melting temperature of Sn at 232 °C. According to the XRD data, the volume fraction of β-Sn increases, and therefore we conclude that new evolving particles should be β-Sn. Changes cannot be explained by the bulk investigations, and therefore *in situ* experiments have been performed to image a potential diffusion process.

In situ imaging in the TEM during heating cycles up to nominal 220 °C with a temperature-controllable grid holder have been carried out. Videos show several processes during the heat treatment with clear similarities between processes observed in two $Ge_{0.72}Sn_{0.28}$ NRs. Video S1 is also used in Figure 7, while another NR is imaged in Video S2 and Video S3 in the Supporting Information. In a first step during heat treatment, the hemispherical Sn seed grows slightly, and the initial interface between the terminating Sn particle and the initial $Ge_{0.72}Sn_{28}$ segment changes on the left in Figure 7b. A mass diffusion can be observed by migrating species with a different diffraction contrast toward the initial nucleation side (Figure 7c). As soon as this diffusing species reaches the initial nucleation site with the α-Sn nucleus, a sudden but permanent change in diffraction contrast takes place. However, the bulk/subsurface diffusion continues, and further locations with varying diffraction contrast appear along the NR with some mobility. During the diffusion, the Sn volume and thus the diffusing mass with different diffraction contrast increases because of a collection of Sn from the phase segregation (Figure 7e,f). The diffusion appears to be within the structural boundaries, and the general shape before and after the temperature treatment remains the same. In addition, the conversion of $Ge_{1-x}Sn_x$ to material with lower Sn content could be related to an epitaxial growth of $Ge_{1-y}Sn_y$ ($y < x$) by redeposition from the migrating β-Sn segment (with increasing volume fraction observed in the XRD studies *vide supra*).
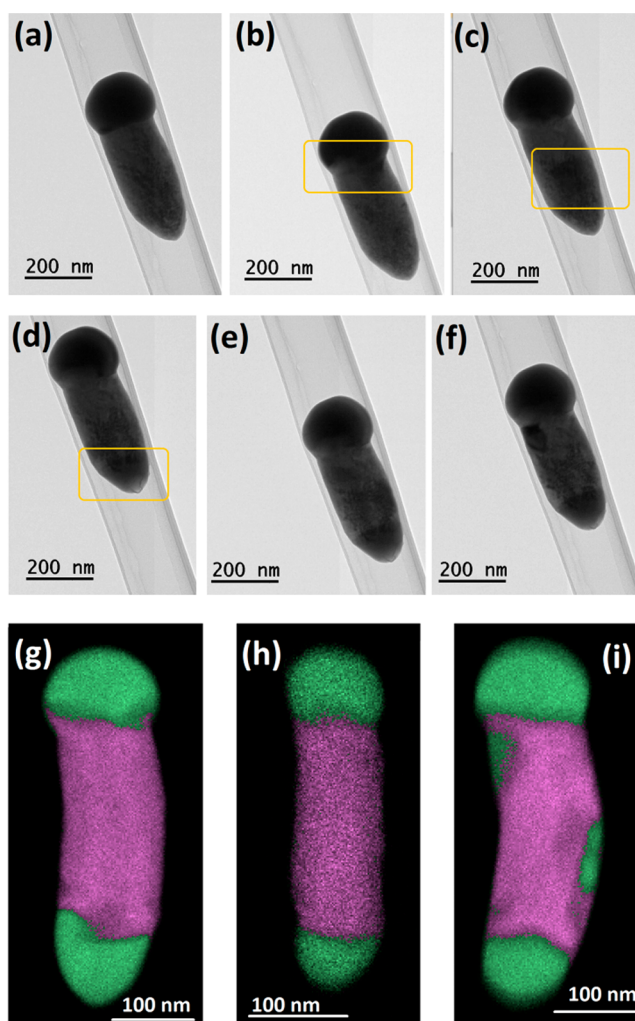

Figure 7. (a–f) TEM images obtained under temperature treatment using $Ge_{0.72}Sn_{0.28}$ NRs showing different steps in the phase segregation process which is imaged at a nominal temperature of 200 °C of the holder and TEM grid. STEM-EDX images after temperature treatment for 10 min at 220 °C (g, h) in the TEM and (i) for a sample heated to 180 °C in squalane for ~20 min.

Moreover, the onset of the diffusion process seems to originate exclusively at the bigger Sn particle, which points toward the importance of the initial $Sn/Ge_{1-x}Sn_x$ interface for this low-temperature structural/compositional conversion process being initiated.

It is noteworthy that all these processes take place below the melting point of Sn (232 °C). $Ge_{0.72}Sn_{28}$ NRs treated in the TEM at 220 °C for ~10 min and prior diffusion at 200 °C show preferential Sn enrichment at the two extremes (Figure 7 g,h), while treatment for 20 min at 180 °C in squalane shows more large patches of Sn-enriched regions between the extremes (Figure 7i). The NRs do not show distinct morphological changes in the SEM images before and after the temperature treatment (Figure S11c,d). TEM images of these NRs also show predominantly two darker segments at the extremes due to a different diffraction contrast, which have not been observed in the as-grown samples. More examples for the formation of phase-separated Sn patches are shown in Figure S11e–g, but fewer of the obvious Sn regions between the two extremes are observed in STEM-EDX images when the samples have been treated at higher temperatures. The reason for shape

retention could be either the surface termination with amino functionalities, a slight surface oxidation layer, or simply and most likely the bulk conversion/diffusion at these temperatures below the melting point of the elements involved. STEM-EDX images help to identify the segment composition. The $Ge_{1-x}Sn_x$ segment is not as defined anymore, suggesting also Ge diffusion and rearrangement processes (Figure 7g−i). The aforementioned mass transport is most likely initiated by a solution/redeposition process involving the diffusing β-Sn precipitate. The redeposited material contains less Sn in the Ge host structure; therefore, the process is driving toward the thermodynamically favored Ge-rich lattice, and a gain in lattice energy during the process can be expected. The redeposition/recrystallization of $Ge_{1-y}Sn_y$ ($x > y$) is made evident and most obvious by comparing the Ge mapping after the temperature treatment with the initial distribution (Figure S12e−h). A striking difference is visible at the initial nucleation site, where no Ge can be found after this process, and at the sites of the Sn patches along a NR where the Ge is completely replaced by Sn.

Differences in thermal stability of these structures when compared to other studies on $Ge_{1-x}Sn_x$ should be mentioned. The most important difference is the presence of the Sn metal, which can dissolve and recrystallize $Ge_{1-x}Sn_x$ while a metal first has to be formed when pure $Ge_{1-x}Sn_x$ decomposes and Sn segregates. This process of spinoidal decomposition requires a partial breakdown of the crystalline structure, and thus more thermal energy has to be provided to overcome the lattice energy. Thus, a removal of the Sn seed material from the NRs and NWs by exposure to 5% hydrochloric acid for 5 min should lead to increased thermal stability. Figure S13 compares variable-temperature XRD results of $Ge_{0.72}Sn_{0.28}$ NRs with and without the Sn seeds demonstrating the expected increased thermal stability with temperatures up to ~220 °C without decomposition, which is ~70 °C above the onset of a material conversion in the presence of Sn. A similar measurement using $Ge_{0.83}Sn_{0.17}$ NWs illustrates the same effect and stability up to 250 °C (versus ~190 °C with Sn seeds in Figure 5, and for comparison without Sn in Figure S14). Temperature stability for an extended time is usually observed ~30 °C below these values as shown *vide supra*. In addition, the results presented here can nicely explain the low-temperature crystallization of amorphous $Ge_{1-x}Sn_x$ layers from a laser-annealed region forming highly crystalline $Ge_{1-x}Sn_x$ material.[65] This process resembles metal-induced crystallization of Ge occurring at higher temperatures,[66] but leads to a metastable material composition.

Bulk Ge exhibits a fundamental indirect bandgap of 0.67 eV and a direct gap at 0.80 eV. Incorporation of Sn in the Ge crystal reduces both energy gaps, but the direct one to a larger degree than the indirect. Therefore, a direct semiconductor material is expected for the high Sn contents described herein. For a demonstration of the optical bandgap of the not thermally degraded $Ge_{1-x}Sn_x$ material, Figure 8 shows the direct bandgap of $Ge_{0.72}Sn_{0.28}$ NRs and $Ge_{0.83}Sn_{0.17}$ NWs described herein. From IR absorption experiments, a Tauc plot was prepared to determine the bandgap energy. A Tauc plot is a common way to determine the optical bandgap of semiconductors.

A determination of the bandgap in the material is achieved by plotting $(\alpha h\nu)^n$ versus $h\nu$ and relating the factor n to an indirect ($n = 1/2$) or direct ($n = 2$) bandgap and the absorption coefficient (α).[67,68] Approximate bandgaps of 0.29 eV for $Ge_{0.72}Sn_{0.28}$ NRs and 0.40 eV for $Ge_{0.83}Sn_{0.17}$ NWs were
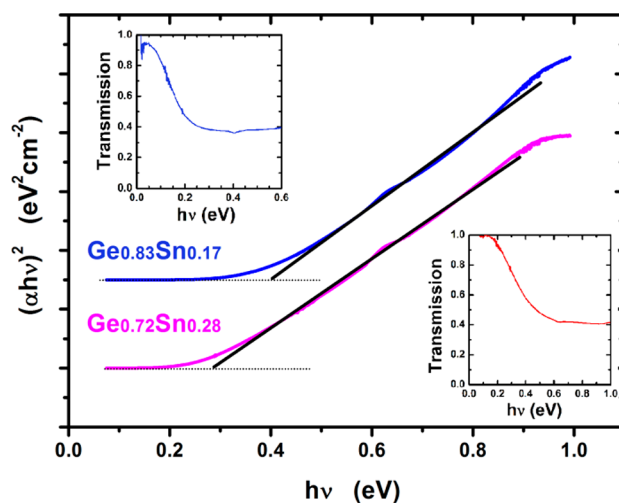

Figure 8. Tauc plot from IR absorption (insets) used to determine the direct bandgap energy of the NRs and NWs.

determined by extrapolating a tangential line from the linear portion of the Tauc plot to the abscissa. The direct bandgaps observed in these NRs and NWs are far below the usual bandgaps of Ge, which is expected for a successful incorporation of Sn in $Ge_{1-x}Sn_x$ above ~9% for a relaxed material and could be an indication that these NRs and NWs are indeed direct bandgap materials.[34] More detailed physical characterization of the presented materials is out of the scope of this paper.

CONCLUSIONS

A low-temperature growth at 140 °C for the formation of $Ge_{1-x}Sn_x$ NRs with a very high Sn content of 28% has been established. The typical low-temperature α-Sn phase has been observed during the formation of the NRs, and all the anisotropic structures remained a Sn-rich region at the nucleation site, which cannot be observed at nucleation at higher temperatures. Therefore, we propose a growth mechanism for this particular set of parameters that is based on a Ge-stabilized α-Sn intermediate. Moreover, the thermal stability of two sets of NRs and NWs with different Sn content has been investigated via XRD, and the data reveal decomposition at a low temperature that has to be considered for the determination of their physical properties as well as the potential device operation. In addition, the low-temperature decomposition of $Ge_{1-x}Sn_x$ appears to be related to a solid diffusion of Sn as observed as mobile sections with different diffraction contrast during *in situ* TEM annealing experiments. The segregated Sn accumulates at low temperatures at the extremes of NRs and also as patches in between. The continuous release of Sn accompanied by the formation of crystalline $Ge_{1-x}Sn_x$ with lower Sn content and also spacial distribution of the elements suggest dissolution and recrystallization events facilitated by diffusing Sn. Removal of the metallic Sn from the $Ge_{1-x}Sn_x$ results in enhanced stability toward thermal decomposition by ~70 °C for $Ge_{0.72}Sn_{0.28}$ NRs and ~60 °C for $Ge_{0.83}Sn_{0.17}$ NWs. Finally, a direct bandgap in the starting materials with such high Sn contents has been demonstrated via absorption experiments and the use of graphical illustration in Tauc plots.

ASSOCIATED CONTENT

S Supporting Information

The Supporting Information is available free of charge on the ACS Publications website at DOI: 10.1021/acs.chemmater.7b03969.

Additional SEM, TEM, EDX, and XRD data (PDF)

Video S1: TEM images obtained under temperature treatment using $Ge_{0.72}Sn_{0.28}$ NRs showing different steps in the phase segregation process (AVI)

Video S2: Additional NR imaging (AVI)

Video S3: Additional NR imaging (AVI)

AUTHOR INFORMATION

Corresponding Author

*E-mail: sven.barth@tuwien.ac.at. Fax: +43 158801 165 99. Phone: +43 158801 165 207.

ORCID

Michael S. Seifner: 0000-0001-9101-5520

Sven Barth: 0000-0003-3900-2487

REFERENCES

(1) Barth, S.; Hernandez-Ramirez, F.; Holmes, J. D.; Romano-Rodriguez, A. Synthesis and applications of one-dimensional semiconductors. *Prog. Mater. Sci.* **2010**, *55*, 563.

(2) Nam, D.; Sukhdeo, D.; Cheng, S.-L.; Roy, A.; Chih-Yao Huang, K.; Brongersma, M.; Nishi, Y.; Saraswat, K. Electroluminescence from strained germanium membranes and implications for an efficient Si-compatible laser. *Appl. Phys. Lett.* **2012**, *100*, 131112.

(3) Jain, J. R.; Hryciw, A.; Baer, T. M.; Miller, D. A. B.; Brongersma, M. L.; Howe, R. T. A micromachining-based technology for enhancing germanium light emission via tensile strain. *Nat. Photonics* **2012**, *6*, 398.

(4) Suess, M. J.; Geiger, R.; Minamisawa, R. A.; Schiefler, G.; Frigerio, J.; Chrastina, D.; Isella, G.; Spolenak, R.; Faist, J.; Sigg, H. Analysis of enhanced light emission from highly strained germanium microbridges. *Nat. Photonics* **2013**, *7*, 466.

(5) Wirths, S.; Geiger, R.; Von Den Driesch, N.; Mussler, G.; Stoica, T.; Mantl, S.; Ikonic, Z.; Luysberg, M.; Chiussi, S.; Hartmann, J. M.; Sigg, H.; Faist, J.; Buca, D.; Grützmacher, D. Lasing in direct-bandgap GeSn alloy grown on Si. *Nat. Photonics* **2015**, *9*, 88.

(6) Ghetmiri, S. A.; Du, W.; Margetis, J.; Mosleh, A.; Cousar, L.; Conley, B. R.; Domulevicz, L.; Nazzal, A.; Sun, G.; Soref, R. A.; Tolle, J.; Li, B.; Naseem, H. A.; Yu, S.-Q. Direct-bandgap GeSn grown on silicon with 2230 nm photoluminescence. *Appl. Phys. Lett.* **2014**, *105*, 151109.

(7) Lu Low, K.; Yang, Y.; Han, G.; Fan, W.; Yeo, Y.-C. Electronic band structure and effective mass parameters of Ge1-xSnx alloys. *J. Appl. Phys.* **2012**, *112*, 103715.

(8) Gupta, S.; Chen, R.; Magyari-Kope, B.; Lin, H.; Yang, B.; Nainani, A.; Nishi, Y.; Harris, J. S.; Saraswat, K. C. GeSn technology: Extending the Ge electronics roadmap. In *Technical Digest—International Electron Devices Meeting*; IEDM, 2011.

(9) Stange, D.; Wirths, S.; Geiger, R.; Schulte-Braucks, C.; Marzban, B.; Von Den Driesch, N.; Mussler, G.; Zabel, T.; Stoica, T.; Hartmann, J.-M.; Mantl, S.; Ikonic, Z.; Grützmacher, D.; Sigg, H.; Witzens, J.; Buca, D. Optically Pumped GeSn Microdisk Lasers on Si. *ACS Photonics* **2016**, *3*, 1279.

(10) Al-Kabi, S.; Ghetmiri, S. A.; Margetis, J.; Pham, T.; Zhou, Y.; Dou, W.; Collier, B.; Quinde, R.; Du, W.; Mosleh, A.; Liu, J.; Sun, G.; Soref, R. A.; Tolle, J.; Li, B.; Mortazavi, M.; Naseem, H. A.; Yu, S.-Q. An optically pumped 2.5 μm GeSn laser on Si operating at 110 K. *Appl. Phys. Lett.* **2016**, *109*, 171105.

(11) Buca, D.; Von Den Driesch, N.; Stange, D.; Wirths, S.; Geiger, R.; Braucks, C. S.; Mantl, S.; Hartmann, J. M.; Ikonic, Z.; Witzens, J.; Sigg, H.; Grutzmacher, D. GeSn lasers for CMOS integration. In *Technical Digest—International Electron Devices Meeting*; IEDM, 2017.

(12) Conley, B. R.; Margetis, J.; Du, W.; Tran, H.; Mosleh, A.; Ghetmiri, S. A.; Tolle, J.; Sun, G.; Soref, R.; Li, B.; Naseem, H. A.; Yu, S.-Q. Si based GeSn photoconductors with a 1.63 A/W peak responsivity and a 2.4 μm long-wavelength cutoff. *Appl. Phys. Lett.* **2014**, *105*, 221117.

(13) Pham, T. N.; Du, W.; Conley, B. R.; Margetis, J.; Sun, G.; Soref, R. A.; Tolle, J.; Li, B.; Yu, S. Q. Si-based Ge0.9Sn0.1 photodetector with peak responsivity of 2.85 A/W and longwave cutoff at 2.4 μm. *Electron. Lett.* **2015**, *51*, 854.

(14) Tseng, H. H.; Wu, K. Y.; Li, H.; Mashanov, V.; Cheng, H. H.; Sun, G.; Soref, R. A. Mid-infrared electroluminescence from a Ge/Ge0.922Sn0.078/Ge double heterostructure p-i-n diode on a Si substrate. *Appl. Phys. Lett.* **2013**, *102*, 182106.

(15) Gupta, J. P.; Bhargava, N.; Kim, S.; Adam, T.; Kolodzey, J. Infrared electroluminescence from GeSn heterojunction diodes grown by molecular beam epitaxy. *Appl. Phys. Lett.* **2013**, *102*, 251117.

(16) Chang, C.; Chang, T.-W.; Li, H.; Cheng, H. H.; Soref, R.; Sun, G.; Hendrickson, J. R. Room-temperature 2-μm GeSn P-I-N homojunction light-emitting diode for inplane coupling to group-IV waveguides. *Appl. Phys. Lett.* **2017**, *111*, 141105.

(17) Schulze, J.; Blech, A.; Datta, A.; Fischer, I. A.; Hähnel, D.; Naasz, S.; Rolseth, E.; Tropper, E.-M. Vertical Ge and GeSn heterojunction gate-all-around tunneling field effect transistors. *Solid-State Electron.* **2015**, *110*, 59.

(18) Kouvetakis, J.; Menendez, J.; Chizmeshya, A. V. G. Tin-based group IV semiconductors: New Platforms for Opto- and Microelectronics on Silicon. *Annu. Rev. Mater. Res.* **2006**, *36*, 497.

(19) Sau, J. D.; Cohen, M. L. Possibility of increased mobility in Ge-Sn alloy system. *Phys. Rev. B: Condens. Matter Mater. Phys.* **2007**, *75*, 045208.

(20) Liu, L.; Liang, R.; Wang, J.; Xu, J. Investigation on the effective mass of Ge 1− x Sn x alloys and the transferred-electron effect. *Appl. Phys. Express* **2015**, *8*, 031301.

(21) Wang, S.; Zheng, J.; Xue, C.; Li, C.; Zuo, Y.; Cheng, B.; Wang, Q. Device simulation of GeSn/GeSiSn pocket n-type tunnel field-effect transistor for analog and RF applications. *Superlattices Microstruct.* **2017**, *111*, 286.

(22) Olesinski, R. W.; Abbaschian, G. J. The Ge−Sn (Germanium−Tin) system. *Bull. Alloy Phase Diagrams* **1984**, *5*, 265.

(23) Sukhdeo, D. S.; Hai, L.; Donguk, N.; Ze, Y.; Vulovic, B. M.; Gupta, S.; Harris, J. S.; Dutt, B.; Saraswat, K. C. Approaches for a viable Germanium laser: Tensile strain, GeSn alloys, and n-type doping. In *Optical Interconnects Conference*; IEEE, 2013.

(24) Cho, Y. J.; Kim, C. H.; Im, H. S.; Myung, Y.; Kim, H. S.; Back, S. H.; Lim, Y. R.; Jung, C. S.; Jang, D. M.; Park, J.; Lim, S. H.; Cha, E. H.; Bae, K. Y.; Song, M. S.; Cho, W. I. Germanium-tin alloy nanocrystals for high-performance lithium ion batteries. *Phys. Chem. Chem. Phys.* **2013**, *15*, 11691.

(25) Esteves, R. J. A.; Ho, M. Q.; Arachchige, I. U. Nanocrystalline Group IV Alloy Semiconductors: Synthesis and Characterization of Ge1−xSnx Quantum Dots for Tunable Bandgaps. *Chem. Mater.* **2015**, *27*, 1559.

(26) Alan Esteves, R. J.; Hafiz, S.; Demchenko, D. O.; Ozgur, U.; Arachchige, I. U. Ultra-small Ge1-xSnx quantum dots with visible photoluminescence. *Chem. Commun.* **2016**, *52*, 11665.

(27) Ramasamy, K.; Kotula, P. G.; Fidler, A. F.; Brumbach, M. T.; Pietryga, J. M.; Ivanov, S. A. SnxGe1−x Alloy Nanocrystals: A First Step toward Solution-Processed Group IV Photovoltaics. *Chem. Mater.* **2015**, *27*, 4640.

(28) Křenek, T.; Bezdička, P.; Murafa, N.; Šubrt, J.; Pola, J. Laser CVD of Nanodisperse Ge−Sn Alloys Obtained by Dielectric Breakdown of SnH4/GeH4Mixtures. *Eur. J. Inorg. Chem.* **2009**, *2009*, 1464.

(29) Assali, S.; Dijkstra, A.; Li, A.; Koelling, S.; Verheijen, M. A.; Gagliano, L.; Von Den Driesch, N.; Buca, D.; Koenraad, P. M.; Haverkort, J. E. M.; Bakkers, E. P. a. M. Growth and Optical Properties of Direct Band Gap Ge/Ge0.87Sn0.13 Core/Shell Nanowire Arrays. *Nano Lett.* **2017**, *17*, 1538.

(30) Biswas, S.; Doherty, J.; Saladukha, D.; Ramasse, Q.; Majumdar, D.; Upmanyu, M.; Singha, A.; Ochalski, T.; Morris, M. A.; Holmes, J. D. Non-equilibrium induction of tin in germanium: towards direct bandgap Ge1−xSnx nanowires. *Nat. Commun.* **2016**, *7*, 11405.

(31) Biswas, S.; Barth, S.; Holmes, J. D. Inducing imperfections in germanium nanowires. *Nano Res.* **2017**, *10*, 1510.

(32) Seifner, M. S.; Biegger, F.; Lugstein, A.; Bernardi, J.; Barth, S. Microwave-Assisted Ge1−xSnx Nanowire Synthesis: Precursor Species and Growth Regimes. *Chem. Mater.* **2015**, *27*, 6125.

(33) Barth, S.; Seifner, M. S.; Bernardi, J. Microwave-assisted solution-liquid-solid growth of Ge1-xSnx nanowires with high tin content. *Chem. Commun.* **2015**, *51*, 12282.

(34) Lan, H. S.; Chang, S. T.; Liu, C. W. Semiconductor, topological semimetal, indirect semimetal, and topological Dirac semimetal phases of Ge1-xSnx alloys. *Phys. Rev. B: Condens. Matter Mater. Phys.* **2017**, *95*, 201201.

(35) Oehme, M.; Kostecki, K.; Schmid, M.; Oliveira, F.; Kasper, E.; Schulze, J. Epitaxial growth of strained and unstrained GeSn alloys up to 25% Sn. *Thin Solid Films* **2014**, *557*, 169.

(36) Gurdal, O.; Desjardins, P.; Carlsson, J. R. A.; Taylor, N.; Radamson, H. H.; Sundgren, J. E.; Greene, J. E. Low-temperature growth and critical epitaxial thicknesses of fully strained metastable Ge1−xSnx (x≲0.26) alloys on Ge(001)2 × 1. *J. Appl. Phys.* **1998**, *83*, 162.

(37) He, G.; Atwater, H. A. Synthesis of epitaxial SnxGe1−x alloy films by ion-assisted molecular beam epitaxy. *Appl. Phys. Lett.* **1996**, *68*, 664.

(38) Zaima, S.; Nakatsuka, O.; Taoka, N.; Kurosawa, M.; Takeuchi, W.; Sakashita, M. Growth and applications of GeSn-related group-IV semiconductor materials. *Sci. Technol. Adv. Mater.* **2015**, *16*, 043502.

(39) Taoka, N.; Capellini, G.; Schlykow, V.; Montanari, M.; Zaumseil, P.; Nakatsuka, O.; Zaima, S.; Schroeder, T. Electrical and optical properties improvement of GeSn layers formed at high temperature under well-controlled Sn migration. *Mater. Sci. Semicond. Process.* **2017**, *57*, 48.

(40) Grzybowski, G.; Beeler, R. T.; Jiang, L.; Smith, D. J.; Kouvetakis, J.; Menéndez, J. Next generation of Ge1−ySny (y = 0.01−0.09) alloys grown on Si(100) via Ge3H8 and SnD4: Reaction kinetics and tunable emission. *Appl. Phys. Lett.* **2012**, *101*, 072105.

(41) Roskamp, C. A.; Roskamp, E. J. Germanium Dichloride−Dioxane Complex. In *Encyclopedia of Reagents for Organic Synthesis*; John Wiley & Sons, Ltd.: 2001.

(42) Lappert, M. F.; Power, P. P. Di- and Trivalent Trimethylsilyl-Substituted Tin Amides and Related Compounds Such as Sn[N-(SiMe3)2]2. In *Organotin Compounds: New Chemistry and Applications*, Vol. 157; American Chemical Society, 1976; pp 70−81.

(43) Vnuk, F.; De Monte, A.; Smith, R. W. The effect of pressure on the semiconductor-to-metal transition temperature in tin and in dilute Sn−Ge alloys. *J. Appl. Phys.* **1984**, *55*, 4171.

(44) Hochst, H.; Engelhardt, M. A.; Bowman, R. C., Jr.; Adams, P. M. Characterisation of MBE-grown α-Sn films and α-Sn 1-x Ge x alloys. *Semicond. Sci. Technol.* **1990**, *5*, S240.

(45) Farrow, R. F. C.; Robertson, D. S.; Williams, G. M.; Cullis, A. G.; Jones, G. R.; Young, I. M.; Dennis, P. N. J. The growth of metastable, heteroepitaxial films of α-Sn by metal beam epitaxy. *J. Cryst. Growth* **1981**, *54*, 507.

(46) Im, H. S.; Cho, Y. J.; Lim, Y. R.; Jung, C. S.; Jang, D. M.; Park, J.; Shojaei, F.; Kang, H. S. Phase Evolution of Tin Nanocrystals in Lithium Ion Batteries. *ACS Nano* **2013**, *7*, 11103.

(47) Bauer, M.; Taraci, J.; Tolle, J.; Chizmeshya, A. V. G.; Zollner, S.; Smith, D. J.; Menendez, J.; Hu, C.; Kouvetakis, J. Ge−Sn semiconductors for band-gap and lattice engineering. *Appl. Phys. Lett.* **2002**, *81*, 2992.

(48) Beeler, R.; Roucka, R.; Chizmeshya, A. V. G.; Kouvetakis, J.; Menéndez, J. Nonlinear structure-composition relationships in the Ge1-ySny/Si(100) (y < 0.15) system. *Phys. Rev. B: Condens. Matter Mater. Phys.* **2011**, *84*, 035204.

(49) Gencarelli, F.; Grandjean, D.; Shimura, Y.; Vincent, B.; Banerjee, D.; Vantomme, A.; Vandervorst, W.; Loo, R.; Heyns, M.; Temst, K. Extended X-ray absorption fine structure investigation of Sn local environment in strained and relaxed epitaxial Ge1−xSnx films. *J. Appl. Phys.* **2015**, *117*, 095702.

(50) Lin, H.; Chen, R.; Huo, Y.; Kamins, T. I.; Harris, J. S. Raman study of strained Ge1−xSnx alloys. *Appl. Phys. Lett.* **2011**, *98*, 261917.

(51) D'costa, V. R.; Tolle, J.; Roucka, R.; Poweleit, C. D.; Kouvetakis, J.; Menéndez, J. Raman scattering in Ge1−ySny alloys. *Solid State Commun.* **2007**, *144*, 240.

(52) Li, S. F.; Bauer, M. R.; Menéndez, J.; Kouvetakis, J. Scaling law for the compositional dependence of Raman frequencies in SnGe and GeSi alloys. *Appl. Phys. Lett.* **2004**, *84*, 867.

(53) Su, S.; Wang, W.; Cheng, B.; Hu, W.; Zhang, G.; Xue, C.; Zuo, Y.; Wang, Q. The contributions of composition and strain to the phonon shift in Ge1−xSnx alloys. *Solid State Commun.* **2011**, *151*, 647.

(54) Sanchez-Soares, A.; Greer, J. C. A Semimetal Nanowire Rectifier: Balancing Quantum Confinement and Surface Electronegativity. *Nano Lett.* **2016**, *16*, 7639.

(55) Von Den Driesch, N.; Stange, D.; Wirths, S.; Mussler, G.; Holländer, B.; Ikonic, Z.; Hartmann, J. M.; Stoica, T.; Mantl, S.; Grützmacher, D.; Buca, D. Direct Bandgap Group IV Epitaxy on Si for Laser Applications. *Chem. Mater.* **2015**, *27*, 4693.

(56) Moutanabbir, O.; Isheim, D.; Blumtritt, H.; Senz, S.; Pippel, E.; Seidman, D. N. Colossal injection of catalyst atoms into silicon nanowires. *Nature* **2013**, *496*, 78.

(57) Moutanabbir, O.; Senz, S.; Scholz, R.; Alexe, M.; Kim, Y.; Pippel, E.; Wang, Y.; Wiethoff, C.; Nabbefeld, T.; Meyer Zu Heringdorf, F.; Horn-Von Hoegen, M. Atomically Smooth p-Doped Silicon Nanowires Catalyzed by Aluminum at Low Temperature. *ACS Nano* **2011**, *5*, 1313.

(58) Wen, C. Y.; Tersoff, J.; Reuter, M. C.; Stach, E. A.; Ross, F. M. Step-Flow Kinetics in Nanowire Growth. *Phys. Rev. Lett.* **2010**, *105*, 195502.

(59) Gamalski, A. D.; Ducati, C.; Hofmann, S. Cyclic Supersaturation and Triple Phase Boundary Dynamics in Germanium Nanowire Growth. *J. Phys. Chem. C* **2011**, *115*, 4413.

(60) Feutelais, Y.; Legendre, B.; Fries, S. G. Thermodynamic evaluation of the system germanium — tin. *CALPHAD: Comput. Coupling Phase Diagrams Thermochem.* **1996**, *20*, 109.

(61) Zhang, Y. M.; Evans, J. R. G.; Yang, S. The prediction of solid solubility of alloys: developments and applications of Hume-Rothery's rules. *J. Cryst. Phys. Chem.* **2010**, *1* (2), 103−109.

(62) Barrio, R. A.; Querales Flores, J. D.; Fuhr, J. D.; Ventura, C. I. Non-substitutional Sn Defects in Ge1−x Sn x Alloys for Opto- and Nanoelectronics. *J. Supercond. Novel Magn.* **2013**, *26*, 2213.

(63) Asom, M. T.; Kortan, A. R.; Kimerling, L. C.; Farrow, R. C. Structure and stability of metastable α-Sn. *Appl. Phys. Lett.* **1989**, *55*, 1439.

(64) Wang, B.; Ouyang, G.; Yang, Y. H.; Yang, G. W. Anomalous thermal stability of cubic tin confined in a nanotube. *Appl. Phys. Lett.* **2007**, *90*, 121905.

(65) Matsumura, R.; Chikita, H.; Kai, Y.; Sadoh, T.; Ikenoue, H.; Miyao, M. Low-temperature (∼180 °C) position-controlled lateral solid-phase crystallization of GeSn with laser-anneal seeding. *Appl. Phys. Lett.* **2015**, *107*, 262106.

(66) Park, J.-H.; Tada, M.; Kapur, P.; Peng, H.; Saraswat, K. C. Self-nucleation free and dimension dependent metal-induced lateral

crystallization of amorphous germanium for single crystalline germanium growth on insulating substrate. *J. Appl. Phys.* **2008**, *104*, 064501.

(67) Tauc, J. Optical properties and electronic structure of amorphous Ge and Si. *Mater. Res. Bull.* **1968**, *3*, 37.

(68) Tauc, J.; Grigorovici, R.; Vancu, A. Optical Properties and Electronic Structure of Amorphous Germanium. *Phys. Status Solidi B* **1966**, *15*, 627.

Check for updates

Electrical characterization and examination of temperature-induced degradation of metastable Ge$_{0.81}$Sn$_{0.19}$ nanowires†

M. Sistani, [ID] ‡[a] M. S. Seifner, [ID] ‡[b] M. G. Bartmann,[a] J. Smoliner,[a] A. Lugstein [ID] [a] and S. Barth [ID] *[b]

Metastable germanium–tin alloys are promising materials for optoelectronics and optics. Here we present the first electrical characterization of highly crystalline Ge$_{0.81}$Sn$_{0.19}$ nanowires grown in a solution-based process. The investigated Ge$_{0.81}$Sn$_{0.19}$ nanowires reveal ohmic behavior with resistivity of the nanowire material in the range of ~1 × 10^{-4} Ω m. The temperature-dependent resistivity measurements demonstrate the semiconducting behavior. Moreover, failure of devices upon heating to moderate temperatures initiating material degradation has been investigated to illustrate that characterization and device operation of these highly metastable materials have to be carefully conducted.

Introduction

Group IV semiconductor nanowires (NWs) are promising building blocks for various fields of application including electronic and sensing devices,[1,2] solar cells,[3,4] lithium ion batteries,[5,6] *etc*. Their electronic properties can be altered by incorporation of well-known dopants in the semiconductor host lattice,[7–9] while recently extraordinary high amounts of these known dopants as well as non-common metal incorporation in nanoscaled group IV elements is described.[10–13] To date, the performance of Si- and Ge-based materials in optics and photonics is limited by the dominating, intrinsic indirect bandgap of their thermodynamically most stable allotropes with diamond cubic crystal structures.

A direct bandgap material based on Ge can be obtained by physical strain engineering in the semiconductor[14–16] or an effective alloying with high Sn concentrations of ~8–10 at% in Ge$_{1-x}$Sn$_x$,[17,18] which exceeds the thermodynamic solubility limit (~1 at% Sn).[19] Since these Ge$_{1-x}$Sn$_x$ alloys are isostructural with Si and thus compatible with CMOS processing, this material is a very promising candidate for optoelectronics and optical devices operating in the infrared spectral region, such as lasers,[17,20–22] photodetectors,[23,24] light emitting diodes[25–27]

or biological sensors.[28] Moreover, the electronic properties are also altered upon Sn incorporation in the Ge host lattice which should result in an enhanced electron and hole mobility making Ge$_{1-x}$Sn$_x$ interesting for high-speed electronics.[29–33] Besides a large body of data related to the thin film growth on single crystalline substrates and significant recent advancements in this field,[17,22,34–36] the number of reports on one-dimensional nanostructures and nanoparticles with significant Sn incorporation is still very limited.[37] Top-down approaches based on the post-growth etching of epitaxial films to prepare desired morphologies have been applied[38] and a few reports describing suitable bottom-up approaches for a reliable formation of Ge$_{1-x}$Sn$_x$ nanoparticles[39–43] and one-dimensional nanostructures[44–50] are available. Morphological control to obtain shape anisotropic single crystalline materials has been achieved using Ge NWs as templates in order to obtain core–shell Ge/Ge$_{1-x}$Sn$_x$ NWs[45] but also non-templated metal-seed supported growth of Ge$_{1-x}$Sn$_x$ NWs *via* gas-phase[46,47] and solution-based synthesis[44,48,49] has been described in literature. To date, anisotropic Ge$_{1-x}$Sn$_x$ nanostructures usually are in the range of 9–13 at% Sn,[45,46] while our microwave-based synthesis procedures gives access to highly crystalline material with very high Sn content of 17–32 at%.[44,49] In general, literature data related to electronic properties of Ge$_{1-x}$Sn$_x$ materials with higher tin contents (>5 at%) are scarce and the provided mobility, charge carrier density or sheet resistance cannot be used to calculate the respective resistivity values, because either the required data are missing, thin films are strained or the material is p- or n-doped.[51,52] This paper describes for the first time the electronic properties of bottom-up grown Ge$_{1-x}$Sn$_x$ NWs integrated in two-point and

[a]*TU Wien, Institute of Solid State Electronics, Floragasse 7, 1040 Vienna, Austria*
[b]*TU Wien, Institute of Materials Chemistry, Getreidemarkt 9, 1060 Vienna, Austria.*
E-mail: sven.barth@tuwien.ac.at

†Electronic supplementary information (ESI) available: A potential failure mechanism and estimation of diffusion lengths is described. In addition, XRD patterns, EDX maps as well as line scans. See DOI: 10.1039/c8nr05296d
‡These authors contributed equally to this study.

four-point configuration, revealing very high conductivity values while still retaining semiconducting properties. The $Ge_{0.81}Sn_{0.19}$ NWs electronic properties have been investigated in the temperature range of 10–298 K. In addition, the behavior of the devices when exposed to elevated temperatures is investigated emulating potential heating effects during device operation.

Experimental

All synthetic procedures and handling of the chemicals for the nanostructure synthesis have been carried out using Schlenk techniques or an argon-filled glove box (MBraun). Butyl lithium, hexamethyldisilazane, $SnCl_2$, 1,1,3,3-tetramethyl-disilioxane, and $GeCl_4$ were purchased from Sigma-Aldrich. All solvents for the precursor synthesis were dried using standard procedures and stored over molecular sieve. Precursors and intermediates have been prepared as described before.[49] Dodecylamine (98%, Sigma-Aldrich) was distilled three times under reduced pressure using additions of 0.5–1 mL of $Sn(N(Si(CH_3)_3)_2)_2$ as described in literature.[44] This procedure allows separation of impurities that can react with $Sn(N(Si(CH_3)_3)_2)_2$ and $Ge(N(Si(CH_3)_3)_2)_2$ in the following material synthesis and ensures the most reliable results.

Nanostructure synthesis and temperature treatment

$Ge_{0.81}Sn_{0.19}$ NWs were synthesized in 10 mL glass cells (Anton Paar GmbH) at 503 K. In a typical experiment, 3 mL of dodecylamine were transferred in a glass microwave reactor. First, $Sn(N(Si(CH_3)_3)_2)_2$ and subsequently $Ge(N(Si(CH_3)_3)_2)_2$ were added to dodecylamine in a Sn : Ge ratio of 1 : 4. The mixture was then heated to ~373 K and stirred at room temperature for 15–17 h. Further information about the pretreatment procedure of the precursor mixture for the synthesis of $Ge_{1-x}Sn_x$ NWs has been described in literature.[44,49] The vial was sealed with a Teflon-coated cap and transferred to the microwave reactor (Monowave 300; Anton Paar GmbH; frequency, 2.46 GHz) equipped with an IR temperature control unit. The vessel was heated up as quick as possible, held 2–10 min at 503 K and finally was cooled down by a gas stream. The synthesized $Ge_{0.81}Sn_{0.19}$ NWs were collected by adding toluene (3 mL) and subsequent centrifugation. The NW material was redispersed in solvent (2× toluene; 3× ethanol, 3× toluene), centrifuged, separated from the supernatant and finally stored under ambient conditions in toluene.

Heat treatment of the NW samples has been carried out using a home-build CVD oven operated at 523 K under helium atmosphere. Before the samples have been heated up, the chamber has been purged by evacuation to 0.1 mbar and replacing the atmosphere by He 5.0. During the annealing a constant flow of 50 sccm He was channeled through the oven.

Nanostructure characterization

Scanning electron microscope images have been acquired using a FEI Inspect F50. $Ge_{0.81}Sn_{0.19}$ NWs were deposited on lacey carbon copper grids (Plano) by drop casting of a toluene

suspension for transmission electron microscope (TEM) characterization. In this study, a FEI TECNAI F20 operated at 200 kV and equipped with high angle annular dark field (HAADF) STEM and EDX detector was used. The EDX elemental maps and point measurements were recorded and quantified using the AMETEK TEAM package. The TEM images were recorded and treated using Digital Micrograph software.

X-ray diffraction (XRD) patterns were recorded on a PANalytical X-Pert PRO PW 3050/60 in Bragg–Brentano geometry using Cu-Kα radiation, while the analysis of the acquired data was performed using X-pert Highscore software. The preparation included drop casting of the nanowire material onto Si (911) wafers as support.

Electrical characterization

The $Ge_{0.81}Sn_{0.19}$ NWs have been deposited onto a highly p-doped Si substrate with a 100 nm thick, thermally grown SiO_2 layer and predefined macroscopic Ti–Au bonding pads. The devices have been prepared by electron beam lithography on a Raith e-LiNE machine (10 kV, PMMA resist) and individual NWs have been contacted with 7 nm Ti and 190 nm thick Au pads by electron beam evaporation using a Leybold e-beam evaporator. The metal pad evaporation was preceded by a short oxygen plasma treatment (300 W, 90 s; Technics plasma GmbH 100-e plasma system) to remove any organic shell and a subsequent HI dip was used to remove germanium oxide. The excess metal has been removed by standard lift-off techniques. Essentially, contacts to the NWs were prepared using established NW processing techniques.[53,54]

The electrical measurements at room-temperature and ambient conditions were performed using a combination of a semiconductor analyzer (HP 4156B) and a probe station. To minimize the influence of ambient light as well as electromagnetic fields, the probe station was placed in a dark box. The resolution limit of the used setup is 500 fA and leakage currents of ~1 pA, which is negligible for the here investigated highly conducting material. Low-temperature measurements (10–298 K) were performed in vacuum at a background pressure of approximately 2.5×10^{-5} mbar using a ^{4}He cryostat (Cryo Industries CRC-102) and a semiconductor analyzer (Keysight B1500A).

Results and discussion

The $Ge_{1-x}Sn_x$ NWs have been prepared by a microwave-based synthesis procedure described in literature.[44,49] A description of the process is provided in the Experimental section. Fig. 1a shows a scanning electron micrograph (SEM) image of the prepared NWs after treatment with hydrochloric acid to remove metallic growth seeds resulting in a pure, unaltered $Ge_{1-x}Sn_x$ material. The composition has been calculated from the X-ray diffraction (XRD) pattern (inset in Fig. 1a) according to Vegard's law using the isostructural α-Ge and α-Sn references. The obtained shift of the $Ge_{1-x}Sn_x$ reflections can be associated to 18.8 at% Sn. Scanning transmission electron

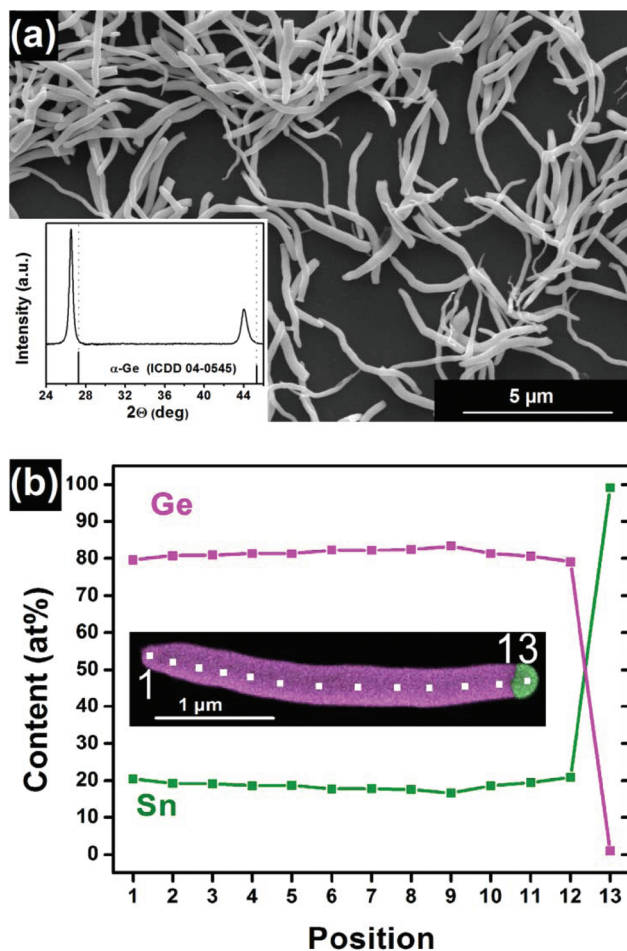**Fig. 1** (a) SEM image of $Ge_{1-x}Sn_x$ NWs and corresponding XRD pattern (inset) after Sn seed removal, showing the shifted signal when compared to the Ge reference. (b) The composition of the $Ge_{1-x}Sn_x$ NW can be also determined by EDX point measurements while the specific locations along the NW are illustrated in the STEM-EDX image. The EDX map also shows the Sn growth seed used to form these nanostructures.

microscopy energy dispersive X-ray spectroscopy (STEM-EDX) maps and line scans are shown in Fig. 1b illustrating a homogeneous distribution of Sn in the Ge matrix with only small fluctuations. Fig. 1b also indicates the metallic Sn growth promoter, which has been removed from all other NWs by HCl treatment for this study. Evaluation of EDX measurement data reveals 18.8 ± 1.2 at% Sn in the $Ge_{1-x}Sn_x$ NWs. Both values from EDX and XRD analysis are in good agreement and consequently, the material will be referred to as $Ge_{0.81}Sn_{0.19}$ NWs.

The electronic properties of the NWs have been investigated in two different geometries on Si substrates with a 100 nm thick, thermally grown SiO_2 layer. The drop casted $Ge_{0.81}Sn_{0.19}$ NWs are contacted by gold pads using standard electron-beam lithography, deposition of metal by evaporation, and lift-off techniques. A specifically small or optimized contact resistance either through formation of interfacial layers based on Ni typically requires thermal annealing (≥ 623 K)[55] or based on Sn electrodes with low Schottky barrier height[56] have been neg-

lected, because the required annealing temperatures or destabilization of the $Ge_{1-x}Sn_x$ material by the metallic contact can lead to undesired material degradation.[44] However, even the $Ge_{0.81}Sn_{0.19}$ NW-based two-terminal devices show ohmic behavior combined with high current levels as can be expected for a semiconductor material with high number and mobility of charge carriers (Fig. 2a). A fluctuation of the resistance values of different devices while diameters in the range of 110–180 nm has been observed with thicker diameters showing typically higher conduction values. The electrical current is two orders of magnitude higher in comparison to intrinsic Ge NW with similar dimension grown by Au mediated CVD as shown in Fig. 2a. In contrast to slightly strained $Ge_{0.86}Sn_{0.14}$ as a high Sn content material,[57] the here presented highly conductive $Ge_{0.81}Sn_{0.19}$ NW devices do not show any gating effect in field effect measurements (between -40 V and 40 V).

In order to investigate the influence of the contacts on the actual NW resistance values, four-terminal devices using indi-
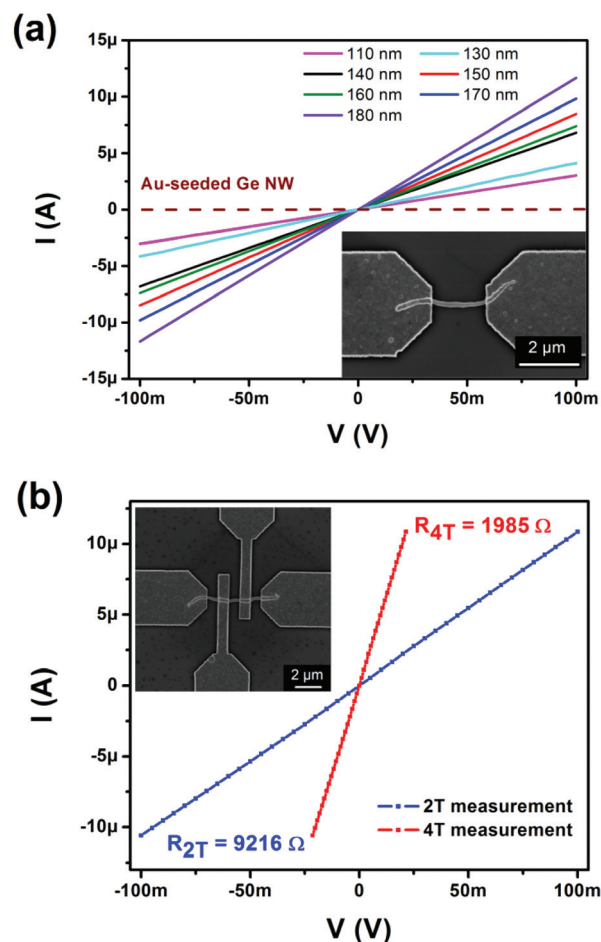

Fig. 2 (a) Two-terminal $I-V$ measurements of $Ge_{0.81}Sn_{0.19}$ NWs with diameters between 110–180 nm and a Au-seeded NW of intrinsic Ge (dashed line) for comparison. (b) Four-terminal devices are used to illustrate the influence of the contact resistance and the corresponding two-terminal measurement using the same NW is illustrated for comparison.

vidual NWs have been prepared. The inset of Fig. 2b shows such a device using a $Ge_{0.81}Sn_{0.19}$ NW of 170 nm thickness. The resistance measured in two-point geometry is about 9.2 kΩ, while the actual resistance of the NW determined in four-probe configuration is only 1.985 kΩ. In general, the devices showed a decrease in resistance to 22–24% of the values determined in two-point configuration. This clearly indicates a high contact resistance between the NW material and the Au contacts, that might be caused by the pretreatment of the NWs with an oxygen plasma to remove any organic groups from the surface, but at the same time oxidizing some of the $Ge_{0.81}Sn_{0.19}$ material at the surface and causing SnO_2 formation that cannot be removed easily in the further process steps.

Fig. 3 illustrates the resistivity-dependence on temperature variation in the range from 298 to 10 K, which was investigated in four-point configuration. At room temperature, resistivity values of $Ge_{0.81}Sn_{0.19}$ NWs ($\sim 1 \times 10^{-4}$ Ω m) are typically 2 orders of magnitude lower than for intrinsic Ge ($\sim 9 \times 10^{-3}$ Ω m),[58] but approximately two orders of magnitude higher than for hyperdoped $Ge_{0.97}Ga_{0.03}$ NWs ($\sim 3 \times 10^{-6}$ Ω m)[11] as shown in Fig. 3. Theoretical predictions consider a significant increase in electron mobility for $Ge_{1-x}Sn_x$ with high tin content when compared to Ge ($\sim$50 times for $x = 0.2$),[59] while the charge carrier concentration increases only slightly according to studies on thin films of Ge and $Ge_{1-x}Sn_x$ with up to 5.8 at% Sn.[60] This corresponds considerably well with the observed difference in resistivity values between intrinsic Ge and our $Ge_{0.81}Sn_{0.19}$ NWs assuming other parameters such as surface scattering would be similar on both types of NWs. Intrinsic Ge NWs grown by Au-seeding show a strong dependence on the temperature and an increase of resistivity by several orders of magnitude upon cooling. In contrast, the $Ge_{0.81}Sn_{0.19}$ NW's resistivity appear to be almost independent on temperature, similar to

hyperdoped $Ge_{0.97}Ga_{0.03}$ NWs[11] as described in literature. A more detailed view reveals an increase in resistivity with decreasing temperatures (inset Fig. 3) typical for a semiconductor while in comparison hyperdoped $Ge_{0.97}Ga_{0.03}$ NWs show quasi-metallic behavior with decreasing resistivity. This change in resistivity and the curve shape is expected for a semiconductor; however, the resistivity increases merely by $\sim$50–60% of the room temperature value when cooled to 10 K.

In general, electronic devices can be exposed to increased temperatures either by *in situ* joule heating or temperature fluctuations of the whole device. Therefore, we studied 18 $Ge_{0.81}Sn_{0.19}$ NWs in two-terminal devices after annealing at 523 K for 15, 30 and 60 min to evaluate their behavior when exposed to temperatures at which segregation processes can be expected (Fig. 4a). Nine of the 18 devices were destroyed after the first heating cycle at 523 K, while only one of these eventually failing devices provides an electronic signal at 15 min annealing with much higher resistivity before the device fails as well at 30 min (α-behavior). The remaining eight devices exclusively show lower resistivity values at room temperature as an indication that the contact resistance was reduced (resistivity in Fig. 4 includes the contact resistance). Four of the surviving devices followed this trajectory and the resistivity decreases further for the whole annealing duration of 60 min (γ-behavior). Another four of the intact devices showed an increased resistivity after annealing for more than 15 min (β-behavior), which can be attributed to the onset of Sn segregation events, while the devices are still intact. An increased resistivity is expected because of the inhomogeneity of the material and lower mobility of $Ge_{1-x}Sn_x$ with lower Sn content.[59] XRD patterns in Fig. 4b of $Ge_{0.81}Sn_{0.19}$ NWs treated for 60 min at 523 K show partial material conversion and segregation processes (enlarged in Fig. S1†). In addition to the observed shoulder of the initial $Ge_{0.81}Sn_{0.19}$ reflections, small β-Sn reflections can be observed. However, this bulk analysis cannot explain the different behavior of devices observed in the electrical characterization.

To illustrate differences in NWs during this heating process, STEM EDX analysis was performed prior and after the heat treatment at 523 K for 60 min. EDX line scans as well as EDX maps before and after the annealing of the same NWs are illustrated in the ESI† showing completely unaltered NWs, segregation onsets and highly modified NWs (Fig. 4c+d and Fig. S2–4†). The EDX line scan in Fig. 4c illustrates a $Ge_{1-x}Sn_x$ NW with pronounced degradation and Sn segregation that could be associated with the device failure (α-behavior), since segregation events are observed in close proximity of the extremes. A partial degradation with the segregation events farther away from the contact material (Fig. 4d) can be responsible for the altered electronic properties resulting in increasing resistivity values (β-behavior). Unaltered $Ge_{0.81}Sn_{0.19}$ NWs after heat treatment are associated with γ-behavior and shown in the ESI (Fig. S2†). EDX maps as well as line scans of as-grown and annealed NWs for all three different cases discussed are illustrated in Fig. S2–S4.†
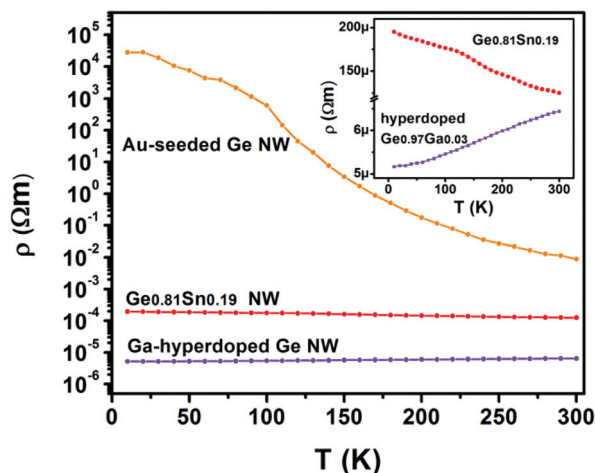

Fig. 3 Evaluation of resistivity changes with temperature in the range 298–10 K for a $Ge_{0.81}Sn_{0.19}$ NW and comparison to other NWs including intrinsic Au-seeded Ge and Ga-hyperdoped Ge.
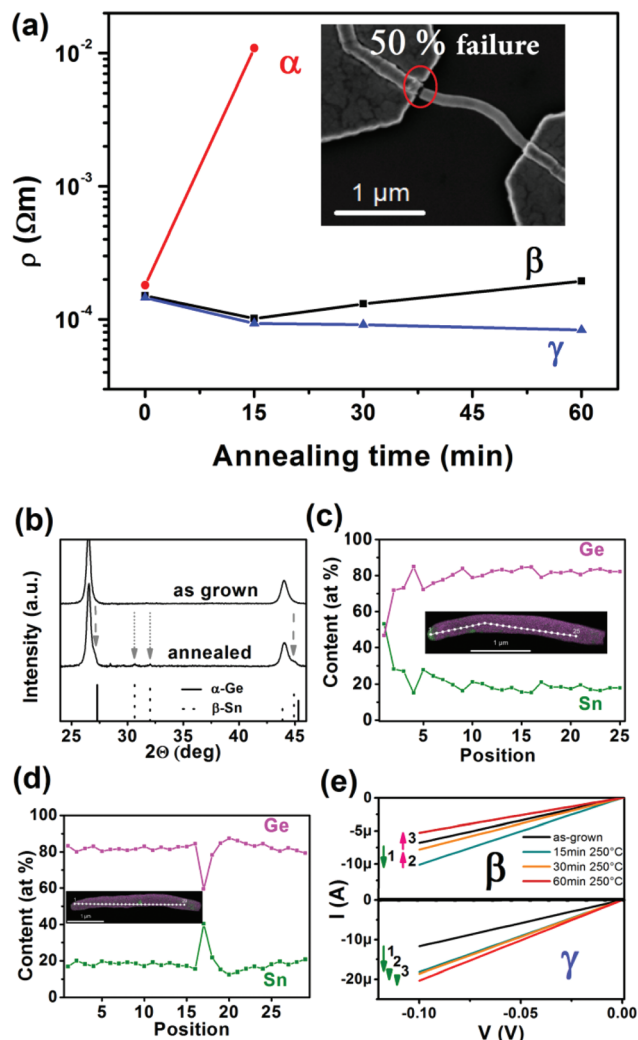
Fig. 4 (a) Electronic behavior of two-terminal $Ge_{0.81}Sn_{0.19}$ NW devices after annealing at 523 K for 15, 30, and 60 min. Three different cases of specific device behavior including device failure (α) with breaking at the electrode-NW contact as shown in the inset, resistivity decrease followed by an increase (β) and a steady decrease in resistivity (γ) can be observed. The data presented are from individual devices and not averaged. (b) The XRD of NW material annealed for 60 min at 523 K show $Ge_{0.81}Sn_{0.19}$ NW degradation and segregation of β-Sn (ICDD 04-0673). (c) An EDX line scan shows a highly degraded $Ge_{1-x}Sn_x$ NW and the corresponding mapping in the inset, which could be associated with α-behavior in (a). A partial segregation is shown in (d) that can be assigned to a β-behavior in (a). The $I–V$ diagrams in (e) illustrate the β- and γ-behavior of devices in another representation as shown in (a).

As mentioned before, the here described $Ge_{0.81}Sn_{0.19}$ NWs represent a highly metastable material and thus elevated temperatures lead to Sn segregation. The threshold temperature depends on the initial composition including potential doping[61] and the here described composition should start to degrade at temperatures of ~523 K.[44] Formation of metallic Sn particles by segregation from $Ge_{0.81}Sn_{0.19}$ NWs is a stochastic process and therefore a difference in device behavior can be expected for the devices. The difference between the completely failing devices and the ones showing only higher resistivity can be related to

diffusion length of the segregated Sn in the $Ge_{0.81}Sn_{0.19}$ crystal and interactions of the metallic Sn and the Au contacts. Therefore the location of the Sn segregation process is also important. For the device failure upon annealing two scenarios, which are most likely both intertwined, have to be considered for the gap formation at the nanostructure-to-contact region (Fig. 4a). The out-diffusion of Sn upon segregation is accompanied with a $Ge_{0.81}Sn_{0.19}$ material conversion to a material with lower Sn content and smaller lattice parameters. This will result in a natural shrinkage of the material and therefore the devices can fail due to mechanical stress indicated by the gap close to the contact in the inset of Fig. 4a. In addition, reaction of the segregated Sn with the Au contact and associated Sn diffusion in the Au contact material can lead to device failure. The probability of this reaction is higher for Sn segregation events in proximity to the Au bond pads leading to failure, while segregation in the middle of a wire does only lead to strain and no structurally weakened NWs. A Au/Sn reaction can cause pronounced formation of pores in diffusion experiments on the Sn side[62] and the diffusion lengths can be in the tens of nanometer as calculated in the ESI.†[63]

Conclusions

We present the first investigation on the electronic properties of $Ge_{1-x}Sn_x$ materials with high Sn content. $Ge_{0.81}Sn_{0.19}$ NWs were prepared by microwave synthesis and investigated in two- and four-point configuration demonstrating high conductivity while the contact resistance dominates the I-V-characteristics in two-terminal devices. All devices investigated revealed ohmic behavior. The resistivity evolution by cooling to 10 K shows semiconductor characteristics with small increase of resistivity. The thermal annealing at moderate temperatures of 523 K results in three sets of device behavior with influences of the material degradation by Sn segregation on the electronic properties and structural device stability.

Conflicts of interest

There are no conflicts to declare.

Acknowledgements

Notes and references

1 S. Barth, F. Hernandez-Ramirez, J. D. Holmes and A. Romano-Rodriguez, *Prog. Mater. Sci.*, 2010, **55**, 563–627.

2 L. Hrachowina, G. Domènech-Gil, A. Pardo, M. S. Seifner, I. Gràcia, C. Cané, A. Romano-Rodríguez and S. Barth, *ACS Sens.*, 2018, **3**, 727–734.

3 J.-H. Yun, Y. C. Park, J. Kim, H.-J. Lee, W. A. Anderson and J. Park, *Nanoscale Res. Lett.*, 2011, **6**, 287.

4 T. J. Kempa, B. Z. Tian, D. R. Kim, J. S. Hu, X. L. Zheng and C. M. Lieber, *Nano Lett.*, 2008, **8**, 3456–3460.

5 T. Kennedy, E. Mullane, H. Geaney, M. Osiak, C. O'Dwyer and K. M. Ryan, *Nano Lett.*, 2014, **14**, 716–723.

6 K. Stokes, H. Geaney, G. Flynn, M. Sheehan, T. Kennedy and K. M. Ryan, *ACS Nano*, 2017, **11**, 10088–10096.

7 S. M. Sze, *Semiconductor Devices: Physics and Technology*, John Wiley & Sons Singapore Pte. Limited, 2012.

8 E. Tutuc, J. O. Chu, J. A. Ott and S. Guha, *Appl. Phys. Lett.*, 2006, **89**, 3.

9 B. Long, G. Alessio Verni, J. O'Connell, M. Shayesteh, A. Gangnaik, Y. M. Georgiev, P. Carolan, D. O'Connell, K. J. Kuhn, S. B. Clendenning, R. Nagle, R. Duffy and J. D. Holmes, *Mater. Sci. Semicond. Process.*, 2017, **62**, 196–200.

10 K. Tabatabaei, H. Lu, B. M. Nolan, X. Cen, C. E. McCold, X. Zhang, R. L. Brutchey, K. van Benthem, J. Hihath and S. M. Kauzlarich, *Chem. Mater.*, 2017, **29**, 7353–7363.

11 M. S. Seifner, M. Sistani, F. Porrati, G. Di Prima, P. Pertl, M. Huth, A. Lugstein and S. Barth, *ACS Nano*, 2018, **12**, 1236–1241.

12 P. Pertl, M. S. Seifner, C. Herzig, A. Limbeck, M. Sistani, A. Lugstein and S. Barth, *Monatsh. Chem.*, 2018, **149**, 1315–1320.

13 O. Moutanabbir, D. Isheim, H. Blumtritt, S. Senz, E. Pippel and D. N. Seidman, *Nature*, 2013, **496**, 78–82.

14 D. Nam, D. Sukhdeo, S.-L. Cheng, A. Roy, K. Chih-Yao Huang, M. Brongersma, Y. Nishi and K. Saraswat, *Appl. Phys. Lett.*, 2012, **100**, 131112.

15 J. R. Jain, A. Hryciw, T. M. Baer, A. B. MillerDavid, M. L. Brongersma and R. T. Howe, *Nat. Photonics*, 2012, **6**, 398–405.

16 M. J. Suess, R. Geiger, R. A. Minamisawa, G. Schiefler, J. Frigerio, D. Chrastina, G. Isella, R. Spolenak, J. Faist and H. Sigg, *Nat. Photonics*, 2013, **7**, 466–472.

17 S. Wirths, R. Geiger, N. von den Driesch, G. Mussler, T. Stoica, S. Mantl, Z. Ikonic, M. Luysberg, S. Chiussi, J. M. Hartmann, H. Sigg, J. Faist, D. Buca and D. Grützmacher, *Nat. Photonics*, 2015, **9**, 88–92.

18 S. A. Ghetmiri, W. Du, J. Margetis, A. Mosleh, L. Cousar, B. R. Conley, L. Domulevicz, A. Nazzal, G. Sun, R. A. Soref, J. Tolle, B. Li, H. A. Naseem and S.-Q. Yu, *Appl. Phys. Lett.*, 2014, **105**, 151109.

19 R. W. Olesinski, N. Kanani and G. J. Abbaschian, *Bull. Alloy Phase Diagrams*, 1985, **6**, 536–539.

20 D. Stange, S. Wirths, R. Geiger, C. Schulte-Braucks, B. Marzban, N. von den Driesch, G. Mussler, T. Zabel, T. Stoica, J.-M. Hartmann, S. Mantl, Z. Ikonic, D. Grützmacher, H. Sigg, J. Witzens and D. Buca, *ACS Photonics*, 2016, **3**, 1279–1285.

21 S. Al-Kabi, S. A. Ghetmiri, J. Margetis, T. Pham, Y. Zhou, W. Dou, B. Collier, R. Quinde, W. Du, A. Mosleh, J. Liu, G. Sun, R. A. Soref, J. Tolle, B. Li, M. Mortazavi, H. A. Naseem and S.-Q. Yu, *Appl. Phys. Lett.*, 2016, **109**, 171105.

22 N. von den Driesch, D. Stange, D. Rainko, I. Povstugar, P. Zaumseil, G. Capellini, T. Schröder, T. Denneulin, Z. Ikonic, J.-M. Hartmann, H. Sigg, S. Mantl, D. Grützmacher and D. Buca, *Adv. Sci.*, 2018, 1700955.

23 B. R. Conley, J. Margetis, W. Du, H. Tran, A. Mosleh, S. A. Ghetmiri, J. Tolle, G. Sun, R. Soref, B. Li, H. A. Naseem and S.-Q. Yu, *Appl. Phys. Lett.*, 2014, **105**, 221117.

24 T. N. Pham, W. Du, B. R. Conley, J. Margetis, G. Sun, R. A. Soref, J. Tolle, B. Li and S. Q. Yu, *Electron. Lett.*, 2015, **51**, 854–856.

25 H. H. Tseng, K. Y. Wu, H. Li, V. Mashanov, H. H. Cheng, G. Sun and R. A. Soref, *Appl. Phys. Lett.*, 2013, **102**, 182106.

26 J. P. Gupta, N. Bhargava, S. Kim, T. Adam and J. Kolodzey, *Appl. Phys. Lett.*, 2013, **102**, 251117.

27 C. Chang, T.-W. Chang, H. Li, H. H. Cheng, R. Soref, G. Sun and J. R. Hendrickson, *Appl. Phys. Lett.*, 2017, **111**, 141105.

28 R. Soref, *Nat. Photonics*, 2010, **4**, 495.

29 J. Schulze, A. Blech, A. Datta, I. A. Fischer, D. Hähnel, S. Naasz, E. Rolseth and E.-M. Tropper, *Solid-State Electron.*, 2015, **110**, 59–64.

30 J. Kouvetakis, J. Menendez and A. V. G. Chizmeshya, *Annu. Rev. Mater. Res.*, 2006, **36**, 497–554.

31 J. D. Sau and M. L. Cohen, *Phys. Rev. B: Condens. Matter Mater. Phys.*, 2007, **75**, 045208.

32 L. Lei, L. Renrong, W. Jing and X. Jun, *Appl. Phys. Express*, 2015, **8**, 031301.

33 S. Wang, J. Zheng, C. Xue, C. Li, Y. Zuo, B. Cheng and Q. Wang, *Superlattices Microstruct.*, 2017, **111**, 286–292.

34 C. Schulte-Braucks, R. Pandey, R. N. Sajjad, M. Barth, R. K. Ghosh, B. Grisafe, P. Sharma, N. Von Den Driesch, A. Vohra, G. B. Rayner, R. Loo, S. Mantl, D. Buca, C. C. Yeh, C. H. Wu, W. Tsai, D. A. Antoniadis and S. Datta, *IEEE Trans. Electron Devices*, 2017, **64**, 2354–2362.

35 V. Reboud, A. Gassenq, N. Pauc, J. Aubin, L. Milord, Q. M. Thai, M. Bertrand, K. Guilloy, D. Rouchon, J. Rothman, T. Zabel, F. A. Pilon, H. Sigg, A. Chelnokov, J. M. Hartmann and V. Calvo, *Appl. Phys. Lett.*, 2017, **111**, 092101.

36 J. Zheng, Z. Liu, C. Xue, C. Li, Y. Zuo, B. Cheng and Q. Wang, *J. Semicond.*, 2018, **39**, 061006.

37 S. Mukherjee, S. Assali and O. Moutanabbir, in *Semiconductors and Semimetals*, ed. S. Mokkapati and C. Jagadish, Elsevier, 2018, vol. 98, pp. 151–229.

38 D. S. Sukhdeo, L. Hai, N. Donguk, Y. Ze, B. M. Vulovic, S. Gupta, J. S. Harris, B. Dutt and K. C. Saraswat, *Approaches for a viable Germanium laser: Tensile strain, GeSn alloys, and n-type doping*, 2013.

39 Y. J. Cho, C. H. Kim, H. S. Im, Y. Myung, H. S. Kim, S. H. Back, Y. R. Lim, C. S. Jung, D. M. Jang, J. Park,

S. H. Lim, E. H. Cha, K. Y. Bae, M. S. Song and W. I. Cho, *Phys. Chem. Chem. Phys.*, 2013, **15**, 11691–11695.

40 R. J. A. Esteves, M. Q. Ho and I. U. Arachchige, *Chem. Mater.*, 2015, **27**, 1559–1568.

41 R. J. Alan Esteves, S. Hafiz, D. O. Demchenko, U. Ozgur and I. U. Arachchige, *Chem. Commun.*, 2016, **52**, 11665–11668.

42 K. Ramasamy, P. G. Kotula, A. F. Fidler, M. T. Brumbach, J. M. Pietryga and S. A. Ivanov, *Chem. Mater.*, 2015, **27**, 4640–4649.

43 T. Křenek, P. Bezdička, N. Murafa, J. Šubrt and J. Pola, *Eur. J. Inorg. Chem.*, 2009, **2009**, 1464–1467.

44 M. S. Seifner, S. Hernandez, J. Bernardi, A. Romano-Rodriguez and S. Barth, *Chem. Mater.*, 2017, **29**, 9802–9813.

45 S. Assali, A. Dijkstra, A. Li, S. Koelling, M. A. Verheijen, L. Gagliano, N. von den Driesch, D. Buca, P. M. Koenraad, J. E. M. Haverkort and E. P. A. M. Bakkers, *Nano Lett.*, 2017, **17**, 1538–1544.

46 S. Biswas, J. Doherty, D. Saladukha, Q. Ramasse, D. Majumdar, M. Upmanyu, A. Singha, T. Ochalski, M. A. Morris and J. D. Holmes, *Nat. Commun.*, 2016, **7**, 11405.

47 S. Biswas, S. Barth and J. D. Holmes, *Nano Res.*, 2017, **10**, 1510–1523.

48 M. S. Seifner, F. Biegger, A. Lugstein, J. Bernardi and S. Barth, *Chem. Mater.*, 2015, **27**, 6125–6130.

49 S. Barth, M. S. Seifner and J. Bernardi, *Chem. Commun.*, 2015, **51**, 12282–12285.

50 A. C. Meng, C. S. Fenrich, M. R. Braun, J. P. McVittie, A. F. Marshall, J. S. Harris and P. C. McIntyre, *Nano Lett.*, 2016, **16**, 7521–7529.

51 B. Vincent, Y. Shimura, S. Takeuchi, T. Nishimura, G. Eneman, A. Firrincieli, J. Demeulemeester, A. Vantomme, T. Clarysse, O. Nakatsuka, S. Zaima, J. Dekoster, M. Caymax and R. Loo, *Microelectron. Eng.*, 2011, **88**, 342–346.

52 Y. S. Huang, F. L. Lu, Y. J. Tsou, C. E. Tsai, C. Y. Lin, C. H. Huang and C. W. Liu, *First Vertically Stacked GeSn Nanowire pGAAFETs with I_{ON}=1850μA/μm (V_{OV}=V_{ds}=−1 V) on Si by GeSn/Ge CVD Epitaxial Growth and Optimum Selective Etching*, 2017.

53 D. Wang, Y.-L. Chang, Q. Wang, J. Cao, D. B. Farmer, R. G. Gordon and H. Dai, *J. Am. Chem. Soc.*, 2004, **126**, 11602–11611.

54 M. Sistani, P. Staudinger, J. Greil, M. Holzbauer, H. Detz, E. Bertagnolli and A. Lugstein, *Nano Lett.*, 2017, **17**, 4556–4561.

55 H. Li, H. H. Cheng, L. C. Lee, C. P. Lee, L. H. Su and Y. W. Suen, *Appl. Phys. Lett.*, 2014, **104**, 241904.

56 S. Akihiro, A. Shunsuke, Y. Jun, K. Kimihiko, K. Masashi, S. Mitsuo, T. Noriyuki, N. Osamu and Z. Shigeaki, *Jpn. J. Appl. Phys.*, 2014, **53**, 04EA06.

57 Z. Liu, H. Cong, F. Yang, C. Li, J. Zheng, C. Xue, Y. Zuo, B. Cheng and Q. Wang, *Sci. Rep.*, 2016, **6**, 38386.

58 C. Zeiner, A. Lugstein, T. Burchhart, P. Pongratz, J. G. Connell, L. J. Lauhon and E. Bertagnolli, *Nano Lett.*, 2011, **11**, 3108–3112.

59 M. Bratati, S. Gopa, B. Rikmantra, M. Shyamal and B. P. Kumar, *Phys. Status Solidi B*, 2017, **254**, 1700244.

60 N. Osamu, T. Norimasa, S. Yosuke, T. Shotaro, S. Akira and Z. Shigeaki, *Jpn. J. Appl. Phys.*, 2010, **49**, 04DA10.

61 C.-E. Tsai, F.-L. Lu, P.-S. Chen and C. W. Liu, *Thin Solid Films*, 2018, **660**, 263–266.

62 C. Ghosh, *Intermetallics*, 2010, **18**, 2178–2182.

63 T. Yamada, K. Miura, M. Kajihara, N. Kurokawa and K. Sakamoto, *Mater. Sci. Eng., A*, 2005, **390**, 118–126.

Epitaxial Ge$_{1-x}$Sn$_x$ Nanowire and Nanocone Growth using Sn Growth Seeds: Effects of the Seed Diameter and Photoluminescence Properties

Michael S. Seifner,[‖] *Alain* Dijkstra,[§] *Andreas Steiger-Thirsfeld,*[¥] *Johannes Bernardi,*[¥] *Masiar Sistani,*[‡] *Alois Lugstein,*[‡] *Erik P. A. M. Bakkers,*[§] *Jos E. M. Haverkort,*[§] *Sven Barth*[‖,$,*]

[‖] Institute of Materials Chemistry, TU Wien, Getreidemarkt 9/BC/02, A-1060 Vienna.

[§] Department of Applied Physics, Eindhoven University of Technology, 5600MB Eindhoven, The Netherlands

[¥] USTEM, University Servicecenter for TEM (USTEM), TU Wien, Wiedner Hauptstrasse 8-10, 1040 Vienna, Austria

[‡] TU Wien, Institute of Solid State Electronics, Gußhausstraße 25-25a, 1040 Vienna, Austria.

[$] Goethe-Universität, Physikalisches Institut, Max-von-Laue-Street 1, 60438 Frankfurt am Main, Germany.

*Corresponding author: S. Barth, E-mail: sven.barth@imw.uni-stuttgart.de; Tel: +49 711 685 61933

KEYWORDS. Germanium; Tin; Alloy; Nanowires; Epitaxy

ABSTRACT.

Highly oriented nanowires (NWs) and nanocones (x up to ~19 at% Sn) are synthesized by a low temperature chemical vapor deposition (CVD) growth technique. The formation of the structures is based on a self-seeding vapor-liquid-solid (VLS) mechanism of this binary semiconductor material using Sn as growth seed and sole source/reservoir. Besides the very high Sn content achieved in this study, the strain relaxation for a lattice mismatch of ε 2.94 % between the Ge(111) substrate and the final composition $Ge_{0.81}Sn_{0.19}$ of NWs is reached within a transition zone of ~80 nm, while micropillars show fivefold longer transition zone which is very similar to epitaxial thin film growth. Effects of the Sn growth promoter on the structural and compositional evolution of $Ge_{1-x}Sn_x$ are described. In addition, the optical properties of the $Ge_{1-x}Sn_x$ NWs and nanocones verify the formation of a direct bandgap material with emission in the mid-infrared region and values expected for unstrained $Ge_{0.81}Sn_{0.19}$ (~0.3 eV).

2

Monolytic integration of photonics and electronics on the same platform based on all-group IV semiconductors requires a localized and efficient way of fabricating light emitters being processed in established complementary metal-oxide-semiconductor (CMOS)-based processes.[1] For this purpose, direct bandgap $Ge_{1-x}Sn_x$ has recently re-gained increased interest.[2-3] Alloying germanium with tin alters the properties of the semiconductor tremendously effecting electronic,[4] optoelectronic[5] and optical[6] properties. However, a direct semiconductor material of this element combination requires superseding the equilibrium solubility of ~1 at%.[7] Thus, processes enabling the incorporation of ~8 at% Sn[8] in Ge have to be carried out under non-equilibrium conditions ruled by kinetics. Additional benefit is the possibility to modulate the bandgap by altering the tin content in the Ge matrix.[9] According to their narrow bandgap, these $Ge_{1-x}Sn_x$ materials are candidates for infrared optoelectronics and optical devices, such as infrared lasers,[8, 10-13] photodetectors[14-15] or light emitting diodes[16-18].

Despite significant progress in thin film growth techniques, there is a limited number of reports available for anisotropic $Ge_{1-x}Sn_x$ crystal growth exceeding the Sn content required to obtain a direct bandgap material. $Ge_{1-x}Sn_x$ NWs have been prepared by using Au seeds for simultaneous decomposition of allyltributylstannane and diphenylgermane leading to $Ge_{0.91}Sn_{0.09}$ showing characteristics of a direct bandgap material.[19 20] Higher tin contents in the range of 17-28 at% have been obtained by applying a liquid-based approach[21-23] The material in this composition range reveals high conductivity values and semiconductor behavior.[24] Low temperature growth preventing a phase separation can lead to extraordinary high doping levels in Ge NWs while retaining excellent crystal quality. For instance, CVD as well as electrochemical synthesis are able to incorporate very high metal concentrations in the semiconductor from the metal seed used to grow the Ge nanocrystals.[25-28] The technique can be described as a low temperature variation of

the self-seeded growth described for In or Ga metal of the respective III-V NWs.[29-30] In this context, Sn has been used in prior studies for the growth of Si[31-32] and Ge[33-34] and nanorods / NWs and segmented Si/Ge heterostructures;[35-36] however, significant incorporation from a Sn reservoir in the growing Ge NW crystal has only been achieved by a low-temperature microwave-based approach[21-23] according to the solution-liquid-solid mechanism and for in-plane migrating NWs[37] using a solid-liquid-solid approach. Moreover, crystallization of initially amorphous $Ge_{0.85}Sn_{0.15}$ micrometer-sized stripes by rapid melting growth shows a Sn segment at the end of the formed Ge crystal.[38] However, the crystal contains a very low Sn content over tens of micrometers and only a few micrometers with significant Sn incorporation close the metallic Sn segment.

Thus far, in regards to control of the growth direction on substrates only one study on Au-catalyzed, oriented $Ge_{1-x}Sn_x$ NWs has been reported. Although the temperature used is in the regime (300-350 °C) where efficient Sn incorporation has been demonstrated for layer growth, the Ge NWs contain only the thermodynamically stable ~1 at% Sn and revealed a Sn-O-enriched shell.[39] A successful strategy has been the growth of $Ge_{1-x}Sn_x$ shells on Ge NWs as substrate material.[40-41] The most efficient incorporation in these studies shows an epitaxial, non-homogeneous $Ge_{0.87}Sn_{0.13}$ shell growth with Sn gradient of 8-13 at%.[40] The shell, accommodates the resulting strain by the aforementioned Sn gradient and also inhomogeneous distribution of Sn in the shells with radial "sunburst stripes" of low (~4 at%) and high Sn content (8-13 at%) alternating segments.[42]

Here we report an efficient CVD growth method of $Ge_{1-x}Sn_x$ structures using metallic Sn as source and crystal growth promoter on Ge(111) substrates. Epitaxial, vertically-grown $Ge_{1-x}Sn_x$ (x = 15-20) structures are demonstrated over a large diameter range ~50-1000 nm. The initial Sn particle acts as both nucleation seed as well as Sn source for the formation of the binary

semiconductor and thus the growth mechanism can be described as a site-selective self-seeding VLS mechanism. Short growth cycles have been intentionally chosen to prevent potential thermal degradation of the material, which we investigated prior to this study.[23] Our results demonstrate a diameter-dependent transition zone between substrate and $Ge_{1-x}Sn_x$ material with very efficient strain relaxation for nanostructures. The obtained $Ge_{0.81}Sn_{0.19}$ NWs and nanocones exhibit photoluminescence with energies in the expected range of 0.29 eV at room temperature for material with a direct bandgap. The PL data illustrate the high crystal quality of the NW material prepared in this study.

RESULTS AND DISCUSSION

The growth of the $Ge_{1-x}Sn_x$ nanostructures has been realized in a two-step CVD approach. In a first step, the Sn growth seeds have been deposited by low pressure CVD on single crystal Ge(111) substrates using $Sn(N(CH_3)_2)_2$ at substrate temperatures of 275-300 °C. The *in situ* formation of the Sn growth seeds avoids their oxidation. Subsequently, the temperature is adjusted to the desired deposition conditions for the tert.-butylgermane precursor as Ge source. Key to the successful formation of $Ge_{1-x}Sn_x$ NWs using Sn is a high supersaturation of the Ge-source to enable a high growth rate at low temperatures of 250-350 °C, since process conditions also effect the material quality and composition as well as the tendency to Sn segregation.[43] The high growth rate is important to prevent the degradation of the $Ge_{1-x}Sn_x$ by diffusion of metallic Sn through the crystal,[23] but causes a parasitic amorphous Ge film that can be easily removed via reactive ion etching as described in literature.[44] Typical scanning electron microscopy (SEM) image recorded perpendicular to the sample surface reveals almost exclusively circular structures and a small number of elongated structures formed off axis as shown in Figure 1a. The actual morphology of

the NWs and their orientation can be visualized either in cross section geometry (Figure 2b) or simply by tilting the substrate off the $\langle 111 \rangle$-viewing direction as demonstrated for fully developed $Ge_{1-x}Sn_x$ nanocones in Figure 2c. The highest number of $\langle 111 \rangle$-oriented NWs (>97 %) was observed for samples with diameters at the interface NW to substrate in the range of 30-130 nm (mean value 81 ± 22 nm; 1σ) as displayed in Figure S1. Transmission electron microscopy (TEM) was used to study microstructural properties of the Ge NWs. For that purpose, $Ge_{1-x}Sn_x$ NWs were deposited onto lacey carbon grids by drop casting of NWs which were mechanically removed from the surface. The TEM image in Figure 1d reveals a smooth surface and shows the partially consumed hemispherical Sn growth seed with different diffraction contrast. The single crystal nature of $Ge_{1-x}Sn_x$ material growing from the Sn seed is revealed in a high resolution TEM (Figure 1e). The Fast Fourier Transformation (FFT) pattern shown in the inset depicts the growth direction of the $Ge_{1-x}Sn_x$ NW to be along the expected $\langle 111 \rangle$-axis according to their perpendicular orientation to the (111) Ge substrate in SEM images.

Significant differences in morphology can be observed with higher amounts of Sn deposited in the first step. Thick micropillars of different height and diameter are obtained after the Ge deposition and accompanied with micron-sized structures migrating on the surface (Figure 2a). Micropillars are very similar to the structures observed in Figure 1b, but with much larger diameter. The surface migrating in-plane microwires, as highlighted by circles in Figure 2a, resemble structures described in literature. In contrast to the conversion of amorphous Ge into $Ge_{1-x}Sn_x$ on silica surfaces,[37] the here observed in-plane microwires are growing on single crystal Ge substrates and therefore strain has to be considered. Differences in the Sn content observed in this study (up to ~4% at 300 °C) and the literature report of in-plane $Ge_{0.78}Sn_{0.22}$ NWs grown at temperatures of 270 °C can be traced back to their formation on a lattice matching Ge substrate

instead of an amorphous SiO_2 layer.[37] Scanning transmission electron microscopy energy dispersive X-ray spectroscopy (STEM-EDX) maps for Sn and Ge are shown Figure S2 in the Supporting Information.

A schematic diagram derived from SEM images can be used to discriminate between three different morphologies observed in the experiments. The starting point in the growth description in Figure 2b is the initial Sn particle. The main difference is the size and the resulting nucleation events. Small Sn particles lift from the surface of the Ge substrate easily, because the decomposing Ge can dissolve in the Sn particle leading to supersaturation with Ge and subsequent nucleation/ film formation underneath the particle via layer-by-layer growth representing a typical VLS growth of group IV NWs on (111)-oriented substrates of Si or Ge. The growth proceeds as long as the liquid Sn particle can facilitate the VLS growth of a single crystal, while it is consumed due to incorporation of Sn in the growing NWs. For thicker Sn particles either an identical process occurs and micropillars are formed underneath the Sn particle. However, in case the nucleation event occurs at an edge of the particle at the triple phase boundary an in-plane migrating microwire can be observed.[45]

Since both thick micropillars and NWs are both growing perpendicular on the Ge(111) substrate, the composition of the formed $Ge_{1-x}Sn_x$ material has to be considered. For this purpose, TEM lamellae have been prepared using focused ion beam preparation methods for cutting and thinning of the sections. Figure 3a shows the composition at different locations along a STEM-EDX map of the micropillars, as illustrated in the inset. A clear trend is visible along the cross section starting at the Ge substrate and a transition zone with increasing Sn content up to 15.4 at% over a length of 430 nm for a microwire of 1.1 μm base diameter. This is in good agreement with a recent study on epitaxial thin film growth of $Ge_{1-x}Sn_x$ with a tin content of ~15 at% at a distance of ~500 nm

on a virtual Ge substrate.[46] In contrast, Figure 3b illustrates a NW with 95 nm base diameter owning a transition length of merely 50 nm for a 15 at% Sn content and 80 nm to reach a composition limit of ~19 at% Sn at the given synthesis parameters (325 °C and 100 µl TBG). The composition along a NW after the transition zone is constant as shown in Figure 3c for a not fully terminated $Ge_{0.81}Sn_{0.19}$ NW (19.3±0.9 at%) with the Sn particle at the top of the growth front. The composition along a fully developed nanocone is also constant, which is shown with the whole set of Ge and Sn maps and their overlays related to Figure 3 in Figures S4-6.

Obviously, the length of the transition zone is diameter-dependent for structures growing in the ⟨111⟩-direction. The substitution of Ge in the crystal by Sn owning 15% larger atomic size results in a mismatch of the Ge substrate and the growing $Ge_{1-x}Sn_x$. In epitaxial thin film growth this strain can be relaxed by defect formation or the crystal remains pseudomorphic resulting in compressively strained films; however, this is not beneficial for the optical properties of the material. In general, the lattice mismatch is given by $\varepsilon = (a_f - a_s)/a_s$, where a_f and a_s are the lattice constants of the film and the substrate materials, respectively. The lattice parameters of unstrained $Ge_{1-x}Sn_x$ scale linear with changes in the atomic ratio and thus calculations according to Vegard's a law can be used for the composition of interest. A large interface area is covered by a micropillar (for a diameter of 1.1 µm this area is 9.5×10^5 nm^2) and the transition zone from pure Ge and $Ge_{0.85}Sn_{0.15}$ with a 2.20 % lattice mismatch is 430 nm (Figure 3a). This is in good agreement to gradients in thin film growth of $Ge_{0.85}Sn_{0.15}$ with good optical properties.[46-47] The same composition is observed for the 95 nm diameter NW within 50 nm from the interface and the even higher equilibrium composition of $Ge_{0.81}Sn_{0.19}$ (lattice mismatch of 2.94 %) is reached after 80 nm which relates to an effective strain compensation by dilatation. Since both, the substrate and the growing material are isotype, the strain can be gradually compensated, which is not possible for

two materials with a fixed composition and lattice parameters such as III-V semiconductor growth on group IV substrates. However, these literature reports demonstrate that NWs can efficiently compensate a large amount of strain and that this effect is more pronounced for thin NWs.[48]

The optical properties of $Ge_{0.81}Sn_{0.19}$ NWs epitaxially grown on Ge are evaluated by temperature- and laser power-dependent PL measurements (Figure 4). For both PL series a signal in the range 2.76 µm - 2.00 µm (0.45 eV - 0.62 eV) can be attributed to the Sb-doped Ge substrate showing indirect bandgap-behavior. The direct bandgap PL signal located at 4.28 µm (0.29 eV) for room temperature can be assigned to the $Ge_{0.81}Sn_{0.19}$ NWs which is in good agreement with theoretical[49] and experimental[50] studies on thin films showing direct bandgap energies for similar compositions in the same range (Figure 4a). Furthermore, a blue-shift of the PL signal upon cooling (Figure 4a) and for increased laser powers (Figure 4b) is observed. The increase of the PL signal upon cooling (Figure 4a) and for higher laser powers (Figure 4b) is a strong hint for the transition of Ge into a direct bandgap semiconductor and these observations agree well with a study about optical transitions in direct bandgap $Ge_{1-x}Sn_x$ alloys.[51] According to literature, the clear evidence of PL from a direct bandgap semiconductor which is dominated by band-to-band recombination is provided by validation of the direct proportionality between the integrated PL intensity (I) and the excitation power (P) ($I \sim P^m$ with m = 1).[51-52] Therefore, the integrated PL intensity is plotted versus the excitation power in a double logarithmic diagram. The slope of the curve is very close to 1 which proves that a $Ge_{0.81}Sn_{0.19}$ NW epitaxially grown on Ge is a direct bandgap semiconductor.

CONCLUSION

A vapor-phase approach for the epitaxial growth of $Ge_{1-x}Sn_x$ nanostructures on a Ge substrate is presented. In a first step Sn particles are deposited on a Ge substrate via a CVD process with high control over the seed diameter. In a subsequent step the gas-phase is highly saturated with a Ge precursor resulting in the self-seeded growth of anisotropic $Ge_{1-x}Sn_x$ nanostructures. Depending on the seed diameter morphologies such as $Ge_{1-x}Sn_x$ NWs, micropillars, and in-plane NWs can be grown with high densities on the Ge substrate. $Ge_{1-x}Sn_x$ NWs and micropillars both grow in the $\langle 111 \rangle$ direction but differ in Sn distribution and content depending on base diameter (~ 81 nm/~ 1 μm). For $Ge_{1-x}Sn_x$ micropillars a strong gradient in Sn content (up to ~ 15 at%) is observed and can be related to strain effects caused by the large lattice mismatch between Ge and the growing alloy. In contrast, $Ge_{1-x}Sn_x$ NWs show an efficient incorporation of Sn (19.3 at%) and only a short transition zone (< 100 nm) due to an effective strain compensation by dilatation. Temperature- and laser power-dependent photoluminescence measurements show a direct bandgap transition of $Ge_{0.81}Sn_{0.19}$ NWs. The slope of the curve obtained by plotting the integrated PL intensity (I) of the signal versus the excitation power (P) in a double logarithmic diagram is very close to a value of 1 which confirms the transition of Ge into a direct bandgap semiconductor.

METHODS

All synthetic procedures and handling of the chemicals for the nanostructure synthesis have been carried out using Schlenk techniques or an argon-filled glove box (MBraun). Solvents have been dried over sodium and stored in a glove box. The bis(dimethylamido)tin(II) precursor ($Sn(N(CH_3)_2)_2$) was prepared by salt elimination using $SnCl_2$ and $Li(N(CH_3)_2)$ in dry hexane/diethylether according to literature.[53] The $Sn(N(CH_3)_2)_2$ was sublimed at reduced pressure before use. All chemicals for the synthesis of the amido precursor were purchased from Sigma-Aldrich. Tert.-butylgermane (TBG; $(C_4H_9)GeH_3$) was purchased from Gelest.

Nanostructure synthesis. Epitaxially grown $Ge_{1-x}Sn_x$ alloy nanostructures are synthesized in a modified cold-wall CVD reactor. In a typical process the Ge(111) substrate is treated with concentrated hydrobromic acid (HBr) for 15 min in an ultrasonic bath to remove native oxides. Subsequently, the substrate is rinsed by distilled water and isopropyl alcohol. The dried substrate is connected to a graphite susceptor by silver paste. The CVD reactor is flushed with pure N_2 for 15 min before separate 10 ml vessels containing 10 mg bis(dimethylamido)tin ($Sn(N(CH_3)_2)_2$) and 50-200 µl tert.-butylgermane are attached to the growth chamber under N_2 flow on separate lines with individual glass gauges. The CVD reactor is evacuated (~1×10^{-3} mbar) and Sn deposition is carried out at substrate temperatures of 300 °C and a temperature of 55 °C of the oven to generate sufficient vapor pressure of the metalorganic precursor. After 10 min the Sn precursor supply is disconnected and the susceptor temperature adjusted (250-350 °C). At the desired susceptor temperature the Ge precursor, which is a colorless liquid at room temperature with a very high vapor pressure, is frozen with liquid N_2. The valve separating the Ge precursor from the reactor is opened, while a valve between susceptor and vacuum pump is closed in order to achieve a high

vapor pressure during the decomposition of the Ge precursor in a reactor volume of ~350 cm^3. The Ge precursor heats up to room temperature and thus filling the whole reaction vessel after approximately 1 min. Ge is deposited for 15 min and the growth is terminated by opening the valve between the susceptor and the vacuum pump. The reactor is cooled down to room temperature after the reactor pressure is $<1 \times 10^{-3}$ mbar.

After the CVD process the substrates are transferred into a RIE etcher (Oxford Plasmalab 80 plus) to remove a parasitic, amorphous Ge layer grown on the substrate and the Ge$_{1-x}$Sn$_x$ structures. A mixture of 80 % CF$_4$ and 20 % O$_2$ is used as process gas. In a typical process the samples are etched with an RF power of 35 W at a pressure of 700 mTorr. Depending on the expected thickness of the Ge layer the etching time is varied between 30 and 75 s. The thin SnO$_2$ layer formed during the etching is removed by treatment in 10 % HCl for 5 min.

Nanostructure characterization. The Ge$_{1-x}$Sn$_x$ NWs were analyzed using a FEI Quanta 250 field emission gun scanning electron microscope (SEM). The Ge$_{1-x}$Sn$_x$ NWs were partially scraped off the Ge substrate and deposited on lacey carbon copper grids by drop-casting of a toluene dispersion for transmission electron microscope (TEM) characterization (Plano). For cross sections, the structures were sputter-coated with carbon (100-500 nm) and Pt was deposited before FIB sectioning and thinning using a FEI-Quanta 200 3D DualBeam-FIB. In this study, a FEI TECNAI F20 operated at 200 kV and equipped with high angle annular dark field (HAADF) STEM and EDX detector was used. The elemental maps were recorded and quantified using the AMETEK TEAM package. The images were recorded and treated using Digital Micrograph software.

ASSOCIATED CONTENT

Supporting Information. Statistics on size of oriented NWs, additional STEM-EDX maps as well as SEM images.

AUTHOR INFORMATION

Corresponding Author

* S. Barth, E-mail: E-mail: sven.barth@imw.uni-stuttgart.de; Tel: +49 711 685 61933

Author Contributions

The manuscript was written through contributions of all authors. All authors have given approval to the final version of the manuscript.

The authors declare no competing financial interest.

Figure 1. Top view (a) and cross section (b) of highly oriented $Ge_{1-x}Sn_x$ nanostructures grown on Ge(111) substrates at 325 °C for 15 min and subsequent reactive ion etching. (c) The 30° tilted view shows fully terminated $Ge_{1-x}Sn_x$ nanocones grown perpendicular to the Ge surface. (d) The TEM image of a NW scraped from the surface clearly illustrated the shrinking diameter due to the incorporation of Sn from the metallic hemispherical nucleation seed and smooth surface of the $Ge_{1-x}Sn_x$. (e) High resolution TEM image of a $Ge_{1-x}Sn_x$ NW reveals the single crystalline nature of the material and also the growth along the $\langle 111 \rangle$-axis can be determined by the Fast Fourier Transformation (FFT) in the inset.
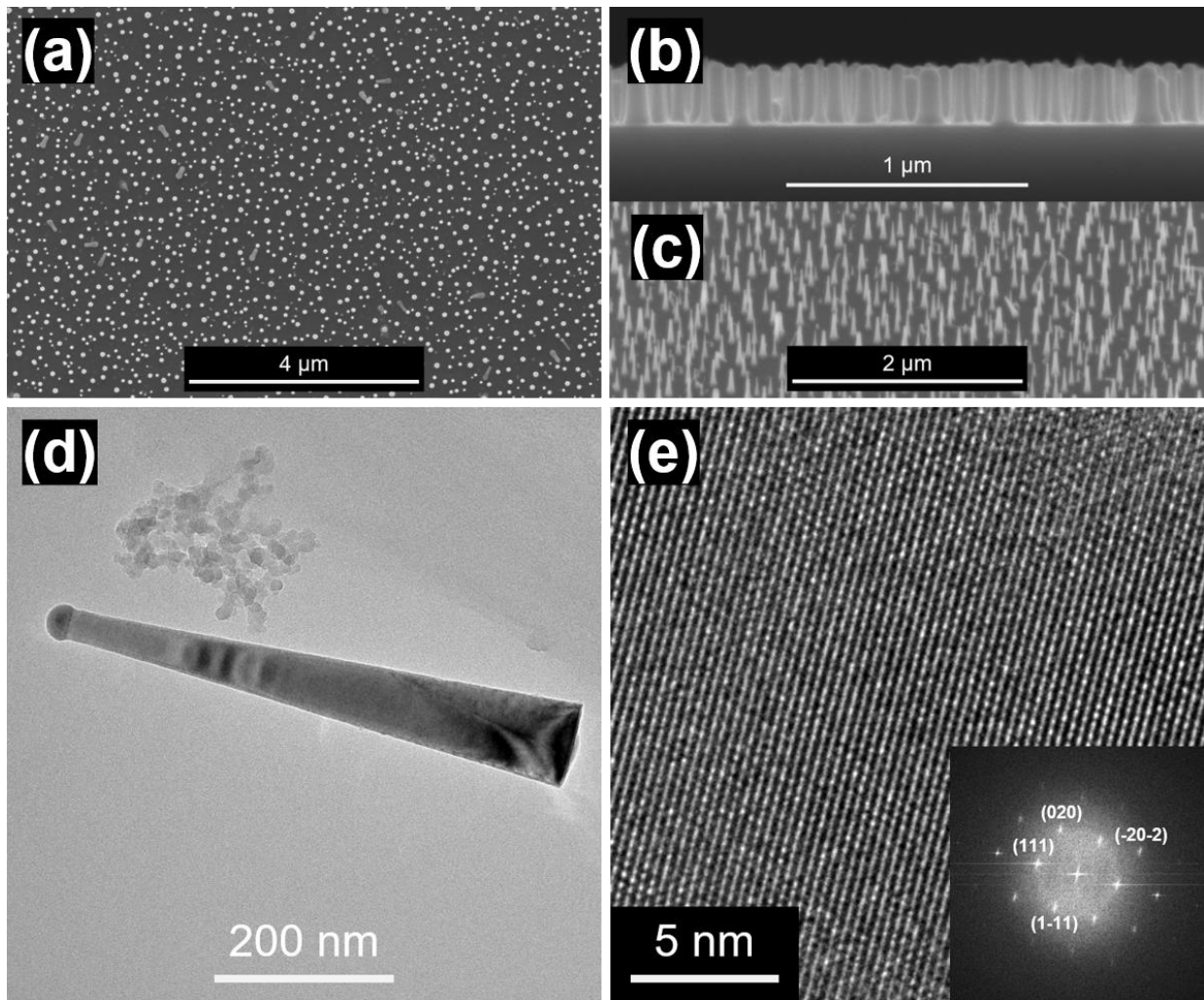
Figure 2. (a) SEM image (30° tilt angle) of structures obtained with higher amount of Sn deposition showing in plane growth of microwires and perpendicular growth of micropillars at growth temperatures of 300 °C. In plane microwires are encircled to guide the eye. (b) gives a schematic illustration of the formation mechanism of the different structures obtained in this study including in plane microwires, micropillars as well as the formation of nanocones in the lower sequence.
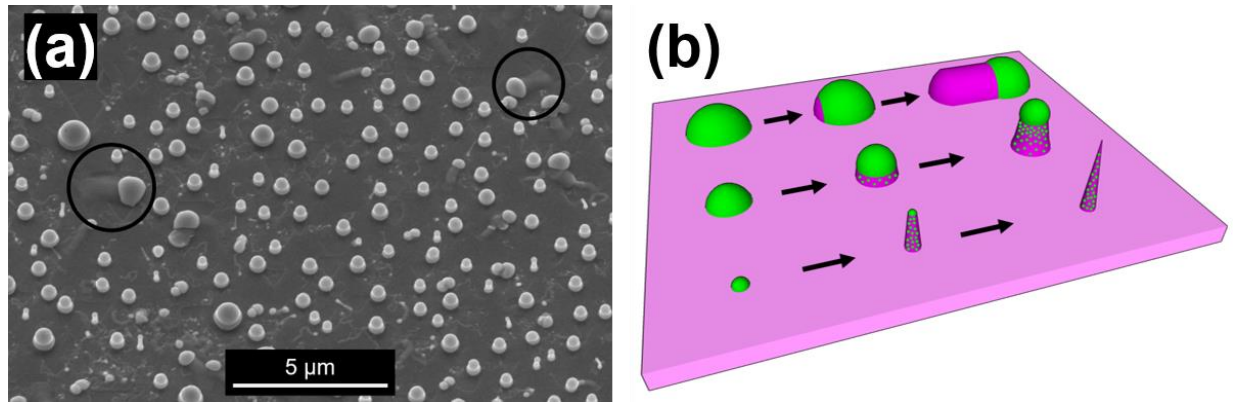
Figure 3. STEM-EDX maps showing the local Sn distribution in the $Ge_{1-x}Sn_x$ structures on the Ge substrate using thin TEM lamellae (a+b) prepared FIB. (a-c). Sn concentration profiles along the growth axis for (a) a micropillar with a base diameter of 1100 nm on the Ge substrate showing a gradual increase of Sn composition over the whole length of the $Ge_{1-x}Sn_x$ segment, (b) the interface region between Ge and the growing $Ge_{1-x}Sn_x$ NW crystal with base diameter of 95 nm, which reaches a constant Sn content (~19 at%) within a length of 80 nm. (c) shows the homogeneous Sn distribution along a $Ge_{1-x}Sn_x$ NW (19.3±0.9 at%)
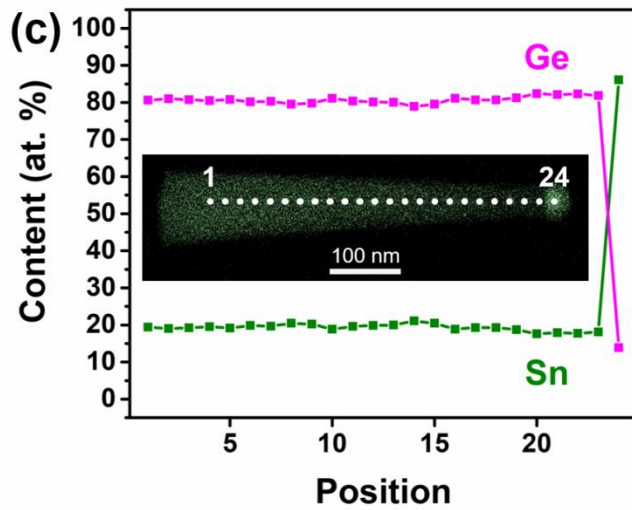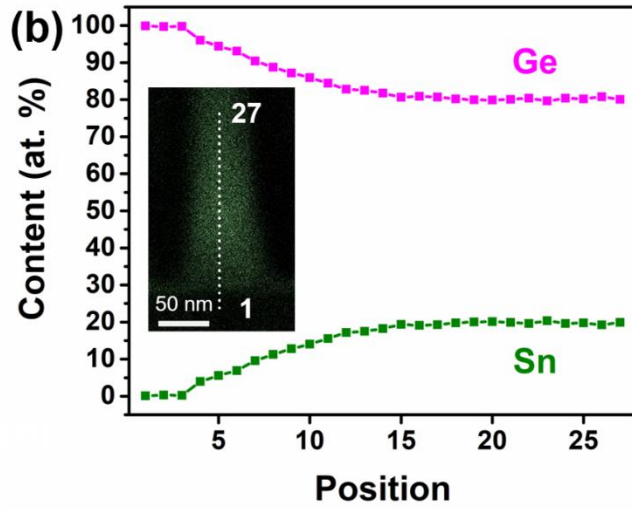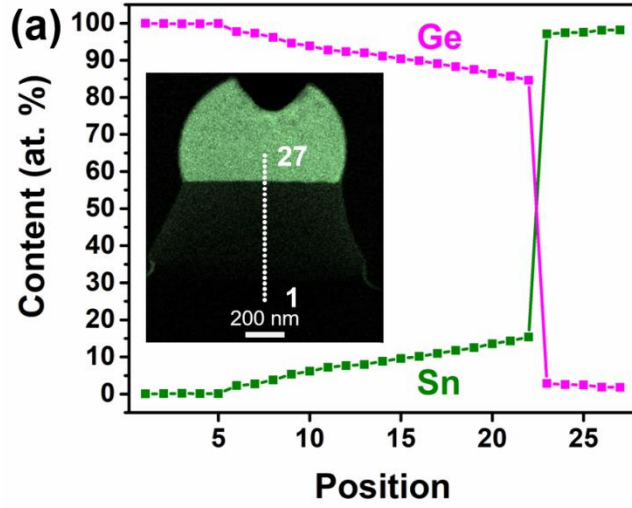
Figure 4. (a) Temperature-dependent photoluminescence measurements show emission of $Ge_{0.81}Sn_{0.19}$ NWs at 4.28 μm (0.29 eV) for room temperature. The signal strongly shifts towards higher energies upon cooling and intensity of this signal increases. (b) A strong shift towards higher energies accompanied with higher intensities can be observed in photoluminescence measurements of these structures for different laser powers. In addition, the signal in the range 2.76 μm – 2.00 μm (0.45 eV – 0.62 eV) can be assigned to the Sb doped Ge substrate showing indirect bandgap-behavior.
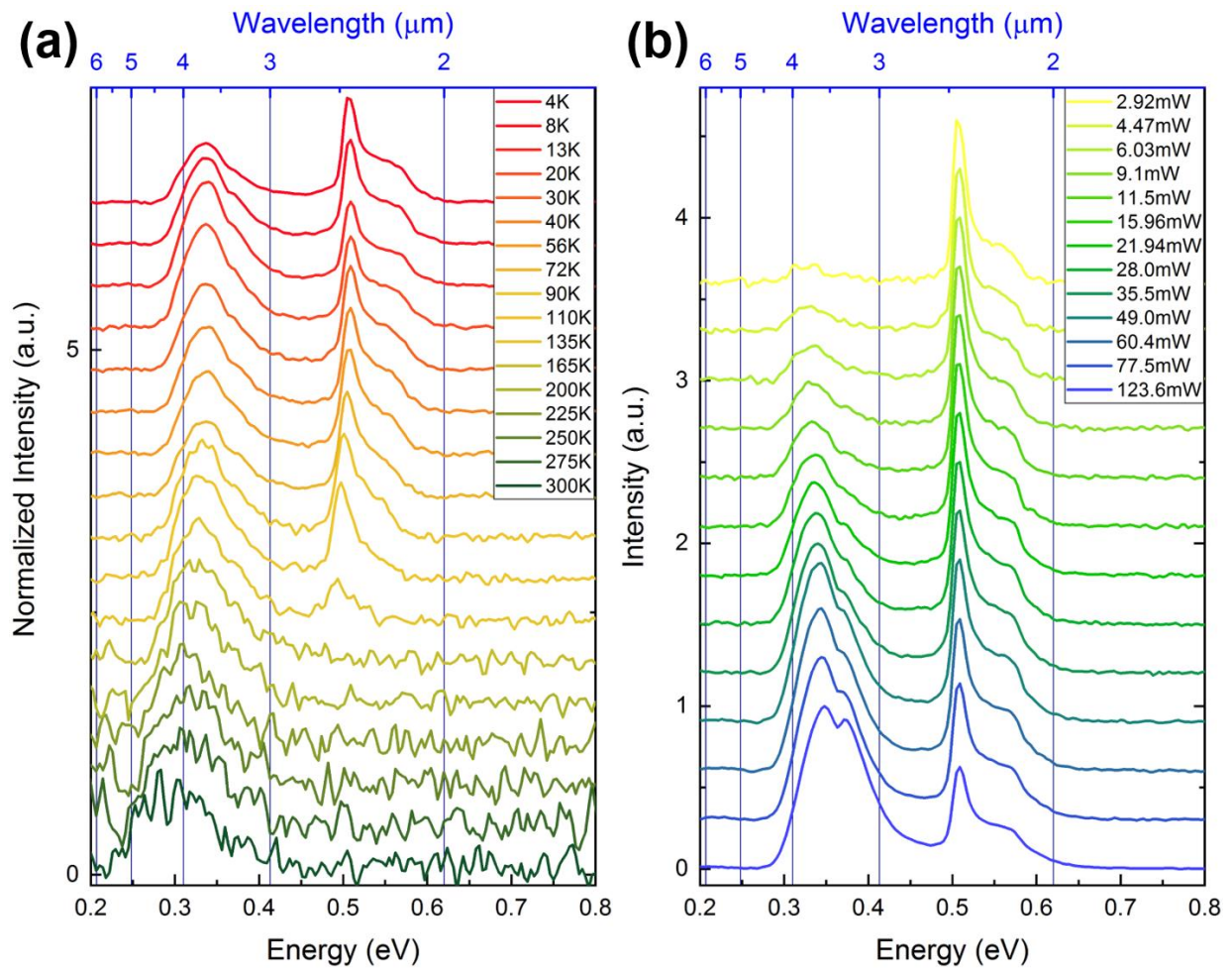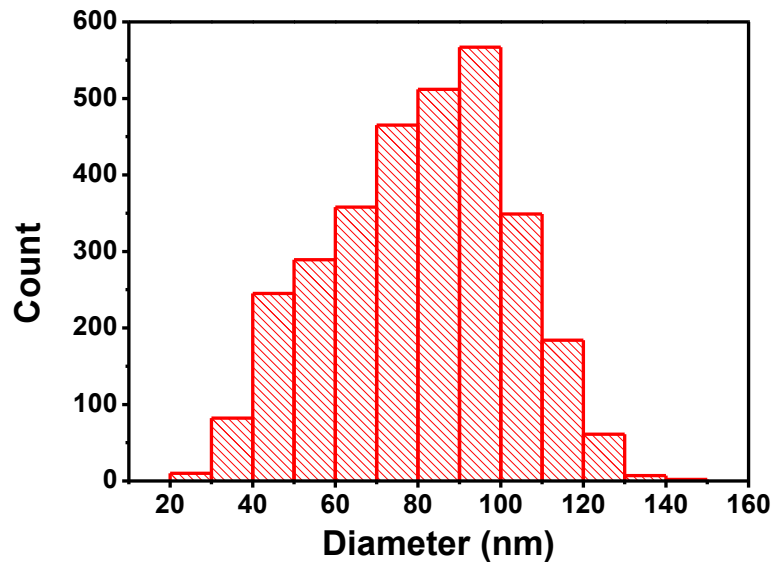
Figure S1. Diameters of the base $Ge_{1-x}Sn_x$ determined using top-side SEM images.
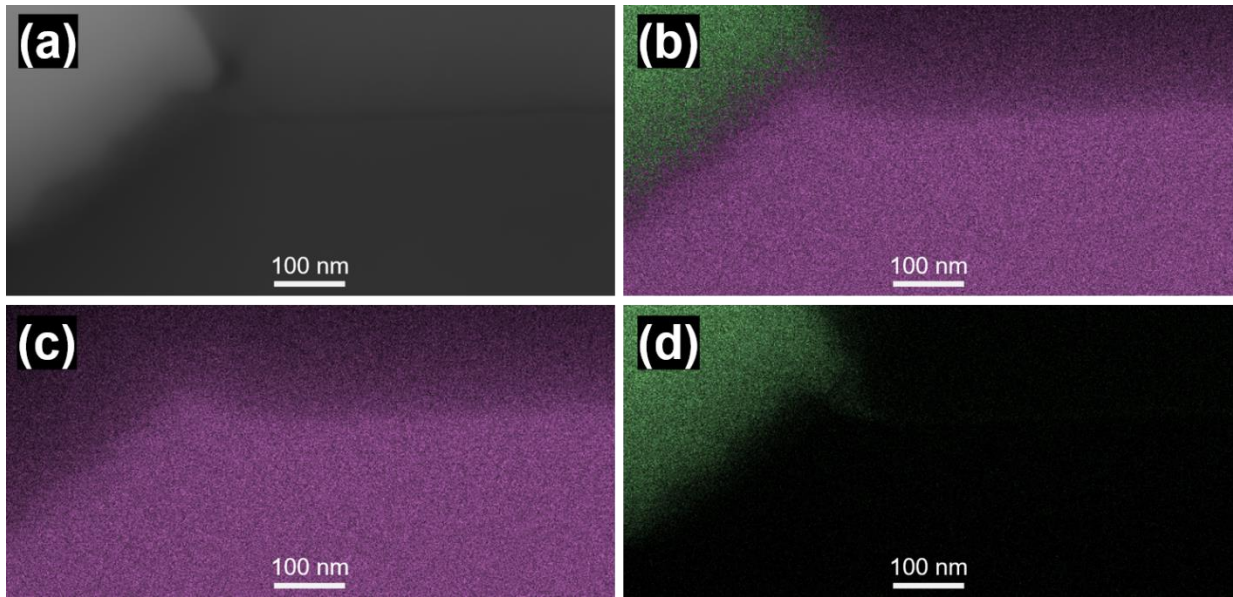
Figure S2. STEM-EDX maps of a TEM lamella cross section showing the interface area of Sn microparticles and in plane microwires. The low Sn content (~4 at%) is not well resolved due to the color gamut in presence of the Sn particle and the low concentration.
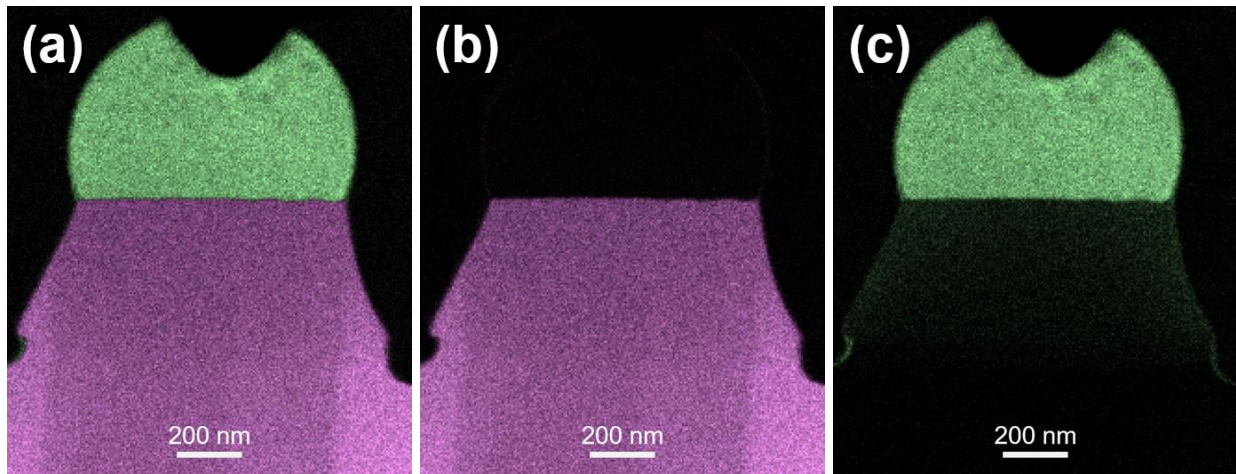
Figure S3. STEM-EDX map of a TEM lamella showing micropillars grown at 300 °C on the Ge substrate with (a) as overlay and individual (b) Ge and (c) Sn map. The line in the middle of the structure is due to a preferential thinning of the Ge and $Ge_{1-x}Sn_x$ underneath the Sn particle due to a channeling effect by the Sn single crystal and therefore increased sputtering/milling. This is caused by a defective Pt protection layer during the lamella formation). The RIE etching has caused a partial removal of the Ge substrate material due to the faster etching of pure Ge and the slower etching of $Ge_{1-x}Sn_x$ by the formation of SnO_2.
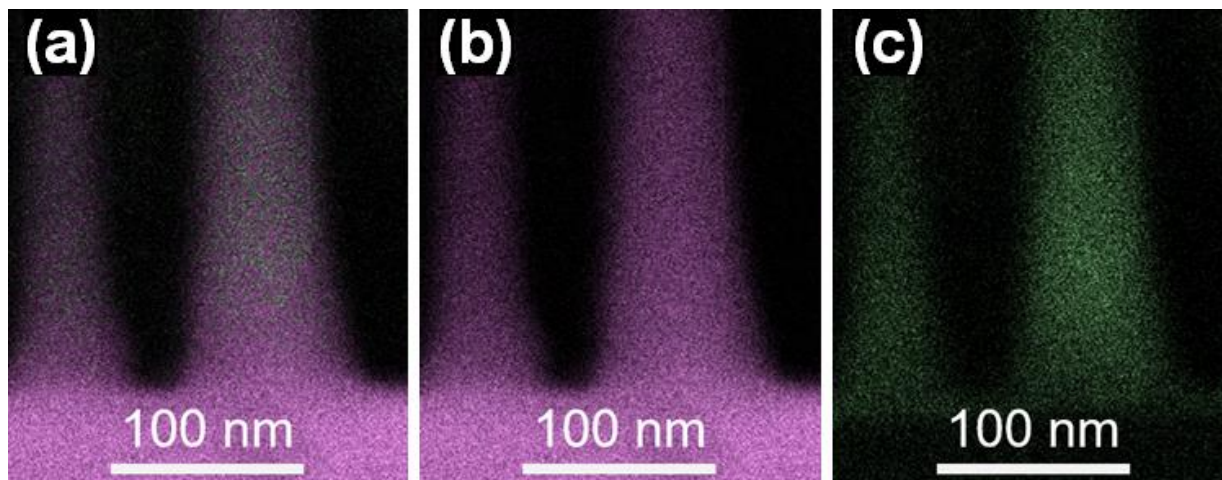
Figure S4. STEM-EDX map of a TEM lamella of a $Ge_{1-x}Sn_x$ NW grown on the Ge substrate with (a) as overlay and individual (b) Ge and (c) Sn map. grown at 325 °C.
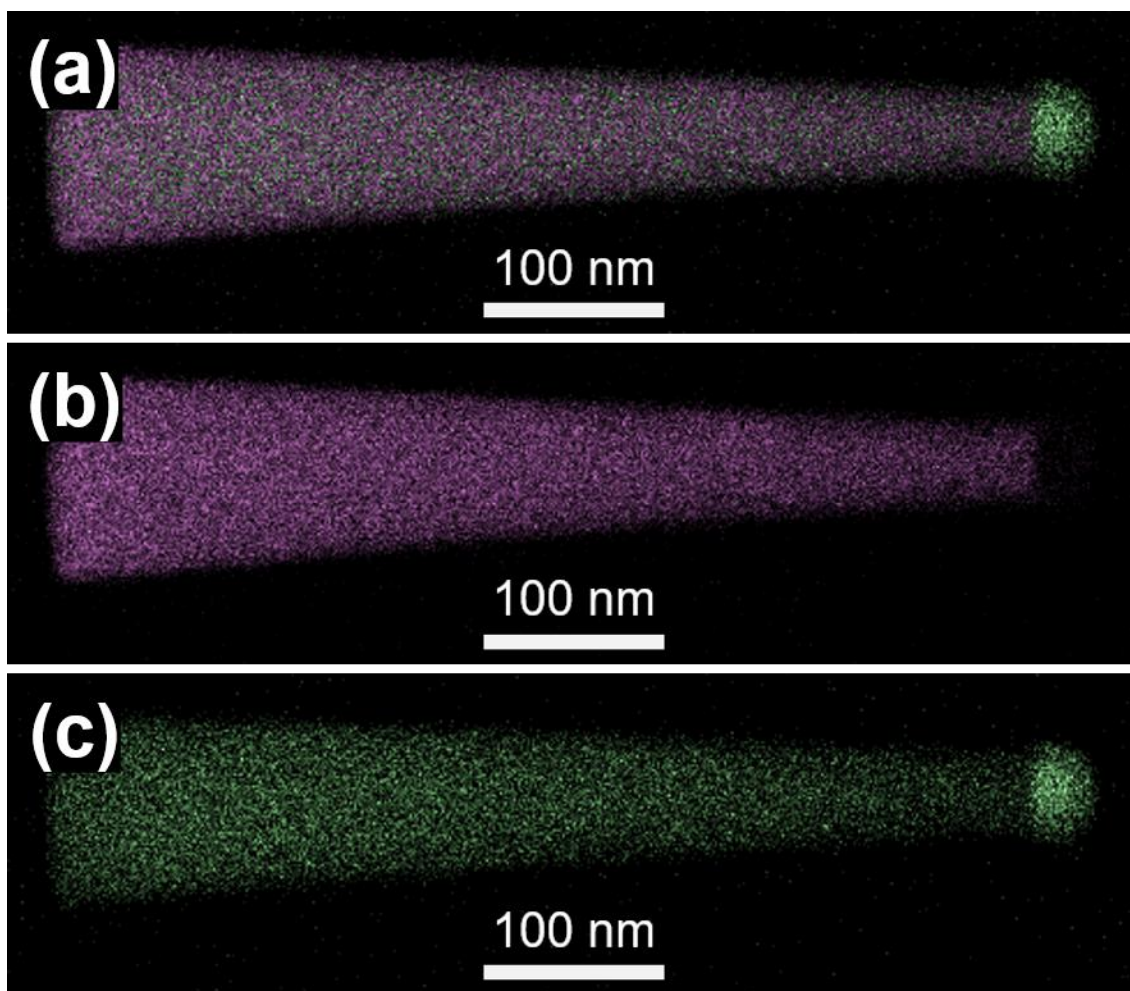
Figure S5. STEM-EDX map of a $Ge_{1-x}Sn_x$ NW grown at 325 °C including the Sn tip with (a) as overlay and individual (b) Ge and (c) Sn map.
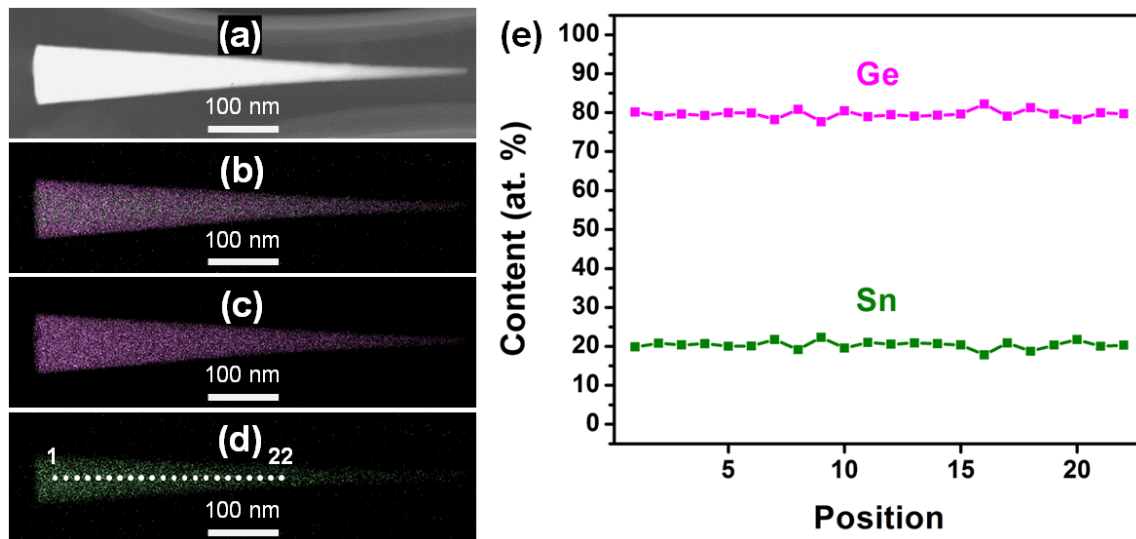
Figure S6. STEM-EDX map of a $Ge_{1-x}Sn_x$ nanocone grown at 325 °C with (a) a STEM image, (b) an overlay of Ge and Sn as well as individual (b) Ge and (c) Sn map. (e) shows the homogeneous composition along the needle axis with a Sn content of 20.41±1.1 at%. The values are corrected by considering the observed Ge shell thickness in the Ge and Sn maps, which is visible for structures without reactive ion etching to remove the parasitic layer.

REFERENCES

1. Soref, R., et al., *Optics and Photonics News* **2016,** *27*, 32-39.
2. Mukherjee, S., et al., Chapter Three - Group IV Nanowires for Carbon-Free Energy Conversion. In *Semiconductors and Semimetals*, Mokkapati, S.; Jagadish, C., Eds. Elsevier: 2018; Vol. 98, pp 151-229.
3. Oehme, M., et al., *Thin Solid Films* **2014,** *557*, 169-172.
4. Schulte-Braucks, C., et al., *Solid-State Electronics* **2017,** *128*, 54-59.
5. Ghetmiri, S. A., et al., *Optics Letters* **2017,** *42*, 387-390.
6. Geiger, R., et al., *Front. Mater.* **2015,** *2*.
7. Olesinski, R. W., et al., *Bull. Alloy Phase Diagrams* **1984,** *5*, 265-271.
8. Wirths, S., et al., *Nat. Photonics* **2015,** *9*, 88-92.
9. von den Driesch, N., et al., *Chem. Mater.* **2015,** *27*, 4693-4702.
10. Stange, D., et al., *ACS Photonics* **2016,** *3*, 1279-1285.
11. Al-Kabi, S., et al., *Appl. Phys. Lett.* **2016,** *109*, 171105.
12. Buca, D., et al. In *GeSn Lasers for CMOS Integration*, Technical Digest - International Electron Devices Meeting, IEDM, 2017; pp 22.3.1-22.3.4.
13. Reboud, V., et al., *Appl. Phys. Lett.* **2017,** *111*, 092101.
14. Conley, B. R., et al., *Appl. Phys. Lett.* **2014,** *105*, 221117.
15. Pham, T. N., et al., *Electron. Lett.* **2015,** *51*, 854-856.
16. Tseng, H. H., et al., *Appl. Phys. Lett.* **2013,** *102*, 182106.
17. Gupta, J. P., et al., *Appl. Phys. Lett.* **2013,** *102*, 251117.
18. Chang, C., et al., *Appl. Phys. Lett.* **2017,** *111*, 141105.
19. Biswas, S., et al., *Nat. Commun.* **2016,** *7*, 11405.
20. Doherty, J., et al., *J. Mater. Chem. C* **2018,** *6*, 8738-8750.
21. Seifner, M. S., et al., *Chem. Mater.* **2015,** *27*, 6125-6130.
22. Barth, S., et al., *Chem. Commun.* **2015,** *51*, 12282-12285.
23. Seifner, M. S., et al., *Chem. Mater.* **2017,** *29*, 9802-9813.
24. Sistani, M., et al., *Nanoscale* **2018,** *10*, 19443-19449.
25. Seifner, M. S., et al., *ACS Nano* **2018,** *12*, 1236-1241.
26. Pertl, P., et al., *Monatsh. Chem.* **2018**, 1345-1350.
27. Acharya, S., et al., *ACS Appl. Nano Mater.* **2018,** *1*, 5553-5561.
28. Fahrenkrug, E., et al., *Nano Letters* **2014,** *14*, 847-852.
29. Woo, R. L., et al., *Nano Letters* **2009,** *9*, 2207-2211.
30. Morral, A. F. i., et al., *Appl. Phys. Lett.* **2008,** *92*, 063112.
31. Rathi, S. J., et al., *J. Phys. Chem. C* **2011,** *115*, 3833-3839.
32. Yu, L., et al., *Nanotechnology* **2009,** *20*, 225604.
33. Mullane, E., et al., *Chem. Mater.* **2013,** *25*, 1816-1822.
34. Lu, X., et al., *Chem. - Eur. J.* **2014,** *20*, 5874-5879.
35. Geaney, H., et al., *Nano Letters* **2013,** *13*, 1675-1680.
36. Flynn, G., et al., *Chem. Commun.* **2018,** *54*, 5728-5731.
37. Azrak, E., et al., *J. Phys. Chem. C* **2018,** *122*, 26236-26242.

38. Liu, Z., et al., *Sci. Rep.* **2016,** *6*, 38386.
39. Haffner, T., et al., *Phys. Stat. Sol.* **2018,** *215*, 1700743.
40. Assali, S., et al., *Nano Lett.* **2017,** *17*, 1538-1544.
41. Meng, A. C., et al., *Nano Lett.* **2016,** *16*, 7521-7529.
42. Albani, M., et al., *Nanoscale* **2018,** *10*, 7250-7256.
43. Loo, R., et al., *Semiconductor Science and Technology* **2018,** *33*, 114010.
44. Gupta, S., et al., *Nano Letters* **2013,** *13*, 3783-3790.
45. Wacaser, B. A., et al., *Adv. Mater.* **2009,** *21*, 153-165.
46. Assali, S., et al., *J. Appl. Phys.* **2019,** *125*, 025304.
47. Dou, W., et al., *Scientific Reports* **2018,** *8*, 5640.
48. Mårtensson, T., et al., *Nano Letters* **2004,** *4*, 1987-1990.
49. Lan, H. S., et al., *Physical Review B* **2017,** *95*.
50. Dou, W., et al., *Opt Lett* **2018,** *43*, 4558-4561.
51. Stange, D., et al., *ACS Photonics* **2015,** *2*, 1539-1545.
52. Schmidt, T., et al., *Physical Review B* **1992,** *45*, 8989-8994.
53. Foley, P., et al., *Inorg. Chem.* **1975,** *14*, 2264-2267.

6.2 Curriculum Vitae

Michael Stanislaus Seifner

Education

2016 - present	PhD student, Institute of Materials Chemistry, TU Wien
	Supervisor: Privatdozent Dr. Sven Barth
2014 - 2016	MSc degree "Chemie und Technologie der Materialien"
	Joint MSc programme of the TU Wien and the University of Vienna
2010 - 2014	BSc "Technische Chemie" at TU Wien

Research experience abroad

Summer 2015	Materials Chemistry and Analysis Group, University College Cork
	Summer intern in the group of Prof. Justin D. Holmes

Awards

2017	"*Best Master Thesis in Chemistry*" awarded by the Austrian Chemical Society (GÖCH) for my master thesis prepared in 2016 at TU Wien
2018	"*Graduate Student Award*" awarded by the European Materials Research Society (E-MRS) in 2018

Memberships

- Gesellschaft Österreichischer Chemiker (GÖCH)

- Materials Research Society (MRS)

Publishing

1. *"Localized and In-Situ Integration of Different Nanowire Materials for Electronic Nose Applications"*
    G. Domènech-Gil*, L. Hrachowina, A. Pardo, **M. S. Seifner**, I. Gràcia, C. Cané, S. Barth, A. Romano-Rodríguez, *Proceedings* **2019,** *2*, 957.

2. *"Electrical Characterization and Examination of Temperature-Induced Degradation of $Ge_{0.81}Sn_{0.19}$ Nanowires"*
    M. Sistani, **M. S. Seifner**, M. G. Bartmann, S. Smoliner, A. Lugstein, S. Barth*, *Nanoscale* **2018,** *10*, 19443-19449.

3. *"Solution-based low-temperature synthesis of germanium nanorods and nanowires"*
    P. Pertl, **M. S. Seifner**, C. Herzig, A. Limbeck, M. Sistani, A. Lugstein, S. Barth*, *Monatshefte der Chemie - Chemical Monthly* **2018,** *149*, 1315-1320.

4. "*Site-specific growth and in situ integration of different nanowire material networks on a single chip: towards a nanowire-based electronic nose for gas detection*"
    L. Hrachowina, G. Domènech-Gil, A. Pardo, **M. S. Seifner**, I. Gràcia, C. Cané, A. Romano-Rodríguez, S. Barth*, *ACS Sensors* **2018,** *3*, 727-734.

5. *"Direct Synthesis of hyperdoped germanium nanowires"*
    M. S. Seifner, M. Sistani, F. Porrati, G. Di Prima, P. Pertl, M. Huth, A. Lugstein, S. Barth*, *ACS Nano* **2018,** *12*, 1236-1241.

6. *"Pushing the composition limit in anisotropic $Ge_{1-x}Sn_x$ nanostructures and evaluation of their thermal stability*"
    M. S. Seifner, S. Hernandez, J. Bernardi, A. Romano-Rodriguez, S. Barth*, *Chemistry of Materials* **2017,** *29*, 9802-9813.

7. *"Aerosol-assisted CVD of thioether-functionalised indium aminoalkoxides"*
    F. Biegger, F. Jungwirth, **M. S. Seifner**, C. Rameshan, S. Barth*, *Monatshefte der Chemie - Chemical Monthly* **2017,** *148*, 1385-1392.

8. *"Site-selectively grown p-type Ge NWs as a gas sensor"*
    J. Samà*, G. Domènech-Gil, I. Gràcia, J. Santander, C. Cané, **M. S. Seifner**, S. Barth, A. Romano-Rodríguez, *Procedia Engineering* **2016,** *168*, 1056-1060.

9. *"Low temperature humidity sensor based on Ge NWs selectively grown on suspended microhotplates"*
    J. Samà, **M. S. Seifner**, G. Domènech-Gil, J. Santander, C. Calaza, I. Gràcia, S. Barth*, A. Romano-Rodríguez*, *Sensors and Actuators B* **2017,** *243*, 669-677.

10. "*Lead-seeding of germanium nanowires*"
M. S. Seifner, P. Pertl, J. Bernardi, S. Biswas, J. D. Holmes, S. Barth*, *Materials Letters* **2016,** *173*, 248-251.

11. "*Neu zusammengesetzt: Gruppe-14-Elemente als Halbleiter*"
S. Barth*, **M. S. Seifner**, *Nachrichten aus der Chemie* **2015,** *63*, 1172-1175.

12. "*Microwave-assisted $Ge_{1-x}Sn_x$ nanowire synthesis: precursor species and growth regimes*"
M. S. Seifner, F. Biegger, A. Lugstein, J. Bernardi, S. Barth*, *Chemistry of Materials* **2015,** *27*, 6125-6130.

13. "*Microwave-assisted solution–liquid–solid growth of $Ge_{1-x}Sn_x$ nanowires with high tin content*"
S. Barth*, **M. S. Seifner**, J. Bernardi, *Chemical Communications* **2015,** *51*, 12282-12285.

14. "*Growth of monocrystalline In_2O_3 nanowires by seed orientation dependent vapour-solid-solid mechanism*"
S. Barth*, **M. S. Seifner**, J. Bernardi, *Journal of Materials Chemistry C* **2014,** *2*, 5747-5751.

Submitted Papers

- "*Guiding plasmonic beams in ultra-thin monocrystalline aluminium nanowires*"
M. Sistani, M. G. Bartmann, H. Keshmiri, **M. S. Seifner**, S. Barth, M. A. Luong, M. I. den Hertog, J. Smoliner, E. Bertagnolli, A. Lugstein*, *submitted*.

- "*Drastic Changes in Material Composition and Electrical Properties for Gallium-seeded Germanium Nanowires*"
M. S. Seifner, M. Sistani, I. Zivadinovic, M. G. Bartmann, A. Lugstein, S. Barth*, *submitted*.

- "*Epitaxial $Ge_{1-x}Sn_x$ Nanowire and Nanocone Growth using Sn Growth Seeds: Effects of the Seed Diameter and Photoluminescence Properties*"
M. S. Seifner, A. Dijkstra, A. Steiger-Thirsfeld, J. Bernardi, M. Sistani, A. Lugstein, E. P. A. M. Bakkers, J. E. M. Haverkort, S. Barth*, *submitted*.